

HYPERSOUND INTERACTION STUDIED BY TIME-RESOLVED INELASTIC LIGHT AND X-RAY SCATTERING

PUBLIKATIONSBASIERTE DISSERTATION

Zur Erlangung des akademischen Grades
“doctor rerum naturalium”
(Dr. rer. nat.)
in der Wissenschaftsdisziplin: “Experimentalphysik”

eingereicht an der
Mathematisch-Naturwissenschaftlichen Fakultät
der Universität Potsdam

von
André Bojahr
geboren am 08.09.1983 in Berlin

Published online at the
Institutional Repository of the University of Potsdam:
URN urn:nbn:de:kobv:517-opus4-93860
<http://nbn-resolving.de/urn:nbn:de:kobv:517-opus4-93860>

to my wife Juliane

ABSTRACT

This publications-based thesis summarizes my contribution to the scientific field of ultrafast structural dynamics. It consists of 16 publications, about the generation, detection and coupling of coherent gigahertz longitudinal acoustic phonons, also called hypersonic waves. To generate such high frequency phonons, femtosecond near infrared laser pulses were used to heat nanostructures composed of perovskite oxides on an ultrashort timescale. As a consequence the heated regions of such a nanostructure expand and a high frequency acoustic phonon pulse is generated. To detect such coherent acoustic sound pulses I use ultrafast variants of optical Brillouin and x-ray scattering. Here an incident optical or x-ray photon is scattered by the excited sound wave in the sample. The scattered light intensity measures the occupation of the phonon modes.

The central part of this work is the investigation of coherent high amplitude phonon wave packets which can behave nonlinearly, quite similar to shallow water waves which show a steepening of wave fronts or solitons well known as tsunamis. Due to the high amplitude of the acoustic wave packets in the solid, the acoustic properties can change significantly in the vicinity of the sound pulse. This may lead to a shape change of the pulse. I have observed by time-resolved Brillouin scattering, that a single cycle hypersound pulse shows a wavefront steepening. I excited hypersound pulses with strain amplitudes until 1 % which I have calibrated by ultrafast x-ray diffraction (UXRD).

On the basis of this first experiment we developed the idea of the nonlinear mixing of narrowband phonon wave packets which we call *nonlinear phononics* in analogy with the nonlinear optics, which summarizes a kaleidoscope of surprising optical phenomena showing up at very high electric fields. Such phenomena are for instance Second Harmonic Generation, four-wave-mixing or solitons. But in case of excited coherent phonons the wave packets have usually very broad spectra which make it nearly impossible to look at elementary scattering processes between phonons with certain momentum and energy.

For that purpose I tested different techniques to excite narrowband phonon wave packets which mainly consist of phonons with a certain momentum and frequency. To this end epitaxially grown metal films on a dielectric substrate were excited with a train of laser pulses. These excitation pulses drive the metal film to oscillate with the frequency given by their inverse temporal displacement and send a hypersonic wave of this frequency into the substrate. The monochromaticity of these wave packets was proven by ultrafast optical Brillouin and x-ray scattering.

Using the excitation of such narrowband phonon wave packets I was able to observe the Second Harmonic Generation (SHG) of coherent phonons as a first example of nonlinear wave mixing of nanometric phonon wave packets.

KURZDARSTELLUNG

Diese publikationsbasierte Dissertation fasst meinen Beitrag zum Forschungsgebiet der ultraschnellen Strukturodynamik zusammen. Diese Arbeit besteht aus 16 Publikationen aus den Bereichen der Erzeugung, Detektion und Kopplung von kohärenten Gigahertz longitudinal-akustischen Phononen, auch Hyperschallwellen genannt. Um solch hochfrequente Phononen zu erzeugen, werden Femtosekunden nahinfrarot Laserpulse benutzt, um Nanostrukturen auf einer ultraschnellen Zeitskala zu erhitzen. Die aufgeheizten Regionen der Nanostruktur dehnen sich aufgrund der hohen Temperatur aus und ein hochfrequenter Schallpuls wird generiert. Um solche akustischen Pulse zu detektieren benutze ich ultraschnelle Varianten der Brillouin- und Röntgenstreuung. Dabei wird ein einfallendes optisches oder Röntgenphoton an der erzeugten Schallwelle gestreut. Die gemessene Streuintensität ist hierbei ein Maß für die Besetzung einzelner Phononenzustände.

Der zentrale Teil dieser Arbeit ist die Untersuchung von kohärenten Phonon-Wellenpaketen mit sehr hoher Amplitude. Diese Wellenpakete können sich nichtlinear verhalten, sehr ähnlich zu Flachwasserwellen bei denen nichtlineare Effekte in Form eines Aufsteilens der Wellenfronten oder der Existenz von Solitonen, bekannt als Tsunamis, äußern. Durch die hohe Amplitude der akustischen Wellenpakete können sich die akustischen Eigenschaften des Festkörpers in der Umgebung des Schallpulses signifikant ändern, welches sich dann in einer Formänderung des Schallpulses widerspiegelt. Ich konnte mittels zeitaufgelöster Brillouinstreuung das Aufsteilen der Wellenfronten eines Hyperschallpulses bestehend aus einem einzigen Oszillationszyklus beobachten. Hierbei wurden Hyperschallwellen mit einer Dehnungsamplitude von bis zu 1% angeregt, wobei ich diesen Wert mittels ultraschneller Röntgenbeugung kalibrieren konnte.

Mit diesem ersten Experiment als Basis entwickelten wir die Idee der nichtlinearen Wellenmischung von schmalbandigen Phonon-Wellenpaketen unter dem Titel *nichtlineare Phononik* in Analogie zur nichtlinearen Optik, welche sich aus einer Reihe von verblüffenden optischen Phänomenen bei sehr hohen elektrischen Feldstärken zusammensetzt. Solche Phänomene sind z. B. die optische Frequenzverdopplung, das Vier-Wellen-Mischen oder Solitone. Nur sind im Falle von kohärenten Phononen die erzeugten Spektren sehr breitbandig, was die Untersuchung von spezifischen Phononen mit festem Impuls und definierter Frequenz fast unmöglich macht.

Aus diesem Grund testete ich verschiedene Methoden um schmalbandige Phonon-Wellenpakete anzuregen, welche im Wesentlichen aus Phononen bestimmten Impulses und definierter Frequenz bestehen. Dafür wurden schließlich epitaktisch auf ein dielektrisches Substrat aufgewachsene Metallfilme mit einem Laserpulszug angeregt. Hier sorgen die Lichtpulse für eine periodische Oszillation des Metalfilms, wobei die Anregungsfrequenz durch den inversen zeitlichen Abstand der Lichtpulse gegeben ist. Diese periodische Oszillation sendet dann ein Hyperschallwellenpaket eben dieser Frequenz ins Substrat. Die Monochromie dieser Wellenpakete konnte dabei mittels ultraschneller Brillouin- und Röntgenstreuung

bestätigt werden. Durch die Benutzung dieser schmalbandigen Phonon-Wellenpakete war es mir möglich, die Frequenzverdopplung (SHG) von kohärenten Phononen zu beobachten, was ein erstes Beispiel für die nichtlineare Wellenmischung von nanometrischen Phonon-Wellenpaketen ist.

CONTENTS

List of Papers	xi
Comments on Papers	xv
List of Figures	xxiii
1 Introduction	1
2 Generation of Hypersound	5
2.1 Two Temperature Model	5
2.2 Stress generation using ultrashort laser pulses	7
2.3 Classification of different phonon excitation mechanisms	9
2.4 The evolution of sound in a solid	11
2.4.1 Harmonic linear chain and acoustic wave equation of a solid	11
2.4.2 Thermoelastic stress as a source for sound	12
2.4.3 The solution of the 1D forced wave equation in free space	12
2.4.4 Describing a photoexcited metal film on a substrate using the 1D forced wave equation	13
3 Light and Sound Interaction	21
3.1 Why photons are influenced by phonons	21
3.2 Kinematic treatment of Brillouin Scattering	23
3.3 Experimental conditions	24
3.4 Dynamical treatment of light scattering on acoustic phonons	26
3.4.1 Maxwell's equations and the wave equation in a stratified medium	26
3.4.2 Reflection of Dirac like change of the dielectric constant	28
3.4.3 Reflection coefficient of a sound wave in a medium	30
3.5 Complete reflection contribution in a pump-probe experiment	30
4 Nonlinear Sound	35
4.1 The Fermi-Pasta-Ulam chain	36
4.2 Continuum approximation of the extended FPU chain	36
4.2.1 Boussinesq equation	37
4.2.2 Korteweg-de Vries equation	38
4.2.3 Viscous Burgers equation	38
4.3 Nonlinear elastic theory	41
5 Summary and Outlook	43
Bibliography	45
Acknowledgments	51

Papers

I	Comparing the oscillation phase in optical pump-probe spectra to ultrafast x-ray diffraction in the metal-dielectric SrRuO ₃ /SrTiO ₃ superlattice	55
II	Ultrafast lattice response of photoexcited thin films studied by X-ray diffraction	63
III	udkm1Dsim - A Simulation Toolkit for 1D Ultrafast Dynamics in Condensed Matter	79
IV	Brillouin scattering of visible and hard X-ray photons from optically synthesized phonon wavepackets	93
V	Detecting optically synthesized quasi-monochromatic sub-terahertz phonon wavepackets by ultrafast x-ray diffraction	105
VI	Direct time-domain sampling of subterahertz coherent acoustic phonon spectra in SrTiO ₃ using ultrafast x-ray diffraction	111
VII	Observing backfolded and unfolded acoustic phonons by broadband optical light scattering	121
VIII	Selective preparation and detection of phonon polariton wavepackets by stimulated Raman scattering	129
IX	Normalization schemes for ultrafast x-ray diffraction using a table-top laser-driven plasma source	139
X	Ultrafast reciprocal-space mapping with a convergent beam	149
XI	Time-domain sampling of x-ray pulses using an ultrafast sample response	157
XII	Ultrafast switching of hard X-rays	163
XIII	Second Harmonic Generation of Nanometric Phonon Wave Packets	171
XIV	Calibrated real-time detection of nonlinearly propagating strain waves	179
XV	Coupling of GHz Phonons to Ferroelastic Domain Walls in SrTiO ₃	187
XVI	Following Strain-Induced Mosaicity Changes of Ferroelectric Thin Films by Ultrafast Reciprocal Space Mapping	195

LIST OF PAPERS

This thesis is based on the accumulation of 16 publications to which I contributed as author or co-author during my PhD thesis. The following is a list of all publications including a short summary and description of my respective contributions to the work. The publications are assigned to the three main topics of this thesis **Generation of Hypersound**, **Light and Sound Interaction** and **Nonlinear Sound**.

Generation of Hypersound

I Comparing the oscillation phase in optical pump-probe spectra to ultrafast x-ray diffraction in the metal-dielectric SrRuO₃ /SrTiO₃ superlattice

A. Bojahr, D. Schick, L. Maerten, M. Herzog, I. Vrejoiu, C. von Korff Schmising, C. J. Milne, S. L. Johnson and M. Bargheer.
Phys. Rev. B **85**, 224302 (2012).

II Ultrafast lattice response of photoexcited thin films studied by X-ray diffraction

D. Schick, M. Herzog, A. Bojahr, W. Leitenberger, A. Hertwig, R. Shayduk and M. Bargheer.
Structural Dynamics **1**, 6 (2014).

III udkm1Dsim - A Simulation Toolkit for 1D Ultrafast Dynamics in Condensed Matter

D. Schick, A. Bojahr, M. Herzog, R. Shayduk, C. von Korff Schmising and M. Bargheer.
Rev. Sci. Instrum. **83**, 025104 (2012).

Light and Sound Interaction

IV Brillouin scattering of visible and hard X-ray photons from optically synthesized phonon wavepackets

A. Bojahr, M. Herzog, S. Mitzscherling, L. Mearten, D. Schick, J. Goldshteyn, W. Leitenberger, R. Shayduk, P. Gaal and M. Bargheer.
Opt. Express **21**, 18 (2013).

V Detecting optically synthesized quasi-monochromatic sub-terahertz phonon wavepackets by ultrafast x-ray diffraction

M. Herzog, A. Bojahr, J. Goldshteyn, W. Leitenberger, I. Vrejoiu, R. Shayduk, D. Khakhulin, M. Wulff, R. Shayduk, P. Gaal and M. Bargheer.
Appl. Phys. Lett. **100**, 094101 (2012).

VI Direct time-domain sampling of subterahertz coherent acoustic phonon spectra in SrTiO₃ using ultrafast x-ray diffraction

R. Shayduk, M. Herzog, A. Bojahr, D. Schick, P. Gaal, W. Leitenberger, H. Navirian, M. Sander, J. Goldshteyn, I. Vrejoiu and M. Bargheer.
Phys. Rev. B **87**, 184301 (2013).

VII Observing backfolded and unfolded acoustic phonons by broadband optical light scattering

L. Maerten, A. Bojahr and M. Bargheer.
Ultrasonics **56**, 148-152 (2015).

VIII Selective preparation and detection of phonon polariton wavepackets by stimulated Raman scattering

J. Goldshteyn, A. Bojahr, P. Gaal, D. Schick and M. Bargheer.
Phys. Status Solidi B **251**, 821-828(2014).

IX Normalization schemes for ultrafast x-ray diffraction using a table-top laser-driven plasma source

D. Schick, A. Bojahr, M. Herzog, C. von Korff Schmising, R. Shayduk, W. Leitenberger, P. Gaal and M. Bargheer.
Rev. Sci. Instrum. **83**, 025104 (2012).

X Ultrafast reciprocal-space mapping with a convergent beam

D. Schick, R. Shayduk, A. Bojahr, M. Herzog, C. von Korff Schmising, P. Gaal and M. Bargheer.
J. Appl. Cryst. **46**, 1372-1377 (2013).

XI Time-domain sampling of x-ray pulses using an ultrafast sample response
P. Gaal D. Schick, M. Herzog, A. Bojahr, R. Shayduk , J. Goldshteyn, H. Navirian,
W. Leitenberger, I. Vrejoiu, D. Khakhulin, M. Wulff, and M. Bargheer.
Appl. Phys. Lett. **101**, 243106 (2012).

XII Ultrafast switching of hard X-rays
P. Gaal D. Schick, M. Herzog, A. Bojahr, R. Shayduk , J. Goldshteyn,
W. Leitenberger, I. Vrejoiu, D. Khakhulin, M. Wulff, and M. Bargheer.
J. Synchrotron Rad. **21**, 380-385 (2014).

Nonlinear Sound

XIII Second Harmonic Generation of Nanometric Phonon Wave Packets
A. Bojahr, M. Roessle, P. Gaal, W. Leitenberger, P. Pudell, M. Reinhard,
A. von Reppert, M. Sander and M. Bargheer.
Phys. Rev. Lett. **115**, 195502 (2015).

XIV Calibrated real-time detection of nonlinearly propagating strain waves
A. Bojahr, M. Herzog, D. Schick, I. Vrejoiu and M. Bargheer.
Phys. Rev. B **86**, 144306 (2012).

XV Coupling of GHz Phonons to Ferroelastic Domain Walls in SrTiO₃
L. Mearten, A. Bojahr, M. Gohlke, M. Roessle and M. Bargheer.
Phys. Rev. Lett. **114**, 047401 (2015).

**XVI Following Strain-Induced Mosaicity Changes of Ferroelectric Thin Films
by Ultrafast Reciprocal Space Mapping**
D. Schick, A. Bojahr, M. Herzog, I. Vrejoiu and M. Bargheer.
Phys. Rev. Lett. **110**, 095502 (2013).

COMMENTS ON PAPERS

Here, I present the respective key statement(s) of the papers listed in the previous section. The summary is followed by an outline of my contributions to each of these papers.

I Comparing the oscillation phase in optical pump-probe spectra to ultrafast x-ray diffraction in the metal-dielectric SrRuO₃ /SrTiO₃ superlattice

In this paper we have investigated the oscillation phase of optical reflectivity and x-ray diffraction of a photoexcited superlattice. This phase contains information about the mechanisms involved in the stress generation process in SrRuO₃. We have found that the phase of the reflectivity measurements is wavelength-dependent and has to be carefully interpreted: around the Fabry-Pérot maxima and minima of the superlattice the phase of the optical reflectivity oscillations shifts depending on the probe wavelength and makes statements about the excitation mechanism difficult. However, after carefully determining time zero with optical reflectivity experiments using the appropriate wavelength region together with x-ray diffraction experiments we discovered a fluence-dependent oscillation phase. The lattice responds faster to an excitation with higher fluence. This quite unusual behavior of SrRuO₃ has led us to the conclusion that, in addition to normal heating, some alternative excitation mechanisms like occupation of antibonding orbitals or temperature dependent Grüneisen coefficients are responsible for the particular behaviour of SrRuO₃.

For this publication I have performed the simulations of the optical reflectivity change after photoexcitation, participated in the optical reflectivity experiments and x-ray diffraction measurements with our x-ray plasma source, and have contributed to build the manuscript. Moreover, I have been actively involved in the interpretation of all of the experimental results.

II Ultrafast lattice response of photoexcited thin films studied by X-ray diffraction

Here we present ultrafast x-ray diffraction results of photoexcited SrRuO₃ thin films. After the excitation with an ultrashort laser pulse the SrRuO₃ film expands and sends a sound pulse into the SrTiO₃ substrate. The observed dynamics in the film are described by an analytical solution of the one-dimensional linear wave equation with an instantaneous excitation of the phonon system.

I have helped to build and align the experimental setup used for the measurements and have participated in the data acquisition process. Furthermore, I have actively contributed to the theoretical treatment of the experimental results.

III `udkm1Dsim` - A Simulation Toolkit for 1D Ultrafast Dynamics in Condensed Matter

In this publication we present a software toolkit based on MATLAB (MathWorks Inc.), which can be used to calculate the one-dimensional lattice response of a material after laser excitation. Therefore we use an N-temperature model and heat-diffusion to describe the differently excited subsystems of the material after excitation and their spatial changes. The underlying model for the calculated lattice dynamics is a linear chain with nearest-neighbour interaction that also can take nonlinear coupling terms into account which can be arbitrarily specified. Moreover, the toolkit allows calculating the transient x-ray diffraction by the temporally changing lattice.

For this work I have developed important parts of the numerical algorithms to calculate the transient changes of the coherent sound and introduced several code enhancements for faster calculations. Moreover, I have been strongly involved in the discussion and implementation of the theoretical concepts used in this toolkit.

IV Brillouin scattering of visible and hard X-ray photons from optically synthesized phonon wavepackets

We present a generalized view of time-resolved visible light and x-ray scattering on acoustic phonons as variants of time domain Brillouin scattering. By subsequent excitation of a SrRuO₃ film with a femtosecond laser pulse train, we are able to generate a narrow-band phonon wave packet. Probing this wave packet with optical light proves that each wave vector component of the probe light is only sensitive to a certain phonon wave vector of the excited wave packet, which allows to probe different wave vectors simultaneously by using a supercontinuum probe. This direct connection between phonon and photon wave vector gives the scattering of light absolutely the same to measure the wave vector of the phonons as in inelastic x-ray scattering.

In this study I have been highly involved in the measurements of the presented optical and x-ray data sets. I have written the manuscript and developed the theoretical concepts presented in the paper.

V Detecting optically synthesized quasi-monochromatic sub-terahertz phonon wavepackets by ultrafast x-ray diffraction

In this work we excite a SrRuO₃ film deposited on a SrTiO₃ substrate with a laser pulse train consisting of 8 pulses. Using time-resolved x-ray diffraction we observe directly after excitation sidepeaks appear around the (002) substrate peak which are displaced by the amount of the central wave vector of the excited wave packet and integer multiples. These measurements show that the wave vector and bandwidth of the excited wave packet can be controlled by shaping the optical pulse train in the desired way. In addition, we observe a very short lifetime of the excited fundamental wave of around 130 ps which we attribute to Akhiezer's mechanism and thermoelastic damping.

For this publication I have been involved in the acquisition of the presented x-ray data sets and in the data analysis. I participated in the development of the manuscript and the writing process.

VI Direct time-domain sampling of subterahertz coherent acoustic phonon spectra in SrTiO₃ using ultrafast x-ray diffraction

A sub-THz longitudinal narrow-band acoustic phonon wave packet has been generated in SrTiO₃ via the ultrafast laser excitation of a SrRuO₃/SrTiO₃ superlattice. We monitor the excited coherent phonon spectrum using time-resolved x-ray diffraction at our BESSY beamline. Our analysis exhibits a wave vector dependent damping of the first and second order of the excited narrowband phonons, which is in good agreement with Akhiezer's model for hypersound attenuation.

I suggested this experiment with this particular superlattice and have been highly involved in the interpretation of the experimental outcomes.

VII Observing backfolded and unfolded acoustic phonons by broadband optical light scattering

In this publication we investigated with broadband time-domain Brillouin scattering photoexcited longitudinal acoustic phonon modes in bulk and nanolayered samples. After Fourier transforming the transient data we compare our results with calculated dispersion relations. Using a superlattice with a large period we are able to detect phonons within nearly the whole Brillouin zone.

For this paper I have performed measurements using broadband time domain Brillouin scattering. Furthermore, I have been involved in the paper writing process and in the fundamental discussion about the underlying physics.

VIII Selective preparation and detection of phonon polariton wavepackets by stimulated Raman scattering

In this publication we demonstrate how to impulsively excite narrow-band phonon polariton wave packets by shining a femtosecond transient grating into a LiNbO₃ crystal. We use a narrow-band probe technique to resolve Stokes and anti-Stokes shifted probe pulses with a spectrometer. These measurements directly prove the inelastic nature of light scattering on moving gratings. By the analysis of the four-wave mixing process we show that these measurements can be understood in terms of two subsequent stimulated Raman scattering events.

For this paper I have supported the experiment, and have been deeply involved in the conceptual development of the experiments and their theoretical description. I also have contributed to the paper writing process.

IX Normalization schemes for ultrafast x-ray diffraction using a table-top laser-driven plasma source

In this paper we present our lab-based femtosecond x-ray diffraction experimental setup based on a commercially available laser-driven x-ray plasma source. We introduce different normalization schemes to reduce the influence of the x-ray source intensity fluctuations on the the acquired datasets, which results in a significantly improved signal-to-noise ratio.

For this paper I have been heavily involved in the construction of the experimental setup. I furthermore developed important parts of the data acquisition software and contributed valuable knowledge to several normalization schemes.

X Ultrafast reciprocal-space mapping with a convergent beam

In this follow-up publication we present how we use our laser-driven plasma x-ray source for reciprocal-space mapping with femtosecond temporal resolution. We show a reciprocal space map of a mosaic sample and showed that this technique is suitable to get high quality, time-resolved data of nearly perfect heterostructures. Furthermore we derive a coordinate transform that transfers from angle to wave vector space.

For this work I have contributed to the construction of the experimental setup, developed important parts of the data acquisition software, and contributed to the finalization of the publication.

XI Time-domain sampling of x-ray pulses using an ultrafast sample response

This work introduces an interesting application for the photoinduced coherent expansion of thin heterostructures. We use a ultra thin SrRuO₃ film on a SrTiO₃ substrate as Bragg reflector with a fixed Bragg angle. The diffraction efficiency can be switched on and off within 5 ps due to the coherent sound generated in the film. Cross-correlation measurements between the laser pump which triggers the coherent sound and the synchrotron x-ray pulse allow us to reconstruct the x-ray pulse shape.

For this work I have performed measurements using the plasma x-ray source at the University of Potsdam and have participated in the measurements at the European Synchrotron Radiation Facility.

XII Ultrafast switching of hard X-rays

Here we show a new concept for shortening x-ray pulses produced by a third-generation synchrotron down to a few picoseconds. The development concludes in a device called PicoSwitch that consists of a thin film, which gets photoexcited, on a substrate. The excitation triggers coherent phonons that change transiently the lattice constants of the film and therefore the Bragg reflection condition changes. The device is tested in a real synchrotron-based pump-probe experiment and offers a greatly enhanced time-resolution.

For this work I performed measurements using the plasma x-ray source at the University of Potsdam and have been involved in the measurements at the European Synchrotron Radiation Facility.

XIII Second Harmonic Generation of Nanometric Phonon Wave Packets

This paper reveals the first observation of the upconversion of nanometric hypersonic phonons using time-resolved x-ray and visible light scattering. We show the second harmonic generation of an excited narrow-band phonon wave packet and describe the results using a chain of nonlinearly coupled oscillators. This paper is an important step in physics, which may enable nonlinear phononics, in a way towards using phonons like photons in nonlinear optics. The result of nonlinear phononics may help to build new functional devices with artificial thermal properties.

For this paper I have developed the experimental setups, measured the time-resolved optical data, and have contributed to the conception of the beamtime and participated in the x-ray diffraction measurements at the European Synchrotron Radiation Facility. In addition I analysed the data sets, developed the theory and wrote the manuscript.

XIV Calibrated real-time detection of nonlinearly propagating strain waves

In this paper we generate high amplitude strain pulses in an epitaxially grown metallic film, which propagate into the substrate. We performed excitation fluence dependent time-resolved optical Brillouin scattering measurements in order to follow the strain pulse evolution. These fluences were calibrated to the induced strain using ultrafast x-ray diffraction measurements. For high fluences the leading compressive part of the strain pulse propagates significantly faster than the trailing expansive part. This behaviour is well explained by a model consisting of a chain of nonlinear interacting oscillators.

For this paper I have performed time-resolved optical Brillouin scattering experiments as well as ultrafast x-ray diffraction measurements at the plasma x-ray source of the University of Potsdam. In addition, I wrote the manuscript and developed the underlying computational code of the linear chain calculation.

XV Coupling of GHz Phonons to Ferroelastic Domain Walls in SrTiO₃

In this publication the linear and nonlinear acoustic response of SrTiO₃ across its ferroelastic phase transition has been studied in detail by time domain Brillouin scattering. For high strain amplitudes we observe a giant slowing down of the sound velocity by 12% and attribute this to the coupling of GHz phonons to ferroelastic twin domain walls. We support our interpretations by a microscopic picture of the underlying coupling mechanism.

Here I was heavily involved in the data analysis process, the interpretation of the results, the model building process, and the finalization of the manuscript.

XVI Following Strain-Induced Mosaicity Changes of Ferroelectric Thin Films by Ultrafast Reciprocal Space Mapping

In this paper we investigate the coherent phonon propagation in a thin ferroelectric PbZr_{0.2}Ti_{0.8}O₃ (PZT) film using time-resolved reciprocal space mapping. For expansive strain the mosaic film exhibits a strong coupling of the out-of-plane and in-plane sound propagation directions which immensely increases the damping of the expansive part of the excited longitudinal strain wave. This coupling is interestingly not visible for compressive strain. This fact is attributed to the presence of columnar defects in the PZT layer.

For this work I have performed measurements using the plasma x-ray source at the University of Potsdam and have taken part in the model calculations of the partially damped propagating strain pulse.

LIST OF FIGURES

2.1	Typical transient change of electronic and phononic temperatures	6
2.2	DECP and ISRS as excitation mechanism	10
2.3	Schematic of a metal film on a substrate	13
2.4	Strain evolution of a photo-excited metal on a dielectric substrate	16
3.1	Visualization of the dominant resonant Raman scattering contributions	22
3.2	Quasi-elastic back-scattering geometry	23
3.3	Scheme of the optical pump-probe setup	25
3.4	Reflection on a sound wave in a medium	28
3.5	Different reflection contributions for front and backside probe	31
4.1	Evolution of a nonlinearly propagating strain pulse in SrTiO ₃ at room temperature	40

INTRODUCTION

Today's high tech is mainly based on electronics. In the last decades engineers have learned to build highly complex electric circuits and shrank it to the nanometer scale. They put millions of logic gates on a square millimeter with transistors working in the GHz range. Such high frequency currents lead inevitably to an enormous friction loss which converts electric energy to waste heat. Due to the size reduction of the integrated circuits this heat production became an intrinsic problem of today's processor generations; it sets limits to the maximal possible computational power of the circuits.

One idea for future integrated circuits is to use photons instead of electrons, but visible light which is easy to manage has a wavelength in the range of hundreds of nanometers. This sets unpractical limits to the size of the possible devices, which can be overcome by the use of surface plasmon polaritons as the information carrying particle in circuits.[1] They are as fast as light which makes it possible to transfer light information directly into plasmons. But surface plasmon polaritons are collective excitations of light and electrons, therefore they also produce heat. Thus, it seems that the heat problem will be there also in next generation technology. The main heat carrying particle in a semiconductor is the phonon.

Phonons are the quantized particles of lattice vibrations. These quasiparticles are bosons and carry a certain energy and momentum. Their quantum mechanical consequences are the low-temperature heat capacity of crystals and the blackbody-radiation. At room temperature the heat capacity of phonons is orders of magnitudes larger than of electrons, as a result the main fraction of heat is carried by phonons.

The ability to manipulate phonons in such a way as we utilize electrons and photons today opens up new opportunities for future technology.[2] Because of the technical importance of a better heat transport on the nanometer scale several groups investigated heat transport in artificial nano-structures.[3–7] The diffusive or ballistic character of heat conduction is determined by phonon-phonon scattering processes. This is also important for new highly efficient thermoelectric materials, which transform waste heat back to electric energy.[8–10]

The key point is to understand, measure and manipulate the coupling between different phonons with frequencies of gigahertz until terahertz, because these are the phonons which contribute mainly to heat. Theory predicts by the use of a modified phonon coupling the possibility of thermal diodes which define the direction of heat flow as well as thermal memory devices.[11, 12] Such rectification of heat current could finally lead to the realization of thermal transistors and thermal logic gates, which implies that future integrated circuits could use phonons directly as information carrying particle.[13]

The aim of this work is to establish measurement techniques in which specific acoustic phonons of such high frequencies as discussed before are coherently excited so the coupling to other degrees of freedom can be investigated. Here I set the main focus to the anharmonic coupling between phonons, which promises a new scientific field called *Nonlinear Phononics* [14], as an analog to nonlinear optics where intense photon packets can interact with each other in a nonlinear medium. In optics this led to a kaleidoscope of different optical effects as the second harmonic generation, the generation of coherent white light or the optical parametric amplification. The use of coherent phonons has the advantage that the mode specific coupling can be directly measured. However in thermal measurements, information is obtained which is the average effect of a large number different phonons, so the main important phonon coupling channels are not visible here.

In the center of this work stands the generation of hypersonic narrow-band coherent phonon wave packets and the measurement of their spectral composition at different times after excitation using time-resolved Brillouin scattering and ultrafast x-ray diffraction. As this dissertation is a cumulative work, the main results are found in the attached publications which are numbered by Roman numerals. I classified the overall 16 publication of this thesis into three categories which are identical with the three chapters **Generation of Hypersound**, **Light and Sound Interaction** as well as **Nonlinear Sound** of this thesis. The assignment of the different publications to these categories is not unique. Several publications discuss physics of all three categories, however the main outcome of each publication is used for assignment.

In the related chapters I condensed important and fundamental knowledge in these three categories. These details go beyond the information in my publications because some of this is anticipated knowledge of the readership and other parts were cut due to the restricted length of scientific papers. I hope that these concise descriptions of the basics needed for conducting experiments and simulations may help students and scientists entering the field.

- The chapter "**Generation of Hypersound**" contains common knowledge about the strain generation processes in solids as well as an analytic discussion of the evolution of sound in a solid after laser excitation. Furthermore the added value of the papers **I**, **II** and **III** to the understanding of the generation of ultrasound in opaque materials is discussed.
- In chapter "**Light and Sound Interaction**" I summarize how visible light interacts with phonons via inelastic light scattering in case of acoustic phonons also known as Brillouin scattering. Then I present the experimental setup for time-resolved optical Brillouin scattering. And finally I show that the reflectivity of a material changes due to induced acoustic waves where the reflectivity change for a certain optical wavelength is a measure of the occupation number of a phonon with a certain energy. The generation and detection of hypersonic narrow-band phonon wave packets is summarized in Paper **IV**.
- The chapter "**Nonlinear Sound**" contains the theory of nonlinear propagating phonon wave packets in form of a Fermi-Pasta-Ulam (FPU) chain which was used in the publications **XIII** and **XIV** and relates this to a number of different nonlinear wave equations used in nonlinear acoustics. The aim of this chapter is to show that the FPU chain is the root of numerous one-dimensional nonlinear wave equations typically used in nonlinear acoustics.

In my opinion the publications **IV**, **XIII** and **XIV** build the central core of this work, where Paper **XIII** presents the main new physics in this thesis. It shows the Second Harmonic Generation of GHz phonon wave packets, and is therefore a first example of nonlinear wave mixing for very high frequency acoustic phonons in analogy to nonlinear optics.

Besides this, I contributed substantially to the establishing of ultrafast x-ray diffraction using a tabletop x-ray source in Potsdam which reflects in the publications **IX**, **X**, **II** and **XVI**. In particular, these papers build the core of the PhD thesis of Daniel Schick [15], whereas the essence of my work stands out by combining ultrafast x-ray diffraction with all-optical pump probe measurements to benefit from the pros of both techniques. Moreover, our group used metal-insulator hetero-structures to excite high frequency phonon modes and detect them by ultrafast optical and x-ray methods. Here I contributed as author and coauthor to the publications **I**, **VI**, **XI** and **XII** where the last two publications describe the application of ultrafast lattice dynamics to switch hard x-ray light due to the modulation of the Bragg diffraction. This is summarized in the PhD thesis of Marc Herzog [16] with whom I performed first experiments to excite hypersonic narrowband phonon wave packets and detected them by x-ray diffraction which can be found in publication **V**. In addition to x-ray scattering I also performed time-resolved optical spectroscopy where in paper **VII** we studied the optical light scattering from phonons excited in hetero-structures and metal films in more detail. Such light scattering on phonons was used in publication **XV** to look at the interaction of GHz acoustic waves with ferroelastic domain walls in strontium titanate. Finally, in publication **VIII** we investigated light scattering on phonon-polaritons which shows nicely the inelastic nature of light scattering on quasi-particles.

GENERATION OF HYPERSOUND

In this chapter I will review a few theoretical concepts, which describe the stress and strain generation in solids. The chapter's aim is to lay out basic knowledge of ultrafast stress generation processes using simple models which can be understood as an introduction to the Papers **I**, **II** and **III**. At first I will discuss the so called Two Temperature Model as the easiest case, neglecting diffusion of carriers and heat and introduce electron-phonon coupling as well as electronic and phononic stress as the main reasons of the hypersound generation in metals. Using this context, I will classify the excitation processes of Displacive Excitation of Coherent Phonons (DECP) and Impulsive Stimulated Raman Scattering (ISRS). Secondly, I will introduce a forced linear and one-dimensional wave equation which describes the dynamics of the excited propagating strain, which mostly fall short in corresponding publications of the chapter. I will present a complete analytic solution of strain dynamics of a photoexcited metal film on a transparent substrate. At the end of this chapter, I will show strain profiles for different excitation conditions and their spectral signature, which are important for probing with x-rays and optical light.

2.1 Two Temperature Model

One way to describe the excitation process of an optically excited material is to divide the material into different subsystems i (electrons, phonons, magnetic system ...), which have some thermal energy $Q_i = c_i T_i$ stored, where c_i and T_i are the specific heat and temperature of the subsystem i . These subsystems are coupled that energy can flow between them. For typical metals it is usually sufficient to describe the whole excitation process using only electrons and phonons as subsystems ($i = e, p$). Mathematically, one can describe such behavior with coupled partial differential equations following Paper **III** as well as [17, 18]:

$$\begin{aligned}
 c_e(T_e) \frac{\partial T_e}{\partial t} &= -g(T_e - T_p) + \frac{\partial}{\partial z} \left(k_e(T_e) \frac{\partial T_e}{\partial z} \right) \\
 c_p(T_p) \frac{\partial T_p}{\partial t} &= g(T_e - T_p) + \frac{\partial}{\partial z} \left(k_p(T_p) \frac{\partial T_p}{\partial z} \right)
 \end{aligned} \tag{2.1}$$

The first term on the right side of eqs. (2.1) describes the coupling between the subsystems of the material with the coupling constant g whereas the second term represents the heat diffusion within the individual subsystem. These partial differential equations are typically nonlinear, because k_i is usually temperature dependent, and can be solved

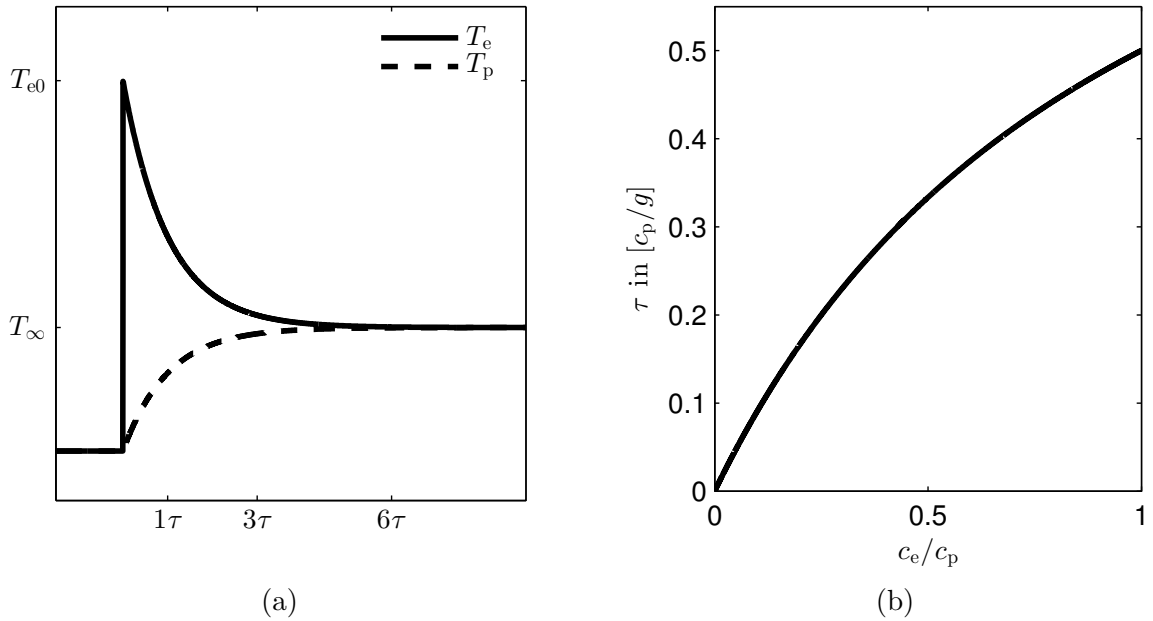


Figure 2.1: (a) Typical transient change of electronic and phononic temperatures. The electronic system is excited at time zero, which drives the entire system out of equilibrium. Energy flows to the phononic system until both subsystems have the same temperature. (b) Change of relaxation time τ in dependence of the ratio of electronic and phononic specific heat. As example: For SrRuO_3 c_e/c_p reaches unity at an electron temperature of $\approx 3400\text{K}$ using the Dulong-Petit limit for phonons and the Sommerfeld coefficient for the electrons as published in [19].

numerically. Our toolkit presented in Paper **III** can solve these equations with given temperature dependencies of the parameters. A spatial dependence is also possible. In this thesis we are content with the case of no diffusion, which simplifies the situation to a set of linear and coupled ordinary differential equations. In the case of a metal we can assume a sole excitation of the electronic system which leads to a non-equilibrium state where $T_e \neq T_p$. This situation can be described by an initial value problem with $T_e(t=0) = T_{e0}$ and $T_p(t=0) = 0$ where T_{e0} is the temperature step of the electronic system due to laser excitation. This simulates a delta-like excitation pulse. Keeping c_e and c_p for simplicity independent of temperature,

$$\begin{aligned} c_e \frac{\partial T_e}{\partial t} &= -g(T_e - T_p) \\ c_p \frac{\partial T_p}{\partial t} &= g(T_e - T_p) \end{aligned} \quad (2.2)$$

can easily be solved using the Laplace transform and its identities for derivatives. The solution of this model is given by:

$$\begin{aligned} T_e(t \geq 0) &= T_\infty \left(1 + \frac{c_p}{c_e} \exp(-r \cdot t) \right) \\ T_p(t \geq 0) &= T_\infty \left(1 - \exp(-r \cdot t) \right) \end{aligned} \quad (2.3)$$

$$r = g \frac{c_e + c_p}{c_e c_p}, \quad T_\infty = T_{0e} \frac{c_e}{c_e + c_p} \quad (2.4)$$

A typical transient situation of both subsystem temperatures can be found in Fig. 2.1a. T_∞ is the temperature of both systems in thermal equilibrium, which is reached for $t = \infty$. One important finding is that the rate r depends on the ratio of the relative magnitudes of the specific heats. Using the definition of r in eq. (2.4), we can plot the inverse rate $\tau = 1/r$ as a function of c_e/c_p assuming constant g and c_p (Fig. 2.1b). As visible in Figure 2.1b, the model predicts a longer relaxation for a higher specific heat of the electrons.

In real physical systems the specific heat of electrons usually rises linearly with temperature whereas for phonons it can be assumed constant.[20, 21]¹ Following this easy model the system needs more time to relax at temperatures well above the Debye temperature, which leads to a less rapid buildup of phononic stress.

The Two Temperature Model is a simplification of the circumstances. First, one assigns temperatures for electrons and phonons but if one would model the systems more precisely one would also need to consider non thermal distributions, as has been done for electrons.[25] Second, diffusive transport of electrons is often a bad approximation because in many materials electrons can travel ballistically over distances of several tens or hundreds of nanometers.[26] Here people changed the diffusive terms to parabolic differential equations or solved the Boltzmann transport equation directly.[27, 28] And third, phonons can transport heat ballistically, too. It was recently shown, that phonon heat transport can significantly deviate from Fourier's law already on a μm length scale.[29]

2.2 Stress generation using ultrashort laser pulses

To understand the origin of laserinduced stress in opaque materials the concept of Grüneisen parameters can be introduced. Microscopically the Grüneisen parameter is the ratio between the relative energy change of a quantum state and the applied relative volume change to the system. A thermodynamic identity for a Grüneisen parameter γ of a physical system with internal energy U , pressure P and volume V is [30, p. 17]

$$\gamma = V \left[\frac{\partial P}{\partial U} \right]_V. \quad (2.5)$$

In words, the Grüneisen parameter describes how the pressure of a gas changes when we change its energy by letting the volume constant. For a metal it is sufficient to think about two gases (electrons and phonons) with specific energies and Grüneisen parameters. Therefore each gas contributes to the overall pressure of the crystal. In crystals it is common to use the concept of stresses σ_i instead of pressure. Stress can be anisotropic and has the opposite sign of pressure. As discussed before the overall stress σ is the sum of electronic (σ_e) and phononic (σ_p) stress. The induced stress after photoexcitation of a crystal along the [001] direction is then given by the occupation number density changes

¹In the Debye model the specific heat of phonons reaches a constant value for high enough temperatures. This is known as Dulong-Petit's law. However phonon-phonon interaction which is neglected in the Debye model leads to a small deviation from this law and a linear temperature dependence of phonon specific heat was found. [22–24]

$\delta n_i(\mathbf{k})$ of the possible state energies $E_i(\mathbf{k})$ and their specific Grüneisen parameters $\gamma_i(k)$. Here, \mathbf{k} represents the wave vector of the phonons and electrons:[31–34]

$$\sigma = \sigma_e + \sigma_p = - \sum_{\mathbf{k}} \gamma_e(\mathbf{k}) E_e(\mathbf{k}) \delta n_e(\mathbf{k}) - \sum_{\mathbf{k}} \gamma_p(\mathbf{k}) E_p(\mathbf{k}) \delta n_p(\mathbf{k}) \quad (2.6)$$

In this content the mode specific Grüneisen parameter is given by the relative energy change of a state with strain ϵ , $\gamma_i(\mathbf{k}) = -\frac{1}{E_i(\mathbf{k})} \frac{\partial E_i(\mathbf{k})}{\partial \epsilon}$. Using this relation eq. (2.6) changes to

$$\sigma = \sum_{\mathbf{k}} \frac{\partial E_e(\mathbf{k})}{\partial \epsilon} \delta n_e(\mathbf{k}) + \sum_{\mathbf{k}} \frac{\partial E_p(\mathbf{k})}{\partial \epsilon} \delta n_p(\mathbf{k}) \quad (2.7)$$

For an arbitrary crystal consisting mainly of electrons and lattice (phonons) eq. (2.7) specifies the overall stress in dependence of the occupation of electrons and phonons. In semiconductor physics the derivative $\frac{\partial E_e(\mathbf{k})}{\partial \epsilon}$ is called deformation potential. It tells us the change of electronic states by stretching or contracting the crystal. The use of eq. (2.7) needs a good knowledge about the excitation process and the involved electronic and phononic states and for complex materials it is the formula of choice. For a metal where only conduction band electrons are excited and under the assumption of thermalized electrons and phonons, we can define temperatures for electrons and phonons separately using fermi-dirac and Bose-Einstein distribution functions. For this case we can simplify eq. (2.6) to

$$\sigma = -\tilde{\gamma}_e \frac{\Delta E_e}{V} - \tilde{\gamma}_p \frac{\Delta E_p}{V} = -\tilde{\gamma}_e c_e \Delta T_e - \tilde{\gamma}_p c_p \Delta T_p \quad (2.8)$$

where c_e , c_p and $\tilde{\gamma}_e$, $\tilde{\gamma}_p$ are the specific heats and macroscopic Grüneisen parameters of electrons and phonons, respectively. [32, 33] Using eqs. (2.3) we get the time-dependent $\sigma(t)$ after photo-excitation:

$$\sigma(t \geq 0) = -\tilde{\gamma}_e c_e T_\infty \left(1 + \frac{c_p}{c_e} \exp(-r \cdot t) \right) - \tilde{\gamma}_p c_p T_\infty \left(1 - \exp(-r \cdot t) \right) \quad (2.9)$$

Because $c_p(T_\infty) \gg c_e(T_\infty)$ we can neglect the static stress contribution of the electrons. Using this, combining terms and introducing the quantity $\sigma_\infty = -\tilde{\gamma}_p c_p T_\infty$ we get a simplified relation for the time-dependent stress after photoexcitation of a metal: [33]

$$\sigma(t) \approx H(t) \sigma_\infty \left(\left(\frac{\gamma_e}{\gamma_p} - 1 \right) \exp(-r \cdot t) + 1 \right) \quad (2.10)$$

Here $H(t)$ represents the Heaviside function which mimics the instantaneous temperature change at $t = 0$. The Grüneisen parameters of both subsystems have usually a value around unity.² Moreover, the constant σ_∞ can be expressed by the heat expansion coefficient α , bulk modulus B as well as the final temperature change ΔT of the crystal yielding $\sigma_\infty = -3B\alpha\Delta T$. [31, 33]

²In case of a free electron gas the Grüneisen parameter of the electrons is given by $\gamma_e = 2/3$. [35, p. 495]

2.3 Classification of different phonon excitation mechanisms

In the literature different phonon excitation mechanisms using ultrashort laser pulses are discussed.

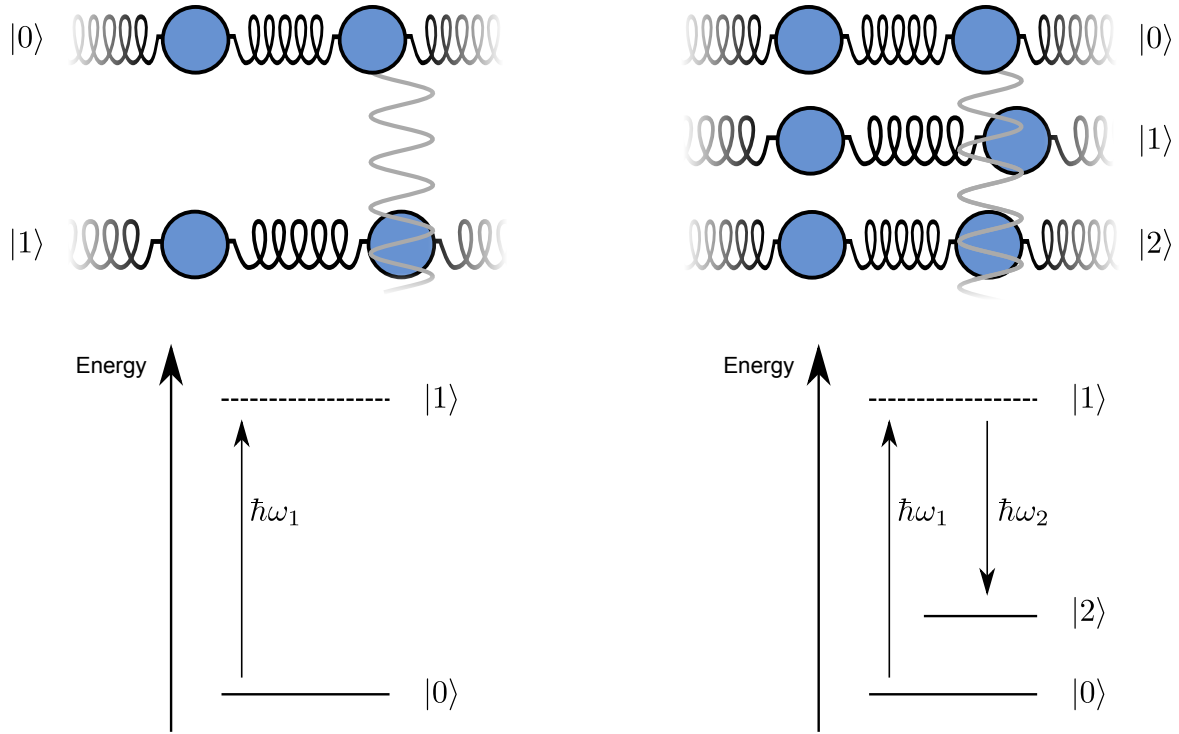
On the one hand scientists investigated opaque media by femtosecond laser pulses and observed excited phonons.[36] For the rapid excitation of coherent phonons in semiconductors a very effective mechanism is the *Displacive Excitation of Coherent Phonons (DECP)*. [37] In this mechanism the laser pulse translates electrons from an occupied electronic band to an unoccupied one, visualized in the lower panel of Fig. 2.2a. Because different electronic bands contribute differently to the bonding of a material, this transition will increase or decrease the equilibrium bond length. The electronic part of eq. (2.7) describes this situation mathematically. For this mechanism two different bands with different deformation potentials are necessary, otherwise the stress change of both bands will compensate - in the first band the electron density goes down whereas in the other one it goes up. Because the lifetime of photoexcited carriers are in the range of ns and longer, those resonant excitations lead to an instantaneous step like change of the electronic stress contribution. Therefore the excited mode has a new equilibrium position and oscillates with a cosine, depicted in the upper panel of Fig. 2.2a.

On the other hand an excitation of lattice vibrations in transparent materials is also possible. This typically non-resonant process is called *Impulsive Stimulated Raman Scattering (ISRS)*. [38] Here, no carriers are excited from one band to another. In the Raman scattering process an incident photon perturbs the material's electronic structure, which leads to an excited state in presence of the photons electric field. A stimulated emission by a second photon with less energy can translate this "virtual" state into a state where the material returns into the electronic ground state plus an excited phonon. In contrast to DECP the equilibrium position of the atoms is not changed. Thus the lattice oscillations are sine like. The lifetime of the virtual state is proportional to the inverse energy distance to the nearest eigenstate. In addition to energy conservation depicted in Fig. 2.2b the right scattering geometry has to be chosen to fulfil the conservation of momentum. This can be done by shining both light beams with a defined intersecting angle on the material. [39, 40]

While DECP describes a physical situation where the lifetime of the excited electronic state is much larger than the excited phonon oscillation period, in the non-resonant ISRS the lifetime is much smaller than the excited phonon oscillation period. Although DECP and ISRS seem to be different mechanisms, ISRS can explain DECP results considering resonant scattering, which changes the lifetime of the excited state and adds displacive character to the theory. [41, 42]

Besides those processes, *thermoelastic stress* due to phonon gas heating of a material also initiates a stress change. Once the photons are excited, the material expands due to the anharmonicity of the interatomic potentials. Here phonons with a much longer oscillation period than the stress driving phonons can be coherently excited. Remembering the Two Temperature Model from section 2.1, one additionally needs a fast electron phonon coupling to drive high frequency phonons by thermoelastic stress following an optical excitation.

Our observations for SrRuO₃ in Paper I showed a very short electron phonon coupling time of approximately 150 fs. In addition we saw a fluence dependent change of the excited phonon phase which means that the stress generation is faster for higher excitation



(a) The energy diagram describes an electronic transition of the material. In this state the equilibrium position of the atoms is immediately changed which finally leads to an oscillatory motion of the lattice with a cosine phase.

(b) Two photons trigger a stimulated Raman excitation process visualized in the energy diagram. The equilibrium position of the atoms is unchanged. The instantaneous velocity change finally leads to an oscillatory motion of the lattice with a sine phase.

Figure 2.2: Energy diagrams for ISRS and DECP excitation mechanisms. The atoms and springs visualize the equilibrium positions of the atoms in the individual states.

energies. This is in direct contradiction to the expected behavior in the Two Temperature Model. Here one would expect a slower phonon-induced stress generation for the case of high excitation fluences considering the expected electronic stress is negligible. The heat capacity of electrons grows linearly with temperature, which would lead to a slower energy transfer to the phonons see Figure 2.1b. These experimental observations led us to the conclusion that another mechanism becomes important at high excitation densities. One can speculate that the electron transfer in other states adds a DECP character to the SrRuO₃ excitation which contains an instantaneous stress generation by electrons. For sufficient high intensities this DECP character dominates the excitation and finally results in an instantaneous excitation. Also temperature dependent Grüneisen parameter of the electrons could explain this, and might be a result of the non-fermi-liquid behavior of SrRuO₃.^[43] Moreover, it was recently shown for TiO₂ combining experiments and Density Functional Theory (DFT) calculations that the cooling of electrons can also have an important influence on the displacive forces of the material.^[44]

2.4 The evolution of sound in a solid

2.4.1 Harmonic linear chain and acoustic wave equation of a solid

One way to think about sound in a crystalline solid is to imagine atoms with mass m_i which are nearest neighbor coupled by springs with spring constants k_i describing the interatomic interaction. The displacement u_i of an atom i in such a network launches a distortion which will propagate through the lattice of these coupled atoms.

By focusing on longitudinal sound waves and propagation in a certain direction, we can simplify this network of atoms to a one-dimensional linear chain. Using the simplification of Hooke's law which postulates a linear increase of the spring forces with the distance between neighboring atoms we can describe the whole problem with N second order ordinary differential equations (ODEs), where N is the number of oscillators

$$m\ddot{u}_i = k [(u_{i+1} - u_i) - (u_i - u_{i-1})]. \quad (2.11)$$

Focusing on waves which have much longer wavelength than the interatomic distance a , we can simplify the set of ODEs to a partial differential equation (PDE) describing the displacement $u(x, t)$ where x is the position on the chain. In that sense $u_{i-1} \rightarrow u(x - a, t)$, $u_i \rightarrow u(x, t)$ and $u_{i+1} \rightarrow u(x + a, t)$. Inserting the Taylor approximations

$$u(x - a, t) = u(x) - \frac{\partial}{\partial x}u(x, t)a + \frac{1}{2} \frac{\partial^2}{\partial x^2}u(x, t)a^2 \quad (2.12)$$

$$u(x + a, t) = u(x) + \frac{\partial}{\partial x}u(x, t)a + \frac{1}{2} \frac{\partial^2}{\partial x^2}u(x, t)a^2 \quad (2.13)$$

into eq. (2.11) yields finally the wave equation

$$\frac{\partial^2}{\partial t^2}u(x, t) = v^2 \frac{\partial^2}{\partial x^2}u(x, t) \quad (2.14)$$

where $v = \sqrt{\frac{k}{m}}a$ is the speed of sound in the medium.

In general, a medium e. g. a crystal can be anisotropic. This leads to direction dependent elastic properties of the material which can be expressed in the form of a stiffness tensor c_{ijkl} , which is defined by Hooke's law for anisotropic materials:

$$\sigma_{ij} = c_{ijkl} \frac{\partial u_l}{\partial x_k} \quad (2.15)$$

σ_{ij} is the stress tensor where the diagonal elements describe the contraction or expansion along the directions (x, y, z) , whereas the off-diagonal elements are defined by the coupling between two directions due to Poisson's ratio. The quantity $\epsilon_{kl} := \frac{\partial u_l}{\partial x_k}$ is the corresponding strain tensor. In combination with the dynamic field equation coming from Newton's law where ρ is the density of the medium, [45, p. 177]

$$\rho \frac{\partial^2 u_i}{\partial t^2} = \frac{\partial \sigma_{ij}}{\partial x_j} \quad (2.16)$$

we can write down the wave equation for anisotropic media:

$$\rho \frac{\partial^2 u_i}{\partial t^2} = c_{ijkl} \frac{\partial^2 u_l}{\partial x_j \partial x_k} \quad (2.17)$$

This result is the general version of eq. (2.14) which describes only a longitudinal wave along a certain propagation direction. Eq. (2.17), in contrast, describes the linear acoustics including anisotropic materials and different wave polarisations in one formula.

2.4.2 Thermoelastic stress as a source for sound

As discussed in section 2.2 shining a near infrared laser pulse on a metal film will generate stress. Firstly, let us assume that the investigated spot is much smaller than the excited one yielding a laterally homogenous excitation condition. Under this condition in-plane forces cancel and only stresses perpendicular to the metal surface are unbalanced. Secondly, we make the assumption that the generated stress in the metal is due to quasi-instantaneous phonon heating. Using those assumptions we can write down the stress perpendicular to the metal surface acting at a position x : [31]

$$\sigma_{33} = 3 \frac{1 - \nu}{1 + \nu} B \epsilon_{33} - 3B\alpha \Delta T(x_3, t) \quad (2.18)$$

Combining this with eq. (2.16) and using the definition of strain ϵ_{33} we finally get a one dimensional forced wave equation which describes the dynamics of photoexcited sound waves

$$\rho \frac{\partial^2 u_3}{\partial t^2} - 3 \frac{1 - \nu}{1 + \nu} B \frac{\partial^2 u_3}{\partial x_3^2} = -3B\alpha \frac{\partial \Delta T(x_3, t)}{\partial x_3}. \quad (2.19)$$

variable	definition
u	u_{33}
z	x_3
v^2	$3 \frac{1 - \nu}{1 + \nu} \frac{B}{\rho}$
$\theta(z, t)$	$\frac{3B\alpha}{\rho} \Delta T(z, t) = \frac{3B\alpha}{\rho c_V} \Delta \Phi(z, t)$
$g(z, t)$	$-\frac{\partial \theta(z, t)}{\partial z}$

Table 2.1: Variable definitions to simplify eq. (2.19). c_V represents the volumetric specific heat and $\Delta \Phi$ the change in energy density due to photo-excitation. The second representation of $\theta(z, t)$ is often more useful due to the similar temperature dependence of the linear thermal expansion coefficient α and c_V making the set of parameters in front of $\Delta \Phi$ in first order independent of temperature.

2.4.3 The solution of the 1D forced wave equation in free space

Using the definitions in table 2.1 we can simplify eq. (2.19) to

$$\frac{\partial^2 u}{\partial t^2} - v^2 \frac{\partial^2 u}{\partial z^2} = g(z, t), \quad (2.20)$$

where u is the acoustic amplitude, v the speed of sound and $g(x, t)$ the driving acceleration of each position due to thermoelastic forces. This is the inhomogeneous wave equation. A solution for the Cauchy problem can be found using Green's theorem. [46, 47] To find an explicit solution in free space (no additional boundary $-\infty < z < \infty$) one needs to define the initial conditions

$$u(z, 0) = \phi(z), \quad \frac{\partial u}{\partial t}(z, 0) = \psi(z), \quad (2.21)$$

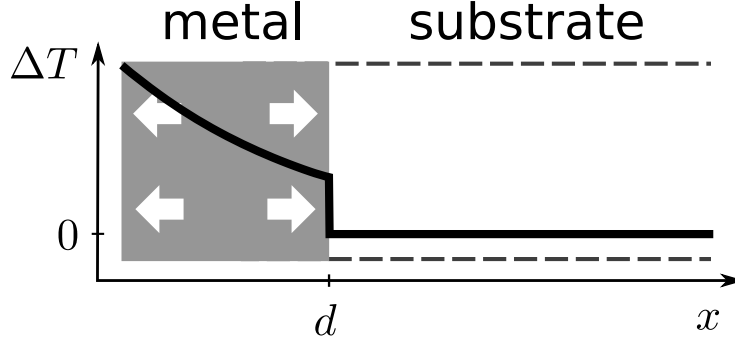


Figure 2.3: Schematic picture of a metal film with thickness d grown on top a substrate. The black line depicts the profile of the temperature change directly after photoexcitation. The white arrows symbolize that the metal wants to expand into the new equilibrium position.

yielding a solution given by [46, p. 89]

$$u(z, t) = \frac{1}{2} [\phi(z + vt) + \phi(z - vt)] + \frac{1}{2v} \int_{z-vt}^{z+vt} \psi(s) ds + \frac{1}{2v} \int_0^t \int_{z-v(t-s)}^{z+v(t-s)} g(y, s) dy ds \quad (2.22)$$

2.4.4 Describing a photoexcited metal film on a substrate using the 1D forced wave equation

In this section we use the previous mathematics to solve an explicit problem, a laser heated metal film with thickness d grown on top of a substrate, as schematically shown in Fig. 2.3. We predefine that there is no sound in the sample before excitation. This assumption fixes the initial conditions to

$$\phi(z) = 0, \quad \psi(z) = 0, \quad (2.23)$$

and simplifies the expression for $u(z, t)$ using the definition of $g(z, t)$ from table 2.1 to

$$u(z, t) = -\frac{1}{2v} \int_0^t \int_{z-v(t-s)}^{z+v(t-s)} \frac{\partial \theta(y, s)}{\partial y} dy ds \quad (2.24)$$

Now we make some helpful assumption to the function $\theta(z, t)$, which is essentially given by the temperature profile after excitation. This makes eq. (2.24) finally simpler and more useful in practical cases. At first let us assume that $\theta(z, t) = Z(z)T(t)$ is a function where we can factorize the dependencies on z and t . Assuming this, the integration of $\partial \theta / \partial y$ is trivial and we can write:

$$u(z, t) = -\frac{1}{2v} \int_0^t [\theta(z + v(t-s), t) - \theta(z - v(t-s), t)] ds \quad (2.25)$$

This formula is good for temporally changing temperature profiles. By assuming further that $\theta(z, t)$ does not depend explicitly on t we can also integrate eq. (2.25) by defining $\Gamma(\xi) = \int \theta(\xi) d\xi$ as the primitive of $\theta(\xi)$, yielding

$$u(z, t) = \frac{1}{2v^2} [2\Gamma(z) - \Gamma(z + vt) - \Gamma(z - vt)] \quad (2.26)$$

In case of the strain ϵ we get

$$\epsilon(z, t) = \frac{\partial u(z, t)}{\partial z} = \frac{1}{2v^2} [2\theta(z) - \theta(z + vt) - \theta(z - vt)] \quad (2.27)$$

This means, that $\epsilon(z, t)$ is mainly given by a sum of spatially shifted energy density profiles $\Delta\Phi(z, t)$ after excitation (see table 2.1). The equations (2.26) and (2.27) are the solutions of the Cauchy problem which describes a quasi-instantaneously heated slab in between two unexcited regions. To get a solution ϵ_h for the half-space we have to fulfill the boundary condition $\epsilon_h(0, t) = 0$. We can find an appropriate solution using the symmetry of the problem, combining two Cauchy solutions and ignoring the left half space of the coordinate z :

$$u_h(z \geq 0, t) = u(z, t) + u(-z, t) \quad (2.28)$$

$$\epsilon_h(z \geq 0, t) = \epsilon(z, t) - \epsilon(-z, t) \quad (2.29)$$

Using the assumption that $\theta(z < 0) = 0$ leads finally to the strain $\epsilon_h(z, t)$ of the half-space solution given by

$$\epsilon_h(z, t) = \frac{H(z)}{2v^2} \left[\underbrace{2\theta(z)}_{\text{static heat}} - \underbrace{\theta(z + vt)}_{\text{left propagating wave}} + \underbrace{\theta(-z + vt)}_{\text{reflected left wave}} - \underbrace{\theta(z - vt)}_{\text{right propagating wave}} \right] \quad (2.30)$$

where $H(z)$ is the Heaviside function. Eq. (2.30) contains four different terms where the first is independent of time and describes the induced static heat. The second term belongs to the excited wave packet propagating to the sample surface, where it is reflected. This is described by the third term. The fourth term finally belongs to the excited wave packet propagating to the substrate.

In the last step we have to consider the interface at $x = d$. In general, layer and substrate regions can have different acoustic impedances $Z_i = \rho_i v_i$ and sound velocities v_i . Let us call the layer region 1 and the substrate region 2. The solution of the wave equation has to fulfill two boundary conditions. The displacement u_i and the overpressure $\delta p_i = -Z_i v_i \epsilon_i$ have to be continuous. Assuming perfect acoustic impedance matched layer and substrate, those conditions lead to a perfectly transmitting interface. The continuity of overpressure yields for the strain: [45, p. 27, 39]

$$\epsilon_2(d - v_1 t) = \frac{v_1}{v_2} \epsilon_1(d - v_2 t) \quad (2.31)$$

Due to this boundary condition and the fact that ϵ_2 has to be a solution of the wave equation in region 2, we can find an explicit relation for $\epsilon_2(z, t)$.

$$\epsilon_2(z, t) = H(z - d) \frac{v_1}{v_2} \epsilon_1 \left(\frac{v_1}{v_2} z + \left(1 - \frac{v_1}{v_2} \right) d, t \right) \quad (2.32)$$

The solution of $\epsilon_1(z, t)$ in the layer region is given by $\epsilon_h(z, t)$. Now we can write down the solution of the whole problem using $v = v_1$ and defining $l := \left(1 - \frac{v_1}{v_2} \right) d$.

$$\epsilon_\delta(z, t) = \frac{1}{2v_1^2} \begin{cases} H(z) [2\theta(z) - \theta(z + v_1 t) + \theta(-z + v_1 t)] - \theta(z - v_1 t) & z \leq d \\ \frac{v_1}{v_2} \left[\theta \left(-\frac{v_1}{v_2} (z - v_2 t) - l \right) - \theta \left(\frac{v_1}{v_2} (z - v_2 t) + l \right) \right] & z > d \end{cases} \quad (2.33)$$

Remembering the definition of θ from table 2.1 which is essentially given by the energy density change after excitation, we can write down the solution for the photo-excited strain wave in dependence of the change in energy density $\Delta\Phi(z)$

$$\epsilon_{\delta}(z, t) = \frac{\alpha}{2c_V} \frac{1 + \nu}{1 - \nu} \begin{cases} H(z)[2\Delta\Phi(z) - \Delta\Phi(z + v_1t) + \Delta\Phi(-z + v_1t) - \Delta\Phi(z - v_1t)] & z \leq d \\ \frac{v_1}{v_2} \left[\Delta\Phi\left(-\frac{v_1}{v_2}(z - v_2t) - l\right) - \Delta\Phi\left(\frac{v_1}{v_2}(z - v_2t) + l\right) \right] & z > d \end{cases} \quad (2.34)$$

Equations (2.33) and (2.34) represent the acoustic answer of the treated system: a metal film on a substrate disturbed by an infinitesimally short laser pulse, which is absorbed in the metal, assuming no intrinsic delay in the stress generation process. In practice it might be interesting to know the system's answer to an arbitrary pulse pattern. Due to the linearity of the wave equation one can calculate this by a convolution of eqs. (2.33) or (2.34) with the normalized temporal excitation profile $\tilde{I}(t) = \frac{I(t)}{\int_{-\infty}^{\infty} I(t)dt}$:

$$\epsilon(z, t) = \int_{-\infty}^{\infty} \epsilon_{\delta}(z, \tau) \tilde{I}(t - \tau) d\tau \quad (2.35)$$

where $\Delta\Phi(z)$ represents the excitation profile with $t \rightarrow \infty$, the time when the laser pulse pattern has excited the layer completely.

As one example for $\Delta\Phi(z)$ we could imagine a laser pulse which is absorbed in the metal film, where the induced profile of energy change instantaneously produces stress. Due to the Lambert-Beer law the internal intensity in the metal film has the profile $I_{\text{int}}(z, t) = (1 - R)I(t) \exp(-z/\eta)$, where R is the reflection from the air/metal interface, $I(t)$ the incoming intensity envelope of the pulse pattern and η the penetration depth of the laser light. The overall absorbed energy density profile $\Delta\Phi$ can be calculated by

$$\Delta\Phi(z) = (H(z) - H(z - d)) \int_{-\infty}^{\infty} -\frac{\partial}{\partial z} I_{\text{int}}(z, t) dt = \frac{(1 - R)F}{\eta} \exp\left(-\frac{z}{\eta}\right) (H(z) - H(z - d)) \quad (2.36)$$

where $F = \int_{-\infty}^{\infty} I(t)dt$ is the overall deposited fluence.

Using the equations (2.34) and (2.36) as well as material parameters for the SrRuO₃ metal film and the SrTiO₃ substrate which are listed in table (2.2), we can plot the strain evolution in this sample system. To keep it simple, I used a fluence of $F = 20 \text{ mJ/cm}^2$, a reflectivity $R = 0$ and a film thickness $d = 35 \text{ nm}$. Figure 2.4 shows the calculated strain

quantity	symbol	value	citation
Penetration depth of 795 nm light in SrRuO ₃	η	48 nm	Paper II
Sound velocity of SrRuO ₃	v_1	6.312 $\frac{\text{nm}}{\text{ps}}$	[48]
Sound velocity of SrTiO ₃	v_2	8 $\frac{\text{nm}}{\text{ps}}$	Paper XIV
Linear thermal expansion of SrRuO ₃	α	$1.03 \cdot 10^{-5}$	[48]
Poisson's ratio of SrRuO ₃	ν	0.3	[49]
Specific heat per volume of SrRuO ₃	c_V	$3.424 \cdot 10^6 \frac{\text{J}}{\text{m}^3\text{K}}$	[19]

Table 2.2: Important quantities for the strain calculation of a photo-excited SrRuO₃ metal film on a SrTiO₃ substrate including symbol and used value.

evolution of the photo-excited SrRuO₃ film on the SrTiO₃ substrate. Here the upper part

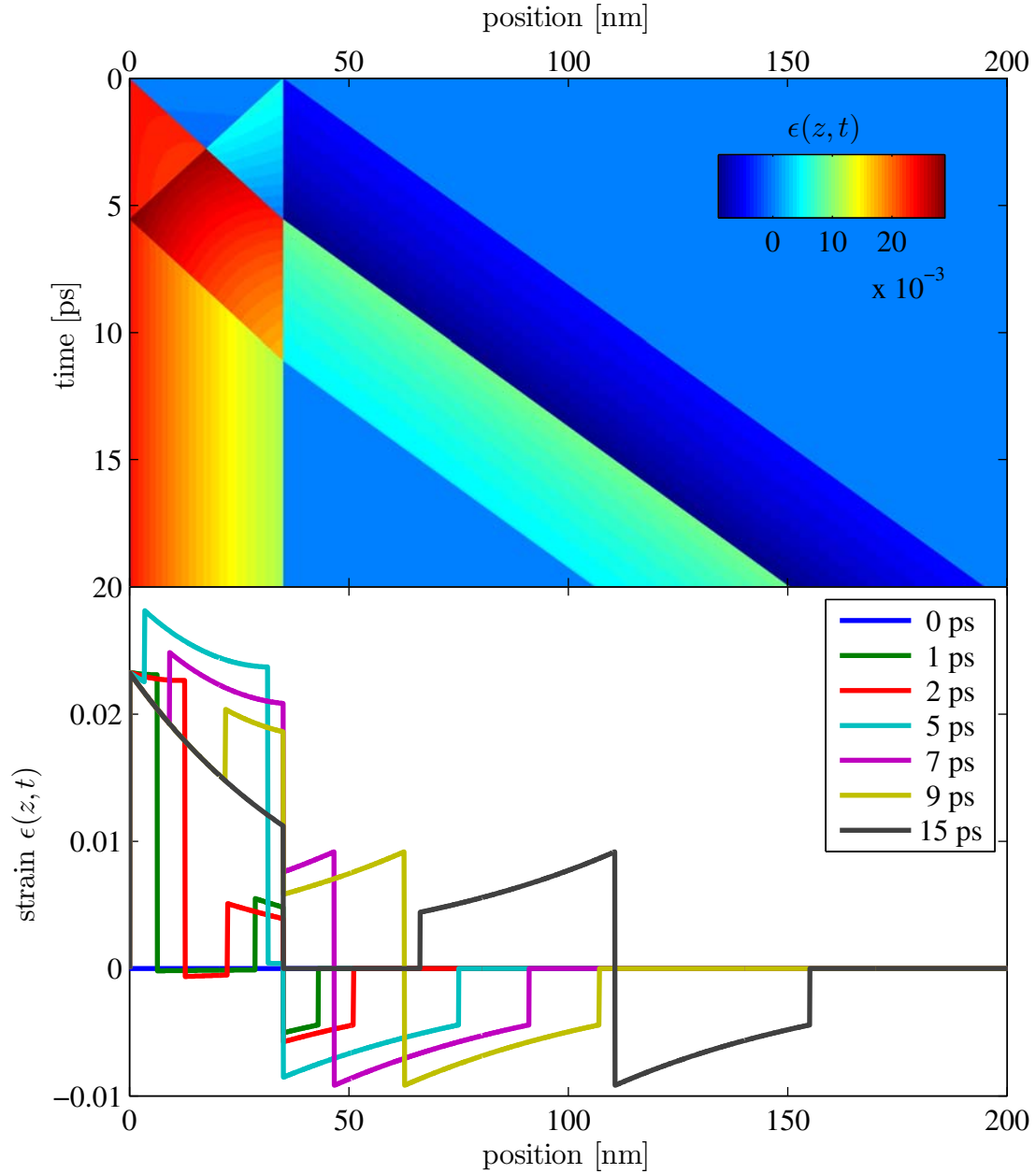


Figure 2.4: Shows the calculated strain evolution of a photo-excited SrRuO₃ film with thickness $d = 35$ nm grown on the dielectric substrate SrTiO₃.

depicts the strain evolution as a color coded plot. The lower part shows some selected time cuts.

In Paper II we used ultrafast x-ray diffraction (UXRD) experiments to observe the photo-excited sound wave in the film. A change of the lattice constant due to the sound propagating in the metal film is measured and fits quantitatively to the expected stress profile given by Lambert-Beer's law. The analytic solution of the wave equation for the layer is used to explain that the film is partly contracted after photo-excitation although the whole film wants to expand. This is due to inhomogeneously stressed film and is only observed for thick enough layers.

As we will see in the next chapter the Fourier spectrum of the excited wave packet defines the Brillouin oscillation amplitude in the probing process. For that reason the tables (2.3) - (2.4) show an overview of different wave packets with strain $\epsilon(z > d, t)$ and their corresponding Fourier amplitudes defined by:

$$\epsilon(q) := \left| \int_{-\infty}^{\infty} \epsilon(z > d, 0) \exp(-iqz) dz \right| \quad (2.37)$$

For shorter formulas we define the prefactor A which contains all important parameters for the quantitative calculation of the strain by

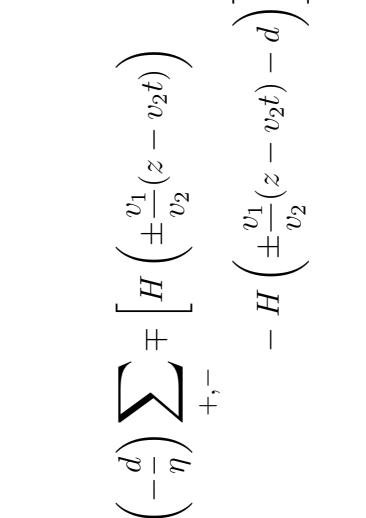
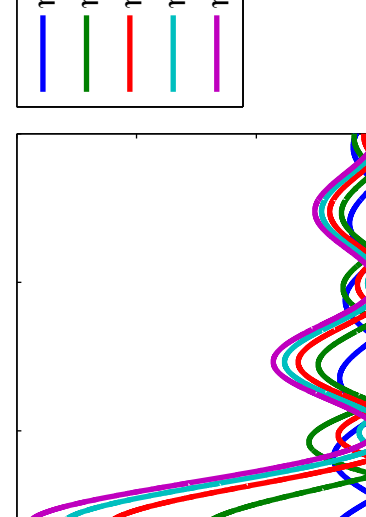
$$A = \frac{(1 - R)F\alpha}{2\eta c_V} \frac{1 + \nu v_1}{1 - \nu v_2}. \quad (2.38)$$

For the plots in tables (2.3) - (2.4) I set $A = 1$ and varied the penetration depth η in fractions of d . By setting A the penetration depth dependence of $A \sim 1/\eta$ is ignored in the graphs for better visualization. For correct amplitude ratios the graphs have to be weighted by $1/\eta$. Despite this, the plots of the spectrum for different ratios of η and d nicely show that for low values of η/d the magenta spectrum ($\eta \gg d$) is smeared out. This is because the spectrum of a strain pulse with an arbitrary η/d is given by a convolution of the complex spectrum of a rectangular shaped strain pulse ($\eta = \infty$) with length $2d$ and a Lorentzian function with the half width at the half maximum of $1/\eta$ which is the Fourier transform of the exponential decaying profile.

Table 2.3: Excitation from the air/film interface and profile given by Lambert-Beer's law

plot of wave packet	formula for $\epsilon(z, t)$
	$A \sum_{+,-} \mp \left[H \left(\pm \frac{v_1}{v_2} (z - v_2 t) \right) - H \left(\pm \frac{v_1}{v_2} (z - v_2 t) - d \right) \right] \exp \left(\mp \frac{v_1 z - v_2 t}{v_2 \eta} \right)$
spectrum of wave packet	spectrum formula
	$A \frac{2\eta}{\eta^2 q^2 + \left(\frac{v_1}{v_2} \right)^2} \left \eta q \left[1 - \exp \left(-\frac{d}{\eta} \right) \cos \left(\left(\frac{v_1}{v_2} \right)^{-1} dq \right) \right] - \frac{v_1}{v_2} \exp \left(-\frac{d}{\eta} \right) \sin \left(\left(\frac{v_1}{v_2} \right)^{-1} dq \right) \right $

Table 2.4: Excitation from the substrate/film interface and profile given by Lambert-Beer's law

plot of wave packet	formula for $\epsilon(z, t)$
 <p style="text-align: center;">in units of $v_2/v_1 \cdot d$</p>	$A \exp\left(-\frac{d}{\eta}\right) \sum_{+,-} \left[H\left(\pm \frac{v_1}{v_2}(z - v_2 t)\right) - H\left(\pm \frac{v_1}{v_2}(z - v_2 t) - d\right) \right] \exp\left(\pm \frac{v_1 z - v_2 t}{v_2 \eta}\right)$
spectrum of wave packet	spectrum formula
 <p style="text-align: center;">in units of π/d</p>	$A \frac{2\eta}{\eta^2 q^2 + \left(\frac{v_1}{v_2}\right)^2} \exp\left(-\frac{d}{\eta}\right) \left \eta q \left[1 - \exp\left(\frac{d}{\eta}\right) \cos\left(\left(\frac{v_1}{v_2}\right)^{-1} dq\right) \right] + \frac{v_1}{v_2} \exp\left(\frac{d}{\eta}\right) \sin\left(\left(\frac{v_1}{v_2}\right)^{-1} dq\right) \right $

LIGHT AND SOUND INTERACTION

In this chapter I give a more detailed view on how light interacts with sound in a solid medium. For that purpose I will shortly discuss the interaction mechanisms between photons and phonons and present a detailed picture of the kinematics of the photon-phonon scattering process. Then I will introduce the pump-probe scheme as my experimental setup of choice to probe coherent phonon dynamics by measuring the time-dependent reflection of the sample after sound pulse excitation. Subsequently I will use Maxwell's equations to model the transiently changing reflection from the sample which is a superposition of the reflection from the heated sample and the scattering from the excited sound wave. Finally I will interpret the measured relative reflectivity oscillation amplitudes as phonon amplitude proportional quantities. Here I will focus on photons in the visible spectrum. In my thesis I also used x-ray photons which scatter on the crystal lattice planes, because sound is nothing else but moving lattice planes this is also sensitive to phonons. In publication **IV** I discuss the correspondence of inelastic light and x-ray scattering on phonons. Moreover, Paper **III** presents a detailed way how to calculate the time-resolved x-ray diffraction on longitudinal acoustic phonons. Detailed discussions about ultrafast x-ray scattering can be found in the review of Bargheer *et al.* [50] and the book of Authier [51].

3.1 Why photons are influenced by phonons

Let's assume we have a piece of a transparent crystal of an arbitrary material in front of us. At room temperature phonons are thermally excited. This lets the atoms oscillate randomly. Shining light on the crystal, a part of the light would reflect at the interface between air and the solid whereas the remaining part would penetrate into the crystal. Thinking about different ions in the unit cell of the crystal we could drive a oscillation of these ions against each other using the right frequency of the light wave (usually infrared). By this process photons will be directly coupled to the phonons and build quasi-particles called phonon-polaritons.[52][**VIII**] The lattice displacement and the electro-magnetic wave are mutually dependent and can only exist together.

Now assume we have light frequencies far away from those phonon resonances or a homopolar crystal like Silicon, why would we expect an interaction of the light with the excited phonons? The answer is, because of electrons. Electrons mediate the interaction process in solids because they are coupled to both, photons and phonons. Figure 3.1 (a) visualizes the dominating contribution of a resonant Stokes Raman scattering process as a Feynman Graph.[53] A photon with energy $\hbar\omega_i$ generates an electron-hole pair via

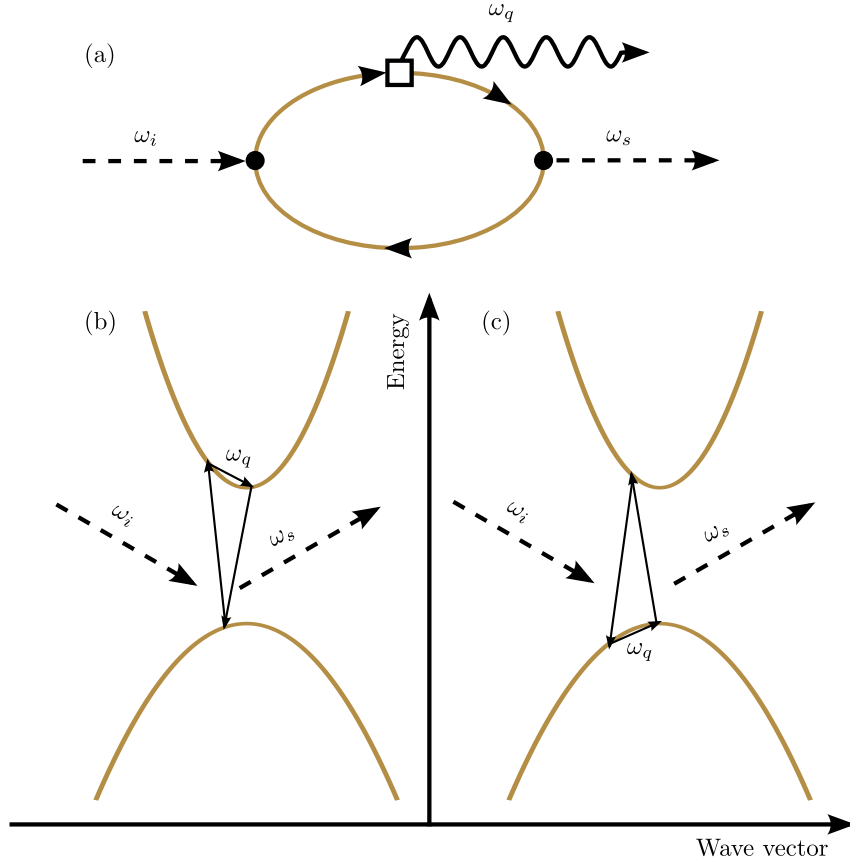


Figure 3.1: (a) shows a Feynman Graph describing a Stokes Raman scattering process mediated by a virtually excited electron hole pair in the crystal. (b) depicts this process where an electron decays into a phonon and a new electron in a band structure of an arbitrary material. (c) shows the same process for holes *adapted from [54, 55]*

an interaction of electrons and photons. The electron can then relax to a new electron and emit a phonon fulfilling momentum conservation governed by the electron phonon coupling. After that process a photon with energy $\hbar\omega_s$ is generated by the annihilation of the electron-hole pair. Figure 3.1 (b) shows a schematic picture of this process for an arbitrary band structure and (c) the corresponding process in which phonons were emitted via annihilation and creation of holes.[54, 55]

It turns out that also for photon energies far away from such interband resonances depicted in Fig. 3.1 (b) and (c) these scattering processes are quite probable especially in case of high photon or phonon occupation numbers which can stimulate those Raman scattering processes.

In case of light scattering on acoustic phonons also called Brillouin scattering one can describe the electron phonon coupling in a quasi-static picture where the long wavelength strain wave (phonon) modulates spatially the band structure of the material.[54, p. 41-43] This behavior is quantified by the deformation potential which I have introduced in chapter 2. Because the dielectric function is directly coupled to the band structure [55, p. 85-92], an acoustic wave modulates the optical properties of the material which finally leads to light scattering from phonons.

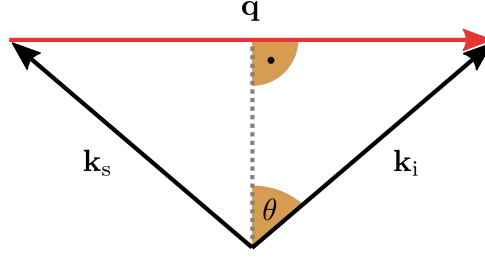


Figure 3.2: The energy and momentum conservation for a scattering process between a phonon, an incident and scattered photon is visualized. The dispersion of light is 10^5 times steeper than the dispersion of acoustic phonons. This leads to a quasi-elastic geometry where $|\mathbf{k}_i| \approx |\mathbf{k}_s|$ also known as Bragg geometry.

3.2 Kinematic treatment of Brillouin Scattering

Brillouin scattering has to fulfill energy and momentum conservation as every scattering process. It is helpful to have a look at these conservation laws to get an idea which geometry is the right choice for light scattering from acoustic phonons (Brillouin Scattering). Following Paper IV, the conservation laws can be written as:

$$\omega_s - \omega_i = \pm \omega_q \quad (3.1)$$

$$\mathbf{k}_s - \mathbf{k}_i = \pm \mathbf{q} \quad (3.2)$$

Here plus and minus signs correspond to the annihilation (anti-Stokes) and the creation (Stokes) of a phonon with frequency ω_q and wave vector \mathbf{q} . The indices i and s mark the wave vector \mathbf{k} and frequency ω of the incident and scattered photon, respectively. Let's assume an acoustic phonon branch with a sound velocity of v . In the center of the Brillouin zone we can describe the phonon dispersion of this branch by $\omega_q = v|\mathbf{q}|$. Using the speed of light c in the medium we can write down the connection between frequency and wave vector of the light with $\omega_{i,s} = c|\mathbf{k}_{i,s}|$. The dot product of eq. (3.2) with itself leads to

$$|\mathbf{q}|^2 = |\mathbf{k}_i|^2 + |\mathbf{k}_s|^2 - 2|\mathbf{k}_i||\mathbf{k}_s| \cos(2\theta) \quad (3.3)$$

with 2θ defining the angle between \mathbf{k}_i and \mathbf{k}_s . Using eq. (3.1) we can substitute \mathbf{k}_s by $\mathbf{k}_i \pm r|\mathbf{q}|$ where $r = v/c$. A rearrangement of terms and the identity $1 - \cos(2\theta) = 2\sin^2(\theta)$ yields

$$0 = (r^2 - 1)|\mathbf{q}|^2 \pm 4r|\mathbf{k}_i| \sin^2(\theta)|\mathbf{q}| + 4|\mathbf{k}_i|^2 \sin^2(\theta). \quad (3.4)$$

For each sign these quadratic equations have only one physical solution:

$$|\mathbf{q}|_{\pm} = 2|\mathbf{k}_i| \sin(\theta) \frac{\sqrt{r^2 \sin^2(\theta) - r^2 + 1} \pm r \sin(\theta)}{1 - r^2} \quad (3.5)$$

Equation (3.5) tells us from which acoustic phonon with wave vector \mathbf{q} an incident photon with vector \mathbf{k}_i can scatter. Here plus and minus correspond to the anti-Stokes and Stokes processes, respectively. In case of acoustic phonons $r \sim 10^{-5} \approx 0$ which makes the differentiation between creation and annihilation of phonons for the probed phonon wave vector mostly irrelevant. In that case we can approximate the scattering of photons from acoustic phonons as a quasi-elastic process ($|\mathbf{k}_i| \approx |\mathbf{k}_s|$) which simplifies eq. (3.5) to

$$\boxed{|\mathbf{q}| \approx 2|\mathbf{k}_i| \sin(\theta)} \quad (3.6)$$

Figure 3.2 shows the scattering geometry in case of quasi-elastic backscattering. This formula is known as the phase matching condition of Brillouin backscattering.[56, p. 389-391] The parallel wave vector component of the probed phonon is two times larger than the component of the incident and scattered photon. For a phonon wave propagating with the incident photon, the photon can only be back-scattered by a Stokes process whereas a phonon wave propagating against the photon direction leads only to anti-Stokes backscattering.

3.3 Experimental conditions

To make an experiment in which we excite a certain phonon wave packet and probe it by Brillouin scattering we can use the time-resolved pump-probe scheme in which an initial laser pulse excites a sample and launches a sound wave, as discussed in chapter 2. A delayed probe pulse impinging the excited area on the sample scatters from the sound wave and can then be detected. Knowing the incident angle and the wavelength of the probing electromagnetic wave we can use eq. (3.6) to calculate the probed phonon wave-vector. The scattered intensity at this particular photon wavelength is then a measure of the occupation of phonons with the wave vector given by eq. (3.6). This correspondence between diffraction Intensity and phonon amplitude will be shown in the next part of this chapter. Moreover, the scattered light from the sound wave will interfere on the detector with the reflection of the photo-excited sample. This leads to a homodyne amplification of the scattered field by the sound wave and enables a measurement of phonon amplitude and phase.

During my thesis I used two different kinds of probe schemes, probing with a broadband coherent picosecond white light pulse and probing with femto- and picosecond x-ray pulses. In the first variant on which I will mainly focus in this thesis we fix the incident angle of the white light probe pulse and detect the scattered light using a spectrometer which finally leads to a discrimination of different phonon wave-vectors using eq. (3.6). For the second variant where we probe with x-rays a monochromator is used to get narrowband x-ray probe pulses. Here we change the incident angle of the probing x-ray photons to probe different phonon wave vectors. For x-rays the backscattering condition is a little bit different from eq. (3.6) because x-rays are so short in wavelength that they scatter usually from lattice planes which changes the momentum conservation law in that way that on the right side of eq. (3.2) a reciprocal lattice vector \mathbf{G} has to be added.[IV V VI]

Figure 3.3 shows a schematic picture of the optical pump-probe setup used for hypersound experiments in this thesis. A 100 fs laser pulse from a Ti:Sapphire regenerative amplifier is divided into two parts. Approximately $\sim 90\%$ of the beam are transmitted through a beam sampler and used as pump (red). The remaining part is reflected and used as probe (black). The probe beam is focused into a sapphire plate, where the high electric field amplitude in the sapphire leads to a supercontinuum generation process.[57, 58] This broad band laser pulse (450 – 800 nm) is then send to the sample in the cryostat. The temporal structure of the pump beam can be manipulated by changing the chirp using a grating compressor and interferometers to generate replica of the pump pulse in defined temporal distances.[similar to XIII], [59] Afterwards the pump is deflected over a changeable delay path which defines the temporal displacement between pump and probe pulses. The pump power is set by a combination of a polarizer and a $\lambda/2$ wave plate and the pump footprint on the sample is adjustable by the distance of two lenses.

A chopper was added to the pump path where beam cross section is as small as possible

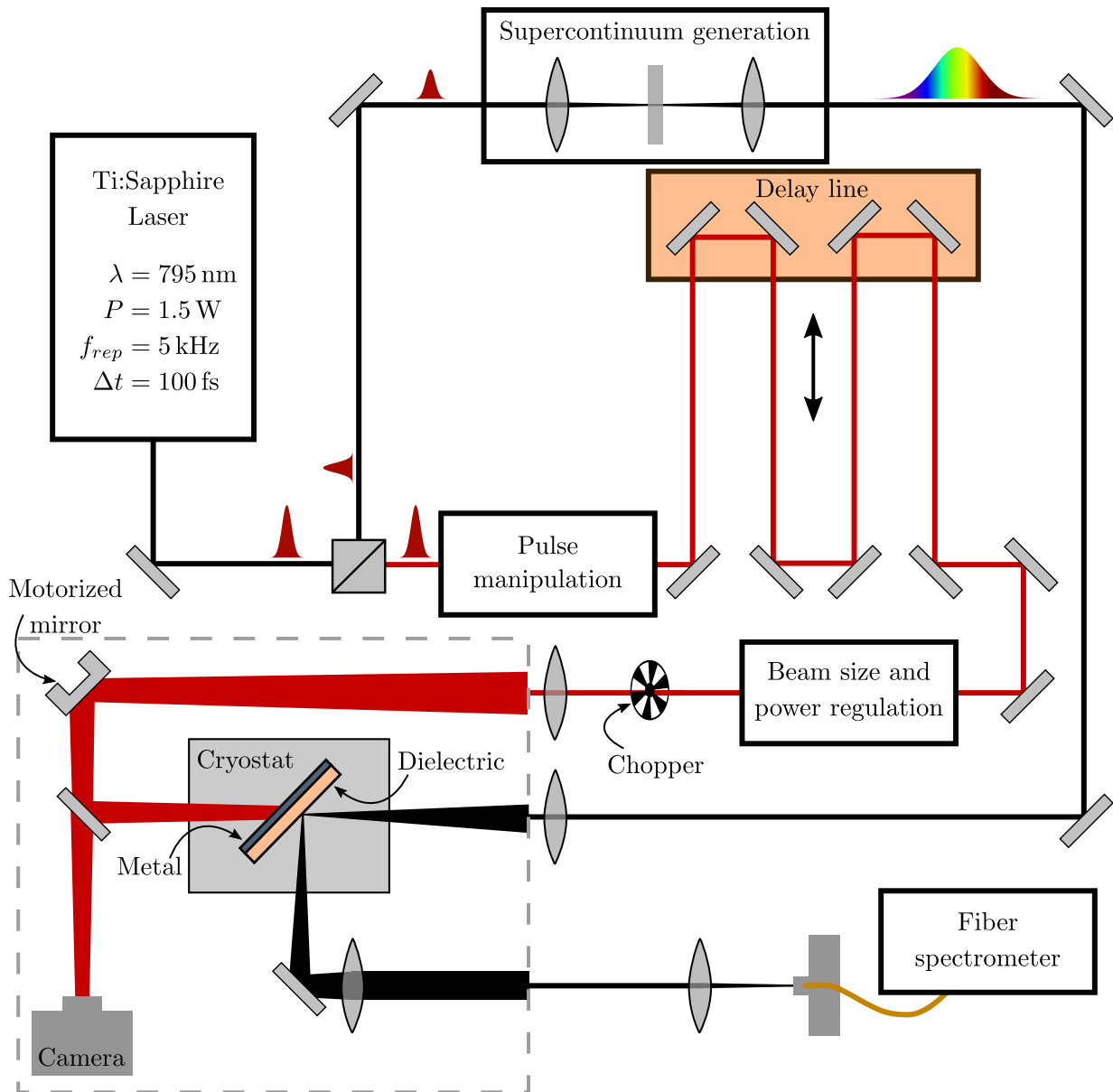


Figure 3.3: Further details can be found in section 3.3

without ablating material from the chopper surface. The chopper reduces the influence of long time fluctuations of the experimental setup by measuring pumped and unpumped intensity of the probe light on a short timescale. The chopper frequency is generated by dividing the 5kHz laser trigger frequency which belongs to the repetition rate f_{rep} of the laser system by a factor of 20. This signal is then send into the chopper controller, where is is additionally divided in frequency by 2. This leads to a chopper frequency of $f_{rep}/40 = 125 \text{ Hz}$. The spectrometer used for detecting the probe pulses reflected from the sample is triggered by the previously generated trigger with $f_{rep}/20 = 250 \text{ Hz}$. The doubled frequency with respect to the chopper ensures two measurement events: one where the chopper blade is open and the pump is reaching the sample and the other where the sample is unpumped.

In the sketched setup the sample is excited from the metal side and probed through the substrate. As discussed in chapter 2 the pumping from back or front side changes the excited phonon spectrum so it is important to consider this while designing such an

experiment. For the probe it is usually better to send the pulse from that side where it will be less absorbed before reaching the excited phonon wave packet on which it will be partially diffracted. This leads to a more sensitive probe of the coherent phonons. So in case of a metal on a substrate it will be better to send the probe pulse from the dielectric side into the sample.

To probe a large region of delays after pumping the sample, the pump was sent twice over the delay line which yields a maximum delay between pump and probe of ~ 8 ns. These long beam path changes lead inevitably to slight motions of the pump footprint on the sample. Even for a perfect beam adjustment the wobbling of the linear delay line is not negligible. To compensate the movements of the pump beam on the sample surface, a camera permanently measures the beam. Footprint and position are analyzed by a computer program and the motorized mirror finally readjusts the beam path such that the pump always shines on the same position on the camera. Without this tool a interpretation of long delay measurements would be rather problematic.

The measured quantities $I_p(\lambda, t)$ and $I_u(\lambda, t)$, the reflected intensities of the pumped (p) and the unpumped (u) sample are combined to the relative reflectivity change

$$\frac{\Delta R}{R_0} = \frac{I_p(\lambda, t) - I_u(\lambda, t)}{I_u(\lambda, t)} \quad (3.7)$$

where ΔR describes the reflectivity change and R_0 the reflectivity of the unpumped sample. Due to the chopper I_p and I_u are measured rather shortly after each other. The normalization by $I_u(\lambda, t)$ in $\Delta R / R_0$ reduces the influence of long term drifts and low frequency noise in the measurement setup.

3.4 Dynamical treatment of light scattering on acoustic phonons

To get a more quantitative explanation how light is diffracted by acoustic phonons we want to have a look in this section on a special scattering problem and find a solution using Maxwell's equations.

Let us imagine a plane sound wave with some spatial profile which propagates in z -direction into the material. Such sound wave will change spatially the optical properties of that material. The optical properties of this material can be described by a z -dependent electric permittivity $\varepsilon(z)$ and magnetic permeability $\mu(z)$. To calculate the light reflection by this sound wave we want to find at first a solution for the reflection by a Dirac like sound pulse, a small change of the optical properties between z and $z + dz$ of the medium.

3.4.1 Maxwell's equations and the wave equation in a stratified medium

For answering the question: how a reflected electric field coming from a stratified medium $\varepsilon(z)$ looks like – we want to go back to Maxwell's equations as a profound basis. Maxwell's

equations in SI-units are [60, p. 2]

$$\nabla \times \mathbf{H} = \dot{\mathbf{D}} + \mathbf{j} \quad (3.8)$$

$$\nabla \times \mathbf{E} = -\dot{\mathbf{B}} \quad (3.9)$$

$$\nabla \cdot \mathbf{D} = \rho \quad (3.10)$$

$$\nabla \cdot \mathbf{B} = 0 \quad (3.11)$$

where \mathbf{H} , \mathbf{E} , \mathbf{D} and \mathbf{B} are the vectors of the *magnetic field*, *electric field*, *electric displacement* and the *magnetic induction*, respectively. Assuming a linear response of the medium we can write:

$$\mathbf{D} = \varepsilon \mathbf{E} \quad (3.12)$$

$$\mathbf{B} = \mu \mathbf{H} \quad (3.13)$$

With no additional macroscopic charges $\rho = 0$ and currents $\mathbf{j} = 0$ we can substitute \mathbf{B} from eq. (3.9) using eq. (3.13). Dividing the result by μ and applying the curl on the whole equation yields

$$\nabla \times \left(\frac{1}{\mu} \nabla \times \mathbf{E} \right) = -\nabla \times \dot{\mathbf{H}} \stackrel{(3.8)}{=} -\ddot{\mathbf{D}} \stackrel{(3.12)}{=} -\varepsilon \ddot{\mathbf{E}} \quad (3.14)$$

The last step on the right side of eq. (3.14) assumes that there is no intrinsic time dependence of ε . This is an approximation which holds well because the investigated acoustic waves are much slower than the diffracting light wave. With this assumption we neglect any kind of retardation in the problem, which means that this theory approximates the light scattering process as a quasi-elastic one and shows now Doppler-shift which we would expect if we could measure very precisely. Using the identities $\nabla \times (u\mathbf{v}) = (\nabla u) \times \mathbf{v} + u \nabla \times \mathbf{v}$ and $\nabla \times (\nabla \times \mathbf{v}) = \nabla(\nabla \cdot \mathbf{v}) - \Delta \mathbf{v}$ we can rewrite eq. (3.14):

$$\Delta \mathbf{E} - \mu \varepsilon \ddot{\mathbf{E}} - \frac{\nabla(1/\mu)}{1/\mu} \times (\nabla \times \mathbf{E}) - \nabla(\nabla \cdot \mathbf{E}) = 0 \quad (3.15)$$

The last term of eq. (3.15) can be substituted using eqs. (3.10) and (3.12) yielding $\nabla \cdot (\varepsilon \mathbf{E}) = \varepsilon \nabla \cdot \mathbf{E} + \mathbf{E} \cdot \nabla \varepsilon = 0$ which finally translates eq. (3.15) to [61, p. 11]

$$\Delta \mathbf{E} - \frac{\mu_r \varepsilon_r}{c_0^2} \ddot{\mathbf{E}} + \nabla \ln \mu_r \times (\nabla \times \mathbf{E}) - \nabla(\mathbf{E} \cdot \nabla \ln \varepsilon_r) = 0 \quad (3.16)$$

Here I used the definitions $\mu = \mu_0 \mu_r$, $\varepsilon = \varepsilon_0 \varepsilon_r$ as well as $c_0 = 1/\sqrt{\mu_0 \varepsilon_0}$ and wrote the relative derivatives of μ and ε as logarithmic derivatives. In this formula $\varepsilon_r(x, y, z)$ and $\mu_r(x, y, z)$ are scalar functions. Let's restrict our considerations to the case of non-magnetic materials which leads to the assumption of $\mu_r(z) = 1$, which makes the third term in eq. (3.16) zero. Now let's assume that ε_r depends only on the dimension z . In case of an s-polarized wave, a linear polarized wave with an electric field perpendicular to the plane of incidence, the last term of eq. (3.16) vanishes also, and we get:

$$\Delta \mathbf{E} - \frac{\varepsilon_r(z)}{c_0^2} \ddot{\mathbf{E}} = 0 \quad (3.17)$$

For a p-polarized wave, a linear polarized wave with electric field parallel to the plane of incidence, the last term would not vanish and has to be considered. In case of a s-polarized wave we consider without any loss of generality a wave with a field along the x-direction

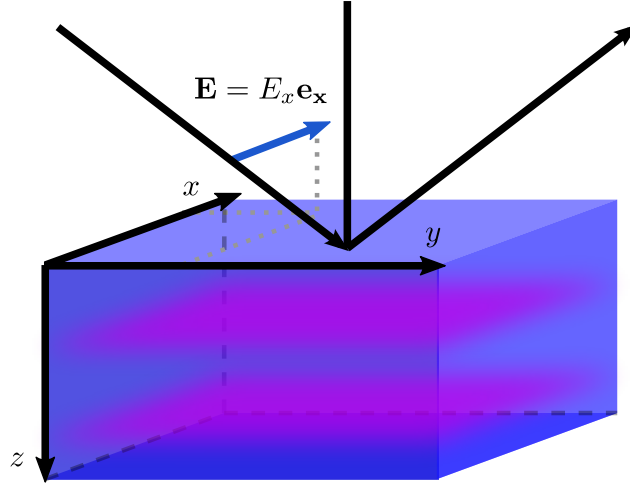


Figure 3.4: A incident light ray with the electric field \mathbf{E} polarized along the x-axis is reflected on a sample surface and partly from the spatially non constant dielectric function $\varepsilon(z)$. The violet regions in the blue material cube visualize the strained regions in the material which change the dielectric properties along the propagation direction z of the sound wave.

$\mathbf{E} = (E_x, 0, 0) \exp(-i\omega t)$ as depicted in Fig. 3.4. This simplifies eq. (3.17) to its first row. Using the definition $k_0^2 = \omega^2/c_0^2$, where k_0 represents the light wave vector in vacuum, we get:

$$\frac{\partial^2}{\partial y^2} E_x + \frac{\partial^2}{\partial z^2} E_x + \varepsilon_r(z) k_0^2 E_x = 0 \quad (3.18)$$

This partial differential equation can be translated into two ordinary differential equations by separating the variables y and z with the ansatz $E_x(y, z) = Y(y)\mathcal{E}(z)$. This leads to the equations [61, p. 56]

$$\frac{\partial^2}{\partial y^2} Y(y) = -k_y^2 Y(y) \quad (3.19)$$

$$\frac{\partial^2}{\partial z^2} \mathcal{E}(z) = -(\varepsilon_r(z) k_0^2 - k_y^2) \mathcal{E}(z) \quad (3.20)$$

where eq. (3.19) is easily solvable and therefore the solution for $E_x(y, z)$ can be written as

$$E_x(y, z) = \mathcal{E}(z) \exp(ik_y y). \quad (3.21)$$

With eq. (3.21) k_y can be interpreted as the y-component of the wave vector of the incoming light wave which is a constant and given by Snell's law.

3.4.2 Reflection of Dirac like change of the dielectric constant

In this part we want to use eq. (3.20) to find the reflection coefficient of a Dirac like change in the dielectric constant i. e. a change of $\varepsilon_r(z)$ in an infinitesimal small region $[z, z + dz]$. For this purpose it is helpful to describe the dielectric property $\varepsilon_r(z) = \varepsilon_r + \Delta\varepsilon_r(z)$ as a sum of the unperturbed and constant ε_r and a function $\Delta\varepsilon_r(z)$ which describes small changes of the dielectric "constant" around the value ε_r . With the use of Snell's law we can write $k_y^2 = k_0^2 \varepsilon_r \sin^2(\beta)$ with β defining the refraction angle in the medium. This simplifies eq. (3.20) to [31]

$$\frac{\partial^2}{\partial z^2} \mathcal{E}(z) = -k_0^2 [\varepsilon_r' + \Delta\varepsilon_r(z)] \mathcal{E}(z) \quad (3.22)$$

by using the definition $\varepsilon'_r := \varepsilon_r \cos^2(\beta)$. Let's assume $\Delta\varepsilon_r(z)$ is given by the function $F\delta(z - z')$ where δ represents the Dirac delta function:

$$\frac{\partial^2}{\partial z^2} \mathcal{E}(z) = -k_0^2 [\varepsilon'_r + F\delta(z - z')] \mathcal{E}(z) \quad (3.23)$$

The value of $\delta(z - z')$ is only different from zero at z' which makes it easy to solve eq. (3.23) for $z \neq z'$. In those regions the solution $\mathcal{E}(z)$ is given by plane waves

$$\mathcal{E}(z) = \begin{cases} \mathcal{E}_0 [\exp(ik_0 n' z) + r_\delta \exp(-ik_0 n' z)] & \text{for } z < 0 \\ \mathcal{E}_0 t_\delta \exp(ik_0 n' z) & \text{for } z > 0 \end{cases} \quad (3.24)$$

where the incoming wave $\mathcal{E}_0 \exp(ik_0 n' z)$ is partially reflected by the δ peak with the reflection coefficient r_δ and partially transmitted with the transmission coefficient t_δ . Note that

$$n' = \sqrt{\varepsilon'_r} = \sqrt{\varepsilon_r \cos^2(\beta)} = n \cos(\beta) \quad (3.25)$$

where n is the refractive index of the medium and $\beta = 90^\circ - \theta$ with θ described in section 3.2. To find r_δ and t_δ we can use the continuity of $\mathcal{E}(z)$ and the defined discontinuity of $\mathcal{E}'(z) = \frac{\partial \mathcal{E}(z)}{\partial z}$ given by eq. (3.23).

With a small number $\sigma > 0$ we can express the continuity condition of $\mathcal{E}(z)$ as eq. (3.26) which yields eq. (3.27) by using the plane wave solutions (3.24).

$$\lim_{\sigma \rightarrow 0} [\mathcal{E}(z' - \sigma) - \mathcal{E}(z' + \sigma)] = 0 \quad (3.26)$$

$$1 + r_\delta \exp(-i2k_0 n' z') = t_\delta \quad (3.27)$$

The discontinuity of $\mathcal{E}'(z)$ due to the Dirac function can be quantified by integrating eq. (3.23) around z' which can be expressed as eq. (3.28) yielding eq. (3.29) which finally translates into eq. (3.30) by using eq. (3.24) and its first derivatives with respect to z .

$$\lim_{\sigma \rightarrow 0} \int_{z' - \sigma}^{z' + \sigma} \frac{\partial^2}{\partial z^2} \mathcal{E}(z) + k_0^2 [\varepsilon'_r + F\delta(z - z')] \mathcal{E}(z) dz = 0 \quad (3.28)$$

$$\lim_{\sigma \rightarrow 0} [\mathcal{E}'(z' - \sigma) - \mathcal{E}'(z' + \sigma)] = -k_0^2 F \mathcal{E}(z') \quad (3.29)$$

$$ik_0 n' [(t_\delta - 1) \exp(ik_0 n' z') + r_\delta \exp(-ik_0 n' z')] = -k_0^2 F t_\delta \exp(ik_0 n' z') \quad (3.30)$$

By the use of eq. (3.27) and eq. (3.30) we can determine r_δ and t_δ which yields [31]

$$r_\delta = -\frac{k_0 F}{k_0 F + i2n'} \exp(i2k_0 n' z') \approx \frac{ik_0 F}{2n'} \exp(i2k_0 n' z') \quad (3.31)$$

$$t_\delta = \frac{i2n'}{k_0 F + i2n'} \quad (3.32)$$

The last term in eq. (3.31) represents the first order approximation in F of the reflection coefficient coming from a delta spike in the spatially changing dielectric constant $\varepsilon_r(z)$. It is valid for r_δ far away from unity, where multiple reflection of the incoming light beam can be neglected.

3.4.3 Reflection coefficient of a sound wave in a medium

The complete reflection from a medium varying dielectric constant along the z coordinate can be approximated by the integral of eq. (3.31) over z , where F was the amplitude of the δ -like $\Delta\varepsilon_r(z)$. [31]

$$r[\Delta\varepsilon_r(z)] = \frac{ik_0}{2n \cos(\beta)} \int_0^{\infty} \Delta\varepsilon_r(z) \exp(iqz) dz \quad (3.33)$$

Here $q = 2k_0n \cos(\beta) = 2k_0n \sin(\theta)$ which can be interpreted as the magnitude of a phonon wave vector along the z coordinate as shown in eq. (3.6). The connection of the strain ϵ with the induced change of dielectric constant $\Delta\varepsilon_r$ is given by the photoelastic constants which are defined by $\Delta\varepsilon_{rI} = P_{IJ}\epsilon_J$. Using this definition we can rewrite eq. (3.33) and get eq. (3.34).

$$r_{\epsilon, \text{spol}}[\epsilon(z, t)] = P_{12} \frac{ik_0}{2n \cos(\beta)} \int_0^{\infty} \epsilon(z, t) \exp(iqz) dz \quad (3.34)$$

$$r_{\epsilon, \text{ppol}}[\epsilon(z, t)] = (P_{12} \cos^2(\beta) - P_{11} \sin^2(\beta)) \frac{ik_0}{2n \cos(\beta)} \int_0^{\infty} \epsilon(z, t) \exp(iqz) dz \quad (3.35)$$

Eq. (3.35) is the corresponding equation for p-polarized light, its derivation is not shown here but can be comprehended with literature.[62] The equations (3.34) and (3.35) give us the possibility to calculate the reflection coefficient of a sound wave with strain $\epsilon(z, t)$ in the medium with refractive index n . The reflection coefficient is in both cases proportional to the Fourier transform of the strain function $\epsilon(z, t)$. The resulting dependency q is the corresponding magnitude of the phonon wave vector. Despite the difference of the formulas (3.34) and (3.35) in the prefactor depending on the elastic constants and the incoming photon angle β with respect to the normal of the sample surface, both reflection coefficients are weighted with the incoming photon wave vector magnitude k_0 . Consequently this probing process is more sensitive to Fourier components of higher wave vectors.

3.5 Complete reflection contribution in a pump-probe experiment

For the optical pump-probe experiments in this thesis two different probing schemes were used. The phonons in the excited sample could be probed by using a probe beam coming from the metal film side (**A**) or from the substrate side (**B**). Both beam paths undergo different reflections and transmissions which yield different contributions of phonons to the signal. Figure 3.5 depicts this situation. In this section we want to find explicit formulas which describe the reflection of the sample including strain in the substrate. We define $z = 0$ to the position of the metal substrate interface. The scattered light coming from phonons will interfere in each case with the light coming from this interface.

$$\mathbf{A}: r_{\mathbf{A}} = r_L + t_L \tilde{t}_L r_{\epsilon} \quad (3.36)$$

$$\mathbf{B}: r_{\mathbf{B}} = t_{02} t_{20} e^{i\delta} (\tilde{r}_L + \tilde{r}_{\epsilon} + \tilde{r}_L^2 r_{\epsilon}), \quad \delta = \frac{4\pi}{\lambda} sn \cos(\beta) \quad (3.37)$$

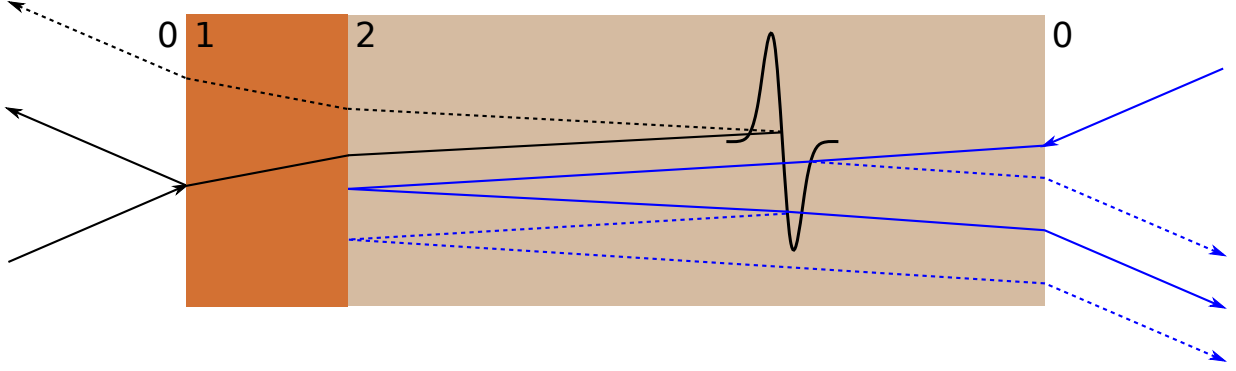


Figure 3.5: In the experiments of this thesis two different probing geometries were used. On the one hand we can probe the phonons with a probe beam coming from the metal (orange) surface side, and on the other hand a probe beam coming from the substrate surface. The last version has the advantage that the probe light does not have to penetrate through the metal film, which finally leads to more reflected light from phonons. On the other side a high reflective metal film leads to a additional reflection from the phonons which have to be considered.

Eqs. (3.36) and (3.37) are the overall reflection coefficients for scenario **A** and **B**. r_L and \tilde{r}_L are the reflection coefficients of the layer for a light ray coming from left or right, respectively, as depicted in Fig. 3.5. Numbered variables refer to the transmission (t) and reflection (r) coefficients given by Fresnel's formulas.[63, p. 61 u. 63] The numbers define the interface which has to be considered. The values of r_ϵ and \tilde{r}_ϵ refer to the reflection of light from the strain in the substrate. The direct reflection of the strain in scenario **B** is described by \tilde{r}_ϵ . Here the light is reflected from the opposite side in comparison with the reflection from the strain after the layer reflection given by $\tilde{r}_L^2 r_\epsilon$. The variable δ is the phase change coming from the propagation of the light ray twice though the substrate with thickness s and complex refractive index n . In this consideration it's mainly important if the absorption of the substrate is not negligible. Note, the variables r_L , \tilde{r}_L , t_L , \tilde{t}_L as well as r_ϵ and \tilde{r}_ϵ are time-dependent quantities. The reflection and transmission of the photoexcited layer are changed mainly due to heat conduction which leads to layer-cooling. These coefficients are explicitly given by time-dependent Fresnel coefficients describing reflection and transmission of the air-metal and metal-substrate interfaces including multiple reflections within the metal film, which are important for films thinner than the optical penetration depth.

$$r_L = \frac{r_{01} + r_{12}e^{i2\phi}}{1 + r_{01}r_{12}e^{i2\phi}}, \quad \tilde{r}_L = \frac{r_{21} + r_{10}e^{i2\phi}}{1 + r_{21}r_{10}e^{i2\phi}} \quad (3.38)$$

$$t_L = \frac{t_{01}t_{12}e^{i\phi}}{1 + r_{01}r_{12}e^{i2\phi}}, \quad \tilde{t}_L = \frac{t_{21}t_{10}e^{i\phi}}{1 + r_{21}r_{10}e^{i2\phi}} \quad (3.39)$$

The variable ϕ represents the phase shift coming from the light propagation through the metal film and is given by the layer thickness d , the complex refractive index of the layer n_L the vacuum probing wavelength λ and the refraction angle ϑ in the layer are given by Snell's law.

$$\phi = \frac{2\pi}{\lambda}dn_L \cos(\vartheta) \quad (3.40)$$

The phonon reflection coefficient r_ϵ is given by eqs. (3.34) or (3.35) depending on the polarization of the incoming probe light. The coefficient \tilde{r}_ϵ is slightly different from r_ϵ ,

because the probe beam reflects from the other side of the strain wave and the beam path gets shorter as the strain wave propagates which leads to a inverted phase change with respect to reflection r_ϵ . These two differences can be considered by flipping the z -axis ($z \mapsto -z$) of the strain $\epsilon(z, t)$. With this follows that $\tilde{r}_\epsilon[\epsilon(z, t)] = r_\epsilon[\epsilon(-z, t)]$ considering an integration over the negative half space $[-\infty, 0]$ which is the same as flipping the phase factor in eqs. (3.34) and (3.35) to a minus sign:

$$\tilde{r}_{\epsilon, \text{spol}}[\epsilon(z, t)] = P_{12} \frac{ik_0}{2n \cos(\beta)} \int_0^\infty \epsilon(z, t) \exp(-iqz) dz \quad (3.41)$$

$$\tilde{r}_{\epsilon, \text{ppol}}[\epsilon(z, t)] = (P_{12} \cos^2(\beta) - P_{11} \sin^2(\beta)) \frac{ik_0}{2n \cos(\beta)} \int_0^\infty \epsilon(z, t) \exp(-iqz) dz \quad (3.42)$$

To find an explicit form of eq. (3.7) for scenario **A** and **B** it is helpful to translate all complex coefficients to their magnitude and angle in the form $D = |D| \exp(i\phi_D)$. Furthermore, we add to the subscript of reflection and transmission coefficients of the layer a subscript, an u for the unpumped and a p for the pumped case. For the unpumped intensity I_u and pumped intensity I_p detected in the spectrometer we get:

$$\mathbf{A}: I_p = |r_{L,p} + t_{L,p} \tilde{t}_{L,p} r_\epsilon|^2 \quad (3.43)$$

$$I_u = |r_{L,u}|^2 \quad (3.44)$$

$$\mathbf{B}: I_p = |t_{02} t_{20}|^2 e^{-2\text{Im}(\delta)} |\tilde{r}_{L,p} + \tilde{r}_\epsilon + \tilde{r}_{L,p}^2 r_\epsilon|^2 \quad (3.45)$$

$$I_u = |t_{02} t_{20}|^2 e^{-2\text{Im}(\delta)} |\tilde{r}_{L,u}|^2 \quad (3.46)$$

Neglecting higher order terms of r_ϵ and \tilde{r}_ϵ , the relative reflected intensity (3.7) measured in the pump-probe scheme is given by:

$$\mathbf{A}: \frac{\Delta R}{R_0} = \frac{|r_{L,p}|^2 + 2|r_{L,p}| |t_{L,p}| |\tilde{t}_{L,p}| |r_\epsilon| \cos(\phi_\epsilon + \phi_{t_{L,p}} + \phi_{\tilde{t}_{L,p}} - \phi_{r_{L,p}})}{|r_{L,u}|^2} - 1 \quad (3.47)$$

$$\mathbf{B}: \frac{\Delta R}{R_0} = \frac{|\tilde{r}_{L,p}|^2 + 2|\tilde{r}_{L,p}| |\tilde{r}_\epsilon| \cos(\Delta\phi_1) + 2|\tilde{r}_{L,p}|^3 |r_\epsilon| \cos(\Delta\phi_2)}{|\tilde{r}_{L,u}|^2} - 1 \quad (3.48)$$

$$\Delta\phi_1 = \phi_{\tilde{r}_\epsilon} - \phi_{\tilde{r}_{L,p}} = -(\phi_{r_\epsilon} + \phi_{\tilde{r}_{L,p}})$$

$$\Delta\phi_2 = \phi_{r_\epsilon} + 2\phi_{\tilde{r}_{L,p}} - \phi_{\tilde{r}_{L,p}} = \phi_{r_\epsilon} + \phi_{\tilde{r}_{L,p}}$$

$$\mathbf{B}: \frac{\Delta R}{R_0} = \frac{|\tilde{r}_{L,p}|^2 + 2|\tilde{r}_{L,p}| |r_\epsilon| (1 + |\tilde{r}_{L,p}|^2) \cos(\phi_{r_\epsilon} + \phi_{\tilde{r}_{L,p}})}{|\tilde{r}_{L,u}|^2} - 1 \quad (3.49)$$

The equations (3.47) and (3.49) are the final results for the relative reflected intensity of the scenarios **A** and **B**. Interestingly the higher order reflection from phonons by a double reflection on the metal film in scenario **B** adds perfectly up to the first order reflection coming from the phonons.

In case of scenario **B** with negligible multireflection $|\tilde{r}_{L,p}|^2 \ll 1$ it is possible to determine a quantity out of the measured relative reflectivity change which is not influenced by the pumped metal film and proportional to the phonon reflection r_ϵ . Therefore we rearrange eq. (3.49) in a way where we have separated the slowly varying part S_L from the

fast oscillating contribution S_H .

$$\frac{\Delta R}{R_0} = \underbrace{\frac{|\tilde{r}_{L,p}|^2}{|\tilde{r}_{L,u}|^2} - 1}_{S_L} + \underbrace{\frac{2|\tilde{r}_{L,p}||r_\epsilon| \cos(\phi_{r_\epsilon} + \phi_{\tilde{r}_{L,p}})}{|\tilde{r}_{L,u}|^2}}_{S_H} \quad (3.50)$$

S_L typically changes much slower (\sim ns) than S_H (\sim 10 ps) and therefore we can get both quantities by using high and low pass filters. Let's define P as

$$P = \frac{S_H}{\sqrt{S_L + 1}} = \frac{2|r_\epsilon| \cos(\phi_{r_\epsilon} + \phi_{\tilde{r}_{L,p}})}{|\tilde{r}_{L,u}|}. \quad (3.51)$$

The quantity P is independent of the reflectivity of the heated layer and depends transiently only on the temporal variation of r_ϵ . To compare different probe wavelengths it is important to consider the wavelength dependent reflection $|\tilde{r}_{L,u}(\lambda)|$ of the layer. A multiplication of $|\tilde{r}_{L,u}(\lambda)|$ and P lead then to a quantity which is direct proportional to the phonon spectral amplitude.

NONLINEAR SOUND

In this chapter we want to go beyond the linear behavior of sound in crystals, similar to the field of nonlinear optics where the refractive index depends on the electric field of an existing light wave. In optics this has produced new physical effects like frequency mixing, supercontinuum generation and the existence of optical solitons.[64–66] Today, such nonlinear effects build the fundament of new laser applications e. g. in information technology and ultrafast laser science. In case of phonons the anharmonicity of the lattice potential leads to a finite thermal conductivity and a nonzero thermal expansion of crystals. Especially for heat conduction the coupling of phonons with frequencies in the high GHz range until THz is important. It defines how phonons are scatter with each other and how fast energy can be transported by them. One possibility to study the coupling of high frequency phonons is the investigation of high amplitude coherent hypersonic waves by ultrafast techniques such as optical pump-probe or time-resolved x-ray diffraction.

For hypersound, sound with a wavelength in the nanometer range, nonlinear effects in crystals are currently under investigation. In the linear regime of sound in a crystal the forces acting on atoms are proportional to their displacement from the equilibrium position. This is the case only in perfect parabolic crystal potentials. In real physical systems the interaction of atoms goes usually down if we take them apart from each other and goes up if we try to bring them together. This behavior is mainly given by the intrinsic nonlinearity of the underlying interactions: the electrostatic forces, dipole-dipole interactions and the pauli-repulsion.

The nonlinear interaction leads to a sound amplitude dependent speed of sound (corresponding to the refractive index in optics) of the material. In the last years the self-steepening of a sound pulse front which can be seen as acoustic analog of the supercontinuum generation was observed by several groups.[XIV][67–69] In addition, non-dispersive and nanometer long wave packets also called solitons were produced and detected.[70–73] In all these experiments broadband acoustic pulses were used. To investigate the coupling of specific phonon modes with a certain frequency, narrow band phonon wave packets have to be used. Therefore one can excite a nanometric metal film on a substrate by a train of laser pulses where the excited phonon frequency is given by the inverse of the temporal pulse displacement.[IV][74]

My main contribution to the field of nanoscale nonlinear acoustics is the experimentally observed second harmonic generation (SHG) of nanoscale longitudinal acoustic phonons in SrTiO₃ excited by a train of chirped laser pulses [75] and probed via ultrafast x-ray diffraction and time-resolved Brillouin scattering.[XIII] While these nonlinear modifications of the waves can be explained by coupled sinusoidal waves on a fixed crystal lattice,

our group found in addition mechanisms where phonon wave packets couple to the lattice structure directly. First, we found that short and intense sound pulses can change the mosaicity of a material which leads to a coupling of out-of-plane phonons to in-plane phonons.[XVI] And second, we observed a softening of acoustic phonons in SrTiO₃ below the anti-ferro-distortive phase transition which is connected with a coupling of phonons to domain walls.[XV]

This chapter is a resumé of the theory of nonlinear phonons used in the papers **XIV** and **XIII** which essentially only report the experimental findings and the results of the simulations. I will introduce the Fermi-Pasta-Ulam (FPU) chain, a linear chain as eq. (2.11) but with additional anharmonic terms describing the nearest neighbor forces. Furthermore I will show the connection of the FPU chain to the standard acoustic nonlinear wave equation and its third order elastic constants, the Boussinesq equation, the Burgers equation, as well as the Korteweg-de Vries equation. All these nonlinear partial differential equations follow from the FPU-chain. The Burgers equation can describe the nonlinear behavior of self-steepening and second harmonic generation whereas the Korteweg-de Vries equation has acoustic soliton solutions, where these solitons are the reason that for large times after excitation the third order anharmonicity in the chain does not lead to a thermal equilibration of the energy, which was originally expected by Fermi and coworkers.

4.1 The Fermi-Pasta-Ulam chain

To describe lattice vibrations of an anharmonic lattice in 1D the famous Fermi-Pasta-Ulam- α - β chain can be used.[76, 77] This model is essentially a chain of oscillators coupled by nonlinear springs. I extended the FPU chain by an empirical acoustic damping term which mimics the quadratic frequency dependence of phonon damping due to thermoelastic damping and the Herring process.[78–82] The equations of motion of each oscillator i with displacement u_i is given by

$$m_M \ddot{u}_i = k_M [(u_{i+1} - u_i) - (u_i - u_{i-1})] + \alpha_M [(u_{i+1} - u_i)^2 - (u_i - u_{i-1})^2] \\ + \beta_M [(u_{i+1} - u_i)^3 - (u_i - u_{i-1})^3] + m_M \gamma_M [(\dot{u}_{i+1} - \dot{u}_i) - (\dot{u}_i - \dot{u}_{i-1})] + F_i(t) \quad (4.1)$$

Here m and k are the oscillator mass and the spring constant. The parameters α and β are the cubic and quartic contributions of the lattice potential, whereas γ measures the phonon damping. In general the chain can describe a sample with different materials which have different material parameters. This is indicated with the material index M . The last term in eq. (4.1) stands for the external forces acting on the chain. To calculate the forces, the thermoelastic stress discussed in chapter 2 can be used. $F_i = m_M g(a \cdot i, t)$ where a is the lattice constant and $i = 0..N - 1$ where N is the number of oscillators in the chain. The function $g(z, t)$ is defined in 2.4.2. It is essentially the local acceleration acting on the mass i .

4.2 Continuum approximation of the extended FPU chain

Let's assume that the chain is composed of only one material so we can ignore the index M of eq. (4.1). Furthermore we want to look at a unforced region of the chain and set $\beta = 0$, because in our simulations β is usually a small number which does not change the

main outcomes of the calculation. It ensures only that the lattice potential will not go to $-\infty$ as $u_i \rightarrow \infty$. This translates eq. (4.1) to the FPU- α chain with viscoelastic damping.

$$m\ddot{u}_i = k[(u_{i+1} - u_i) - (u_i - u_{i-1})] + \alpha[(u_{i+1} - u_i)^2 - (u_i - u_{i-1})^2] + m\gamma[(\dot{u}_{i+1} - \dot{u}_i) - (\dot{u}_i - \dot{u}_{i-1})] \quad (4.2)$$

Similar to the calculation in 2.4.1 we can now transform the set of differential equations in eq. (4.2) to a partial differential equation which describes the physics in the long wavelength regime where the wavelength $\lambda \gg a$, with a representing the lattice constant of the chain. Using the following Taylor approximations we can translate $u_i \rightarrow u(x)$, $u_{i-1} \rightarrow u(x - a)$ and $u_{i+1} \rightarrow u(x + a)$.

$$u(x - a, t) \approx u(x) - \frac{\partial}{\partial x}u(x, t)a + \frac{1}{2} \frac{\partial^2}{\partial x^2}u(x, t)a^2 - \frac{1}{6} \frac{\partial^3}{\partial x^3}u(x, t)a^3 + \frac{1}{24} \frac{\partial^4}{\partial x^4}u(x, t)a^4 \quad (4.3)$$

$$u(x + a, t) \approx u(x) + \frac{\partial}{\partial x}u(x, t)a + \frac{1}{2} \frac{\partial^2}{\partial x^2}u(x, t)a^2 + \frac{1}{6} \frac{\partial^3}{\partial x^3}u(x, t)a^3 + \frac{1}{24} \frac{\partial^4}{\partial x^4}u(x, t)a^4 \quad (4.4)$$

Inserting these equations into eq. (4.2) considering approximations only until second order in a for the squared differences and the damping terms, we get the following partial differential equation (PDE).

$$\underbrace{\frac{\partial^2 u}{\partial t^2} = \frac{ka^2}{m} \frac{\partial^2 u}{\partial x^2}}_{\text{Wave equation}} + \underbrace{\gamma a^2 \frac{\partial}{\partial t} \frac{\partial^2 u}{\partial x^2}}_{\text{Damping}} + \underbrace{\frac{2\alpha a^3}{m} \frac{\partial u}{\partial x} \frac{\partial^2 u}{\partial x^2}}_{\text{First order anharmonicity}} + \underbrace{\frac{ka^4}{12m} \frac{\partial^4 u}{\partial x^4}}_{\text{Higher order dispersion}} \quad (4.5)$$

Differentiating eq. (4.5) by x and using the definition of strain $\epsilon = \partial u / \partial x$ leads to the following equation describing the strain in a nonlinear medium with damping.

$$\frac{\partial^2 \epsilon}{\partial t^2} = \frac{ka^2}{m} \frac{\partial^2 \epsilon}{\partial x^2} + \gamma a^2 \frac{\partial}{\partial t} \frac{\partial^2 \epsilon}{\partial x^2} + \frac{2\alpha a^3}{m} \frac{\partial}{\partial x} \left(\epsilon \frac{\partial \epsilon}{\partial x} \right) + \frac{ka^4}{12m} \frac{\partial^4 \epsilon}{\partial x^4} \quad (4.6)$$

4.2.1 Boussinesq equation

For the normalized variables $\tilde{\epsilon} = 2\frac{\alpha a}{k}\epsilon$, $\tilde{x} = \frac{\sqrt{12}}{a}x$, $\tilde{t} = \sqrt{12\frac{k}{m}}t$ and assuming no damping ($\gamma = 0$) eq. (4.6) translates to the canonical Boussinesq equation.[83]

$$\frac{\partial^2 \tilde{\epsilon}}{\partial \tilde{t}^2} = \frac{\partial^2 \tilde{\epsilon}}{\partial \tilde{x}^2} + \frac{\partial}{\partial \tilde{x}} \left(\tilde{\epsilon} \frac{\partial \tilde{\epsilon}}{\partial \tilde{x}} \right) + \frac{\partial^4 \tilde{\epsilon}}{\partial \tilde{x}^4} \quad (4.7)$$

This equation was derived by Boussinesq and describes shallow water waves which can have soliton character. Such a solitary wave was firstly documented by Scott-Russel, who observed a water wave packet propagating along a canal over a distance of around two miles without changing its shape.[84] Solitons are often discussed as quasiparticles because they are stable after collision with other solitons. The main reason why the Boussinesq equation shows such soliton solutions is that the anharmonicity, which can be imagined as a strain dependent sound velocity, cancels out the higher order dispersion which effectively leads to linear dispersion in the region of the soliton.

4.2.2 Korteweg-de Vries equation

If we are only interested in waves propagating in a certain direction, let's say a propagation to the right, it is possible to transform eq. (4.6) with $\gamma = 0$ into a moving frame of reference by the coordinate transform $y = x - ct$ and $\tau = t$ where $c = \sqrt{\frac{k}{m}}a$ is the sound velocity of a wave with small amplitude (linear regime).[85, p. 18] Neglecting the second time derivative of ϵ and transforming to the normalized coordinates $\bar{\epsilon} = \frac{1}{6} \frac{\alpha a}{k} \epsilon$, $\bar{y} = \frac{\sqrt{24}}{a} y$ and $\bar{\tau} = \sqrt{24 \frac{k}{m}} \tau$ we get the Korteweg-de Vries (KdV) equation.[86]

$$\frac{\partial \bar{\epsilon}}{\partial \bar{t}} + 6\bar{\epsilon} \frac{\partial \bar{\epsilon}}{\partial \bar{y}} + \frac{\partial^3 \bar{\epsilon}}{\partial \bar{y}^3} = 0 \quad (4.8)$$

This equation originally found by Boussinesq describes the nonlinear behavior of right propagating waves in various fields of physics like hydrodynamics, nonlinear plasma physics as well as high amplitude acoustics in crystals. The KdV equation has two kinds of particular solutions. The first is a soliton solution described by a squared hyperbolic secant and the second are cnoidal waves which can be expressed in form of squares of Jacobi elliptic functions.[85, p. 21] The solitons were found first numerically by Zabusky and Kruskal and were documented in their famous publication.[87] This publication was an important step in understanding why the FPU-chain shows the so called Fermi-Pasta-Ulam recurrence instead of ergodic behavior, what was expected before Fermi, Pasta, Ulam and Tsingou made first numerical experiments.[88]

While in the experiments of this thesis no solitons are observed because of the high phonon damping in SrTiO₃ even more at low temperature where the anti-ferro-distortive phase transition leads to additional damping [XV], [59], current investigations in our group are running, using different materials such as GaAs and DyScO₃ to generate acoustic solitons at low temperature and investigate their behavior by time-resolved optical and x-ray methods.

4.2.3 Viscous Burgers equation

In the sections before we ignored the viscoelastic damping term of eq. (4.7) which yields the Boussinesq and KdV equation. Microscopically the phonon damping is due to the coupling of phonons to other degrees of freedom such as thermally excited phonons [82], free electrons [89, 90] or defects [91, 92].

In a dielectric where free electrons are not present, the phonon attenuation usually goes down with temperature. Neglecting the damping in the description of wave propagation is therefore only valuable for low temperatures. The typical power law frequency dependence of the anharmonic damping makes that high phonon frequencies damp out rapidly.[79] Consequently solitons which have also high frequency contributions are not stable at high temperatures. For such temperatures it is more appropriate to consider the damping term in eq. (4.7) and neglect the higher order dispersion which originally stabilized the solitons in the Boussinesq and KdV equation.

Doing this, transforming the equation into the moving frame of reference by the coordinate transform $y = x - ct$ as well as $\tau = t$ as in the case of the KdV and neglecting the second order terms with time derivatives of ϵ yields,

$$\frac{\partial \epsilon}{\partial \tau} + \frac{\alpha a^3}{mc} \epsilon \frac{\partial \epsilon}{\partial y} = \frac{\gamma a^2}{2} \frac{\partial^2 \epsilon}{\partial y^2}. \quad (4.9)$$

A translation of this equation to the new coordinates $\hat{y} = \frac{2\alpha a}{m\gamma c}y$ and $\hat{\tau} = \frac{2\alpha^2 a^4}{m^2\gamma c^2}\tau$ yields the viscous Burgers equation.

$$\frac{\partial \epsilon}{\partial \hat{\tau}} + \epsilon \frac{\partial \epsilon}{\partial \hat{y}} = \frac{\partial^2 \epsilon}{\partial \hat{y}^2} \quad (4.10)$$

This equation describes nonlinear sound propagation, where the strain modulates the sound velocity in the vicinity of the strain pulse. This leads in normal materials ($\alpha < 0$) to compressive strain parts which propagate faster than low amplitude sound (supersonic) and tensile strain parts which propagate slower than the sound velocity (subsonic).

In paper **XIV** we present the observation of a nonlinearly propagating bipolar strain pulse and used a linear chain to explain this interesting nonlinear effect which can be understood as an analog to the supercontinuum generation of light mentioned in the chapter before (3.3). Here, I would like to use the Burgers equation, although it is an extensive simplification of the FPU-chain it describes the self-steepening of the strain fronts quantitatively and shows that this effect depends mainly on the anharmonicity of the lattice potential, whereas higher order dispersion has essentially no influence. Interestingly, although the viscous Burgers equation is a nonlinear equation one can transform it into a linear diffusion equation using the Hopf-Cole transform and solve the initial value problem.[93, 94] This leads to the solution [95, ch. 1.1.5]

$$\epsilon(\hat{y}, \hat{\tau}) = -2 \frac{\partial}{\partial \hat{y}} \ln \left\{ \frac{1}{\sqrt{4\pi\hat{\tau}}} \int_{-\infty}^{\infty} \exp \left[-\frac{(\hat{y} - \xi)^2}{4\hat{\tau}} - \frac{1}{2} \int_0^{\xi} \epsilon(\xi', 0) d\xi' \right] d\xi \right\}. \quad (4.11)$$

Using the same bipolar strain pulse as in Fig. 2.4 on page 16 as initial condition (only substrate part), we can follow the shape changes due to the self-modulation of the sound velocity shown in Fig. 4.1. Because of the velocity difference between the tensile and compressive part of the pulse, the pulse fronts move apart from each other and the main spectral components of the pulse shift to longer wavelength (smaller wave vectors).

As discussed in the chapter before, optical light scattering on a sound wave is nicely described by a Fourier transform of the strain field (Eqns. 3.34 and 3.35). The whole spectrum shifts now to smaller wave vectors which leads to a change of the Brillouin oscillation amplitude. In other words a fraction of the probe light is reflected from the leading edge of the compressive pulse and another part on the trailing edge of tensile side of the N-wave. At certain points in time both reflections destructively interfere with each other and the Brillouin oscillation amplitude gets zero. After that both strain fronts move further apart from each other and the scattering gets non zero again. This beating frequency is highly dependent on the acoustic nonlinearity [96]. In paper **XIV** we used this beating frequency in combination with the measurement of the acoustic pulse amplitude by ultrafast x-ray diffraction to determine the first order anharmonicity of the lattice for longitudinal soundwaves propagating along the [001] direction.

In case of multi-cycle strain pulses which can be generated by a train of laser pulses which excite a metal film as shown in paper **IV**, the positive and negative strain contribution cannot move apart from each other, because of neighboring counteracting strain components which want to move in the opposite direction. This leads to a stabilization of the fundamental excited mode, but via propagation through the nonlinear medium energy of the fundamental is transferred to higher harmonics.[**XIII**]

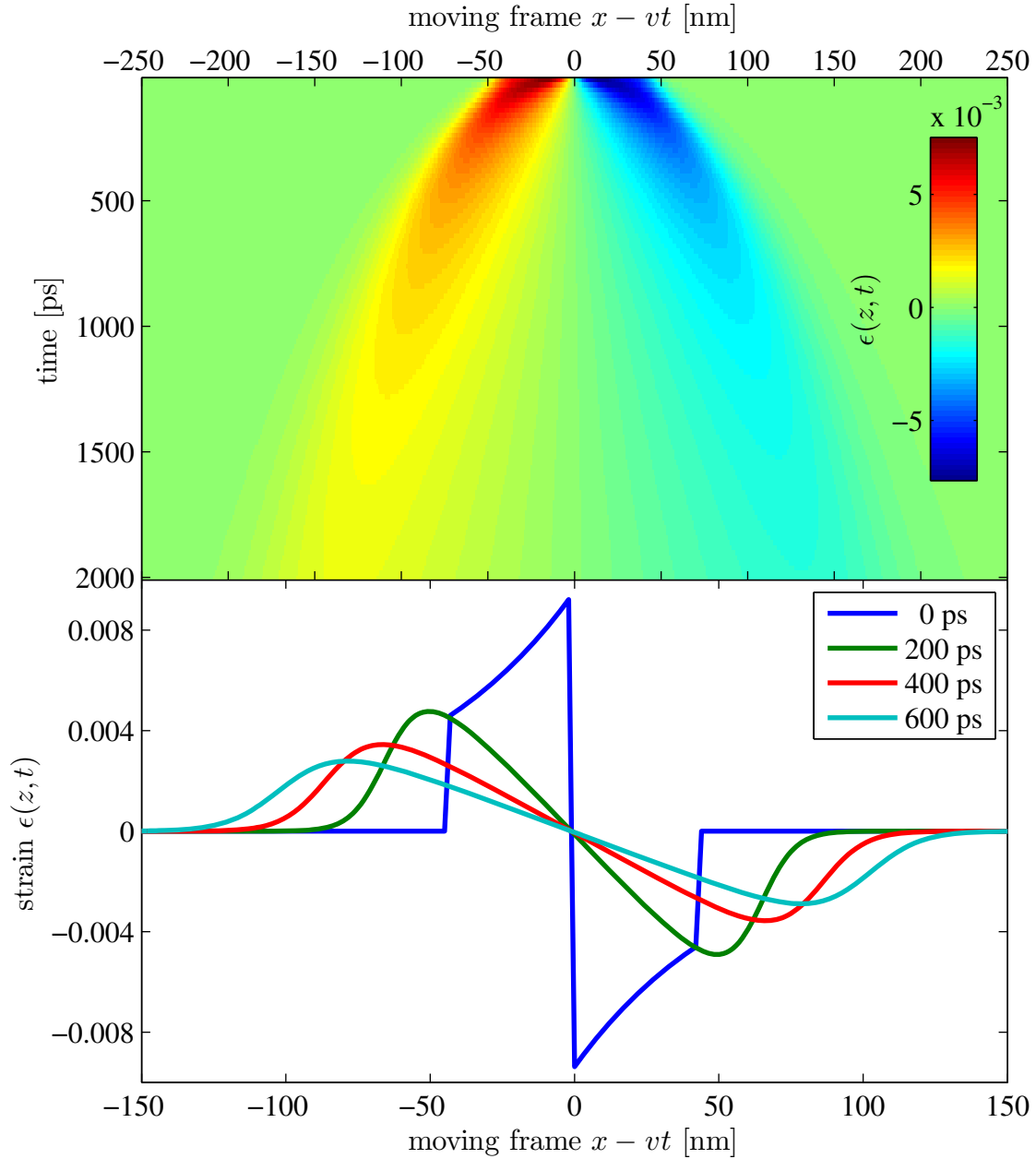


Figure 4.1: The figure shows the calculated strain profile changes of a bipolar strain pulse propagating through the nonlinear acoustic medium SrTiO_3 . The cubic lattice potential contribution leads to a strain dependent sound velocity where expansive crystal regions get softer (lower sound velocity) and tensile regions harder (higher sound velocity). This leads finally to a self-steepening of the strain fronts and to a building of N-Waves.

4.3 Nonlinear elastic theory

In the theory of nonlinear elasticity the third order elastic constants are used to describe the anharmonicity of a material. Using the standard equation of nonlinear elasticity for waves in a cubic crystal propagating along one dimension (x-direction), we get [70, 97]

$$\rho_0 \frac{\partial^2 u}{\partial t^2} = C_{11} \frac{\partial^2 u}{\partial x^2} + (C_{111} + 3C_{11}) \frac{\partial u}{\partial x} \frac{\partial^2 u}{\partial x^2} \quad (4.12)$$

We see directly by comparison of eq. (4.12) with the continuum approximation of the extended FPU-chain eq. (4.5) that the viscoelastic damping term and higher order dispersion are not present. While damping can be discussed in form of imaginary elastic constants, higher order dispersion is in this theory usually neglected because of the focus on long wavelengths.

Comparing the existing coefficients of eq. (4.12) and eq. (4.5) gives us the possibility to translate the FPU model parameters into the second order C_{11} and the third order C_{111} elastic constants of the crystal. Note that ρ_0 is the density of unperturbed medium and is therefore given by $\rho_0 = \frac{m}{a^3}$.

$$\boxed{C_{11} = \frac{k}{a}, \quad C_{111} = 2\alpha - 3\frac{k}{a}} \quad (4.13)$$

SUMMARY AND OUTLOOK

The highlights of this thesis are the three Papers **IV**, **XIII** and **XIV** for which I combined time-resolved optical pump-probe experiments and ultrafast x-ray diffraction.

Paper **IV** presents a perspective on ultrafast x-ray and optical light scattering for investigating the transient spectral content of nanometric narrowband coherent acoustic phonons in a unified way.

Paper **XIV** is a study of very high amplitude single cycle longitudinal acoustic pulses propagating through SrTiO₃ by time-resolved optical Brillouin scattering. I calibrated the strain amplitude of the excited acoustic pulse by ultrafast x-ray diffraction, which allowed me to determine the anharmonicity of the crystal potential. Due to this anharmonicity, tensile regions of the sound pulse propagate faster than expansive ones. This changes the shape of the pulse and therefore also its spectral content which was measured by time-resolved optical Brillouin scattering. The experimentally observed spectral shape is in excellent agreement with a numerical model describing the nonlinear pulse propagation. The anharmonicity serves as the central first parameter of this model.

Paper **XIII** presents the main new physics of this thesis. The observed second harmonic generation of nanometric acoustic phonons by ultrafast variants of inelastic visible light and x-ray scattering is a first important step to make the interaction of very high frequency hypersonic phonon wave packets visible and utilizable. It is the first observation of a phase-matched acoustic phonon mixing process in the nanometer range.

In addition to these publications, I presented in this thesis an analytical description of the thermoelastic excitation of acoustic phonon wave packets by ultrafast heating of a nanometric metal film on a dielectric substrate. An important outcome of this discussion is an analytic formula for the strain of the excited wave packet. Furthermore, I showed that the Fourier transform of this strain function can be used to calculate the scattered light intensities of different probe wavelengths coming from the excited phonon wave packet in an optical pump-probe experiment. In the last part of this thesis I presented the model which was used to describe the nonlinear behavior of the wave packets in papers **XIII** and **XIV**. This model is a Fermi-Pasta-Ulam (FPU) chain with additional phonon damping, which is essentially a system of masses coupled by anharmonic springs with damping. To establish the connection to the field of nonlinear acoustics, I presented a viscous nonlinear wave equation as the continuum approximation of the FPU chain and how this relates to various nonlinear wave equations.

For future technology, the investigation of short wavelength and high frequency phonon scattering processes is of huge importance. The knowledge how to manipulate such processes could improve the heat transport in nanostructures and the efficiency of thermo-

electric materials or might open the path to the use of phonons as information carrying particle in logic gates.

From the physical point of view, it would be interesting to transfer well known concepts from nonlinear optics to the new field *nonlinear phononics* like the parametric amplification. This is a conversion process where high frequency phonons are stimulated by a lower frequency phonon wave packet to decay into the phonon with the lower frequency and its energy and momentum conserving counterpart. Such four wave mixing processes could be investigated for different phonon polarizations (transversal, longitudinal) as well as for optical and acoustic phonon branches. Due to the intrinsic anisotropy of acoustic properties a non-collinear wave mixing geometry could be used to fulfill the phase matching condition for the phonon mixing of different branches.

To investigate scattering processes of those phonons contributing mainly to heat, acoustic phonons with a very short wavelength in the nm or sub-nm range have to be investigated. Due to diffraction limits, for detection x-ray short wavelength radiation as x-ray pulses could be used instead of visible light. Here free electron lasers (FELs) as the first available coherent and femtosecond pulsed x-ray sources hold a great promise to be the perfect tool for such studies. Finally FELs could also be used to generate such high frequency phonons directly by Impulsive Stimulated Raman Scattering (ISRS) which was shown until now only for optical light which provides no phase-matching for high frequency acoustic phonons.[39] Here one would have to cross two FEL beams with a certain angle between them. The interference of these beams in a material would induce a transient polarization grating which could act as a driving force of an THz acoustic phonon excitation.

BIBLIOGRAPHY

1. E. Ozbay. “Plasmonics: Merging Photonics and Electronics at Nanoscale Dimensions”. *Science* **311**, 189 (2006).
2. M. Maldovan. “Sound and heat revolutions in phononics”. *Nature* **503**, 209 (2013).
3. M. E. Siemens, Q. Li, R. Yang, K. A. Nelson, E. H. Anderson, M. M. Murnane and H. C. Kapteyn. “Quasi-ballistic thermal transport from nanoscale interfaces observed using ultrafast coherent soft X-ray beams”. *Nat. Mater.* **9**, 26. 10.1038/nmat2568 (2010).
4. M. N. Luckyanova, J. Garg, K. Esfarjani, A. Jandl, M. T. Bulsara, A. J. Schmidt, A. J. Minnich, S. Chen, M. S. Dresselhaus, Z. Ren, E. A. Fitzgerald and G. Chen. “Coherent Phonon Heat Conduction in Superlattices”. *Science* **338**, 936 (2012).
5. M.-H. Bae, Z. Li, Z. Aksamija, P. N. Martin, F. Xiong, Z.-Y. Ong, I. Knezevic and E. Pop. “Ballistic to diffusive crossover of heat flow in graphene ribbons”. *Nat Commun* **4**, 1734 (2013).
6. M. Maldovan. “Narrow Low-Frequency Spectrum and Heat Management by Thermocrystals”. *Phys. Rev. Lett.* **110**, 025902 (2013).
7. J. Ravichandran, A. K. Yadav, R. Cheaito, P. B. Rossen, A. Soukiassian, S. J. Suresha, J. C. Duda, B. M. Foley, C.-H. Lee, Y. Zhu, A. W. Lichtenberger, J. E. Moore, D. A. Muller, D. G. Schlom, P. E. Hopkins, A. Majumdar, R. Ramesh and M. A. Zurbuchen. “Crossover from incoherent to coherent phonon scattering in epitaxial oxide superlattices”. *Nat Mater* **13**, 168 (2014).
8. R. Venkatasubramanian, E. Siivola, T. Colpitts and B. O’Quinn. “Thin-film thermoelectric devices with high room-temperature figures of merit”. *Nature* **413**, 597. 10.1038/35098012 (2001).
9. B. Poudel, Q. Hao, Y. Ma, Y. Lan, A. Minnich, B. Yu, X. Yan, D. Wang, A. Muto, D. Vashaee, X. Chen, J. Liu, M. S. Dresselhaus, G. Chen and Z. Ren. “High-Thermoelectric Performance of Nanostructured Bismuth Antimony Telluride Bulk Alloys”. *Science* **320**, 634 (2008).
10. K. Biswas, J. He, I. D. Blum, C.-I. Wu, T. P. Hogan, D. N. Seidman, V. P. Dravid and M. G. Kanatzidis. “High-performance bulk thermoelectrics with all-scale hierarchical architectures”. *Nature* **489**, 414. 10.1038/nature11439 (2012).
11. B. Li, L. Wang and G. Casati. “Thermal Diode: Rectification of Heat Flux”. *Phys. Rev. Lett.* **93**, 184301 (2004).
12. L. Wang and B. Li. “Thermal Memory: A Storage of Phononic Information”. *Phys. Rev. Lett.* **101**, 267203 (2008).
13. N. Li, J. Ren, L. Wang, G. Zhang, P. Hänggi and B. Li. “Colloquium : Phononics: Manipulating heat flow with electronic analogs and beyond”. *Rev. Mod. Phys.* **84**, 1045 (2012).
14. M. Forst, C. Manzoni, S. Kaiser, Y. Tomioka, Y. Tokura, R. Merlin and A. Cavalleri. “Nonlinear phononics as an ultrafast route to lattice control”. *Nat. Phys.* **7**, 854. 10.1038/nphys2055 (2011).
15. D. Schick. “Ultrafast Lattice Dynamics in Photoexcited Nanostructures”. Ph.D. thesis, Universität Potsdam (2013).

16. M. Herzog. “Structural Dynamics of Photoexcited Nanolayered Perovskites Studied by Ultrafast X-ray Diffraction”. Ph.D. thesis, Universität Potsdam (2012).
17. S. I. Anisimov, B. L. Kapeliovich and T. L. Perel’man. “Electron emission from metal surfaces exposed to ultrashort laser pulses”. *Sov. Phys. JETP* **39**, 375 (1974).
18. M. Bonn, D. N. Denzler, S. Funk, M. Wolf, S. S. Wellershoff and J. Hohlfeld. “Ultrafast electron dynamics at metal surfaces: Competition between electron-phonon coupling and hot-electron transport”. *Phys. Rev. B* **61**, 1101 (2000).
19. T. Petr, K. Karel, W. Anke and H. Jí. “On the physical properties of $\text{Sr}_{1-x}\text{Na}_x\text{RuO}_3$ ($x = 0.19$)”. *Solid State Sciences* **12**, 1112 (2010).
20. J. Sólyom. *Fundamentals of the physics of solids*, vol. 2: Electronic properties : with 40 tables (Springer, Berlin, 2009).
21. C. Kittel. *Introduction to solid state physics* (Wiley, New York [u.a.], 1996), 7th edn..
22. J. M. Keller and D. C. Wallace. “Anharmonic Contributions to Specific Heat”. *Phys. Rev.* **126**, 1275 (1962).
23. R. A. Cowley. “Anharmonic crystals”. *Reports on Progress in Physics* **31**, 123 (1968).
24. K. Mukherjee and S. M. Hossain. “Effect of anharmonicity on the phonon density of states and specific heat of a monoatomic, one-dimensional crystal lattice”. *Phys. Rev. B* **78**, 224308 (2008).
25. B. Rethfeld, A. Kaiser, M. Vicanek and G. Simon. “Ultrafast dynamics of nonequilibrium electrons in metals under femtosecond laser irradiation”. *Phys. Rev. B* **65**, 214303 (2002).
26. R. N. Stuart, F. Wooten and W. E. Spicer. “Mean Free Path of Hot Electrons and Holes in Metals”. *Phys. Rev. Lett.* **10**, 7 (1963).
27. J. K. Chen, D. Y. Tzou and J. E. Beraun. “A semiclassical two-temperature model for ultrafast laser heating”. *Int. J. Heat Mass Transfer* **49**, 307 (2006).
28. T. Q. Qiu and C. L. Tien. “Heat Transfer Mechanisms During Short-Pulse Laser Heating of Metals”. *Journal of Heat Transfer* **115**, 835. 10.1115/1.2911377 (1993).
29. J. A. Johnson, A. A. Maznev, J. Cuffe, J. K. Eliason, A. J. Minnich, T. Kehoe, C. M. S. Torres, G. Chen and K. A. Nelson. “Direct Measurement of Room-Temperature Nondiffusive Thermal Transport Over Micron Distances in a Silicon Membrane”. *Phys. Rev. Lett.* **110**, 025901 (2013).
30. R. E. Taylor and C. Y. Ho. *Thermal Expansion of Solids* (Asm Intl, 1998).
31. C. Thomsen, H. T. Grahn, H. J. Maris and J. Tauc. “Surface generation and detection of phonons by picosecond light pulses”. *Phys. Rev. B* **34**, 4129 (1986).
32. O. B. Wright. “Ultrafast nonequilibrium stress generation in gold and silver”. *Phys. Rev. B* **49**, 9985 (1994).
33. M. Nicoul, U. Shymanovich, A. Tarasevitch, D. von der Linde and K. Sokolowski-Tinten. “Picosecond acoustic response of a laser-heated gold-film studied with time-resolved x-ray diffraction”. *Appl. Phys. Lett.* **98**, 191902 (2011).
34. P. Ruello and V. E. Gusev. “Physical mechanisms of coherent acoustic phonons generation by ultrafast laser action”. *Ultrasonics* **56**, 21 (2015).
35. N. D. Ashcroft and N. W. Mermin. *Solid state physics* (Saunders College, Fort Worth, 1976), 1st edn..
36. T. K. Cheng, J. Vidal, H. J. Zeiger, G. Dresselhaus, M. S. Dresselhaus and E. P. Ippen. “Mechanism for displacive excitation of coherent phonons in Sb, Bi, Te, and Ti_2O_3 ”. *Applied Physics Letters* **59**, 1923 (1991).

37. H. J. Zeiger, J. Vidal, T. K. Cheng, E. P. Ippen, G. Dresselhaus and M. S. Dresselhaus. “Theory for displacive excitation of coherent phonons”. *Phys. Rev. B* **45**, 768 (1992).
38. Y.-X. Yan, E. B. Gamble and K. A. Nelson. “Impulsive stimulated scattering: General importance in femtosecond laser pulse interactions with matter, and spectroscopic applications”. *The Journal of Chemical Physics* **83**, 5391 (1985).
39. K. A. Nelson, R. Casalegno, R. J. D. Miller and M. D. Fayer. “Laser-induced excited state and ultrasonic wave gratings: Amplitude and phase grating contributions to diffraction”. *The Journal of Chemical Physics* **77**, 1144 (1982).
40. Y.-X. Yan and K. A. Nelson. “Impulsive stimulated light scattering. I. General theory”. *The Journal of Chemical Physics* **87**, 6240 (1987).
41. L. Dhar, J. A. Rogers and K. A. Nelson. “Time-resolved vibrational spectroscopy in the impulsive limit”. *Chemical Reviews* **94**, 157 (1994).
42. T. E. Stevens, J. Kuhl and R. Merlin. “Coherent phonon generation and the two stimulated Raman tensors”. *Phys. Rev. B* **65**, 144304 (2002).
43. P. Kostic, Y. Okada, N. C. Collins, Z. Schlesinger, J. W. Reiner, L. Klein, A. Kapitulnik, T. H. Geballe and M. R. Beasley. “Non-Fermi-Liquid Behavior of SrRuO₃: Evidence from Infrared Conductivity”. *Phys. Rev. Lett.* **81**, 2498 (1998).
44. E. M. Bothschafter, A. Paarmann, E. S. Zijlstra, N. Karpowicz, M. E. Garcia, R. Kienberger and R. Ernstorfer. “Ultrafast Evolution of the Excited-State Potential Energy Surface of TiO₂ Single Crystals Induced by Carrier Cooling”. *Phys. Rev. Lett.* **110**, 067402 (2013).
45. D. Royer and E. Dieulesaint. *Elastic Waves in Solids I, Free and Guided Propagation* (Springer, Heidelberg, 2000).
46. Y. Pinchover and J. Rubinstein. *An introduction to partial differential equations* (Cambridge Univ. Press, Cambridge [u.a.], 2005).
47. C. Tisdell. “How to solve the inhomogeneous wave equation (PDE)”. Video on youtube.com (2013).
48. S. Yamanaka, T. Maekawa, H. Muta, T. Matsuda, S. Kobayashi and K. Kurosaki. “Thermophysical properties of SrHfO₃ and SrRuO₃”. *J. Solid State Chem.* **177**, 3484 (2004).
49. G. Vasta, T. Jackson, A. Frommhold, J. Bowen and E. Tarte. “Residual stress analysis of all perovskite oxide cantilevers”. *Journal of Electroceramics* **27**, 176 (2011).
50. M. Bargheer, N. Zhavoronkov, M. Woerner and T. Elsaesser. “Recent Progress in Ultrafast X-ray Diffraction”. *ChemPhysChem* **7**, 783 (2006).
51. A. Authier. *Dynamical theory of X-ray diffraction*. Monographs on crystallography ; 11 (Oxford Univ. Press, Oxford [u.a.], 2008), repr. edn.. Includes indexes.
52. D. L. Mills and E. Burstein. “Polaritons: the electromagnetic modes of media”. *Reports on Progress in Physics* **37**, 817 (1974).
53. R. Loudon. “The Raman effect in crystals”. *Advances in Physics* **13**, 423–482 (1964).
54. M. Cardona. *Light Scattering in Solids I - Introductory Concepts* (Springer, 1983), 2nd edn..
55. C. Hamaguchi. *Basic semiconductor physics : with 25 tabl.* (Springer, Berlin, 2001).
56. R. W. Boyd. *Nonlinear Optics* (Elsevier Academic Press, Amsterdam, 2008), 3. edn..
57. M. Bradler, P. Baum and E. Riedle. “Femtosecond continuum generation in bulk laser host materials with sub-J pump pulses”. *Applied Physics B* **97**, 561 (2009).

58. E. Pontecorvo, M. Ortolani, D. Polli, M. Ferretti, G. Ruocco, G. Cerullo and T. Scopigno. “Visualizing coherent phonon propagation in the 100 GHz range: A broadband picosecond acoustics approach”. *Appl. Phys. Lett.* **98**, 011901 (2011).
59. V. Kuxhaus. “Breitbandige zeitaufgelöste Brillouin-Streuung an Perovskiten”. Diplomarbeit, Universität Potsdam (2015).
60. J. D. Jackson. *Classical electrodynamics* (Wiley, New York [u.a.], 1999), 3rd edn..
61. M. Born and E. Wolf. *Principles of optics : electromagnetic theory of propagation, interference and diffraction of light* (Cambridge University Press, Cambridge [u.a.], 2009), 7. (expanded) ed., repr. edn..
62. O. Matsuda, M. C. Larciprete, R. L. Voti and O. B. Wright. “Fundamentals of picosecond laser ultrasonics”. *Ultrasonics* **56**, 3 (2015).
63. M. V. Klein and T. E. Furtak. *Optik : mit 10 Tab.* Springer-Lehrbuch (Springer, Berlin, 1988).
64. P. A. Franken, A. E. Hill, C. W. Peters and G. Weinreich. “Generation of Optical Harmonics”. *Phys. Rev. Lett.* **7**, 118 (1961).
65. R. R. Alfano and S. L. Shapiro. “Emission in the Region 4000 to 7000 Å Via Four-Photon Coupling in Glass”. *Phys. Rev. Lett.* **24**, 584 (1970).
66. L. F. Mollenauer, R. H. Stolen and J. P. Gordon. “Experimental Observation of Picosecond Pulse Narrowing and Solitons in Optical Fibers”. *Phys. Rev. Lett.* **45**, 1095 (1980).
67. P. J. S. van Capel and J. I. Dijkhuis. “Optical generation and detection of shock waves in sapphire at room temperature”. *APL* **88**, 151910 (2006).
68. P. J. S. van Capel, H. P. Porte, G. van der Star and J. I. Dijkhuis. “Interferometric detection of acoustic shock waves”. *Journal of Physics: Conference Series* **92**, 012092 (2007).
69. V. V. Temnov. “Ultrafast acousto-magneto-plasmonics”. *Nat Photon* **6**, 728. 10.1038/nphoton.2012.220 (2012).
70. H. Y. Hao and H. J. Maris. “Experiments with acoustic solitons in crystalline solids”. *Phys. Rev. B* **64**, 064302 (2001).
71. O. L. Muskens and J. I. Dijkhuis. “High Amplitude, Ultrashort, Longitudinal Strain Solitons in Sapphire”. *Phys. Rev. Lett.* **89**, 285504 (2002).
72. W. Singhsomroje and H. J. Maris. “Generating and detecting phonon solitons in MgO using picosecond ultrasonics”. *Phys. Rev. B* **69**, 174303 (2004).
73. E. Péronne and B. Perrin. “Generation and detection of acoustic solitons in crystalline slabs by laser ultrasonics”. *Ultrasonics* **44**, **Supplement**, e1203 (2006).
74. C. Klieber, E. Peronne, K. Katayama, J. Choi, M. Yamaguchi, T. Pezeril and K. A. Nelson. “Narrow-band acoustic attenuation measurements in vitreous silica at frequencies between 20 and 400 GHz”. *Appl. Phys. Lett.* **98**, 211908 (2011).
75. A. Bojahr, M. Gohlke, W. Leitenberger, J. Pudell, M. Reinhardt, A. von Reppert, M. Roessle, M. Sander, P. Gaal and M. Bargheer. “Supplement Material: Second Harmonic Generation of Nanoscale Phonon Wave Packets”. *Phys. Rev. Lett.* **115**, 195502 (2015).
76. G. P. Berman and F. M. Izrailev. “The Fermi-Pasta-Ulam problem: Fifty years of progress”. *Chaos: An Interdisciplinary Journal of Nonlinear Science* **15**, (2005).
77. D. K. Campbell, P. Rosenau and G. M. Zaslavsky. “Introduction: The Fermi-Pasta-Ulam problem – The first fifty years”. *Chaos: An Interdisciplinary Journal of Nonlinear Science* **15**, (2005).
78. A. Akhieser. “On the absorption of sound in solids”. *J. Phys. (USSR)* **1**, 277 (1939).

-
79. C. Herring. "Role of Low-Energy Phonons in Thermal Conduction". *Phys. Rev.* **95**, 954 (1954).
80. S. Simons. "The absorption of very high frequency sound in dielectric solids". *Mathematical Proceedings of the Cambridge Philosophical Society* **53**, 702 (1957).
81. T. O. Woodruff and H. Ehrenreich. "Absorption of Sound in Insulators". *Phys. Rev.* **123**, 1553 (1961).
82. H. J. Maris. "6 - Interaction of Sound Waves with Thermal Phonons in Dielectric Crystals". In W. P. MASON and R. N. THURSTON (Eds.), *Principles and Methods*, vol. 8 of *Physical Acoustics*, 279 – 345 (Academic Press, 1971).
83. J. Boussinesq. "Theorie des ondes et des remous qui se propagent le long d'une canal rectangulaire horizontal, et communiquant au liquide contenu dans ce canal des vitesses sensiblement pareilles de la surface au fond". *J. Math. Pures. Appl., Ser. 2* **17**, 55 (1872).
84. J. Scott-Russell. "Report on Waves". *Proc. Roy. Soc. Edinburgh* 319320 (1844).
85. M. Toda. "Studies of a non-linear lattice". *Physics Reports* **18**, 1 (1975).
86. D. J. Korteweg and G. de Vries. "On the Change of Form of Long Waves Advancing in a Rectangular Canal, and on a New Type of Long Stationary Waves". *Phil. Mag.* **39**, 422 (1895).
87. N. J. Zabusky and M. D. Kruskal. "Interaction of "Solitons" in a Collisionless Plasma and the Recurrence of Initial States". *Phys. Rev. Lett.* **15**, 240 (1965).
88. E. Fermi, J. R. Pasta and S. Ulam. "Studies of nonlinear problems I, Los Alamos Report LA1940 (1955)". *Collected papers of Enrico Fermi, Vol. II, University of Chicago Press, IL (1965), p. 978 Lectures in Applied Mathematics* **15** (1974).
89. W. P. Mason. "Ultrasonic Attenuation Due to Lattice-Electron Interaction in Normal Conducting Metals". *Phys. Rev.* **97**, 557 (1955).
90. V. M. Kontorovich. "Dynamic equations of the theory of elasticity of metals". *Soviet Physics Uspekhi* **27**, 134 (1984).
91. H. Dosch, J. Peisl and B. Dorner. "Attenuation of phonon scattering intensities by point defects". *Zeitschrift für Physik B Condensed Matter* **63**, 479 (1986).
92. F. Zeng, S. Agnew, B. Raeisnia and G. Myneni. "Ultrasonic Attenuation Due to Grain Boundary Scattering in Pure Niobium". *Journal of Nondestructive Evaluation* **29**, 93 (2010).
93. E. Hopf. "The partial differential equation $ut + uux = xx$ ". *Communications on Pure and Applied Mathematics* **3**, 201 (1950).
94. J. D. Cole. "On a quasi-linear parabolic equation occurring in aerodynamics." *Quart. Appl. Math.* **9**, 225 (1951).
95. A. D. Poljanin and V. F. Zajcev. *Handbook of nonlinear partial differential equations* (Chapman & Hall/CRC, Boca Raton, Fla. [u.a.], 2004). Includes bibliographical references and index.
96. V. E. Gusev. "Detection of nonlinear picosecond acoustic pulses by time-resolved Brillouin scattering". *Journal of Applied Physics* **116**, 06490 (2014).
97. D. C. Wallace. "Thermoelastic Theory of Stressed Crystals and Higher-Order Elastic Constants". In F. S. Henry Ehrenreich and D. Turnbull (Eds.), *Solid State Physics*, vol. 25, 301 – 404 (Academic Press, 1970).

ACKNOWLEDGMENTS

First of all I would like to express special thanks to my supervisor Prof. Matias Bargheer. You ensured that everybody in our group including myself has an enjoyable job, encouraged me to do fascinating research with femtosecond lasers and supplied the group with financial resources which allowed me to make cutting edge research. You were always on stage to give experimental or theoretical support and often generated new ideas which helped to interpret surprising experimental data in the right way.

Moreover, I want to thank Prof. Martin Weinelt for organizing the graduate school "Dynamics in new Light" which funded a great part of my work and enabled a number of summer and winter schools as well as other scientific meetings in which all participating students including me invited scientists from all over the world to give talks.

Special thanks to my former colleagues Marc Herzog and Daniel Schick. To work with you was really fun and productive. The harmony and combination of skills in this three person group was enormous fruitful which is not at last the reason for such a high number of publications.

Many thanks also to all of my colleagues of the Ultrafast Dynamics in Condensed Matter group at the University of Potsdam. We had several unforgettable journeys to conferences, beamtimes with sleepless nights at synchrotrons and great physical and non-physical discussions in our coffee breaks. All these experiences, I will not forget.

Last but not least, I want to thank my family, especially my wife Juliane and my little baby Marlene for accepting long working days and loving me also in times when I was not there.

Comparing the oscillation phase in optical pump-probe spectra to ultrafast x-ray diffraction in the metal-dielectric $\text{SrRuO}_3 / \text{SrTiO}_3$ superlattice

A. Bojahr, D. Schick, L. Maerten, M. Herzog, I. Vrejoiu,
C. von Korff Schmising, C. J. Milne, S. L. Johnson and
M. Bargheer.

Phys. Rev. B **85**, 224302 (2012).

Comparing the oscillation phase in optical pump-probe spectra to ultrafast x-ray diffraction in the metal-dielectric SrRuO₃/SrTiO₃ superlattice

André Bojhr,¹ Daniel Schick,¹ Lena Maerten,¹ Marc Herzog,¹ Ionela Vrejoiu,² Clemens von Korff Schmising,³ Chris Milne,⁴ Steven L. Johnson,⁵ and Matias Bargheer^{1,6,*}

¹*Institute of Physics and Astronomy, University of Potsdam, Karl-Liebknecht-Strasse 24-25, 14476 Potsdam, Germany*

²*Max-Planck-Institut für Mikrostrukturphysik, Weinberg 2, 06120 Halle, Germany*

³*Institut für Optik und Atomare Physik, TU Berlin, Strasse des 17. Juni 135, 10623 Berlin*

⁴*Swiss Light Source, Paul Scherrer Institut, 5232 Villigen PSI, Switzerland and Laboratoire de Spectroscopie Ultrarapide, Ecole Polytechnique Federale de Lausanne, 1015 Lausanne, Switzerland*

⁵*Institute for Quantum Electronics, ETH Zurich, Wolfgang-Pauli-Strasse 16, 8093 Zurich, Switzerland*

⁶*Helmholtz Zentrum Berlin, Albert-Einstein-Strasse 15, 12489 Berlin, Germany*

(Received 6 April 2012; revised manuscript received 16 May 2012; published 19 June 2012)

We measured the ultrafast optical response of metal-dielectric superlattices by broadband all-optical pump-probe spectroscopy. The observed phase of the superlattice mode depends on the probe wavelength, making assignments of the excitation mechanism difficult. Ultrafast x-ray diffraction data reveal the true oscillation phase of the lattice which changes as a function of the excitation fluence. This result is confirmed by the fluence dependence of optical transients. We set up a linear chain model of the lattice dynamics and successfully simulated the broadband optical reflection by unit-cell resolved calculation of the strain-dependent dielectric functions of the constituting materials.

DOI: 10.1103/PhysRevB.85.224302

PACS number(s): 63.20.Ry, 42.65.Es

I. INTRODUCTION

Optical femtosecond spectroscopy is an established tool to infer ultrafast dynamics in molecules and solids. Time constants such as the exponential decay or the oscillation period can often be directly ascribed to microscopic processes such as relaxation or vibration. A detailed modeling of the ultrafast optical response requires the quantum-chemical modeling of molecular potentials in the case of molecular systems or calculation of the dielectric function of solids. With the broader accessibility of various experimental setups for ultrafast x-ray diffraction (UXRD), the findings from all-optical experiments can be cross-checked by directly looking at the lattice motion, including a real time measurement of the absolute atomic amplitudes. In the case of bulk semiconductors UXRD allowed conclusions to be drawn on modifications of the strain fronts induced by the fast diffusion of hot carriers.¹⁻³ For bulk bismuth UXRD in combination with *ab initio* simulations revealed how the lattice potential changes with the time-dependent carrier density.⁴ UXRD and ultrafast electron-diffraction studies show that, for increasing excitation fluence, electronic pressure gains importance versus phonon pressure in metallic systems.^{5,6} All these processes influence the oscillation phase of the excited phonons. In reverse, measuring the oscillation phase elucidates the excitation mechanisms.

The influence of Raman excitation has been discussed in bulk systems, superlattices, and multilayers.⁷ Under strictly nonresonant conditions this excitation causes a sine-like phase of the lattice motion. In contrast the so-called dispersive excitation of coherent phonons (DECP)⁸ results in a cosine-like lattice motion.⁹ DECP is exclusively observed in opaque materials and can be described by the imaginary part of the Raman tensor.¹⁰ Additional excitation mechanisms which show a displaced equilibrium of the lattice oscillation

are surface charge screening, the photo Dember effect, or heating of the lattice by rapid electron-phonon scattering.¹¹ In many cases the oscillation phase was measured by all-optical techniques and ascribed to the phase of the lattice motion. Raman scattering with real and imaginary tensor contributions is held responsible for the excitation of coherent phonons in metallic systems (Cd, Zn, Zr) as well.^{12,13} In the most intensively investigated material, the semimetal Bi, the microscopic interpretation of the excitation is developed in detail. Theory predicts the time-dependent change of the interatomic potential during the relaxation of photoexcited carriers.^{4,14} A similarly detailed interpretation of the excitation in terms of quasiparticle generation is exemplified for Si.¹⁵ UXRD would yield direct experimental information on the lattice motion in this case. However, there is only a single UXRD experiment that measures lattice dynamics (polaritons) induced by nonresonant Raman excitation.¹⁶

Several all-optical studies measured a fluence dependent phase of oscillations, which was ascribed to the simultaneous action of DECP and Raman mechanisms.¹⁷ Superlattices exhibit phonon modes which are very well suited for fundamental tests, as their periods can be tuned via the layer thickness. Especially for UXRD experiments they yield high signal-to-noise ratio of the experimental signal. The nanosized layers support zone folded acoustic phonons¹⁸ with few-picosecond oscillation periods, well suited for distinguishing tiny phase differences. Optical excitation of the opaque constituent of a superlattice yields a standing strain wave where the opaque material is periodically expanded while the transparent material is compressed. For GaAs/AlGaAs superlattices a UXRD study under high fluence conditions revealed a dominant DECP mechanism¹⁹ whereas all-optical measurements under low-fluence conditions suggest the Raman mechanism.⁷ Although it is well established to use such ultrafast structural techniques, the problem of determining the arrival time of the x-ray or

electron pulses with high precision relative to the pump pulse persists. A direct and detailed comparison of ultrafast optical response over a broad spectral range with the actual lattice motion determined by ultrafast diffraction techniques under identical excitation conditions is lacking.

In this contribution we revisit the metal-dielectric superlattice (SL) composed of SrRuO₃ (SRO) and SrTiO₃ (STO), for which it was shown by UXRd measurements that there are at least two contributing mechanisms for photoexcited lattice dynamics: thermal expansion by electron-phonon and phonon-phonon interaction and ultrafast magnetostriction.²¹ We present a fluence-dependent UXRd study which shows a relative phase shift of about 130 fs of the lattice motion, indicating that for high fluence the photon energy is coupled more rapidly to the expansion. At high fluences the measured phase of the lattice motion is consistent with an instantaneous DECP mechanism within the experimental error. In broadband optical reflectivity measurements we find that the oscillation phase of the all-optical signal strongly depends on the probe wavelength; however, we can confirm the relative shift of the oscillation phase with fluence. To determine the absolute phase of the lattice oscillation we perform a combined optical pump-probe and UXRd experiment without moving any components.

In order to better understand the broadband optical response, the lattice dynamics are calculated in a masses-and-springs model and calibrated in phase and amplitude using the UXRd data. The calculated spatiotemporal strain pattern is used to simulate the optical response by using the strain-dependent dielectric functions of SRO and STO, where the dependence $\partial N_{\text{SRO}}/\partial \eta$ of the complex refractive index N_{SRO} on the strain η is the only freely adjustable parameter. The agreement of these x-ray calibrated simulations with the optical response is very good. These data directly show that all-optical pump-probe data can exhibit nearly arbitrary oscillation phases, even if the lattice dynamics are fixed.

II. SETUP AND EXPERIMENTAL RESULTS

The sample consists of 10 double layers of STO/SRO (13 nm/7.5 nm) deposited by pulsed laser deposition on an STO substrate.²² In all experiments presented in this manuscript we use pump pulses with a wavelength of $\lambda_{\text{pump}} = 800$ nm. Figure 1(a) presents fluence-dependent UXRd data recorded at the MicroXAS-FEMTO beamline of the Swiss Light Source (SLS).²³ The amplitude of the oscillation has been analyzed²⁴ and discussed previously.²⁰ The according strain amplitude is reproduced in Fig. 1(b). Panel 1(c) shows the delay t_0^{osc} of the oscillation phase extracted from fitting the data in panel 1(a) to an analytical function [Eq. (1)] describing the sample response, which will be further discussed in Sec. IV. In short, the symmetric superlattice-phonon mode of the metallic/insulating superlattice is excited by expanding the metal layers. For the highest fluence the oscillation starts approximately 130 fs earlier. Figure 2(a) shows the transient optical reflectivity of the sample at $\lambda_{\text{probe}} = 670$ nm. The rapid rise of the reflectivity originates from quasi-instantaneous heating of the metal electrons. The rising edge determines the arrival time of the optical pump pulse. The slanted arrows indicate the delay of the oscillation for lower pump fluence. For

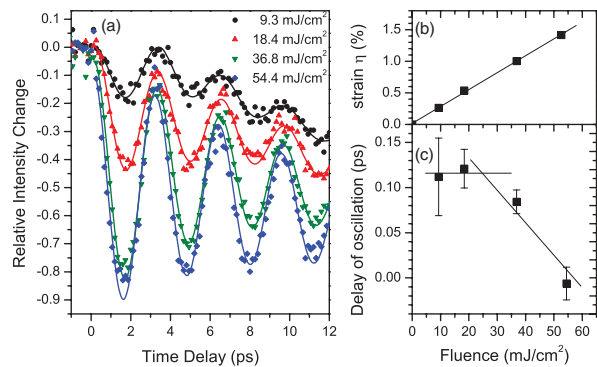


FIG. 1. (Color online) (a) UXRd measurements of the (0 0 116) reflection of the SRO/STO SL recorded at the SLS $\lambda_{\text{pump}} = 800$ nm for different fluences. (b) Strain amplitude derived from the data in panel (a) by comparison to a dynamical x-ray diffraction simulation (Ref. 20). (c) Oscillation phase extracted from the measured data using the fit function of eq. 1. The error bars correspond to a 68% confidence interval from fitting the relative phase. The absolute phase is obtained by comparison to the experiments at the laser-based plasma source discussed in Fig. 4.

an accurate evaluation we subtract the incoherent background (dotted line) and fit oscillations to the data. The resulting linear fluence dependence of the amplitude is shown in Fig. 2(b). The phase delay is plotted in Fig. 2(c) and compared to the UXRd result. The excellent agreement suggests that indeed for low fluence the oscillation is delayed by about 130 fs due to a finite electron-phonon coupling time as the expansion is dominated by phonon-phonon interaction. In contrast, for high fluence the

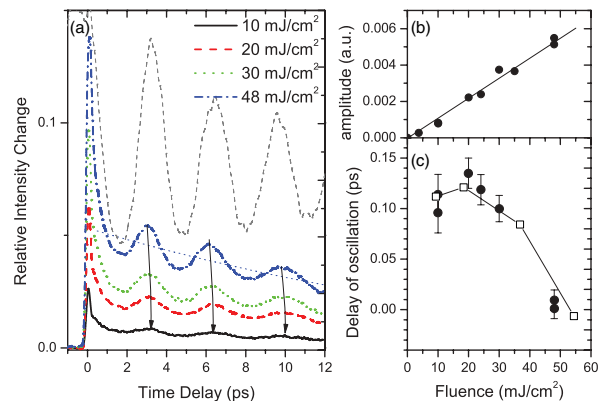


FIG. 2. (Color online) (a) Measured optical reflectivity $\lambda_{\text{probe}} = 670$ nm for different fluences. The dotted line indicates the incoherent background contribution which is subtracted from each transient to fit the oscillations and to plot Fig. 3(a). The thin dashed line shows the UXRd measurement for comparison. (b) Oscillation amplitude as a function of the fluence. (c) Comparison of the relative oscillation phase of the optical signal (solid circles) to the phase determined by UXRd [open squares reproduced from Fig. 1(c)]. The error bars of phases are determined from the maximum deviation of phases in two measurement series. The absolute phase is shifted to agree with the UXRd data.

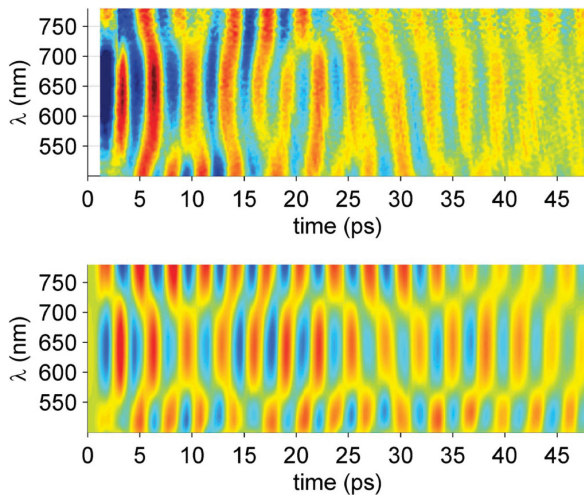


FIG. 3. (Color) (a) Experimentally measured change of the optical reflectivity from $\lambda_{\text{probe}} = 500$ to 780 nm at normal incidence after exciting the sample at $\lambda_{\text{pump}} = 800$ nm as a function of time delay. The electronic response and a slowly varying signal contribution have been subtracted as exemplified in Fig. 2(a). (b) Results from the simulation described in the text. The slowly varying background has been subtracted as well. The simulations show that the spectral position of the phase change at 560 and 720 nm is given by an interference of light reflected from the surface and the interface to the substrate.

time for coupling the energy into the expansion mode is so fast that we cannot distinguish it from an instantaneous response.

Our broadband optical pump-probe setup is similar to those reported in the literature,^{25,26} where a white-light continuum serves as the probe pulse. Hence, we not only measure the data at 670 nm (Fig. 2) but over the full visible range. The analysis teaches us to interpret all-optical data with great care. After subtraction of the slowly varying background for each wavelength as exemplified by the dotted line in Fig. 2(a), the broadband data exhibit complex dependence of the phase on the probe wavelength [Fig. 3(a)].

A general problem in UXRD experiments is the precise determination of the time zero. For all-optical pump-probe data we cross-checked that the rising edge of the signal corresponds to $t = 0$ by sum-frequency generation of pump and probe in a beta-Barium-Borate (BBO) crystal. To calibrate the time origin of the UXRD data, we repeated the UXRD experiment at the laser-based femtosecond diffractometer at the University of Potsdam.²⁷ We removed the x-ray optic which is used for the standard operation of the diffractometer.^{27,28} The Bragg condition selects a small angular range of the generated x-ray pulses which are diffracted from the sample (hatched beam in the schematic in Fig. 4). We introduce slits along this x-ray beam to ensure that, after removing the copper tape for x-ray generation, only laser photons propagating along this x-ray probe path impinge on the sample, now as optical probe pulses.

To switch between optical and x-ray probes, only the copper band and a $10 \mu\text{m}$ thick plastic film are removed from the beam path. The optical probe pulse and the x-ray probe-pulse have

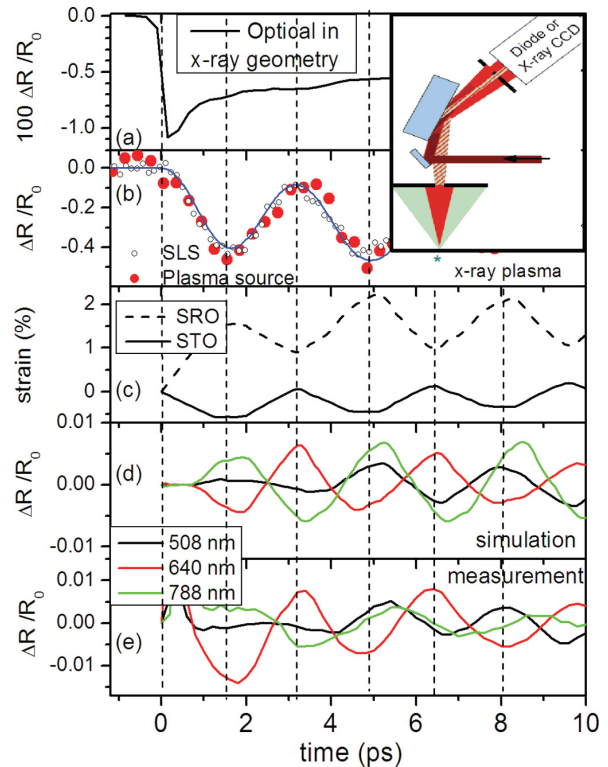


FIG. 4. (Color) (a) All-optical response measured in the same configuration for $\lambda_{\text{pump}} = 800$ nm and $\lambda_{\text{probe}} = 800$ nm. The schematic shows the combined optical/x-ray pump-probe geometry. Optical (red) and x-ray (green) probe pulses collinearly propagate through a slit towards the sample. Both emerge from the laser focus on the copper tape which generates the x-ray pulses and which is removed for optical probing. (b) UXRD data from the laser-based plasma source (red dots) with removed x-ray optics to precisely determine the zero time delay. The signal is shifted by 250 fs to earlier times with respect to the data as measured, according to the analysis described in the text. For comparison we show the UXRD data measured at the SLS [open circles, reproduced from Fig. 1(a)]. The blue line is the simulated UXRD signal based on the calculated lattice dynamics. (c) Simulated average strain in STO (solid) and SRO (dashed) pattern which is consistent with the observed x-ray diffraction signal. (d) Simulated optical reflectivity for three selected probe wavelengths. (e) Corresponding color-coded horizontal cuts through Fig. 3(a).

the same geometric path. The optical path is different due to the decreased group velocities c^* in air for x rays ($c_{\text{xray}}^* - c$)/ $c < 10^{-6}$ and 800 nm light pulses ($c_{\text{opt}}^* - c$)/ $c = 3 \times 10^{-4}$. The 300 mm path in air behind the laser focus makes the x rays arrive 300 fs earlier than the laser pulse traveling the same path in the all-optical experiment. In addition the laser passes through 5 cm of vacuum before the focus in the x-ray experiment, which is replaced by an air path in the optical experiment, adding another 50 fs to the time delay. A contribution in the opposite direction is the additional time delay of the x-ray pulses due to the propagation of electrons in the metal target before the x-ray production. This leads to a temporally extended x-ray

pulse with a duration in the 100–200 fs range²⁹ as compared to the 40 fs laser pulses. In essence this delays the x-ray pulse by about 100 fs, since the leading edge of the x-ray pulse must coincide with the optical excitation pulse as the first generated x rays travel at the speed of light, and the trailing edge is delayed by the x-ray pulse duration which is given by the hot electrons moving through the copper target.³⁰

In short, the time axis of the UXR D experiment must be shifted by 250 fs with respect to the all-optical experiment. Time zero is determined by the steepest slope due to the electronic heating in SRO detected in the all-optical experiment [Fig. 4(a)], which is consistent with the time overlap determined in a thin BBO crystal for second-harmonic generation. Now the UXR D signal is measured in exactly the same configuration and plotted in Fig. 4(b) already shifted as discussed above. For comparison the data from Fig. 1(a) measured at the SLS are shown as well. Panel 4(c) compares this to simulations discussed below, which also predict the optical response for three selected wavelengths [panel 4(d)], which are in excellent agreement with the measured data at these wavelengths [panel 4(e)]. The pump fluence in both the UXR D and the optical experiment was approximately 20 mJ/cm². In total, Fig. 4 summarizes how time zero is compared in all-optical and UXR D experiments and how both data sets are linked to the simulation of lattice dynamics discussed in the next section.

Earlier UXR D measurements on the very same STO/SRO SL reported an additional delay of approximately 500 fs for weak excitation.^{21,31,32} Very careful analysis of all experiments shows that this discrepancy can be partly ascribed to a modified oscillation phase for the higher pump fluence and partly to the group-velocity delay of the optical pulses and x-ray pulses in air which was neglected at that time.

III. SIMULATIONS

As a theoretical support of our interpretations, we have set up a linear chain model of the superlattice in which instantaneous stress is generated by optically induced heating of the lattice. The elastic constants are known and the spatio-temporal strain pattern has been previously calculated.³³ On the timescale $t < 10$ ps heat diffusion can be neglected and it is not relevant for the stress generation.³⁴ In the optical signal it gives rise to a slowly varying background that is subtracted before considering the oscillations. The average strain in the SRO and STO layers resulting from this calculation is given in Fig. 4(c). The simulated strain map with unit-cell resolution is the common starting point to predict both the UXR D signal [panel 4(b)] and the all-optical signal [panel 4(d)]. The simulated solid line in panel 4(b) is obtained from using the calculated spatio-temporal strain pattern³³ in a dynamical x-ray diffraction simulation.²⁰

To calculate the optical response we specify the complex index of refraction $N(z, t) = n + i\kappa$ for each unit cell along growth direction of the superlattice for each timestep and calculate the optical reflectivity in a standard optical matrix formalism. For STO both the wavelength-dependent index of refraction $n_{\text{STO}}(\lambda)$ and its derivative $dn_{\text{STO}}/d\eta = 0.5$ with respect to strain η are taken from the literature.^{35–37} The complex refractive index $N_{\text{SRO}}(\lambda) = n_{\text{SRO}}(\lambda) + i\kappa_{\text{SRO}}(\lambda)$ of SRO

is derived from the literature.³⁸ The derivatives for SRO are unknown and hence we use $dn_{\text{SRO}}/d\eta$ and $d\kappa_{\text{SRO}}/d\eta$ as fitting parameters to match the observed data simultaneously for all probe wavelengths. We already obtain a reasonable agreement [compare Figs. 3(a) and 3(b) and Figs. 4(d) and 4(e)] if we assume $dn_{\text{SRO}}/d\eta = dn_{\text{STO}}/d\eta = 0.5$ and $d\kappa_{\text{SRO}}/d\eta = 1.5$ independent of wavelength. Additional variations of the optical constants with the wavelength could yield even more accurate agreement. However, already at the current level of simulation the agreement of the optical broadband data with simulations presented in Fig. 3(b) gives us confidence in our interpretation. From an experimental point of view the validation via UXR D is a preferable cross-check.

IV. DISCUSSION

For $t > 0$ the UXR D signals can be well fitted by the following function:

$$S(t) = -A \sin\left(\pi \frac{t - t_0^{\text{osc}}}{T_{\text{osc}}}\right)^2 \exp\left(-\frac{t - t_0^{\text{osc}}}{T_{\text{dec}}}\right) - m(t - t_0^{\text{lin}}). \quad (1)$$

The shape of this fitting function is uniquely determined by the physics contained in the simulation. The oscillatory part originates from the excitation of a single zone-folded LA phonon mode which modulates the x-ray diffraction structure factor of the superlattice reflection, and the decay is essentially due to the propagation of the excitation into the substrate.²⁰ The linear slope on the signal is explained by the shift of the Bragg reflection due to the average heat expansion of the superlattice.

Such a simple fitting function does not exist for the all-optical counterpart. Figure 3 illustrates that the optical signals suffer from a beating due to the interference of probe pulses reflected from the interfaces, from the phonons in the SL, and from the propagating sound wave. Despite this complicated situation, the straightforward simulation yields excellent agreement.

Now we turn to the discussion of the phase shift observed in both experiments. From the carefully determined time zero of the UXR D signal with an accuracy of about ± 100 fs, we can directly conclude that the assumption of an instantaneous stress generation in our simulation is very good, since the phase of the signal at the highest fluence corresponds to a perfect cosine, i.e., to a displacive excitation without considerable additional delay due to electron-phonon coupling. The phase of the lattice motion in the simulation is in good agreement with by the UXR D measurement.

The fluence dependent study in Fig. 1 shows that for lower fluence the lattice stress starts about 130 fs later, yielding an estimate of the electron-phonon coupling time. Although the absolute determination of the time zero is only accurate within ± 100 fs, the relative phase delay of 130 ± 50 fs is determined with sufficient accuracy. The same clear trend is observed in the oscillation phase of the all-optical signal at 670 nm [Fig. 2(c)]. Below a fluence of about 20 mJ/cm² the electronic pressure is likely negligible compared to the lattice contribution to the expansion. Hence, below this fluence the phase is set by the electron-phonon coupling time in SRO. In the simplest models for metals, the electronic heat capacity rises linearly with the temperature and the lattice contribution

saturates to the Doulong-Petit limit. However, calculations based on the electronic density of states (DOS) show that for most metals this is not true under strong nonequilibrium conditions.³⁹ Since for the case of the bad metal SRO with strong electron correlations, simulations of the DOS strongly depend on the method used,⁴⁰ and we do not attempt to predict the electronic stress contributions.

In the semiconducting material InSb a phase shift of the oscillations towards earlier times was observed for higher fluence.² This was attributed to a decreasing lattice heating time for strong excitation, essentially because the reduced lifetime of LO phonons⁴¹ limits the carrier-lattice thermalization dynamics.⁴² Similar arguments could apply in the case of SRO. Specifically, the observation of an oscillation starting earlier for higher fluence is in contrast to the observation of electronic pressure in elementary metallic systems such as aluminum and gold.^{5,6} In these metals a larger electron-phonon coupling time leads to larger effect size in the opposite direction, namely because the electron-lattice heat transfer takes longer for high fluence. We cannot rule out that contributions from impulsive Raman scattering play a role in the phase shift; however, all processes in question—Raman, electronic pressure, lattice heat expansion—scale linearly with the pump fluence in the simplest models and would not explain a fluence dependence

of the phase. Therefore we think that time- and temperature-dependent modification of the electron-phonon interaction must be responsible for the observed phase delay.

In conclusion, we have presented ultrafast x-ray diffraction (UXRD) and all-optical pump-probe experiments on the metal-dielectric superlattice STO/SRO. Only the combination of both methods allows one to experimentally deduce the absolute phase of the optically induced lattice motion. From fluence-dependent UXRD we extract a relative shift of the oscillation phase of the lattice which is readily ascribed to electronic pressure. The same fluence dependence of the phase is observed in all-optical experiments. However, the complex wavelength dependence of the broadband data highlight that the oscillation phase of all-optical experiments must be interpreted with care. Our x-ray calibrated simulations of the all-optical data validates the detailed interpretation.

ACKNOWLEDGMENTS

We thank R. van der Veen for her valuable experimental support at the MicroXAS-FEMTO beamline. We gratefully acknowledge the financial support by the BMBF via Grant No. 03WKP03A and the Deutsche Forschungsgemeinschaft (DFG) (Grant No. BA2281/3-1).

^{*}bargheer@uni-potsdam.de

¹A. Morak, T. Kaempfer, I. Uschmann, A. Luebecke, E. Foerster, and R. Sauerbrey, *Phys. Status Solidi B* **243**, 2728 (2006).

²F. S. Krasniqi, S. L. Johnson, P. Beaud, M. Kaiser, D. Grolimund, and G. Ingold, *Phys. Rev. B* **78**, 174302 (2008).

³P. Sondhaus, O. Synnergren, T. N. Hansen, S. E. Canton, H. Enquist, A. Srivastava, and J. Larsson, *Phys. Rev. B* **78**, 115202 (2008).

⁴D. M. Fritz, D. A. Reis, B. Adams, R. A. Akre, J. Arthur, C. Blome, P. H. Bucksbaum, A. L. Cavalieri, S. Engemann, S. Fahy *et al.*, *Science* **315**, 633 (2007).

⁵J. Li, R. Clinite, X. Wang, and J. Cao, *Phys. Rev. B* **80**, 014304 (2009).

⁶M. Nicoul, U. Shymanovich, A. Tarasevitch, D. von der Linde, and K. Sokolowski-Tinten, *Appl. Phys. Lett.* **98**, 191902 (2011).

⁷A. Bartels, T. Dekorsy, H. Kurz, and K. Köhler, *Phys. Rev. Lett.* **82**, 1044 (1999).

⁸H. J. Zeiger, J. Vidal, T. K. Cheng, E. P. Ippen, G. Dresselhaus, and M. S. Dresselhaus, *Phys. Rev. B* **45**, 768 (1992).

⁹C.-K. Sun, J.-C. Liang, and X.-Y. Yu, *Phys. Rev. Lett.* **84**, 179 (2000).

¹⁰T. E. Stevens, J. Kuhl, and R. Merlin, *Phys. Rev. B* **65**, 144304 (2002).

¹¹T. Dekorsy, G. Cho, and H. Kurz, in *Light Scattering in Solids VIII*, Vol. 76 of *Topics in Applied Physics*, edited by M. Cardona and G. Güntherodt (Springer, Berlin, 2000), pp. 169–209.

¹²V. V. Kruglyak, R. J. Hicken, G. P. Srivastava, M. Ali, B. J. Hickey, A. T. G. Pym, and B. K. Tanner, *Phys. Rev. B* **76**, 012301 (2007).

¹³M. Hase, K. Ishioka, J. Demsar, K. Ushida, and M. Kitajima, *Phys. Rev. B* **71**, 184301 (2005).

¹⁴S. L. Johnson, P. Beaud, C. J. Milne, F. S. Krasniqi, E. S. Zijlstra, M. E. Garcia, M. Kaiser, D. Grolimund, R. Abela, and G. Ingold, *Phys. Rev. Lett.* **100**, 155501 (2008).

¹⁵M. Hase, M. Kitajima, A. Constantinescu, and H. Petek, *Nature (London)* **426**, 51 (2003).

¹⁶A. Cavalleri, S. Wall, C. Simpson, E. Statz, D. W. Ward, K. A. Nelson, M. Rini, and R. W. Schoenlein, *Nature (London)* **442**, 664 (2006).

¹⁷K. J. Yee, Y. S. Lim, T. Dekorsy, and D. S. Kim, *Phys. Rev. Lett.* **86**, 1630 (2001).

¹⁸C. Colvard, T. A. Gant, M. V. Klein, R. Merlin, R. Fischer, H. Morkoc, and A. C. Gossard, *Phys. Rev. B* **31**, 2080 (1985).

¹⁹M. Bargheer, N. Zhavoronkov, Y. Gritsai, J. C. Woo, D. S. Kim, M. Woerner, and T. Elsaesser, *Science* **306**, 1771 (2004).

²⁰M. Herzog, D. Schick, W. Leitenberger, R. Shayduk, R. M. van der Veen, C. J. Milne, S. L. Johnson, I. Vrejoiu, and M. Bargheer, *New J. Phys.* **14**, 013004 (2012).

²¹C. von Korff Schmising, A. Harpoeth, N. Zhavoronkov, Z. Ansari, C. Aku-Leh, M. Woerner, T. Elsaesser, M. Bargheer, M. Schmidbauer, I. Vrejoiu *et al.*, *Phys. Rev. B* **78**, 060404 (2008).

²²M. Herzog, W. Leitenberger, R. Shayduk, R. van der Veen, C. J. Milne, S. L. Johnson, I. Vrejoiu, M. Alexe, D. Hesse, and M. Bargheer, *Appl. Phys. Lett.* **96**, 161906 (2010).

²³P. Beaud, S. L. Johnson, A. Streun, R. Abela, D. Abramsohn, D. Grolimund, F. S. Krasniqi, T. Schmidt, V. Schlott, and G. Ingold, *Phys. Rev. Lett.* **99**, 174801 (2007).

²⁴The strain amplitude is derived by comparing the model and experimental data in the inset of Fig. 3(a) in Ref. 20. Since the agreement is nearly perfect, the mapping of fluence on strain yields

the linear function presented in Fig. 1(b). We do not attempt to discuss the tiny deviations, as we focus here on the phase of the oscillations.

- ²⁵I. Bozovic, M. Schneider, Y. Xu, R. Sobolewski, Y. H. Ren, G. Lüpke, J. Demsar, A. J. Taylor, and M. Onellion, *Phys. Rev. B* **69**, 132503 (2004).
- ²⁶S. Brivio, D. Polli, A. Crespi, R. Osellame, G. Cerullo, and R. Bertacco, *Appl. Phys. Lett.* **98**, 211907 (2011).
- ²⁷D. Schick, A. Bojahr, M. Herzog, C. von Korff Schmising, R. Shayduk, W. Leitenberger, P. Gaal, and M. Bargheer, *Rev. Sci. Instrum.* **83**, 025104 (2012).
- ²⁸F. Zamponi, Z. Ansari, C. von Korff Schmising, P. Rothhardt, N. Zhavoronkov, M. Woerner, T. Elsaesser, M. Bargheer, T. Trobitzsch-Ryll, and M. Haschke, *Appl. Phys. A* **96**, 51 (2009).
- ²⁹F. Zamponi, Z. Ansari, M. Woerner, and T. Elsaesser, *Opt. Express* **18**, 947 (2010).
- ³⁰C. Reich, P. Gibbon, I. Uschmann, and E. Förster, *Phys. Rev. Lett.* **84**, 4846 (2000).
- ³¹C. von Korff Schmising, M. Bargheer, M. Kiel, N. Zhavoronkov, M. Woerner, T. Elsaesser, I. Vrejoiu, D. Hesse, and M. Alexe, *Appl. Phys. B* **88**, 1 (2007).
- ³²M. Woerner, C. von Korff Schmising, M. Bargheer, N. Zhavoronkov, I. Vrejoiu, D. Hesse, M. Alexe, and T. Elsaesser, *Appl. Phys. A* **96**, 83 (2009).
- ³³M. Herzog, D. Schick, P. Gaal, R. Shayduk, C. von Korff Schmising, and M. Bargheer, *Appl. Phys. A* **106**, 489 (2012).
- ³⁴R. Shayduk, H. A. Navirian, W. Leitenberger, J. Goldshteyn, I. Vrejoiu, M. Weinelt, P. Gaal, M. Herzog, C. von Korff Schmising, and M. Bargheer, *New J. Phys.* **13**, 093032 (2011).
- ³⁵M. Cardona, *Phys. Rev.* **140**, A651 (1965).
- ³⁶A. Giardini, *J. Opt. Soc. Am.* **47**, 726 (1957).
- ³⁷M. L. Hassel Ledbetter and S. Kim, *Phase Transitions* **23**, 61 (1990).
- ³⁸P. Kostic, Y. Okada, N. C. Collins, Z. Schlesinger, J. W. Reiner, L. Klein, A. Kapitulnik, T. H. Geballe, and M. R. Beasley, *Phys. Rev. Lett.* **81**, 2498 (1998).
- ³⁹Z. Lin, L. V. Zhigilei, and V. Celli, *Phys. Rev. B* **77**, 075133 (2008).
- ⁴⁰H.-T. Jeng, S.-H. Lin, and C.-S. Hsue, *Phys. Rev. Lett.* **97**, 067002 (2006).
- ⁴¹K. T. Tsen, J. G. Kiang, D. K. Ferry, and H. Morkoc, *Appl. Phys. Lett.* **89** (2006).
- ⁴²A. H. Chin, R. W. Schoenlein, T. E. Glover, P. Balling, W. P. Leemans, and C. V. Shank, *Phys. Rev. Lett.* **83**, 336 (1999).

**Ultrafast lattice response of
photoexcited thin films studied by
X-ray diffraction**

D. Schick, M. Herzog, A. Bojahr, W. Leitenberger, A.
Hertwig, R. Shayduk and M. Bargheer.

Structural Dynamics **1**, 6 (2014).



Ultrafast lattice response of photoexcited thin films studied by X-ray diffraction

Daniel Schick,^{1,2} Marc Herzog,^{1,3} André Bojahr,¹ Wolfram Leitenberger,¹ Andreas Hertwig,⁴ Roman Shayduk,^{2,5} and Matias Bargheer^{1,2,a)}

¹*Institut für Physik und Astronomie, Universität Potsdam, Karl-Liebknecht-Straße 24-25, 14476 Potsdam, Germany*

²*Helmholtz-Zentrum Berlin für Materialien und Energie GmbH, Wilhelm-Conrad-Röntgen Campus, BESSY II, Albert-Einstein-Straße 15, 12489 Berlin, Germany*

³*Abteilung Physikalische Chemie, Fritz-Haber-Institut der Max-Planck-Gesellschaft, Faradayweg 4-6, 14195 Berlin, Germany*

⁴*Bundesanstalt für Materialforschung und -prüfung, Unter den Eichen 87, 12205 Berlin, Germany*

⁵*Deutsches Elektronen-Synchrotron DESY, Notkestraße 85, 22607 Hamburg, Germany*

(Received 5 September 2014; accepted 28 October 2014; published online 18 November 2014)

Using ultrafast X-ray diffraction, we study the coherent picosecond lattice dynamics of photoexcited thin films in the two limiting cases, where the photoinduced stress profile decays on a length scale larger and smaller than the film thickness. We solve a unifying analytical model of the strain propagation for acoustic impedance-matched opaque films on a semi-infinite transparent substrate, showing that the lattice dynamics essentially depend on two parameters: One for the spatial profile and one for the amplitude of the strain. We illustrate the results by comparison with high-quality ultrafast X-ray diffraction data of SrRuO₃ films on SrTiO₃ substrates. © 2014 Author(s). All article content, except where otherwise noted, is licensed under a Creative Commons Attribution 3.0 Unported License. [<http://dx.doi.org/10.1063/1.4901228>]

I. INTRODUCTION

Pump-probe experiments measure the coupling of various degrees of freedom on their intrinsic timescale of femtoseconds to nanoseconds. An increasingly powerful toolbox of time-resolved experimental techniques—ranging from Raman scattering over magneto-optical Kerr (MOKE) measurements^{1,2} to angular-resolved photoelectron spectroscopy (ARPES)³—is applied to directly monitor specific subsystems in solids (charge, spin, orbital, and lattice). The majority of experiments are conducted on thin film samples which have been designed to exhibit the phenomena of interest. Especially for opaque layers, the high energy density deposited in the thin film by the pump pulse not only leads to strong and interesting changes, e.g., in the magnetization or electronic properties, but also to considerable dynamics of the underlying crystal lattice.⁴⁻⁶

Since the pioneering work of Thomsen *et al.* in 1984 and 1986^{7,8} Brillouin scattering methods with optical light have been steadily improved and allow for following the evolution of photoexcited coherent strain pulses.^{7,9} In general, optical light is only an indirect probe for lattice motion, since it is exclusively sensitive to the dielectric function of matter, which is usually strongly modified in pump-probe experiments by the substantial perturbation of the electronic system. More than a decade ago, ultrafast X-ray diffraction (UXRD) techniques emerged as a versatile tool to monitor photoexcited lattice dynamics directly on the relevant length and time scales.¹⁰⁻¹⁶ Recent UXRD studies established this technique for reconstructing photoexcited coherent strain pulses¹⁷ and used it to determine the underlying mechanism for exciting the

^{a)}Electronic mail: bargheer@uni-potsdam.de; URL: <http://www.udkm.physik.uni-potsdam.de>.



atomic motion^{17–23} or to study phonon damping mechanisms.²⁴ In addition, ultrafast electron diffraction also reveals the structural dynamics of photoexcited condensed matter; however, this technique exclusively probes the surface-near regions of the sample.²⁵ Despite this multitude of experimental studies and although the seminal work by Thomsen *et al.* has been cited and elaborated more than 500 times,⁸ a comprehensive study of the ultrafast lattice dynamics and its direct signature in UXR data for the common case of an opaque thin film on a semi-infinite transparent substrate are still missing in the literature. In our opinion, the lattice dynamics form an important basis of all electronic dynamics and especially for solids with complex couplings and collective phenomena a thorough assessment of the lattice dynamics is mandatory.

In this contribution, we choose the “bad metal” SrRuO₃²⁶ as a prototypical optically opaque thin-film material with a very short electron-phonon coupling time which was deposited on the standard substrate material SrTiO₃. We discuss the lattice dynamics after photoexcitation in the two limiting cases, where the photoinduced spatial stress profile $\sigma(z)$ decays on a length scale ζ larger and smaller than the film thickness d . Working out the standard thermoelastic model⁸ in the Appendix and introducing universal temporal and spatial coordinates which are scaled by sound velocity v and film thickness d , respectively, we identify two essential parameters defining the lattice dynamics: $\delta = d/\zeta$ for the spatial profile and α for the amplitude of the strain, where α incorporates all acoustic and thermoelastic parameters. The model correctly describes signatures in the UXR data for $\delta > 1$ which are at first sight surprising: The Bragg peak of the opaque layer first shifts to larger angles, indicating a compression of the film despite the expansive photoinduced stress. The intensity of this initial peak decreases and is transferred to a Bragg peak which emerges at smaller angles. For $\delta < 1$, the observed continuous shift to smaller angles is captured equally well by this model. We demonstrate an elegant way to measure the sound velocity in impedance-matched thin films, which is not easily accessible by other experiments, and discuss how to extract the other parameters from the experimental data. We use the model in its simplest form, for a perfect acoustic impedance match of the thin film and the underlying substrate, for instantaneous stresses driving the lattice dynamics, and for negligible heat diffusion in the sample structure.

In Sec. II, we briefly introduce the analytical model and discuss the predicted lattice dynamics in dependence of the four parameters d , v , δ and α . A detailed derivation of the thermoelastic model is given in the Appendix. Section III describes the experimental setup and results, which are further discussed and related to our analytical model in Sec. IV.

II. THEORY

The strain $\eta(z, t)$ in the one-dimensional thermoelastic response of a semi-infinite crystal due to a photoexcited stress $\sigma(z, t)$ can be well described by the continuum model of Thomsen *et al.*,^{7,8} where z is the depth of the crystal and t is the time. We adopt this model and apply the same nomenclature for the case of an impedance-matched opaque film of thickness d on a transparent semi-infinite substrate. We assume an instantaneous formation of the thermal stress at $t=0$ with the same spatial profile as the photoexcitation (very short electron phonon coupling time in SrRuO₃)^{27,28} and neglect heat diffusion which is not relevant on this ultrashort time scale; $\sigma(z, t \geq 0) = \sigma(z)$. The optical excitation of the opaque film has an exponential spatial profile following Lambert-Beer’s law and is determined by the optical absorption depth ζ , but is abruptly ending at the film interface at the depth $z=d$. For the case of a very thick layer, $d \gg \zeta$, our model coincides with the original work of Thomsen *et al.*

We introduce normalized unitless space $x = z/d$ and time $\tau = vt/d$ coordinates into our thermoelastic model, where v is the longitudinal sound velocity normal to the surface of the thin film. The derivation of the according differential equation (wave equation) after this coordinate transformation is described in the Appendix in detail. A perfect matching of the acoustic impedance $Z = v\rho$ (ρ —mass density) prohibits reflections at the interface. If the sound velocity in the film v and the substrate v_s are different, the amplitude of the sound and the temporal coordinate must be scaled accordingly. The solution $\eta(x, \tau)$ of this wave equation solely depends on two more parameters: a shape parameter $\delta = d/\zeta$ determining the spatial shape of

the lattice excitation; and a scaling factor α which determines the maximum amplitude of the static strain in the film: $\eta(0, \tau) = \alpha$, cf. Eq. (A22). Here, α collects all experimental parameters and material properties which influence the amplitude of lattice distortion of the thin film, such as its heat capacity, thermal expansion coefficient, and excitation fluence. See Table I for a complete list of all parameters.

The solution of the normalized strain $\bar{\eta}(x, \tau) = \eta(x, \tau)/\alpha$ is plotted in Fig. 1 for different values of the shape factor δ for varying normalized delays τ . The two upper panels (a) and (b) represent the solution for the two limiting cases $\delta \ll 1$ and $\delta \gg 1$, where the latter case corresponds to bulk material already discussed by Thomsen *et al.* The two lower panels (c) and (d) show the experimental cases $\delta < 1$ and $\delta > 1$ for the two films of different thickness as described below in the experimental part and discussion.

For $\delta \ll 1$, cf. Fig. 1(a), the photoexcited stress is spatially homogeneous in the opaque film. The resulting lattice dynamics can only start at the surface $x=0$ and interface $x=1$ of the film where the stresses are highly unbalanced. At the interface, a tensile strain front travels into the film which is compensated by a compressive strain front propagating into the substrate which has exactly the same integral strain for perfect impedance matching. At the film surface ($x=0$), the situation is essentially the same, however, the compressive strain front cannot propagate away from the film into the air and is therefore reflected back into the film as an expansion (open boundary condition). At the time $\tau=1$, all tensile strain fronts have traveled once through the film adding up to the maximum integral expansion of the layer which is $\eta_{\text{lay}}(\tau=1)/\eta_{\text{lay}}(\tau \geq 2) = 1.5$, cf. Eq. (A26), independent of any physical parameter of the model. Any significant difference from this ratio would indicate a deviation of the initial assumptions of the analytical model, e.g., that the photoexcited stress is not instantaneous,

TABLE I. Definitions and units of all physical quantities and parameters of the analytical model.

Name	Description	Unit
z	Spatial coordinate (depth)	m
t	Temporal coordinate (time)	s
Q	Energy of a single laser pulse	J
A	Excited area of the sample surface	m ²
ζ	Optical absorption depth	m
C	Specific heat capacity	J/(K m ³)
R	Optical reflectivity coefficient	1
B	Bulk modulus	Pa
ν	Poisson ratio	1
β	Linear thermal expansion coefficient	1/K
ρ	Mass density	kg/m ³
d	Layer thickness	m
δ	Shape parameter	1
v	Longitudinal sound velocity	m/s
α	Scaling of excitation amplitude	m
$T(z)$	Initial temperature profile	K
$\sigma(z, t)$	Dynamical stress	Pa
$u(z, t)$	Dynamical displacement	m
x	Normalized spatial coordinate	1
τ	Normalized temporal coordinate	1
$g(x)$	Spatial temperature profile	1
$f(x)$	Source term of inhom. wave equation	1
$w(x, \tau)$	Normalized dynamical displacement	1
$\eta(x, \tau)$	Dynamical deformation (strain)	1

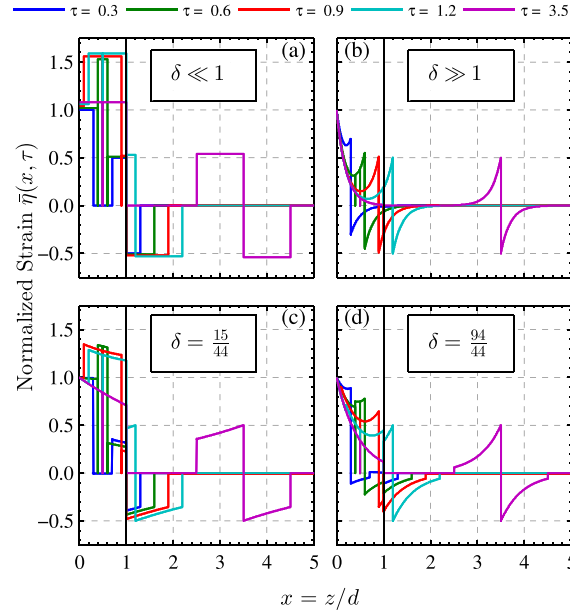


FIG. 1. The normalized strain $\bar{\eta}(x, \tau) = \eta(x, \tau)/\alpha$ is plotted for different shape parameters δ . (a) and (b) represent the limiting cases $\delta \ll 1$ and $\delta \gg 1$, respectively. (c) and (d) represent the experimental cases of $\delta = 15/44 = 0.34$ and $\delta = 94/44 = 2.14$, respectively. For an inhomogeneous spatial stress profile ($\delta > 1$), i.e., panels (b) and (d), the transducer layer ($0 \leq x \leq 1$) is negatively strained for $0 \leq \tau < 1$. Note that in (a) the amplitude of $\bar{\eta}(x, \tau)$ is increased by 2% for each time step for better visibility.

because carrier transport during an extended electron-phonon coupling time occurs. For $\tau > 1$, the tensile strain front originating from the surface leaves the film and enters the substrate, ending the compressive strain in the substrate and starting the tensile part of the strain with the same amplitude $\eta(0, \tau \geq 2)/2$. At the same time, the tensile strain front originating at the film-substrate interface at $x=1$ has reached the surface and is also reflected back into the film as a right-propagating compressive strain front, which reduces the strain at the surface to the final value $\eta(0, \tau \geq 2) = \alpha$. This compressive strain front propagates into the substrate at $\tau=2$, marking the end of the bipolar strain pulse which keeps propagating in the substrate. The bipolar strain pulse has the same integral absolute strain as the remaining static strain in the thin film for $\tau \geq 2$.

For the second limiting case of $\delta \gg 1$, cf. Fig. 1(b), no photoexcitation occurs at the interface $x=1$ but the thermal stresses within the layer are highly unbalanced following the exponentially decaying stress profile. Accordingly, at each point $0 \leq x \leq 1$ a left-propagating tensile strain front and a right-propagating compression strain front are triggered by the photoexcitation. These strain contributions add up to a stationary exponentially decaying component in the film and a propagating bipolar strain pulse with exponential edges. Again, at the time $\tau=1$, the average strain in the layer is: $\eta_{\text{lay}}(1) = 1.5 \eta_{\text{lay}}(\tau \geq 2)$, cf. Eq. (A26). A striking difference compared to the case of $\delta \ll 1$ is the occurrence of compressive strains in the opaque layer, although exclusively expansive stress was applied. This is a result of inhomogeneous excitation, where the larger expansion near the surface requires a compression of the adjacent material, which exceeds its own expansion. The occurrence of these transient compressive strains is solely determined by the shape factor δ and not by the scaling factor α or any other parameter. The experimental cases with the shape factors $\delta = 15/44$ and $\delta = 94/44$, see Figs. 1(c) and 1(d), share the dominant features of the two limiting cases as described above. In the Discussion section, we will show δ is experimentally derived.

III. EXPERIMENTAL SETUP AND RESULTS

We choose two thin films of the metallic perovskite SrRuO₃ (SRO) epitaxially grown onto dielectric SrTiO₃ (STO) substrates. SRO proved to be an ideal transducer layer for large-amplitude and high-frequency coherent longitudinal acoustic phonons²⁹ due to its high damage threshold³⁰ and its fast electron phonon coupling time of ≈ 200 fs (Refs. 27 and 28) resulting in a quasi-instantaneous stress after photoexcitation. The lattice constants as well as the layer thickness of the two films were determined by static X-ray diffraction measurements at the ID9 beamline at the ESRF (European Synchrotron Radiation Facility, Grenoble, France) and the XPP beamline at BESSY II (Helmholtz-Zentrum Berlin, Germany) for the thin and thick film, respectively, as $c_{\text{SRO}} = 3.949$ Å and $c_{\text{STO}} = 3.905$ Å as well as $d_{\text{SRO}}^{(1)} = 15.4$ nm and $d_{\text{SRO}}^{(2)} = 94.8$ nm.

Figures 2(a) and 2(b) show a comparison of the static $\theta/2\theta$ scans around the (002) Bragg peaks of SRO and STO of the two samples (gray circles) and the simulation by dynamical X-ray diffraction theory (gray lines).^{31,32} As expected, the thicker SRO film [Fig. 2(b)] exhibits a narrow and intense Bragg reflection whereas the Bragg peak of the thinner SRO film [Fig. 2(a)] is much broader and weaker. The good agreement between the experimental and theoretical diffraction curves highlights the crystalline perfection of the coherently grown SRO films on the STO substrate.³³ The acoustic impedances of SRO ($v_{\text{SRO}} = 6.312$ nm/ps,³⁴ $\rho_{\text{SRO}} = 6526$ kg/m³) and STO ($v_{\text{STO}} = 7.8$ nm/ps,^{35,36} $\rho_{\text{STO}} = 5117$ kg/m³) match almost perfectly

$$\frac{Z_{\text{SRO}}}{Z_{\text{STO}}} = \frac{\rho_{\text{SRO}} v_{\text{SRO}}}{\rho_{\text{STO}} v_{\text{STO}}} = 1.03.$$

The time-resolved data in Figs. 2(c) and 2(d) were recorded at the Plasma X-ray Source (PXS) at the University of Potsdam, Germany, which provides 150 fs Cu K α X-ray pulses with a repetition rate of 1 kHz.^{37,38} For the data evaluation, a convergence correction routine was applied in order to increase the resolution in reciprocal space for the high-quality thin film samples while preserving the maximum counting statistics.³⁹ Compared to the high-resolution

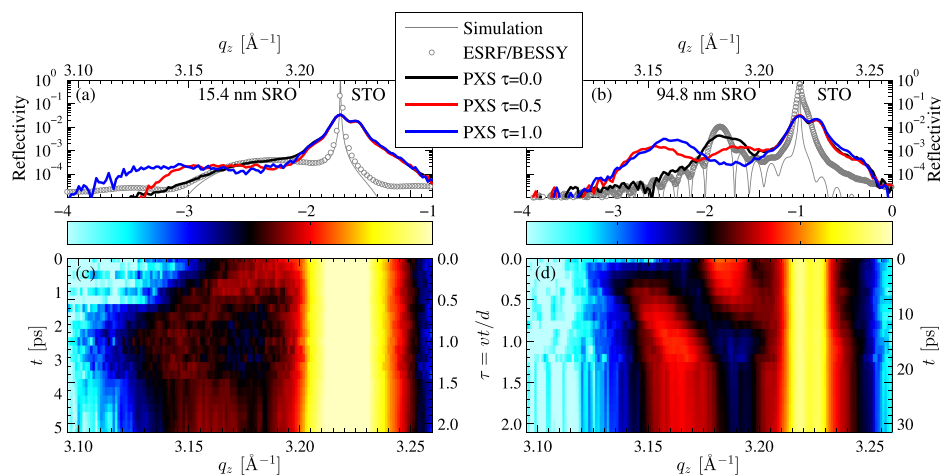


FIG. 2. Static and time-resolved $\theta/2\theta$ -scans of the 15.4 nm SRO sample (left column [(a) and (c)]) and of the 94.8 nm SRO sample (right column [(b) and (d)]) around the (002) Bragg reflections of the layer at small q_z and of the substrate at larger q_z . (a) and (b) Static simulation (thin gray line) and static $\theta/2\theta$ -scan (gray circles) acquired at the ESRF and BESSY II, respectively. The thick lines represent the time-resolved $\theta/2\theta$ -scans measured at the PXS for different snapshots of the coherent lattice dynamics extracted from (c) and (d). [(c) and (d)] Time-resolved $\theta/2\theta$ -scans measured at the PXS under incident laser fluence of $F_1 = 30$ mJ/cm². The color code represents the logarithmic diffracted intensity and is differently scaled, because of the much weaker reflectivity of the thin 15.4 nm SRO film. The outer y-axes represent the actual pump-probe delay t and the inner y-axes the normalized time coordinate τ .

synchrotron diffraction data, the Bragg peaks in the time-resolved measurements are significantly broadened by the resolution function of the PXS and exhibit a typical doubling due to the Cu $K\alpha_{1+2}$ natural line emission.³⁹ The thin film samples were excited by $\lambda = 800$ nm laser pulses with a duration of 40 fs and incident laser fluence of $F_1 = 30$ mJ/cm² and additionally $F_2 = 20$ mJ/cm² only for the thicker SRO film (data not shown). In Figures 2(c) and 2(d), the inner y-axis represents the normalized time coordinate τ which is determined by the propagation time $d_{\text{SRO}}^1/v_{\text{SRO}} = 2.44$ ps and $d_{\text{SRO}}^2/v_{\text{SRO}} = 15.02$ ps of the coherent phonons across the 15.4 nm and 94.8 nm thick SRO layers, respectively.

For both samples, the transient lattice dynamics are triggered after the photoexcitation at $\tau = 0$ and reach a quasi-static state for all delays $\tau \geq 2$. In the range between $0 \leq \tau < 2$, the transient $\theta/2\theta$ -scans show significantly different features for the two SRO films, namely, a continuous shift of the (002) Bragg peak towards small angles vs. a shift to larger angles combined with an intensity transfer to a peak that emerges at a smaller angle. Details about this observed splitting of the Bragg peak are discussed and related to the thermoelastic model in Sec. IV. In addition to the obvious lattice dynamics of the thin films, weak shoulders at the low- and high- q side of the (002) substrate Bragg reflection emerge at different pump-probe delays, which are best visible for the thicker SRO sample, cf. Fig. 2(d). The lattice dynamics of the substrate are beyond the scope of this work and have been discussed elsewhere in detail.^{10,17,29,40}

IV. DISCUSSION

The direct correspondence between material-specific diffraction signals and the relevant transient structural parameters provides the strength of UXR methods in following lattice dynamics on the atomic length scale in real-time. The one-dimensional Laue condition

$$q_z = nG = n \frac{2\pi}{c}, \quad n \in \mathbb{N}$$

connects the position of a specular Bragg reflection q_z to the average lattice constant c in this material along the specific crystal axis for all orders n of the Bragg peak. For small changes of the transient relative peak position $\Delta q_z/q_z(0) = [q_z(t) - q_z(0)]/q_z(0) < 1\%$ [$q_z(t) \approx q_z(0)$], the average strain in the layer can be approximated by the relative peak shift

$$\eta_{\text{lay}}(t) = \frac{c(t) - c(0)}{c(0)} \approx - \frac{q_z(t) - q_z(0)}{q_z(0)}. \quad (1)$$

For an evaluation of the experimental signal in the spirit of unitless normalized coordinates, we employ the film thickness d as obtained from the static X-ray diffraction data. In order to determine the sound velocity in the SRO film, we recall that the integrated intensity of the Bragg peaks is proportional to the thickness of the scattering layer. We know that the peak emerging at small angles corresponds to the expanding region of the thin film near the surface and plot the integrated intensity of this peak I_2 as a function of time in Fig. 3. After $t = 0$, it increases linearly until the entire layer is expanded after $t = 15.02$ ps. The two kinks in the intensity clearly mark the normalized time moments $\tau = 0$ and $\tau = 1$. The sound velocity is therefore determined as $v_{\text{SRO}} = 94.8$ nm/15.02 ps = 6.312 nm/ps. As a cross check, we also plot the integrated intensity at the original Bragg peak position I_1 in Fig. 3. For both fluences, the decrease of the original Bragg peak and the increase of the emerging peak confirm this sound velocity.

The above procedure experimentally fixes the horizontal time axis in Fig. 4, where we compare the averaged normalized peak shift $\bar{\eta}_{\text{lay}}(\tau) = \eta_{\text{lay}}(\tau)/\eta_{\text{lay}}(\tau \geq 2)$ of the experimental and theoretical results. We determine the transient positions $q_z(t)$ of the (002) SRO Bragg peaks of both thin film samples by Gaussian fits and derive the according strain in the layer using Eq. (1). For the thick SRO layer, a fit of two Gaussian functions determines the peak shift for the compressed and expanded regions of the thin film, separately. For the thinner film sample, the (002) substrate Bragg peak is subtracted from the signal in advance, because the broad thin

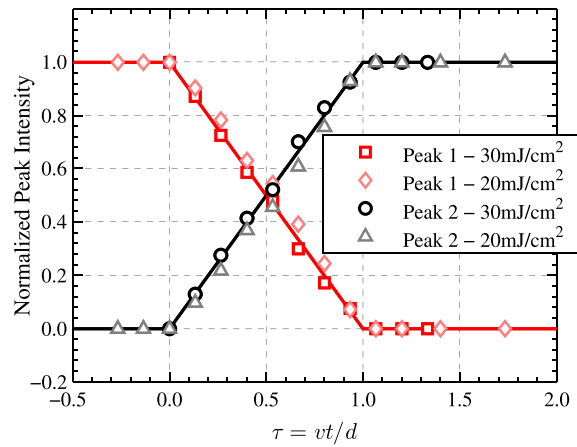


FIG. 3. Normalized integrated intensities $I_{1,2}(\tau)/(I_1(\tau) + I_2(\tau))$ of the initial (red) and emerging Bragg peak (black) of the thick SRO sample for two different excitation fluences $F_1 = 30 \text{ mJ/cm}^2$, $F_2 = 20 \text{ mJ/cm}^2$. Solid lines represent the normalized average strain of the compressive (red) and tensile (black) strain-regions in the layer as derived from the analytical model.

film peak merges with the substrate peak. Figure 4 shows the gradual expansion of the thinner film up to $\bar{\eta}_{\text{lay}}(1) = 1.5$ (red triangles), when the tensile strain front has traveled once through this layer and gives rise to the maximum expansion. Between $1 \leq \tau < 2$ the average strain decreases to its final value $\bar{\eta}_{\text{lay}}(2) = 1$. For the case of the thicker SRO layer, the experimental data for the expanded fraction of the film coincide with the thin film value $\bar{\eta}_{\text{lay,exp}}(1) = 1.5$. The compressed fraction of the crystal is clearly visible in Fig. 4. It merges towards a negative average strain of $\bar{\eta}_{\text{lay,comp}}(1) = -1$, however, since the corresponding intensity of the peak as a measure of the contributing thickness approaches zero, this Bragg peak vanishes just before $\tau = 1$. For a comparison to the thin film values, we calculate the center of mass (CoM) of the Bragg peak position for the thicker SRO layer (black asterisks and gray crosses). The striking agreement is an experimental verification of the universal features of the excited lattice

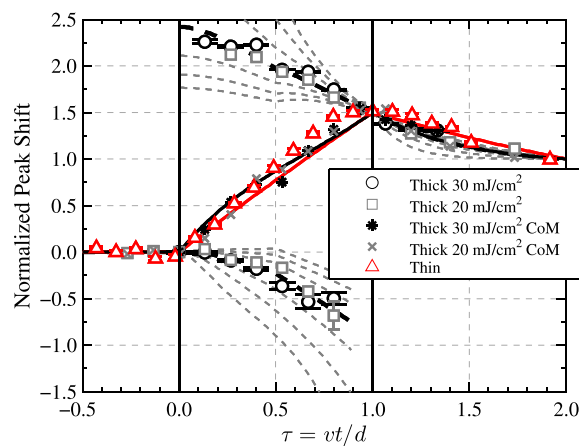


FIG. 4. The normalized peak shift $\Delta q_z(\tau)/\Delta q_z(\tau \geq 2)$ is plotted for both SRO films and fluences as open symbols (Gaussian fits) and crosses (center of mass [CoM]). The solid lines show the normalized average strain $\bar{\eta}_{\text{lay}} = \eta_{\text{lay}}(\tau)/\eta_{\text{lay}}(\tau \geq 2)$ in the SRO layer as determined from the analytical model for the two different samples. The dashed lines represent the normalized strain of the initial and splitted Bragg peak for the thick SRO layer for different values of $\delta = d/\zeta$ ($\zeta = 14, 24, 34, 44, 54, 64$, and 74 nm from outside to inside). The black dashed line shows the best fit for $\zeta = 44 \text{ nm}$.

dynamics. It should be noted that from the data in Fig. 2 not only the normalized strain $\bar{\eta}_{\text{lay}}(\tau)$ can be determined, but also the absolute value of the quasi-static average strain: $\eta_{\text{lay}}(\tau \geq 2) = 0.006$ and 0.0047 for the thick layer and the two excitation fluences, respectively, as well as 0.008 for the thin layer. The normalized average strain from the thermoelastic model is plotted in Fig. 4 as black and red solid lines for the thick and thin layer, respectively.

Now we compare the experimental analysis to the analytical thermoelastic model. We can independently determine the two remaining input parameters from the experiment: The shape parameter δ is best determined from the peak shifts of the split Bragg peak of the thick layer. Figure 4 shows the results of the analytical model for different $\delta = d/\zeta$ as dashed lines. The best fit is obtained for a stress pattern decaying exponentially with $\zeta = 44$ nm. This value is therefore assumed for all simulations. The remaining parameter α can be calculated from Eqs. (A24) or (A25) in the Appendix, e.g.,

$$\eta_{\text{lay}}(\tau \geq 2) = \frac{\alpha}{\delta}(1 - e^{-\delta}).$$

For the fluence range used in our experiments on the SRO thin films $\alpha \approx 0.01$.

The pronounced difference in the transient UXRD data is solely due to the different thickness of the two layers and the accordingly different shape factor δ . As discussed above, for the thicker film, $\delta > 1$, parts of the photoexcited SRO layer are transiently compressed for $0 < \tau < 1$. In principle, the Bragg peak of the thinner SRO film also exhibits a splitting due to the presence of three differently strained regions for $0 < \tau < 1$. Since all of these three regions are positively strained, the difference in the Bragg peak position is rather small and due to the small thickness of the layer and instrumental function of the PXS, the Bragg peak is initially rather broad. Thus the crystal regions with different strain only lead to a broadening of the Bragg peak. Generally, the Bragg peak width provides information about the inhomogeneous spatial strain profiles but the initial structural broadening of the film's Bragg peak and the instrumental function of the UXRD diffractometer render a quantitative analysis difficult. In a recent publication, the shape factor $\delta \sim 1$ was large enough in order to conclude on the spatial profile of the driving stresses of the lattice dynamics.¹⁹ The experimentally derived exponential decay constant of the thicker SRO layer's stress profile $\zeta = 44$ nm (see Fig. 4) is slightly smaller than the optical absorption depth determined by optical ellipsometry as 48 nm for this sample and the accepted literature value of 52 nm.²⁶ This decreased value of ζ cannot be explained by transport phenomena of the photoexcited electrons in SRO which would naturally result in a broader spatial profile of the thermal stresses. For the high excitation fluences used here ($F = 20 - 30$ mJ/cm²) non-linear absorption processes or possibly a temperature-dependent Grüneisen parameter⁴¹ might lead to this slight steepening of the spatial stress profile in SRO.

Finally, we compare experimental $\theta/2\theta$ -scans to dynamical X-ray diffraction calculation of the photoexcited crystal structure which include the instrumental resolution function of the diffractometer.³² Figure 5 shows the excellent agreement not only of the peak positions but also of the complete Bragg peak shapes for the thicker SRO layer.

V. CONCLUSION

We introduced an analytical thermoelastic model which depends only on four parameters (the film thickness, its longitudinal sound velocity, a scaling factor, and a shape factor) for the calculation of photoexcited coherent acoustic phonon dynamics in an opaque thin film grown onto an impedance-matched transparent substrate. We presented fluence-dependent UXRD data of two SRO films of different thickness epitaxially grown on STO substrates and showed that the significantly different UXRD transients, namely, a continuous shift vs. a splitting of the (002) SRO Bragg peak, solely depend on the shape factor δ of our thermoelastic model. The variation of the shape factor δ can also be achieved by employing different excitation wavelengths instead of thin film samples of different thickness. All transient peak shifts exhibit the same universal ratio of $3/2$ between the maximum shift at $\tau = 1$ and

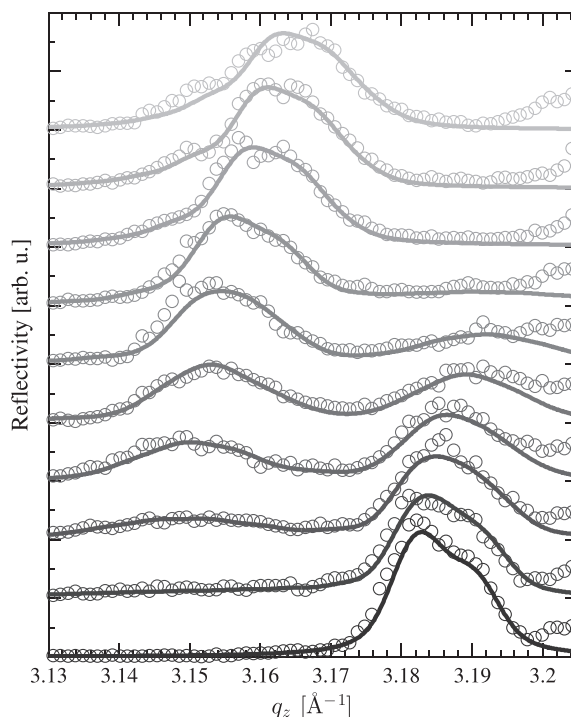


FIG. 5. The time-resolved $\theta/2\theta$ -scans of the thick SRO film after $F_1 = 30 \text{ mJ/cm}^2$ laser excitation are plotted as circles from 0 to 18 ps in 2 ps steps from bottom to top. The solid lines represent dynamical X-ray diffraction calculations of the strained sample as determined from the analytical solution of the thermoelastic model.

the quasi-static shift for $\tau \geq 2$. Moreover, we described a procedure to quantify all four parameters of the analytical model from the experimental data. Compared to UXR experiments on semi-infinite crystals, the usage of thin film samples with well separated Bragg reflections of the layer and the substrate suppress complex dynamical effect and strong contributions from unexcited regions of the bulk in the UXR experiments. Similar to the original work of Thomsen *et al.*, the assumption of negligible diffusion processes of the energy-carrying particles in the photoexcited regions is not generally valid and the thermoelastic model has to be adapted, e.g., for heat diffusion processes. Similar modifications can be applied for non-instantaneous thermal stresses after photoexcitation which requires more parameters of the model.

ACKNOWLEDGMENTS

We gratefully thank Ionela Vrejoiu for providing the samples. We thank the BMBF for funding the project via Grant No. 05K10IP1 and the DFG via Grant No. BA2281/3-1. A.B. thanks the Leibnitz graduate school “Dynamics in new Light” for financial support.

APPENDIX: THERMOELASTIC CONTINUUM MODEL FOR A THIN FILM ON A SEMI-INFINITE SUBSTRATE

We consider the 1D thermoelastic response of a thin photoexcited film of the thickness d on a semi-infinite transparent substrate which is both acoustically impedance-matched. In order to discuss the structural dynamics of the thin film, it is equivalent to consider a semi-infinite crystal

with an initial excitation profile being truncated at the depth $z = d$, e.g., the initial temperature profile. Thomsen *et al.*⁸ solved this problem for a continuous initial excitation profile, i.e., for $\zeta \ll d$, where ζ represents the optical absorption depth.

First, we briefly recall the formalism introduced by Thomsen *et al.* and reformulate the according equations into the inhomogeneous wave equation by simultaneously reducing the number of parameters of the problem. We limit ourselves to a time-independent thermal excitation, i.e., we neglect diffusion of energy carriers.

The thermoelastic equations described by Thomsen *et al.*⁸ have the form

$$T(z) = (1 - R) \frac{Q}{A\zeta C} e^{-\frac{z}{\zeta}} \mathcal{H}(z), \quad (\text{A1})$$

$$\sigma(z, t) = 3 \frac{1 - \nu}{1 + \nu} B \eta(z, t) - 3B\beta T(z), \quad (\text{A2})$$

$$\rho \frac{\partial^2}{\partial t^2} u(z, t) = \frac{\partial}{\partial z} \sigma(z, t), \quad (\text{A3})$$

$$\eta(z, t) = \frac{\partial}{\partial z} u(z, t). \quad (\text{A4})$$

Here, $\sigma(z, t)$, $\eta(z, t)$, and $u(z, t)$ are the stress tensor, strain tensor, and displacement vector, respectively, which are scalar functions for the 1D case. $T(z)$ is the time-independent temperature distribution in the sample after the initial optical excitation and $\mathcal{H}(z)$ is the Heaviside step function. All physical quantities and parameters are listed in Table I. Equations (A2)–(A4) have to be solved on a semi-infinite spatial and temporal domain ($z > 0$, $t > 0$) with the initial conditions (ICs)

$$\eta(z, 0) = 0, \quad \sigma(z, 0) = -3B\beta T(z), \quad (\text{A5})$$

and the boundary condition (BC)

$$\sigma(0, t) = 0. \quad (\text{A6})$$

In order to rewrite the above equations into an inhomogeneous wave equation, we can write the square of the sound velocity as

$$v^2 = 3 \frac{1 - \nu B}{1 + \nu \rho} \quad (\text{A7})$$

and introduce the normalized coordinates

$$\tau = \frac{vt}{d}, \quad (\text{A8})$$

$$x = \frac{z}{d}. \quad (\text{A9})$$

For the case of a semi-infinite crystal without transducer layer,⁸ it might be more convenient to introduce the normalized coordinates as $\tau' = vt/\zeta$ and $x' = z/\zeta$, respectively.

With the normalized coordinates x and τ Eqs. (A2)–(A4) become

$$\begin{aligned} \frac{\partial^2}{\partial \tau^2} u(x, \tau) - \frac{\partial^2}{\partial x^2} u(x, \tau) &= -\frac{3B\beta d}{\rho v^2} \frac{\partial}{\partial x} T(x), \\ \frac{\partial^2}{\partial \tau^2} u(x, \tau) - \frac{\partial^2}{\partial x^2} u(x, \tau) &= -\alpha d \frac{\partial}{\partial x} g(x), \end{aligned} \quad (\text{A10})$$

where

$$\alpha = (1 - R) \frac{3B\beta Q}{\zeta \rho v^2 AC}, \quad (\text{A11})$$

and

$$g(x) = e^{-\delta x} \mathcal{H}(x) \quad (\text{A12})$$

is the spatial profile of the initial temperature distribution with $\delta = d/\zeta$ as shape factor. With the introduction of the normalized dynamical displacement

$$w(x, \tau) = \frac{u(x, \tau)}{\alpha d} \quad (\text{A13})$$

and the definition of the source term

$$f(x) = -\frac{\partial}{\partial x} g(x) \quad (\text{A14})$$

we obtain the simplified inhomogeneous wave equation

$$\frac{\partial^2}{\partial \tau^2} w(x, \tau) - \frac{\partial^2}{\partial x^2} w(x, \tau) = f(x). \quad (\text{A15})$$

The ICs and BC become

$$w(x, 0) = 0, \quad \frac{\partial}{\partial t} w(x, 0) = 0, \quad \frac{\partial}{\partial x} w(0, \tau) = 1 \quad (\text{A16})$$

and the strain rewrites as

$$\eta(x, \tau) = \alpha \frac{\partial}{\partial x} w(x, \tau). \quad (\text{A17})$$

The general solution for this problem is given by⁴²

$$w(x, \tau) = \frac{1}{2} \begin{cases} p(x, \tau) + q(x, \tau) - \int_0^{\tau-x} \phi(s) ds, & x < \tau \\ \int_{0x-\tau+\vartheta}^{\tau x+\tau-\vartheta} f(y) dy d\vartheta, & x > \tau, \end{cases} \quad (\text{A18})$$

where

$$p(x, \tau) = \int_0^{\tau-x} \left(\int_0^{\tau-\vartheta-x} f(y) dy + \int_0^{\tau-\vartheta+x} f(y) dy \right) d\vartheta, \quad (\text{A19})$$

$$q(x, \tau) = \int_{\tau-x}^{\tau} \int_{x-\tau+\vartheta}^{x+\tau-\vartheta} f(y) dy d\vartheta, \quad (\text{A20})$$

and $\phi(s) = 1$ for the BC in Eq. (A16). In general, the source term $f(x)$ may also be time dependent, e.g., if diffusion processes are not negligible, which alters the solution for $\eta(x, \tau)$ accordingly.

For the case of an abrupt end of the initial excitation profile at the depth $z = d$ or $x = 1$, we have to change the spatial profile of the initial temperature distribution $g(x)$, cf. Eq. (A12), to

$$g(x) = e^{-\delta x}(\mathcal{H}(x) - \mathcal{H}(x - 1)). \quad (\text{A21})$$

The solution is plotted in Fig. 1 for different sets of parameters. It follows from the BC in Eq. (A16) and the definition of the strain in the normalized coordinates, cf. Eq. (A17), that the amplitude of the strain at $x = 0$ is only determined by the scaling factor α

$$\eta(0, \tau) = \alpha \frac{\partial}{\partial x} w(0, \tau) = \alpha. \quad (\text{A22})$$

Moreover, the shape of the strain pulse depends solely on the parameter δ which defines the exponential decay of the initial temperature profile $T(x)$. The temporal dimension of the phonon dynamics is scaled by the ratio v/d .

We obtain more general properties of the solution for the thin opaque layer on a semi-infinite transparent substrate by defining the integral strain in the opaque layer ($0 < x < 1$) as

$$\eta_{\text{lay}}(\tau) = \int_0^1 \eta(x, \tau) dx. \quad (\text{A23})$$

The solution at time $\tau = 1$ corresponds to the total layer strain after the coherent sound wave has traversed the layer once and it reads

$$\eta_{\text{lay}}(\tau = 1) = \frac{3\alpha}{2\delta}(1 - e^{-\delta}). \quad (\text{A24})$$

Due to the impedance matching of the layer and the substrate, for all times $\tau \geq 2$ the strain in the layer is constant since all coherent phonons have left it and the integral strains is given by

$$\eta_{\text{lay}}(\tau \geq 2) = \frac{\alpha}{\delta}(1 - e^{-\delta}). \quad (\text{A25})$$

Thus, the ratio

$$\frac{\eta_{\text{lay}}(\tau = 1)}{\eta_{\text{lay}}(\tau \geq 2)} = \frac{3}{2} \quad (\text{A26})$$

is independent of any physical parameter.

- ¹E. Beaupaire, J.-C. Merle, A. Daunois, and J.-Y. Bigot, *Phys. Rev. Lett.* **76**, 4250 (1996).
- ²B. Koopmans, G. Malinowski, F. D. Longa, D. Steiauf, M. Fähnle, T. Roth, M. Cinchetti, and M. Aeschlimann, *Nature Mater.* **9**, 259 (2010).
- ³U. Bovensiepen and P. Kirchmann, *Laser Photonics Rev.* **6**, 589 (2012).
- ⁴T. Huber, S. Mariager, A. Ferrer, H. Schäfer, J. Johnson, S. Grübel, A. Lübcke, L. Huber, T. Kubacka, C. Dornes, C. Lauhe, S. Ravy, G. Ingold, P. Beaud, J. Demsar, and S. Johnson, *Phys. Rev. Lett.* **113**, 026401 (2014).
- ⁵M. Först, R. Mankowsky, H. Bromberger, D. Fritz, H. Lemke, D. Zhu, M. Chollet, Y. Tomioka, R. Merlin, J. Hill, S. Johnson, and A. Cavalleri, *Solid State Commun.* **169**, 24 (2013).
- ⁶S. Wall, D. Wegkamp, L. Foglia, K. Appavoo, J. Nag, R. F. Haglund, J. Stähler, and M. Wolf, *Nat. Commun.* **3**, 721 (2012).
- ⁷C. Thomsen, J. Strait, Z. Vardeny, H. Maris, J. Tauc, and J. Hauser, *Phys. Rev. Lett.* **53**, 989 (1984).
- ⁸C. Thomsen, H. Grahn, H. Maris, and J. Tauc, *Phys. Rev. B* **34**, 4129 (1986).
- ⁹O. Wright and K. Kawashima, *Phys. Rev. Lett.* **69**, 1668 (1992).
- ¹⁰C. Rose-Petrucci, R. Jimenez, T. Guo, A. Cavalleri, C. W. Siders, F. Rksi, J. A. Squier, B. C. Walker, K. R. Wilson, and C. P. J. Barty, *Nature* **398**, 310 (1999).
- ¹¹A. Rousse, C. Rischel, and J.-C. Gauthier, *Rev. Mod. Phys.* **73**, 17 (2001).
- ¹²K. Sokolowski-Tinten, C. Blome, J. Blums, A. Cavalleri, C. Dietrich, A. Tarasevitch, I. Uschmann, E. Förster, M. Kammler, M. Horn-von Hoegen, and D. von der Linde, *Nature* **422**, 287 (2003).
- ¹³M. Bargheer, N. Zhavoronkov, Y. Gritsai, J. C. Woo, D. S. Kim, M. Woerner, and T. Elsaesser, *Science* **306**, 1771 (2004).

- ¹⁴H. A. Navirian, D. Schick, P. Gaal, W. Leitenberger, R. Shayduk, and M. Bargheer, *Appl. Phys. Lett.* **104**, 021906 (2013).
- ¹⁵R. Shayduk, M. Herzog, A. Bojahr, D. Schick, P. Gaal, W. Leitenberger, H. Navirian, M. Sander, J. Goldshteyn, I. Vrejoiu, and M. Bargheer, *Phys. Rev. B* **87**, 184301 (2013).
- ¹⁶A. Loether, Y. Gao, Z. Chen, M. F. DeCamp, E. M. Dufresne, D. A. Walko, and H. Wen, *Struct. Dyn.* **1**, 024301 (2014).
- ¹⁷Y. Gao, Z. Chen, Z. Bond, A. Loether, L. E. Howard, S. LeMar, S. White, A. Watts, B. C. Walker, and M. F. DeCamp, *Phys. Rev. B* **88**, 014302 (2013).
- ¹⁸D. Daranciang, M. J. Highland, H. Wen, S. M. Young, N. C. Brandt, H. Y. Hwang, M. Vattilana, M. Nicoul, F. Quirin, J. Goodfellow, T. Qi, I. Grinberg, D. M. Fritz, M. Cammarata, D. Zhu, H. T. Lemke, D. A. Walko, E. M. Dufresne, Y. Li, J. Larsson, D. A. Reis, K. Sokolowski-Tinten, K. A. Nelson, A. M. Rappe, P. H. Fuoss, G. B. Stephenson, and A. M. Lindenberg, *Phys. Rev. Lett.* **108**, 087601 (2012).
- ¹⁹D. Schick, M. Herzog, H. Wen, P. Chen, C. Adamo, P. Gaal, D. G. Schlom, P. G. Evans, Y. Li, and M. Bargheer, *Phys. Rev. Lett.* **112**, 097602 (2014).
- ²⁰M. Nicoul, U. Shymanovich, A. Tarasevitch, D. von der Linde, and K. Sokolowski-Tinten, *Appl. Phys. Lett.* **98**, 191902 (2011).
- ²¹M. DeCamp, D. Reis, A. Cavalleri, P. Bucksbaum, R. Clarke, R. Merlin, E. Dufresne, D. Arms, A. Lindenberg, A. MacPhee, Z. Chang, B. Lings, J. Wark, and S. Fahy, *Phys. Rev. Lett.* **91**, 165502 (2003).
- ²²D. Reis, M. DeCamp, P. Bucksbaum, R. Clarke, E. Dufresne, M. Hertlein, R. Merlin, R. Falcone, H. Kapteyn, M. Murnane, J. Larsson, T. Missalla, and J. Wark, *Phys. Rev. Lett.* **86**, 3072 (2001).
- ²³S. Lee, A. Cavalleri, D. Fritz, M. Swan, R. Hegde, M. Reason, R. Goldman, and D. Reis, *Phys. Rev. Lett.* **95**, 246104 (2005).
- ²⁴A. Cavalleri, C. Siders, F. Brown, D. Leitner, C. Tóth, J. Squier, C. Barty, K. Wilson, K. Sokolowski-Tinten, M. Horn von Hoegen, D. von der Linde, and M. Kammler, *Phys. Rev. Lett.* **85**, 586 (2000).
- ²⁵A. H. Zewail, *Annu. Rev. Phys. Chem.* **57**, 65 (2006).
- ²⁶P. Kostic, Y. Okada, N. Collins, Z. Schlesinger, J. Reiner, L. Klein, A. Kapitulnik, T. Geballe, and M. Beasley, *Phys. Rev. Lett.* **81**, 2498 (1998).
- ²⁷C. v. Korff Schmising, A. Harpoeth, N. Zhavoronkov, Z. Ansari, C. Aku-Leh, M. Woerner, T. Elsaesser, M. Bargheer, M. Schmidbauer, I. Vrejoiu, D. Hesse, and M. Alexe, *Phys. Rev. B* **78**, 60404 (2008).
- ²⁸A. Bojahr, D. Schick, L. Maerten, M. Herzog, I. Vrejoiu, C. von Korff Schmising, C. Milne, S. L. Johnson, and M. Bargheer, *Phys. Rev. B* **85**, 224302 (2012).
- ²⁹M. Herzog, A. Bojahr, J. Goldshteyn, W. Leitenberger, I. Vrejoiu, D. Khakhulin, M. Wulff, R. Shayduk, P. Gaal, and M. Bargheer, *Appl. Phys. Lett.* **100**, 94101 (2012).
- ³⁰M. Herzog, D. Schick, W. Leitenberger, R. Shayduk, R. M. van der Veen, C. J. Milne, S. L. Johnson, I. Vrejoiu, and M. Bargheer, *New J. Phys.* **14**, 13004 (2012).
- ³¹J. Als-Nielsen and D. McMorrow, *Elements of Modern X-ray Physics* (John Wiley & Sons, Inc., Hoboken, NJ, USA, 2011).
- ³²D. Schick, A. Bojahr, M. Herzog, R. Shayduk, C. von Korff Schmising, and M. Bargheer, *Comput. Phys. Commun.* **185**, 651 (2014).
- ³³I. Vrejoiu, G. Le Rhun, L. Pintilie, D. Hesse, M. Alexe, and U. Gösele, *Adv. Mater.* **18**, 1657 (2006).
- ³⁴S. Yamanaka, T. Maekawa, H. Muta, T. Matsuda, S.-i. Kobayashi, and K. Kurosaki, *J. Solid State Chem.* **177**, 3484 (2004).
- ³⁵Y. H. Ren, M. Trigo, R. Merlin, V. Adyam, and Q. Li, *Appl. Phys. Lett.* **90**, 251918 (2007).
- ³⁶R. Bell and G. Rupprecht, *Phys. Rev.* **129**, 90 (1963).
- ³⁷F. Zamponi, Z. Ansari, C. Korff Schmising, P. Rothhardt, N. Zhavoronkov, M. Woerner, T. Elsaesser, M. Bargheer, T. Trobitzsch-Ryll, and M. Haschke, *Appl. Phys. A* **96**, 51 (2009).
- ³⁸D. Schick, A. Bojahr, M. Herzog, C. von Korff Schmising, R. Shayduk, W. Leitenberger, P. Gaal, and M. Bargheer, *Rev. Sci. Instrum.* **83**, 25104 (2012).
- ³⁹D. Schick, R. Shayduk, A. Bojahr, M. Herzog, C. von Korff Schmising, P. Gaal, and M. Bargheer, *J. Appl. Crystallogr.* **46**, 1372 (2013).
- ⁴⁰M. Herzog, D. Schick, P. Gaal, R. Shayduk, C. Korff Schmising, and M. Bargheer, *Appl. Phys. A* **106**, 489 (2012).
- ⁴¹C. Kittel, *Introduction to Solid State Physics*, 7th ed. (Wiley, New York, 1996).
- ⁴²A. Bitsadze and D. Kalinichenko, *A Collection of Problems on the Equations of Mathematical Physics* (Mir Publishers, Moscow, 1980).

udkm1Dsim - A Simulation Toolkit for 1D Ultrafast Dynamics in Condensed Matter

D. Schick, A. Bojahr, M. Herzog, R. Shayduk,
C. von Korff Schmising and M. Bargheer.
Rev. Sci. Instrum. **83**, 025104 (2012).

UDKM1DSIM - A Simulation Toolkit for 1D Ultrafast Dynamics in Condensed Matter

D. Schick^{a,*}, A. Bojahr^a, M. Herzog^{a,b}, R. Shayduk^c, C. von Korff Schmising^d, M. Bargheer^{a,c}^a*Institut für Physik & Astronomie, Universität Potsdam, Karl-Liebknecht-Straße 24-25, 14476 Potsdam, Germany*^b*Abteilung Physikalische Chemie, Fritz-Haber-Institut der Max-Planck-Gesellschaft, Faradayweg 4-6, 14195 Berlin, Germany*^c*Helmholtz-Zentrum Berlin für Materialien und Energie GmbH, Wilhelm-Conrad-Röntgen Campus, BESSY II, Albert-Einstein-Straße 15, 12489 Berlin, Germany*^d*Institut für Optik und Atomare Physik, Technische Universität Berlin, Straße des 17. Juni 135, 10623 Berlin, Germany***Abstract**

The UDKM1DSIM toolbox is a collection of MATLAB (MathWorks Inc.) classes and routines to simulate the structural dynamics and the according X-ray diffraction response in one-dimensional crystalline sample structures upon an arbitrary time-dependent external stimulus, e.g. an ultrashort laser pulse. The toolbox provides the capabilities to define arbitrary layered structures on the atomic level including a rich database of corresponding element-specific physical properties. The excitation of ultrafast dynamics is represented by an N -temperature model which is commonly applied for ultrafast optical excitations. Structural dynamics due to thermal stress are calculated by a linear-chain model of masses and springs. The resulting X-ray diffraction response is computed by dynamical X-ray theory. The UDKM1DSIM toolbox is highly modular and allows for introducing user-defined results at any step in the simulation procedure.

Keywords: ultrafast dynamics, heat diffusion, N -temperature model, coherent phonons, incoherent phonons, thermoelasticity, dynamical X-ray theory

PROGRAM SUMMARY

Manuscript Title: UDKM1DSIM - A Simulation Toolkit for 1D Ultrafast Dynamics in Condensed Matter

Authors: D. Schick, A. Bojahr, M. Herzog, R. Shayduk, C. von Korff Schmising, M. Bargheer

Program Title: UDKM1DSIM

Journal Reference:

Catalogue identifier:

Licensing provisions: BSD

Programming language: MATLAB (MathWorks Inc.)

Computer: PC/Workstation

Operating system: running MATLAB installation required (tested on MS Win XP - 7, Ubuntu Linux 11.04-13.04)

RAM: MATLAB's typical RAM requirement of 196MB is sufficient for most simulations

Has the code been vectorized or parallelized?: parallelization for dynamical XRD computations

Number of processors used: 1-12 for MATLAB Parallel Computing Toolbox; 1- ∞ for MATLAB Distributed Computing Toolbox

Keywords: ultrafast dynamics, heat diffusion, N -temperature model, coherent phonons, incoherent phonons, thermoelasticity, dynamical X-ray theory

Classification: 7.8 Structure and Lattice Dynamics, 7.9 Transport Properties, 8 Crystallography

External routines/libraries:

optional:

MATLAB Parallel Computing Toolbox, MATLAB Distributed Computing Toolbox

Required (included in the package):

MTIMESX Fast Matrix Multiply for MATLAB by James Tursa, XMLIO_TOOLS by Jaroslaw Tuszynski, TEXTPROGRESSBAR by Paul Proteus

Nature of problem:

Simulate the lattice dynamics of 1D crystalline sample structures due to an ultrafast excitation including thermal transport and compute the corresponding transient X-ray diffraction pattern.

Solution method:

The program provides an object-oriented toolbox for building arbitrary layered 1D crystalline sample structures including a rich database of element-specific parameters. The excitation, thermal transport and lattice dynamics are simulated utilizing MATLAB's ODE solver. Alternatively, the lattice dynamics can also be calculated analytically utilizing MATLAB eigenproblem solver. The dynamical X-ray diffraction is computed in a parallelized matrix formalism.

Restrictions:

The program is restricted to 1D sample structures and is further limited to longitudinal acoustic phonon modes and symmetrical X-ray diffraction geometries.

Unusual features:

The program is highly modular and allows to include user-defined inputs at any time of the simulation procedure.

Running time:

The running time is highly dependent on the number of unit cells in the sample structure and other simulation parameters such as time span or angular grid for X-ray diffraction computations. However, the example files are computed in approx. 1-5 min. each on a 8 Core Processor with 16GB RAM available.

*Corresponding author

Email address: daniel.schick@uni-potsdam.de (D. Schick)

URL: <http://www.udkm.physik.uni-potsdam.de> (M. Bargheer)

1. Introduction

Physics on the ultrafast time scales and nanometer length scales has received enormous attention during the last decade. Ultrafast X-ray diffraction (UXRD) techniques allow for directly studying structural dynamics on the atomic length and time scales. The knowledge of the time-resolved structural response to an ultrafast optical stimulus is essential for the understanding of various condensed matter phenomena.[1–4]

The UDKM1DSIM toolbox is a collection of classes and routines to model 1D crystalline sample structures on the atomic level and to simulate incoherent (heat diffusion) as well as coherent lattice dynamics (acoustic phonons) by semi-coupled equations of thermoelasticity.[5, 6] The resulting transient X-ray diffraction response for the 1D sample structure is computed by dynamical X-ray theory.[7, 8] Due to the high modularity of the toolbox it is easy to introduce user-defined procedures in between the simulation steps. The complete package is written in the MATLAB programming language and requires the installation of the MATLAB software environment. In order to use the multi-core capabilities of MATLAB the Parallel Computing has to be installed but is not required for UDKM1DSIM to work. As a convention for this document, all files and directories are formatted without serifs (`./path/file.ext`) and all MATLAB code is written in typewriter format (`code = [1 10]`). Furthermore, all physical quantities have to be input in SI units and the same applies for all output variables.¹ The latest UDKM1DSIM package files can be downloaded from www.udkm.physik.uni-potsdam.de/udkm1dsim including a detailed documentation and example files. It is highly recommended to be familiar with the basics of MATLAB programming as well as with fundamental object-orientated programming schemes. Please refer to the rich MATLAB documentation on these topics for further help.

In the following, we introduce the implementation and common workflow of the UDKM1DSIM toolbox as well as the underlying physical concepts. Please refer to the specific class documentations in the `./documentation/` folder of the toolbox for detailed information on all available methods and properties. Finally, we provide examples of the UDKM1DSIM package which are compared with selected ultrafast experiments on nano-layered thin film samples.

2. Implementation & Workflow

The UDKM1DSIM package is developed as MATLAB toolbox with a command-line/script-based user-interface. The backbone of the fully object-orientated toolbox is a collection of classes in the `./classes/` folder which hold the complete logic for building 1D sample structures and to

¹A helper class `units` is provided to easily convert physical quantities.

calculate the ultrafast dynamics in these structures. Additional helper routines (`./helpers/`) and material parameter files (`./parameters/`) are included to improve the user experience.

2.1. Structure Generation

The common workflow of a simulation procedure is to create a crystalline sample structure at the beginning. This 1D structure is build of atoms which form unit cells. Unit cells are then grouped to layers/sub-structures which can be further nested, e.g. to build multilayer structures. All physical properties which are necessary for the later simulations are stored in this structural objects. The involved files are `atomBase.m`, `atomMixed.m`, `unitCell.m` and `structure.m`.

2.1.1. Atoms

The smallest building block for a structure is an atom, which is represented by the `atomBase` class. Atomic properties are automatically loaded on construction of each `atomBase` instance from the given parameter files, by providing the correct symbol of the desired chemical element:

```
C = atomBase('C');
H = atomBase('H');
```

By executing the command `C.disp()` all properties of the corresponding `atomBase` object are displayed. Solid solutions, i.e. stoichiometric atomic substitutions, can be modelled by the `atomMixed` class. Here, `atomBase` objects can be added with an according relative amount to the solution:

```
ZrTi = atomMixed('0.2 Zirconium/0.8 Titanium');
ZrTi.addAtom(atomBase('Zr'), 0.2);
ZrTi.addAtom(atomBase('Ti'), 0.8);
```

The resulting mixed atomic properties are the weighted average of the constituent's properties.

2.1.2. Unit Cells

The `unitCell` class holds most of the physical properties which are necessary for the further simulations. In addition to structural information, i.e. the position of atoms in the unit cell, thermal and mechanical properties are stored here. The only required parameters on initialization of a `unitCell` instance are a unique identifier (ID), name, and the *c*-axis (lattice parameter normal to the sample surface) of the unit cell. All other properties can be optionally handed over within a parameter struct on construction, or can be added/modified later:

```
cAxis = 3.95e-10; % [m]
prop.soundVel = 5100; % [m/s]
.
.
prop.heatCapacity = 465; % [J/kg K]
% SrRuO3 - Perovskite
SRO = unitCell('SRO', 'SrRuO3', cAxis, prop);
```

After the construction of a `unitCell` object, one can add `atomBase` or `atomMixed` object at relative positions in the 1D unit cell, e.g. for the cubic SrRuO_3 (SRO) perovskite unit cell:

```
SRO.addAtom(Sr, 0 );
SRO.addAtom(O , 0 );
SRO.addAtom(Ru, 0.5);
SRO.addAtom(O , 0.5);
SRO.addAtom(O , 0.5);
```

In the 1D approximation the lateral position of the atoms in the unit cell is not relevant. One needs to determine the position of the individual atoms in the unit cell along their projection onto the surface normal of the sample. Moreover, it is not possible to add fractions of atoms at certain unit cell position. Hence, one has to translate the origin of the unit cell accordingly.

All available unit cell properties can be easily displayed by executing the command `SRO.display()`. The position of atoms in the unit cell can be visualized by executing `SRO.visualize()`.

2.1.3. Structures

The final 1D crystalline samples are represented by the structure class which only requires a name on initialization. One can add any number of `unitCell` objects to a structure, as well as nested substructures. An example of a $\text{SrRuO}_3/\text{SrTiO}_3$ superlattice with 10 periods on a SrTiO_3 (STO) substrate is shown in the listing below:

```
DL = structure('Double Layer');
% add 13 SRO and 25 STO unit cells to the DL
DL.addSubStructure(SRO,13);
DL.addSubStructure(STO,25);

S = structure('Superlattice Sample');
% add 10 DLs to the sample
S.addSubStructure(DL,10);
% add 1000 STO unit cells to the sample
S.addSubStructure(STO,1000);
```

In order to simplify the sample structure creation, all of the above mentioned steps can be included in an external XML file which holds all information on atoms, unit cells and on the structure itself. Hence, it is easy to store structures outside of MATLAB in a unified and open standard. An example XML file is provided in the `./example/` folder of the toolbox. In order to load the data from the XML file into the MATLAB workspace one needs to execute the following command providing the relative or absolute path to the XML file:

```
S = structure('void', './structure.xml');
```

Again, the structure properties can be displayed with the command `S.display()` and the structure can be visualized by `S.visualize()`.

2.2. Simulation Classes

Besides the 1D sample structures, also all simulations are programmed as classes and inherit from the super-class `simulation`. All `simulation`-inherited classes provide fundamental properties and methods for storing and loading of simulation results from a so-called `/cache/` folder. The `UDKM1DSIM` toolbox can decide independently by comparing a unique hash of all simulation input parameters whether a simulation result (once calculated) can be loaded from the cache folder or needs to be (re-)calculated. The hash algorithm decides also which parameter changes are relevant for a simulation model, e.g. a change of the sound velocity of a unit cell does not change the result of the heat diffusion calculation, however it does change the result of the lattice dynamics simulation. Further functionalities of the `simulation` class are to enable/disable any command-line messages during the simulations, e.g. to display the elapsed time for a simulation step, and to change the mode of progress displaying.

In order to calculate the time-dependent X-ray diffraction response of a 1D crystalline sample structure to an ultrafast stimulus the following three simulations steps are necessary:

1. The excitation is described as temperature changes in an N -temperature model with optional heat diffusion which determines the temperature evolution in the N coupled subsystems.
2. The resulting lattice dynamics due to thermal stress possibly generated by any of the N subsystems are calculated by a 1D linear-chain model.
3. Dynamical X-ray theory is applied to calculate the UXRD response to the lattice dynamics.

These three steps are encapsulated in the simulation classes `heat`, `phonon`, and `XRD` which all require a structure object on initialization.

It is important to note, that each of the simulation steps listed above may be executed independently with user-defined inputs. Thus it is not necessary to execute the heat and phonon simulations if the user needs to calculate the X-ray diffraction result e.g. for artificial or externally calculated lattice dynamics.

2.3. Thermal Excitation & Diffusion

The `UDKM1DSIM` toolbox allows for different excitation scenarios and optional thermal transport. The most general model is an N -temperature model (NTM) which is described in section 2.3.1.[9] However, for various experimental cases it is convenient to simplify the simulation procedure in order to save computational time.

In all cases it is assumed that the sample structure is excited by a light pulse which is absorbed following Lambert-Beer's law:

$$I(z) = I_0 e^{-z/\zeta} \quad , \quad (1)$$

with ζ as optical penetration depth of the material for the considered wavelength. Accordingly, one can define the transmission and absorption in the material as follows:

$$\tau = \frac{I(z)}{I_0} = e^{-z/\zeta} \quad , \quad \alpha = 1 - \tau \quad . \quad (2)$$

Note that we do not consider the reflected laser light here. The deposited optical energy is then given by the spatial derivative of the absorption:

$$\frac{\partial \alpha}{\partial z} = \frac{1}{\zeta} e^{-z/\zeta} \quad . \quad (3)$$

The most simplified excitation scenario is represented by an instantaneous temperature jump of the excited sample structures (infinitely short laser pulse). This assumption is generally valid if the excitation and thermal equilibration between all N subsystems happen much faster than the subsequent thermal and/or lattice dynamics. The instantaneous temperature jump at depth z can be calculated from the energy absorbed by the corresponding unit cell via:

$$\Delta E(z) = \int_{T_1}^{T_2} m c [T(z)] dT(z) \quad , \quad (4)$$

where T_1 is the initial and T_2 is the final temperature of the unit cell, m is the unit cell mass, and $c(T)$ is the temperature-dependent specific heat capacity. In order to calculate the absorbed energy per unit cell at the depth z in the sample structure one can linearize Eq. 3 for small Δz in terms of energy instead of intensity to get

$$\Delta E = \frac{\partial \alpha}{\partial z} E_0 \Delta z \quad , \quad (5)$$

where Δz is the size of the according unit cell. The initial energy E_0 which is incident on the first unit cell can be derived from the incident absorbed fluence $F = E_0/A$, where A is the area of a single unit cell. Hence, one has to minimize the following modulus in order to obtain the final temperature T_2 of a unit cell after optical excitation:

$$\left| \int_{T_1}^{T_2} m c [T(z)] dT(z) - \frac{E_0}{\zeta} e^{-z/\zeta} \Delta z \right| \stackrel{!}{=} 0 \quad . \quad (6)$$

In order to solve the above minimization problem it is necessary that the heat capacity $c(T)$ is input as a polynomial of any order, thus enabling MATLAB to integrate $c(T)$ algebraically with respect to the temperature T .

The temperature jump resulting from the optical excitation at $t = 0$ can be further used as initial condition for solving the 1D heat diffusion equation:

$$c [T(z, t)] \rho \frac{\partial T(z, t)}{\partial t} = \frac{\partial}{\partial z} \left(k [T(z, t)] \frac{\partial T(z, t)}{\partial z} \right) \quad (7)$$

including the thermal conductivity $k(T)$ and mass density ρ of the individual unit cells. The UDKM1DSIM toolbox is capable of calculating the optical excitation and thermal dynamics independently for a given sample structure,

thermal parameters, and excitation scenario. The corresponding code listing for an excitation at $t_0 = 0$ with a fluence of $F = 5 \text{ mJ/cm}^2$ including heat diffusion for a given sample structure S might look as follows:

```
% initialization of heat simulation
H = heat(S, forceRecalc);
% S - structure object
% forceRecalc - boolean
% enable heat diffusion
H.heatDiffusion = true;
% introduces SI units
u = units;
% temporal grid for heat simulations
time = (-20:0.1:200)*u.ps;
% initial temperature of the structure
initTemp = 300*u.K;
% define the excitation
F = 5*u.mJ/u.cm^2;
% the temperature profile is calculated:
[tempMap, deltaTempMap] = ...
    H.getTempMap(time, F, initTemp);
```

Here, `initTemp` is the initial temperature of the sample, which can be defined globally or per unit cell and the vector `time` defines the time grid of the calculation. The actual numerical calculation is executed by the last command in the above listing and requires no further insight into the involved mathematics. The UDKM1DSIM toolbox allows for more sophisticated excitation scenarios, such as optical pulse sequences with arbitrary temporal pulse separations and durations as well as user-defined pulse energy distributions. Please refer to the corresponding examples for further details on this topic.

2.3.1. N -Temperature Model

The so-called N -temperature model (NTM)[9] is a very general model for laser heating of metals and semiconductors. In the NTM materials are described by N thermal subsystems having individual temperatures $T_j(z, t)$, heat capacities $c_j(T_j)$, thermal conductivities $k_j(T_j)$ and coupling terms $G_j(T_1, \dots, T_N)$. The subsystems might be represented by e.g. electrons, lattice, or spins of the according material:

$$\begin{aligned} c_1(T_1) \frac{\partial T_1}{\partial t} &= \frac{\partial}{\partial z} \left(k_1(T_1) \frac{\partial T_1}{\partial z} \right) \\ &\quad + G_1(T_1, \dots, T_N) + S(z, t) \\ &\quad \vdots \\ c_N(T_N) \frac{\partial T_N}{\partial t} &= \frac{\partial}{\partial z} \left(k_N(T_N) \frac{\partial T_N}{\partial z} \right) \\ &\quad + G_N(T_1, \dots, T_N) \quad . \end{aligned} \quad (8)$$

The UDKM1DSIM toolbox limits the excitation of a structure with N subsystem to happen exclusively in the first subsystem. The excitation can be either given as an initial condition due to an instantaneous temperature jump (see above) or by a spatially and temporally varying source term $S(z, t)$. This source term is the energy flux per vol-

ume and time

$$S(z, t) = \frac{\partial^2 E}{A \partial z \partial t} \quad , \quad (9)$$

where A is again the unit cell area. The spatial profile of $S(z, t)$ is given by the absorbed energy density from Eq. 3 and the temporal profile is limited to a Gaussian function, which states as

$$\frac{\partial^2 E}{\partial z \partial t} = \frac{d\alpha}{dz} E_0 \sigma(t) \quad , \quad (10)$$

with $\sigma(t)$ as a normalized Gaussian function in time [s⁻¹] and E_0 as the initial energy incident on the first unit cell. The resulting source term reads as follows:

$$S(z, t) = \frac{d\alpha}{dz} F \sigma(t) \quad . \quad (11)$$

In order to enable the evaluation of the NTM it is necessary to input all material properties in the structure as N -dimensional cell arrays. Each element of the cell array can be either a constant value for the according property or an anonymous function of the j^{th} subsystem temperature T_j . In contrast to simple heat simulations with only a single subsystem one needs to define the additional `unitCell` property `subSystemCoupling` which represents the term $G(T)$ in Eq. 9.

As it is necessary to solve the heat diffusion equation the `UDKM1DSIM` toolbox allows to define boundary conditions of each subsystem, such as isolating boundaries, constant temperature, or constant heat flux on either side of the sample structure. Details on the broad capabilities of the `UDKM1DSIM` toolbox for thermal simulations are given in the example files `heatExample.m`, `heatNTmodelExample.m`, and `heatExcitationExample.m`.

2.4. Lattice Dynamics

The optically induced temperature change usually induce thermal stress in laser-heated materials. This thermal stress eventually relaxes via thermal expansion which is quantified by the linear thermal expansion coefficient:

$$\alpha(T) = \frac{1}{L} \frac{dL}{dT} \quad . \quad (12)$$

Since the temperature change $\Delta T(z, t)$ for each unit cell at each time step is known one can calculate the actual thermal expansion of each unit cell by

$$l = \Delta L = L_1 \left(e^{[A(T_2) - A(T_1)]} - 1 \right) \quad , \quad (13)$$

where L_1 is the initial length (c -axis of the unit cell), $A(T)$ is the integral of $\alpha(T)$, T_1 and T_2 denote the initial and final temperatures of each unit cell, respectively. It is again necessary to define $\alpha(T)$ as a polynomial of any order of the temperature T to enable MATLAB for simple and fast algebraic integration.

The thermally expanded unit cells are only the final state of the laser-excited crystal. In order to calculate

the transient lattice dynamics (including only longitudinal acoustic phonons) towards this final state, we set up a model of a linear chain of masses and springs in which each unit cell represents a mass m_i that is coupled to its neighbors via springs with the spring constant $k_i = m_i v_i^2 / c_i^2$ (c_i - lattice c -axis, v_i - longitudinal sound velocity):[10]

$$m_i \ddot{x}_i = -k_i(x_i - x_{i-1}) - k_{i+1}(x_i - x_{i+1}) + m_i \gamma_i (\dot{x}_i - \dot{x}_{i-1}) + F_i^{\text{heat}}(t) \quad . \quad (14)$$

Here $x_i(t) = z_i(t) - z_i^0$ denotes the shift of each unit cell from its initial position. Furthermore, we introduce an empirical damping term $F_i^{\text{damp}} = \gamma_i (\dot{x}_i - \dot{x}_{i-1})$ and the external force (thermal stress) $F_i^{\text{heat}}(t)$. In order to solve this system of coupled differential equations for each of the $i = 1 \dots N$ unit cells the `UDKM1DSIM` toolbox provides an analytical (`phononAna`) and a numerical model (`phononNum`) which are described in detail below. Examples for both models are given in the example files `phononExample.m`, and `phononAnharmonicExample.m`.

2.4.1. Analytical Solution

To obtain an analytical solution of Eq. 14 we neglect the damping term $F_i^{\text{damp}}(t)$ and derive the homogeneous differential equation in matrix form

$$\frac{d^2}{dt^2} \mathbf{X} = \mathbf{K} \mathbf{X} \quad . \quad (15)$$

Here $\mathbf{X} = (x_1 \dots x_N)$ and \mathbf{K} is the tri-diagonal force matrix. The matrix \mathbf{K} can be diagonalized to obtain the eigenvectors Ξ_j and eigenfrequencies ω_j in order to find the general solution

$$\mathbf{X}(t) = \sum_j \Xi_j (A_j \cos(\omega_j t) + B_j \sin(\omega_j t)) \quad (16)$$

Mathematical details on the analytical model are given in Ref. [10] and in the documentation of the `phononAna` class. Generally, we use MATLAB's capability to solve the eigenproblem for \mathbf{K} in order to get the results for $\mathbf{X}(t)$ for each time step. One can implement the thermal stress as new equilibrium position $x_i^\infty(t)$ /initial conditions for the general solution Eq. 16 by doing an according coordinate transformation. The thermal stress $[F_i^{\text{heat}}(t)]$ can be modeled as spacer sticks l_i in between the unit cells which are calculated from Eq. 13.

As an example listing of the analytical solution of the coherent phonon dynamics we continue the above code, having the structure `S`, `time` and the results of the heat simulation (`tempMap`, `deltaTempMap`) in memory.

```
% initialization of analytical phonon simulation
P = phononAna(S, forceRecalc);
% the strain profile is calculated:
strainMap = ...
P.getStrainMap(time, tempMap, deltaTempMap);
```

The matrix `deltaTempMap` is the temporal derivative of the temperature profile `tempMap`. The analytical model

has the advantage that once the eigenproblem is solved for a fixed \mathbf{K} (fixed sample structure) the strain profile can be easily solved for any excitation profile at any time. In the case of a quasi-instantaneous excitation without heat diffusion this results in an extremely fast calculation since the initial conditions $\mathbf{X}(0)$ change only once for the excitation. However, the analytical model becomes rather slow for time-dependent thermal stress, because of the recalculation of these initial conditions for each time step. Accordingly, the temporal variation of the thermal stress due to damping has not been implemented in this model. The main disadvantage of the analytical model is the limitation to purely harmonic inter-atomic potentials which is overcome by the numerical model, described below. The numerical model is generally also faster in the total computational time and further accounts for phonon scattering and damping effects.

2.4.2. Numerical Solution

Mathematical details on the numerical model for the coherent phonon dynamics can be found in the documentation of the `phononNum` class and in Ref. [11]. Generally, we use MATLAB's ODE solver to calculate the results for Eq. 14 which can be simplified to

$$m_i \ddot{x}_i = F_i^{\text{spring}} + F_i^{\text{damp}} + F_i^{\text{heat}} \quad .$$

Here $F_i^{\text{spring}} = -k_i(x_i - x_{i-1}) - k_{i+1}(x_i - x_{i+1})$ is the force acting on each mass due to the relative shifts in respect to the left and right neighboring masses. The numerical solution also allows for non-harmonic inter-atomic potentials of up to the order M . Accordingly, $k_i = (k_i^{(1)} \dots k_i^{(M-1)})$ can be a vector accounting for higher orders of the potential which is purely quadratic ($k_i = k_i^{(1)}$) in the harmonic case. Thus we can introduce the following term into F_i^{spring} :

$$k_i(x_i - x_{i-1}) = \sum_{j=1}^{M-1} k_i^{(j)}(x_i - x_{i-1})^j \quad , \quad (17)$$

which accounts for the anharmonic interaction. In order to calculate anharmonic phonon propagation, including damping, one needs to set the according properties of the `unitCell` object. For the example of the SRO unit cell defined in Sec. 2.1.2 one has to write

```
SRO.phononDamping = 1e-12;           % [kg/s]
SRO.setHOSpringConstants([-7e12]); % [kg/m s^2]
```

which sets the damping constant to $\gamma_{\text{SRO}} = 10^{-12}$ kg/s and the second-order of the spring constant to $k_{\text{SRO}}^{(2)} = -7 \times 10^{12}$ kg/ms². The actual numerical calculation for the coherent phonon dynamics is similar to the analytical model expect for the initialization of the `phononNum` object at the beginning:

```
% initialization of numerical phonon simulation
P = phononNum(S, forceRecalc);
```

```
% the strain profile is calculated:
strainMap = ...
    P.getStrainMap(time, tempMap, deltaTempMap);
```

We want to highlight, that the analytical and numerical lattice dynamics calculations share the same syntax in order to calculate the strain profile after optical excitations. In addition, the user can input any temperature profile for the thermal stresses and is not limited to the results of the `heat` simulations. In accordance to the NTM described in Sec. 2.3.1, the thermal stresses can account for multiple thermodynamic subsystems in the sample by introducing different `unitCell` linear thermal expansion coefficients $\alpha_j(T_j)$ for the j^{th} subsystem.

2.5. X-Ray Diffraction

In order to probe transient lattice dynamics with atomic resolution, time-resolved XRD techniques have emerged as an appropriate method in experimental physics. The UDKM1DSIM toolbox provides methods to simulate the static and transient XRD response of crystalline sample structures. Due to the limitation to 1D sample structures only symmetrical X-ray diffraction in co-planar geometry is implemented. For the calculation of static XRD curves ($\theta/2\theta$ -scans) for homogeneously strained layers two different theoretical approaches are provided: kinematical and dynamical XRD. In kinematical XRD theory (`XRDkin`) the incident X-ray beam is unaffected by the crystal, since absorption and multiple reflections are neglected.[12] In the `XRDkin` class no refraction correction has been implemented so far. However, the kinematical theory is a rather fast analytical approach for thin crystal layers, ideally imperfect mosaic crystals, and diffraction at the wings of Bragg peaks. For high quality crystals, thick crystals, and diffraction close to the maximum of strong Bragg peaks, so-called dynamical XRD theory (`XRDdyn`) should be considered.[8] Dynamical XRD theory accounts for absorption, refraction, scattering, and multiple reflections (extinction) of the incident beam. In comparison to kinematical theory, dynamical XRD is generally slower to calculate due to its complex matrix formalism. However, in order to calculate the transient XRD response of a 1D sample structure due to ultrafast lattice dynamics only dynamical theory is implemented in the UDKM1DSIM toolbox, since here its matrix formalism has no disadvantageous against the kinematical theory in terms of computational time. Examples on the applications and limitations of the two models are given in the example file `XRDexample.m`.

For both theories the smallest scatterers in each structure are the individual atoms, whose scattering cross sections are given by the atomic form factor f . [8] Generally, these atomic form factors dependent on the energy E and scattering vector $q_z = 2k \sin(\theta)$ of the incident X-ray beam, where $k = 2\pi/\lambda$ is the X-ray wave number and θ is the incidence angle:[8]

$$f(q_z, E) = f_{\text{CM}}(q_z) + \delta f_1(E) - i f_2(E) \quad . \quad (18)$$

The dispersion corrections $\delta f_1(E)$ and absorption correction $f_2(E)$ have been experimentally determined[13] whereas the angle-dependence $f_{\text{CM}}(q_z)$ is a theoretical correction from Hartree-Fock calculations.[14] The values of $f(q_z, E)$ are automatically loaded and calculated from the according parameter files by the `UDKM1DSIM` toolbox for each atom/ion for a given E and q_z and the reader may refer to the documentation of the `atomBase` class for further details. In order to account for the polarization of the X-rays one has to introduce a θ -dependent polarization factor $P(\theta)$ in kinematical and dynamical XRD calculations given by:[8]

$$P(\theta) = \begin{cases} 1 & \text{s-polarized} \\ \cos(2\theta) & \text{p-polarized} \\ \frac{1+\cos(2\theta)}{2} & \text{unpolarized} \end{cases} \quad (19)$$

2.5.1. Kinematical XRD

For the calculation of rocking curves using kinematical theory one further introduces the structure factor of a unit cell

$$S(q_z, E, \epsilon) = \sum_i^N f_i e^{-i q_z z_i(\epsilon)} \quad . \quad (20)$$

The structure factor $S(q_z, E, \epsilon)$ is the summation of all atomic form factors $f_i(q_z, E)$ in a specific unit cell and also depends on the lattice strain ϵ by the position $z_i(\epsilon)$ of the individual atoms in the unit cell. From Ref. [12] one can now calculate the diffracted wave field amplitude at the detector from a single layer of similar unit cells as follows:

$$E_p = \frac{i}{\epsilon_0 m_e c_0^2} \frac{P(\theta) S(q_z, E, \epsilon)}{A q_z} \quad , \quad (21)$$

with e as electron charge, m_e as electron mass, c_0 as vacuum light velocity, ϵ_0 as vacuum permittivity, and A as area of the unit cell in the plane normal to q_z . For the case of N similar planes of unit cells one can then write:

$$E_p^N = \sum_{n=0}^{N-1} E_p e^{i q_z z n} \quad , \quad (22)$$

where z is the distance between the planes (c -axis of the unit cells). The above equation can be simplified to

$$E_p^N = E_p \psi(q_z, z, N) \quad , \quad (23)$$

introducing the interference function

$$\psi(q_z, z, N) = \sum_{n=0}^{N-1} e^{i q_z z n} = \frac{1 - e^{i q_z z N}}{1 - e^{i q_z z}} \quad . \quad (24)$$

The total reflected wave field E_p^t of all $i = 1 \dots M$ homogeneous layers is the summation of the individual wave fields $E_p^{N,i}$:

$$E_p^t = \sum_{i=1}^M E_p^{N,i} e^{i q_z Z_i} \quad , \quad (25)$$

where $Z_i = \sum_{j=1}^{i-1} (N_j z_j)$ is the distance of the i^{th} layer from the surface. Finally, the actual reflectivity of the sample structure is calculated by $R = E_p^t (E_p^i)^*$.

In order to obtain the static kinematical diffraction curve of a given sample structure S one can follow the code listing below:

```
% set the simulation parameters
E      = 8047*u.eV; % X-ray energy
pol    = 0.5; % mixed X-ray polarization
theta  = (22:0.001:24)*u.deg; % angular range
% initialization of XRDkin simulation
K = XRDkin(S, forceRecalc, E, pol);
% set the qz-range by a theta-vector
K.setQzByTheta(theta);
% calculate the static diffraction curve:
Rs = K.homogeneousReflectivity();
```

2.5.2. Dynamical XRD

In dynamical XRD theory a complex matrix formalism is applied to calculate the reflection and transmission of X-rays by individual atomic layers forming the sample structure.[8] The basic building blocks for this formalism are the reflection-transmission matrices of the atomic planes

$$H = \frac{1}{\tau} \begin{pmatrix} (\tau^2 - \rho^2) & \rho \\ -\rho & 1 \end{pmatrix} \quad , \quad (26)$$

and propagation matrices

$$L = \begin{pmatrix} \exp(i\phi) & 0 \\ 0 & \exp(-i\phi) \end{pmatrix} \quad . \quad (27)$$

The matrix elements are defined as follows:

$$\rho = -i \frac{4\pi r_e f(q_z, E) P(\theta) e^{-M}}{q_z A} \quad , \quad (28)$$

$$\tau = 1 - i \frac{4\pi r_e f(0, E) e^{-M}}{q_z A} \quad , \quad (29)$$

$$\phi = \frac{q_z d}{2} \quad , \quad (30)$$

where r_e is the classical electron radius, $M = (\text{dbf} q_z)^2 / 2$ with $\text{dbf}^2 = \langle u^2 \rangle$ as average thermal vibration of the atoms (Debye-Waller factor), and d is the distance between two layers of scattering objects.

In order to obtain the final reflectivity of the sample structure one has to carry out the according matrix multiplications of the H and L matrices. The reflectivity-transmission matrix (RTM) of a single unit cell M_{RT} is calculated from the individual H_i of each atom and the propagation matrices between the atoms L_i :

$$M_{\text{RT}} = \prod_i H_i L_i \quad . \quad (31)$$

For N identical layers of unit cells one can calculate the N^{th} power of the unit cell's RTM (M_{RT}^N) instead of carrying out N matrix multiplications in order to save computational time. The RTM for the homogeneous sample

$M_{\text{RT}}^{\text{hom,tot}}$ consisting of K homogeneous substructures then becomes:

$$M_{\text{RT}}^{\text{hom,tot}} = \prod_{k=1}^K \left(M_{\text{RT}}^{(k)} \right)^{N_k} . \quad (32)$$

For the case of an inhomogeneously strained sample one has to carry out the matrix multiplication for each individually strained unit cell. Thus, the RTM of the inhomogeneous sample $M_{\text{RT}}^{\text{inhom,tot}}$ containing $m = 1 \dots M$ unit cells is calculated by:

$$M_{\text{RT}}^{\text{inhom,tot}} = \prod_{m=1}^M M_{\text{RT}}^{(m)} , \quad (33)$$

which is a rather expensive calculation since it has to be carried out for all differently strained types of unit cells, for all θ or q_z , and for all time steps. The final reflectivity R of the sample is calculated from the matrix elements of the 2×2 RTM matrix as follows:

$$R = \left| M_{\text{RT}(1,2)}^{\text{tot}} / M_{\text{RT}(2,2)}^{\text{tot}} \right|^2 . \quad (34)$$

In the following code listing we refer again to the results of the heat and phonon simulations for the given sample structure S introduced above. For the static case the syntax for kinematical and dynamical XRD is similar. However, the simulation of UXRD from transient lattice dynamics which inevitably involves inhomogeneously strained layers is only implemented in the `XRDdyn` class.

```
% initialization of XRDkin simulation
D = XRDdyn(S, forceRecalc, E, pol);
% set the qz-range by a theta-vector
D.setQzByTheta(theta);
% calculate the static diffraction curve:
Rh = D.homogeneousReflectivity();
% calculate a reduced number of strains per unique
% unit cell in order to save computational time
strainVectors = ...
    P.getReducedStrainsPerUniqueUnitCell(strainMap);
% calculate the transient XRD:
R = D.getInhomogeneousReflectivity(...
    strainMap, strainVectors);
```

2.5.3. Parallel Computing

As mentioned before, the calculation of the transient XRD result is very expensive in computational time, since heavy matrix multiplications for all individually strained unit cells in the sample, for all angles θ and time steps have to be carried out. In order to speed up this calculations the UDKM1DSIM toolbox uses MATLAB's parallel computing capabilities. The Parallel Computing Toolbox has to be installed to enable this feature. In this parallel mode the dynamical XRD results for the individual time steps are calculated parallel, e.g. on a multi-core system or computer-cluster², since the results at different angles

²Cluster calculations require a MATLAB Distributed Computing Server license.

and time steps are independent. The user can individually decide how to calculate the inhomogeneous reflectivity by adding a third input parameter `type` to the function call. The value of the `type` parameter can be 'parallel' (default), 'distributed', or 'sequential', whereas the latter case does not require additional licenses for the MATLAB Parallel or Distributed Computing Toolbox:

```
type = 'sequential';
R = D.getInhomogeneousReflectivity(...
    strainMap, strainVectors, type);
```

3. Examples

In this section we want to provide physical examples for the application of the UDKM1DSIM toolbox. The complete example code can be found in the `./examples/` folder.

3.1. Bragg-Peak Splitting Evidences Inhomogeneous Expansion

Here we consider a 95 nm metallic SRO thin film on a dielectric STO substrate which is photoexcited by an ultrashort laser pulse with a fluence of $F = 20 \text{ mJ/cm}^2$. The excitation is modeled as instantaneous temperature jump and we further neglect heat diffusion. The temperature change at $t = 0$ is shown in Fig. 1 a) and features an exponential decay in the absorbing SRO layer in accordance with Eq. 1. Subsequent coherent phonon dynamics are calculated by the `phononNum` class and the resulting spatio-temporal strain profile is depicted in Fig. 1 b).

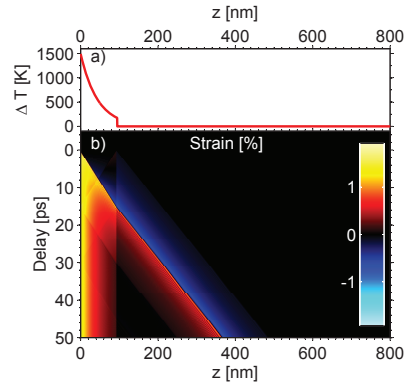


Figure 1: (Color online) a) Temperature change in the SRO thin film after excitation at $t = 0$. b) Spatio-temporal strain profile due to optical excitation of the SRO film. The SRO/STO interface is at $z = 95 \text{ nm}$.

Using the result of the `phononNum` simulation as input for the dynamical XRD calculations (`XRDdyn`) we obtain the UXRD response of the ultrafast excitation of the SRO layer which is shown in Fig. 2 as a waterfall plot. Here, the SRO Bragg peak splits up due to the excited lattice

dynamics and does not continuously shift. Details for this example simulation and comparison to experimental data can be found in Ref. [15].

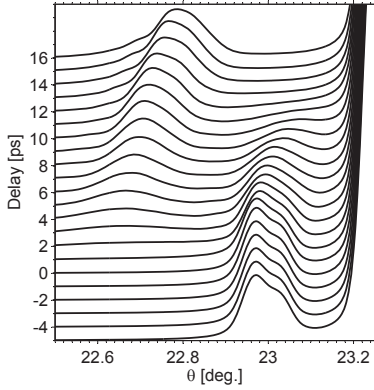


Figure 2: Waterfall plot of the SRO Bragg peak reflectivity for different delays after excitation of the thin film. The SRO peak splits up into two peaks instead of continuously shifting into its new position.

3.2. Superlattice Oscillations

In this example a superlattice (SL) structure is excited by an ultrashort laser pulse with a fluence of $F = 30 \text{ mJ/cm}^2$. The SL consists of 11 double layers (DL) each of which is composed of 20 unit cells of SRO and 38 unit cells of STO. The SL is grown on an STO substrate. The excitation is again modeled as instantaneous temperature jump at $t = 0$ neglecting thermal transport. The temperature profile after excitation is shown in Fig. 3 a). The comb-like temperature profile originates from the alternating metallic and dielectric layers in the SL and exhibits an exponential decay towards the substrate. Due to the excitation profile, a longitudinal optical SL phonon mode, also known as zone-folded longitudinal acoustic phonon (ZFLAP), is excited which results in the complex spatio-temporal strain pattern shown in Fig. 3 b). Here, the strain oscillation directly indicates the frequency of the optical phonon mode.

The SL structure also results in complex static XRD signatures as can be seen in Fig. 4. This static diffraction curve is calculated by the `XRDdyn` class which allows to access also the individual diffraction curves of the repeated substructures. The equidistant Bragg peaks originate from the SL structure and are numerated as SL_i . The most intense Bragg peak is the STO substrate reflection.

The transient X-Ray diffraction calculations using the coherent phonon result as input feature intensity oscillations of the SL Bragg peaks due to the excited longitudinal optical SL phonon. The integrated intensities of the SL_0 and SL_{+2} Bragg peaks are plotted as transients in Fig. 5. For the SL_{+2} peak a non-linear X-ray response is

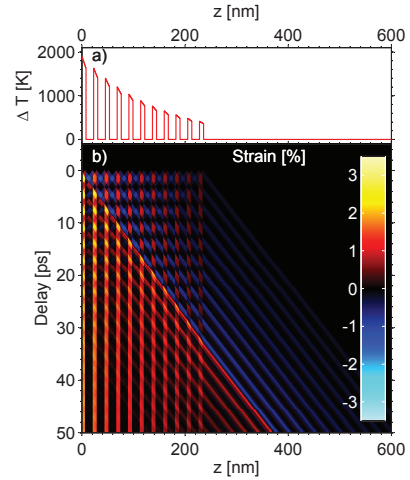


Figure 3: (Color online) a) Temperature change in the SL after excitation at $t = 0$. b) Spatio-temporal strain profile due to optical excitation of the SL film. The SL/Substrate interface is at $z = 235 \text{ nm}$.

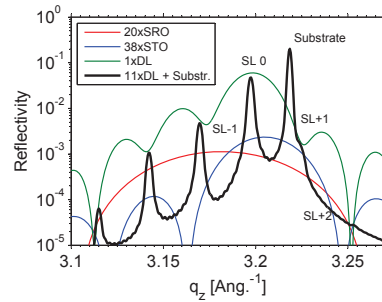


Figure 4: (Color online) The static diffraction curve of the sample structure is convoluted with a Pseudo-Voigt function in order to account for instrumental broadening. The Bragg peaks of the SL are numerated as SL_i . The colored lines represent the diffraction curves of the nested substructures in the sample.

observed. Details on this simulation and a comparison to UXR experiments are given in Ref. [16].

3.3. Quasi-Monochromatic Phonon Wave Packet

In the last example a thin 15 nm SRO layer on an STO substrate is excited by a pulse sequence of 8 ultrashort laser pulses with a pulse separation of 7.2 ps in order to generate a coherent quasi-monochromatic phonon wave packet in the substrate. The average temperature in the SRO layer is plotted in inset of Fig. 6, where the excitation is again modeled as instantaneous temperature jump without heat diffusion. The corresponding transient strain pattern is calculated by the `phononNum` class including damping in the STO substrate. The waterfall plot in Fig. 6 shows the subsequent generation of bi-polar strain pulses in the substrate after each laser excitation.

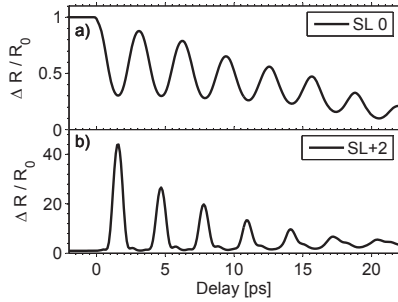


Figure 5: The integrated intensity modulation of the SL0 and SL+2 Bragg peak are plotted over the pump-probe delay. The X-ray response of the SL+2 shows even non-linear behavior.

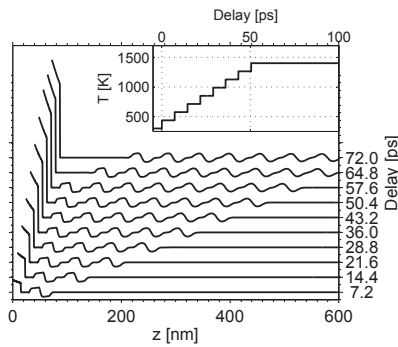


Figure 6: The strain profile for different pump-probe delays are plotted as waterfall diagram. For better visualization, the graphs are also shift along the x -axis. The amplitude of the thermal strain in the SRO layer has a maximum of approx. 1 % and the amplitude of the phonon wave packet is approx. 0.05 %. The inset shows the average temperature in the SRO layer due to the multipulse excitation of the sample.

From this strain pattern we can compute the according transient X-ray reflectivity using the `XRDdyn` class. Fig. 7 depicts the side bands of the STO substrate Bragg reflection for different pump-probe delays. The rise of the first-order side band at $q_z = 3.229 \text{ \AA}^{-1}$ and a second-order side band at $q_z = 3.240 \text{ \AA}^{-1}$ become stronger after each excitation of the sample. Details on this simulation and comparison to experimental data can be found in Ref. [17] and [18].

4. Conclusions

The UDKM1DSIM toolbox enables the user to easily build 1D crystalline structures on the atomic-level using a rich database of element-specific physical parameters. The excitation and thermal transport in such 1D structures is calculated within the frame of an N -temperature model. The results are then plugged into an analytical or numerical model for evaluating the dynamics of coherent longitudinal acoustic phonon in the structure. Kinematical and dynamical XRD theory are provided to further

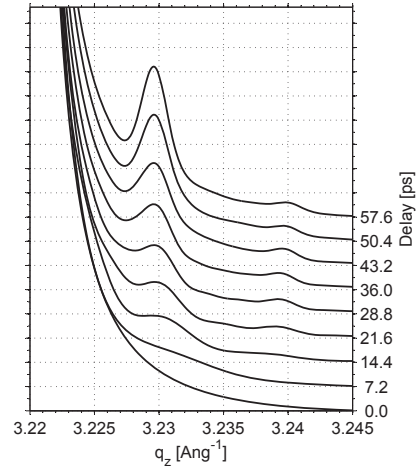


Figure 7: The side bands of the STO substrate Bragg peak are plotted for different pump-probe delays as waterfall diagram. The rise of the 1st order side band at $q_z = 3.229 \text{ \AA}^{-1}$ and even a second order at $q_z = 3.240 \text{ \AA}^{-1}$ of the excited phonon wave packet becomes stronger after each pump event.

calculate the static rocking curves of the structures for symmetrical Bragg reflections in coplanar diffraction geometry. The transient XRD response of the structures due to coherent phonon dynamics is evaluated exclusively by dynamical XRD theory.

The UDKM1DSIM toolbox is programmed fully object-orientated and highly modular in order to allow for user-defined inputs at any step of the simulation procedure. Hence the toolbox is not only applicable for the comparison of experimental UXRD data to the introduced theoretical models but also as an educational/theoretical test ground for students and researchers in the scientific field of ultrafast structural dynamics and ultrafast XRD.

- [1] C. Rose-Petruck, R. Jimenez, T. Guo, A. Cavalleri, C. W. Siders, F. Rksi, J. A. Squier, B. C. Walker, K. R. Wilson, C. P. J. Barty, Picosecond-milliångström lattice dynamics measured by ultrafast X-ray diffraction, *Nature* 398 (6725) (1999) 310–312. doi:10.1038/18631.
- [2] K. Sokolowski-Tinten, C. Blome, J. Blums, A. Cavalleri, C. Di- etrich, A. Tarasevitch, I. Uschmann, E. Förster, M. Kam- mler, M. Horn-von Hoegen, D. von der Linde, Femtosecond X-ray measurement of coherent lattice vibrations near the Lindemann stability limit., *Nature* 422 (6929) (2003) 287–9. doi:10.1038/nature01490.
- [3] M. Bargheer, N. Zhavoronkov, Y. Gritsai, J. C. Woo, D. S. Kim, M. Woerner, T. Elsaesser, Coherent atomic motions in a nanostructure studied by femtosecond X-ray diffraction., *Science* 306 (5702) (2004) 1771–3. doi:10.1126/science.1104739.
- [4] C. Korff Schmising, M. Bargheer, M. Kiel, N. Zhavoronkov, M. Woerner, T. Elsaesser, I. Vrejoiu, D. Hesse, M. Alexe, Cou- pled Ultrafast Lattice and Polarization Dynamics in Ferroelectric Nanolayers, *Physical Review Letters* 98 (25) (2007) 257601. doi:10.1103/PhysRevLett.98.257601.
- [5] I. A. Veres, T. Berer, P. Burgholzer, Numerical modeling of thermoelastic generation of ultrasound by laser irradiation in the coupled thermoelasticity., *Ultrasonics* 53 (1) (2013) 141–149. doi:10.1016/j.ultras.2012.05.001.
- [6] D. Y. Tzou, J. K. Chen, J. E. Beraun, Recent Development of

- Ultrafast Thermoelasticity, *Journal of Thermal Stresses* 28 (6-7) (2005) 563–594. doi:10.1080/01495730590929359.
- [7] S. Stepanov, E. Kondrashkina, R. Köhler, D. Novikov, G. Materlik, S. Durbin, Dynamical x-ray diffraction of multilayers and superlattices: Recursion matrix extension to grazing angles, *Physical Review B* 57 (8) (1998) 4829–4841. doi:10.1103/PhysRevB.57.4829.
- [8] J. Als-Nielsen, D. McMorrow, No Title, John Wiley & Sons, Ltd., New York, 2001. doi:10.1002/9781119998365.
- [9] S. I. Anisimov, B. Kapeliovich, T. Perel'man, Electron emission from metal surfaces exposed to ultrashort laser pulses, *Sov. Phys. JETP* 39 (2) (1975) 375–377.
- [10] M. Herzog, D. Schick, P. Gaal, R. Shayduk, C. von Korff Schmising, M. Bargheer, Analysis of ultrafast X-ray diffraction data in a linear-chain model of the lattice dynamics, *Applied Physics A* 106 (3) (2011) 489–499. doi:10.1007/s00339-011-6719-z.
- [11] A. Bojahr, M. Herzog, D. Schick, I. Vrejoiu, M. Bargheer, Calibrated real-time detection of nonlinearly propagating strain waves, *Physical Review B* 86 (14) (2012) 144306. doi:10.1103/PhysRevB.86.144306.
- [12] B. E. Warren, X-ray diffraction, 2nd Edition, Dover Publications, New York, 1990.
- [13] B. Henke, E. Gullikson, J. Davis, X-Ray Interactions: Photoabsorption, Scattering, Transmission, and Reflection at $E = 50\text{--}30,000$ eV, $Z = 1\text{--}92$, *Atomic Data and Nuclear Data Tables* 54 (2) (1993) 181–342. doi:10.1006/adnd.1993.1013.
- [14] D. T. Cromer, J. B. Mann, X-ray scattering factors computed from numerical HartreeFock wave functions, *Acta Crystallographica Section A* 24 (2) (1968) 321–324. doi:10.1107/S0567739468000550.
- [15] D. Schick, P. Gaal, A. Bojahr, W. Leitenberger, R. Shayduk, A. Hertwig, I. Vrejoiu, M. Herzog, M. Bargheer, Ultrafast x-ray diffraction studies of photoexcited coherent phonons in SrRuO₃ thin films, *arXiv:1301.3324*.
- [16] M. Herzog, D. Schick, W. Leitenberger, R. Shayduk, R. M. van der Veen, C. J. Milne, S. L. Johnson, I. Vrejoiu, M. Bargheer, Tailoring interference and nonlinear manipulation of femtosecond x-rays, *New Journal of Physics* 14 (1) (2012) 13004. doi:10.1088/1367-2630/14/1/013004.
- [17] M. Herzog, A. Bojahr, J. Goldshteyn, W. Leitenberger, I. Vrejoiu, D. Khakhulin, M. Wulff, R. Shayduk, P. Gaal, M. Bargheer, Detecting optically synthesized quasimonochromatic sub-terahertz phonon wavepackets by ultrafast x-ray diffraction, *Applied Physics Letters* 100 (9) (2012) 94101. doi:10.1063/1.3688492.
- [18] A. Bojahr, M. Herzog, S. Mitzscherling, L. Maerten, D. Schick, J. Goldshteyn, W. Leitenberger, R. Shayduk, P. Gaal, M. Bargheer, Brillouin scattering of visible and hard X-ray photons from optically synthesized phonon wavepackets, *Opt. Express* 21 (18) (2013) 21188–21197. doi:10.1364/OE.21.021188.

Brillouin scattering of visible and hard X-ray photons from optically synthesized phonon wavepackets

A. Bojahr, M. Herzog, S. Mitzscherling, L. Mearten,
D. Schick, J. Goldshteyn, W. Leitenberger, R. Shayduk ,
P. Gaal and M. Bargheer.

Opt. Express **21**, 18 (2013).

Brillouin scattering of visible and hard X-ray photons from optically synthesized phonon wavepackets

A. Bojahr,¹ M. Herzog,¹ S. Mitzscherling,¹ L. Maerten,¹ D. Schick,¹ J. Goldshteyn,² W. Leitenberger,¹ R. Shayduk,² P. Gaal,² and M. Bargheer^{1,2,*}

¹Institut für Physik & Astronomie, Universität Potsdam, Karl-Liebknecht-Str. 24-25, 14476 Potsdam, Germany

²Helmholtz Zentrum Berlin, Albert-Einstein-Str. 15, 12489 Berlin, Germany

*bargheer@uni-potsdam.de

<http://www.udkn.physik.uni-potsdam.de>

Abstract: We monitor how destructive interference of undesired phonon frequency components shapes a quasi-monochromatic hypersound wavepacket spectrum during its local real-time preparation by a nanometric transducer and follow the subsequent decay by nonlinear coupling. We prove each frequency component of an optical supercontinuum probe to be sensitive to one particular phonon wavevector in bulk material and cross-check this by ultrafast x-ray diffraction experiments with direct access to the lattice dynamics. Establishing reliable experimental techniques with direct access to the transient spectrum of the excitation is crucial for the interpretation in strongly nonlinear regimes, such as soliton formation.

© 2013 Optical Society of America

OCIS codes: (290.5900) Scattering, stimulated Brillouin; (320.5390) Picosecond phenomena

References and links

1. H. J. Eichler, P. Günter, and D. W. Pohl, *Laser induced dynamic gratings*, vol. 50 of *Springer series in optical sciences* (Springer, Berlin [u.a.], 1986).
2. R. Vacher and L. Boyer, "Brillouin scattering: A tool for the measurement of elastic and photoelastic constants," *Phys. Rev. B* **6**, 639–673 (1972).
3. J. A. Rogers, A. A. Maznev, M. J. Banet, and K. A. Nelson, "Optical generation and characterization of acoustic waves in thin films: Fundamentals and applications," *Annual Review of Materials Science* **30**, 117–157 (2000).
4. V. Wang and C. R. Giuliano, "Correction of phase aberrations via stimulated Brillouin scattering," *Opt. Lett.* **2**, 4–6 (1978).
5. R. Y. Chiao, C. H. Townes, and B. P. Stoicheff, "Stimulated Brillouin scattering and coherent generation of intense hypersonic waves," *Phys. Rev. Lett.* 592–595 (1964).
6. K. A. Nelson, R. Casalegno, R. J. D. Miller, and M. D. Fayer, "Laser-induced excited state and ultrasonic wave gratings: Amplitude and phase grating contributions to diffraction," *J. Chem. Phys.* **77**, 1144–1152 (1982).
7. C. Thomsen, H. T. Grahn, H. J. Maris, and J. Tauc, "Surface generation and detection of phonons by picosecond light pulses," *Phys. Rev. B* **34**, 4129–4138 (1986).
8. H. N. Lin, R. J. Stoner, H. J. Maris, and J. Tauc, "Phonon attenuation and velocity measurements in transparent materials by picosecond acoustic interferometry," *J. Appl. Phys.* **69**, 3816–3822 (1991).
9. P. J. S. van Capel and J. I. Dijkhuis, "Optical generation and detection of shock waves in sapphire at room temperature," *Appl. Phys. Lett.* **88**, 151910 (2006).
10. P. J. S. van Capel, H. P. Porte, G. van der Star, and J. I. Dijkhuis, "Interferometric detection of acoustic shock waves," *J. Phys.: Conf. Ser.* **92**, 012092 (2007).

#190683 - \$15.00 USD Received 16 May 2013; revised 13 Jul 2013; accepted 16 Jul 2013; published 3 Sep 2013
(C) 2013 OSA 9 September 2013 | Vol. 21, No. 18 | DOI:10.1364/OE.21.021188 | OPTICS EXPRESS 21188

11. O. L. Muskens and J. I. Dijkhuis, "High amplitude, ultrashort, longitudinal strain solitons in sapphire," *Phys. Rev. Lett.* **89**, 285504 (2002).
12. P. J. S. van Capel and J. I. Dijkhuis, "Time-resolved interferometric detection of ultrashort strain solitons in sapphire," *Phys. Rev. B* **81**, 144106 (2010).
13. A. Bojahr, M. Herzog, D. Schick, I. Vrejoiu, and M. Bargheer, "Calibrated real-time detection of nonlinearly propagating strain waves," *Phys. Rev. B* **86**, 144306 (2012).
14. T. Pezeril, C. Klieber, S. Andrieu, and K. A. Nelson, "Optical generation of gigahertz-frequency shear acoustic waves in liquid glycerol," *Phys. Rev. Lett.* **102**, 107402 (2009).
15. M. Herzog, A. Bojahr, J. Goldshteyn, W. Leitenberger, I. Vrejoiu, D. Khakhulin, M. Wulff, R. Shayduk, P. Gaal, and M. Bargheer, "Detecting optically synthesized quasi-monochromatic sub-terahertz phonon wavepackets by ultrafast x-ray diffraction," *Appl. Phys. Lett.* **100**, 094101 (2012).
16. S. Brivio, D. Polli, A. Crespi, R. Osellame, G. Cerullo, and R. Bertacco, "Observation of anomalous acoustic phonon dispersion in SrTiO₃ by broadband stimulated Brillouin scattering," *Appl. Phys. Lett.* **98**, 211907 (2011).
17. E. Pontecorvo, M. Ortolani, D. Polli, M. Ferretti, G. Ruocco, G. Cerullo, and T. Scopigno, "Visualizing coherent phonon propagation in the 100 GHz range: A broadband picosecond acoustics approach," *Appl. Phys. Lett.* **98**, 011901 (2011).
18. W. E. Bron, "Spectroscopy of high-frequency phonons," *Reports on Progress in Physics* **43**, 301 (1980).
19. Z. Chen, B. C. Minch, and M. F. DeCamp, "High wavevector optical phonons in microstructured bismuth films," *Opt. Express* **18**, 4365–4370 (2010).
20. G.-W. Chern, K.-H. Lin, Y.-K. Huang, and C.-K. Sun, "Spectral analysis of high-harmonic coherent acoustic phonons in piezoelectric semiconductor multiple quantum wells," *Phys. Rev. B* **67**, 121303 (2003).
21. N. M. Stanton, R. N. Kini, A. J. Kent, M. Henini, and D. Lehmann, "Terahertz phonon optics in GaAs/AlAs superlattice structures," *Phys. Rev. B* **68**, 113302 (2003).
22. M. F. Pascual-Winter, A. Fainstein, B. Jusserand, B. Perrin, and A. Lemaître, "Spectral responses of phonon optical generation and detection in superlattices," *Phys. Rev. B* **85**, 235443 (2012).
23. T. C. Zhu, H. J. Maris, and J. Tauc, "Attenuation of longitudinal-acoustic phonons in amorphous SiO at frequencies up to 440 GHz," *Phys. Rev. B* **44**, 4281–4289 (1991).
24. C. Klieber, E. Peronne, K. Katayama, J. Choi, M. Yamaguchi, T. Pezeril, and K. A. Nelson, "Narrow-band acoustic attenuation measurements in vitreous silica at frequencies between 20 and 400 GHz," *Appl. Phys. Lett.* **98**, 211908 (2011).
25. S. Ayrynhac, M. Foret, A. Devos, B. Rufflé, E. Courtens, and R. Vacher, "Subterahertz hypersound attenuation in silica glass studied via picosecond acoustics," *Phys. Rev. B* **83**, 014204 (2011).
26. E. Burkel, "Phonon spectroscopy by inelastic x-ray scattering," *Rep. Prog. Phys.* **63**, 171 (2000).
27. P. Eisenberger, N. G. Alexandropoulos, and P. M. Platzman, "X-ray Brillouin scattering," *Phys. Rev. Lett.* **28**, 1519–1522 (1972).
28. A. M. Lindenberg, I. Kang, S. L. Johnson, T. Missalla, P. A. Heimann, Z. Chang, J. Larsson, P. H. Bucksbaum, H. C. Kapteyn, H. A. Padmore, R. W. Lee, J. S. Wark, and R. W. Falcone, "Time-resolved x-ray diffraction from coherent phonons during a laser-induced phase transition," *Phys. Rev. Lett.* **84**, 111–114 (2000).
29. D. A. Reis, M. F. DeCamp, P. H. Bucksbaum, R. Clarke, E. Dufresne, M. Hertlein, R. Merlin, R. Falcone, H. Kapteyn, M. M. Murnane, J. Larsson, T. Missalla, and J. S. Wark, "Probing impulsive strain propagation with x-ray pulses," *Phys. Rev. Lett.* **86**, 3072–3075 (2001).
30. K. Sokolowski-Tinten, C. Blome, C. Dietrich, A. Tarasevitch, M. Horn von Hoegen, D. von der Linde, A. Cavalieri, J. Squier, and M. Kammler, "Femtosecond x-ray measurement of ultrafast melting and large acoustic transients," *Phys. Rev. Lett.* **87**, 225701 (2001).
31. M. Bargheer, N. Zhavoronkov, Y. Gritsai, J. C. Woo, D. S. Kim, M. Woerner, and T. Elsaesser, "Coherent atomic motions in a nanostructure studied by femtosecond x-ray diffraction," *Science* **306**, 1771–1773 (2004).
32. M. Trigo, Y. M. Sheu, D. A. Arms, J. Chen, S. Ghimire, R. S. Goldman, E. Landahl, R. Merlin, E. Peterson, M. Reason, and D. A. Reis, "Probing unfolded acoustic phonons with x rays," *Phys. Rev. Lett.* **101**, 025505 (2008).
33. M. Herzog, D. Schick, P. Gaal, R. Shayduk, C. von Korff Schmising, and M. Bargheer, "Analysis of ultrafast x-ray diffraction data in a linear-chain model of the lattice dynamics," *Appl. Phys. A* **106**, 489–499 (2012).
34. A. Bojahr, D. Schick, L. Maerten, M. Herzog, I. Vrejoiu, C. von Korff Schmising, C. J. Milne, S. L. Johnson, and M. Bargheer, "Comparing the oscillation phase in optical pump-probe spectra to ultrafast x-ray diffraction in the metal-dielectric SrRuO₃/SrTiO₃ superlattice," *Phys. Rev. B* **85**, 224302 (2012).
35. H. J. Maris, "6 - interaction of sound waves with thermal phonons in dielectric crystals," in "Principles and Methods," vol. 8 of *Physical Acoustics*, W. P. Mason and R. N. Thurston, eds. (Academic Press, 1971), pp. 279–345.
36. A. Akhieser, "On the absorption of sound in solids," *J. Phys. (USSR)* **1**, 277 (1939).
37. C. Herring, "Role of low-energy phonons in thermal conduction," *Phys. Rev.* **95**, 954–965 (1954).
38. A. Koreeda, T. Nagano, S. Ohno, and S. Saikan, "Quasielastic light scattering in Rutile, ZnSe, Silicon, and SrTiO₃," *Phys. Rev. B* **73**, 024303 (2006).
39. B. C. Daly, K. Kang, Y. Wang, and D. G. Cahill, "Picosecond ultrasonic measurements of attenuation of longitu-

- dinal acoustic phonons in Silicon," Phys. Rev. B **80**, 174112 (2009).
40. M. Cardona, "Optical properties and band structure of SrTiO₃ and BaTiO₃," Phys. Rev. **140**, A651–A655 (1965).
41. V. Mahajan and J. Gaskill, "Doppler interpretation of the frequency shifts of light diffracted by sound waves," J. Appl. Phys. **45**, 2799 (1976).
42. O. L. Muskens and J. I. Dijkhuis, "Inelastic light scattering by trains of ultrashort acoustic solitons in sapphire," Phys. Rev. B **70**, 104301 (2004).

1. Introduction

Brillouin scattering describes the inelastic interaction of photons with acoustic phonons, which can be excited or detected by this process. [1] It has important applications in the determination of elastic and photoelastic properties [2, 3] and is used for optical amplifiers or phase conjugation [4]. Stimulated Brillouin scattering can create intense hypersound waves [5], where the wavevector \vec{Q} can be selected by tuning the transient grating induced by two intersecting laser-pulses. The diffraction of a probe pulse then senses the presence of phonons with the imprinted phonon wavevector \vec{Q} [6]. Ultrashort laser pulse excitation of strongly absorbing materials or transducers on transparent substrates generates even larger phonon amplitudes up to 1% strain and can be detected by picosecond acoustics, the time-domain analog of Brillouin scattering [7, 8]. This proved advantageous for investigating anharmonic propagation and damping of phonons and has generated excitement about ultrashort acoustic solitons [9–13]. Similar to transient gratings, optical multipulse excitation enhances a certain wavelength in the hypersound wave [14, 15]. Recently optical broadband probe pulses were used to access many phonon wavevectors simultaneously in picosecond acoustics experiments. [13, 16, 17]

Visible light only interacts with bulk phonons near the Brillouin-zone center, unless impurities are used to enhance the spectroscopy [18]. Optical phonons with high wavevectors in Bismuth have been accessed by microstructuring the film under investigation [19]. The backfolding of the phonon dispersion relation in superlattices can convert acoustic phonons with large wavevector into quasi-optical phonons with detectably small wavevector [20–22]. Alternatively, the acoustic reflection from the backside of the sample or from an interface propagating back to the transducer yields reflectivity modulations of the transducer which can be detected by a probe pulse [23]. The pulse-echo technique was refined by introducing additional thin detector films and combined with acoustic pulse shaping [24] and was extended to the detection of shear waves in glycerol [14]. The Fourier-transform of real-time signals due to pulse-echoes at the transducer or from Brillouin scattering in the bulk yields the spectrum of acoustic phonons. The analysis of the reflection coefficient of such acoustic perturbations was recently discussed in detail [25].

In order to observe high phonon wavevectors in a bulk material directly, shorter probe wavelengths are needed. The phonon dispersion for larger wavevectors is measured by inelastic X-ray scattering, which is essentially Brillouin scattering of X-rays [26, 27]. The new millennium came along with the rapidly developing scientific field of ultrafast X-ray diffraction (UXRD), which allows direct measurement of the lattice oscillation amplitude associated with propagating strain pulses. [28–32] Very recently optically synthesized quasi-monochromatic phonon wavepackets in the 100 GHz range were clearly detected by UXRD as sidebands to bulk Bragg reflections [15].

In this paper we present a unifying view on UXRD and optical picosecond acoustics as two types of Brillouin scattering. The presence of monochromatic phonons in bulk SrTiO₃ is directly evidenced by the scattering of photons. The conceptually simple analysis provides a real-time perspective on the spectral shaping of high-frequency phonon wavepackets by tailored multipulse excitation. In particular, we demonstrate how the optical supercontinuum probe accomplishes a versatile simultaneous broadband sensing of *bulk* phonon wavevectors constituting a large amplitude phonon wavepacket that decays by anharmonic interactions. We

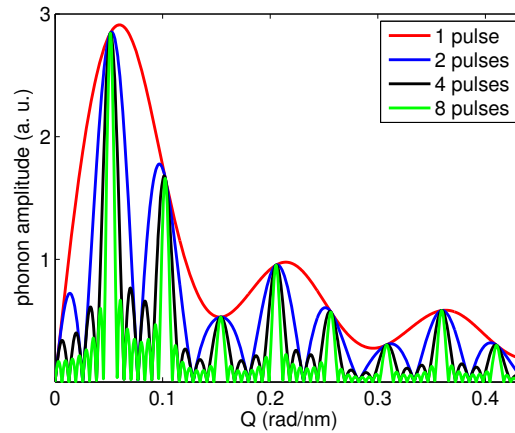


Fig. 1. **Calculated phonon spectra.** Spectral phonon amplitude present in the STO substrate after excitation of a 35 nm LSMO transducer by 1, 2, 4 and 8 pulses with a pulse spacing of $\Delta T = 15.4$ ps. All pulse sequences have the same integrated pulse energy.

believe that this combination of ultrafast X-ray- and optical broadband-detection of phonons will significantly enhance the confidence regarding interpretations of future optical picosecond ultrasound experiments. The supercontinuum detection scheme is also applicable to other quasiparticles such as magnons or polaritons which are generally identified by their dispersion relation $\omega(k)$. The wave-particle duality requires such wave-packet description, in which only a coherent excitation of a broad wavevector-spectrum allows for localization of quasiparticles. Real-time preparation and detection of such wavepackets will aid the understanding and controlling such excitations.

2. Synthesizing quasi-monochromatic phonons

We first discuss how to synthesize coherent quasi-monochromatic phonon wavepackets in the GHz - THz range, using a thin metal transducer of SrRuO₃ (SRO) or La_{0.7}Sr_{0.3}MnO₃ (LSMO) on the material of interest SrTiO₃ (STO). The absorption of an ultrashort light pulse leads to rapid expansion of the metal film. The good acoustic impedance matching of the SRO/LSMO transducer and the STO substrate suppresses reflections at the interface. [13, 33] Consequently, clean bipolar strain pulses without unintended replica are sent into the substrate. [7] The spatio-temporal dynamics can be simulated by a linear-chain model which includes the anharmonicity in the interatomic potentials [13, 33]. In the present simulations we neglected the anharmonic terms according to the moderate excitation fluence. Due to the very fast electron phonon coupling of SRO and LSMO the optically excited electrons are rapidly localized and consequently the spatial profile of the exciting stress corresponds to the absorption of light according to Lambert-Beer's law [34]. A single ultrashort laser pulse generates a broad phonon spectrum in the substrate. The red line in Fig. 1 shows the Fourier-transformed spatial strain pattern of the substrate only. If the heated transducer layer with thickness d is added to the analysis, a strong Fourier-component at $k = 0$ emerges because of the thermally expanded absorbing region. If the pump penetration depth $d_{abs} \gg d$ the calculated excited strain pattern of the substrate yields a bipolar strain pulse with a frequency spectrum centered around $Q = 0.74 \cdot \pi v_t / v_s d$ whereas for $d_{abs} \ll d$ the exponential shaped profile of the induced strain pulse have a spectral maximum at

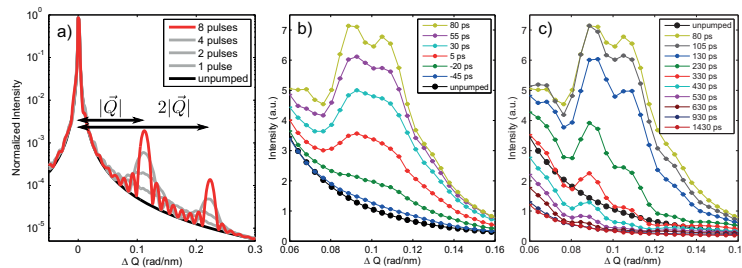


Fig. 2. **Birth and decay of phonon-wavepackets observed by UXR.** (a) Calculated X-ray diffraction pattern for an STO substrate with a coherent phonon spectrum excited by 1 to 8 pulses. (b) UXR data demonstrating the successive sharpening of the diffraction pattern with 8 excitation pulses separated by 7.2 ps. (c) Same UXR data for larger delay time t showing the decay of the coherent phonons.

$Q = v_t/v_s d_{abs}$. Here d , v_t and v_s are the thickness of the transducer film and the sound velocities of transducer and substrate in [001] direction, respectively. Our conditions are well described by the first limit value because $d_{abs} > d$. For longer excitation pulses, the phonon spectrum is suppressed for wavevectors Q corresponding to phonon frequencies $\omega > 2\pi/\tau_{pulse}$ where τ_{pulse} is the temporal duration of the pump pulse.

Successive excitation of the metal transducer with a sequence of light pulses equally spaced by ΔT in time generates a strain wave traveling into the substrate with a fundamental frequency $\nu = 1/\Delta T$ and contributions of its higher harmonics due to the sharp edges of the strain pulses. As an example we simulate the phonon spectra for a transducer thickness $d = 35$ nm and a pulse spacing of $\Delta T = 15.4$ ps. Figure 1 shows how additional pulses in the pump sequence sharpen the spectrum around $Q = 2\pi/\Delta T v_s$ and its higher harmonics by canceling the amplitude of other wavevectors. Note, that in Fig. 1 the integral pump energy is kept fixed in the simulation. As a consequence, the different pulse trains induce a constant phonon amplitude for the constructive interference, whereas the suppressed modes interfere destructively. Hence, for multipulse excitation, less energy is deposited in coherent phonons, compared to single pulse excitation with the same integral fluence. [33]

3. Inelastic light scattering from directed phonons

The energy quantum $\hbar\omega_s$ of such a strain wave is the longitudinal acoustic phonon with a magnitude of the wavevector $|\vec{Q}| = \omega_s/v_s$. Photons with wavevector \vec{k} are scattered by phonons with wavevector \vec{Q} only in accordance with the energy and momentum conservation. In a crystal with reciprocal lattice vectors \vec{G} , the equation for momentum conservation with \vec{k}' as the wavevector of the scattered photon reads

$$\Delta\vec{k} = \vec{k}' - \vec{k} = \vec{G} + \Delta\vec{Q}. \quad (1)$$

Here we discuss the situation where $\Delta\vec{Q} = \pm\vec{Q}$ is the momentum added to the scattering photon by the creation or annihilation of the particular phonon with wavevector \vec{Q} which was synthesized into the crystal. It is important to see that generating phonons with an optical transducer thin film breaks the symmetry, and only phonons with wavevector \vec{Q} directed into the crystal are generated. Figure 3(a) schematically shows how the creation of an additional phonon with wavevector \vec{Q} leads to a scattering with momentum transfer $\vec{G} + \vec{Q}$. In the geometry depicted in Fig. 3(a), i.e. for a phonon propagating into the crystal, the energy conservation imposes a constraint on the angular frequencies ω' of the scattered and ω of the incident photons:

$$\omega' - \omega = \begin{cases} \omega_s, & \text{if } \Delta\vec{Q} = +\vec{Q}; \text{phonon annihilation} \\ -\omega_s, & \text{if } \Delta\vec{Q} = -\vec{Q}; \text{phonon creation} \end{cases}, \quad (2)$$

because the stimulated emission of a phonon with wavevector \vec{Q} directed into the substrate acquires its energy from the scattering photon, whereas the annihilation of a phonon with the same \vec{Q} adds energy to the scattering photon and corresponds to a positive wavevector transfer $\Delta\vec{Q} = +\vec{Q}$.

These equations describe an inelastic scattering process which generally leads to an asymmetric scattering geometry, where the incoming and outgoing photon do not have the same angle with respect to the surface. However, the vast difference of the light and sound velocities implies a very small length change of the scattered photon wavevector with respect to the incident one. This quasi-elastic condition leads to a nearly symmetric scattering geometry with $\Delta\vec{k} = \vec{G} \pm \vec{Q}$.

4. Brillouin scattering of X-rays

We first discuss Brillouin scattering in the hard X-ray range [27]. The simulation of the UXRD signal is shown in Fig. 2(a) for the excitation with an increasing number of pump-pulses. All strain pulses have fully entered the substrate and in contrast to Fig. 1 the deposited fluence rises with each absorbed pulse. Figure 2(a) directly shows how the diffraction feature at $\vec{G} + \vec{Q}$ sharpens as more and more bipolar strain pulses are sculptured into the crystal. We performed the corresponding UXRD experiment at the ID09B beamline at the synchrotron source ESRF which provides ~ 100 ps hard X-ray pulses. The SRO transducer film was excited with eight pulses spaced by $\Delta T = 7.2$ ps, consistent with the calculation of Fig. 2(a). Details of the setup were discussed previously [15]. Here, we show an angular resolved analysis of the data recorded with 100 ps time resolution. The spectral narrowing of the feature around $\vec{G} + \vec{Q}$, is qualitatively confirmed in the experiment. When the synthesis of the quasi-monochromatic phonon wavepacket (Fig. 2(b)) was stopped after eight pulses, we observed that this sideband decayed (c.f. Fig. 2(c)) within 130 ps. This is not much longer than it took to create the wavepacket. The corresponding phonon decay is due to anharmonic phonon-phonon scattering processes within the STO substrate [35–39]. Up to now we have shown that the interference of sound waves (phonons) in the crystal created by multiple pulses in fact leads to the predicted quasi-monochromatic phonon wavepacket. UXRD directly measures the shaping of the quasi-monochromatic phonon spectrum in real time. Moreover, we showed that this wavepacket decays on a 100 ps timescale.

5. Brillouin scattering and picosecond acoustics

Now we turn to Brillouin scattering of optical photons from similar phonon wavepackets. In a classical interpretation of Brillouin scattering, the incident electromagnetic wave with wavelength $\lambda_m = \lambda/n(\lambda)$ in the material is diffracted from the Bragg grating given by the strain-induced refractive index modulation according to the photoelastic effect. Here λ and $n(\lambda)$ are the wavelength of the incident electromagnetic wave in vacuum and the wavelength dependent refractive index of the material, respectively. For visible light STO has a refractive index of $n \approx 2.4$. [40] The scattering angle is given by Bragg's law [1]

$$\lambda_m = 2\lambda_s \cdot \sin \theta, \quad (3)$$

implying that for a given scattering angle θ an optical photon with wavelength $\lambda_m = 2\pi n/|\vec{k}|$ is diffracted from a refractive index grating induced by phonons with wavelength $\lambda_s = 2\pi/|\vec{Q}|$ as schematically shown in Fig. 3(b). For a phonon propagating perpendicular to the sample

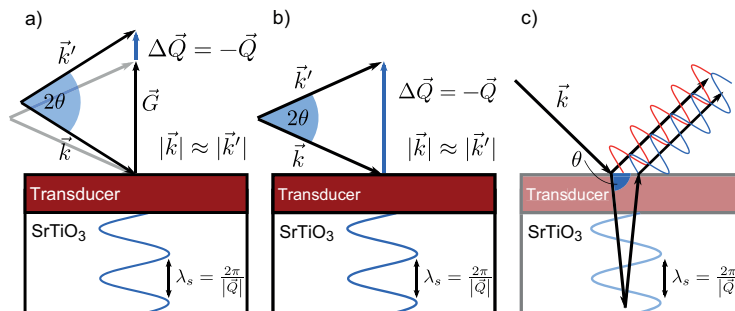


Fig. 3. **Schematics of Brillouin scattering and picosecond acoustics.** (a) Schematic of the inelastic X-ray scattering with creation of a phonon with wavevector $+\vec{Q}$. (b) Schematic of the Brillouin scattering with creation of a phonon with wavevector $+\vec{Q}$. (c) Schematic showing the interference of waves which is used for a time-domain explanation of the observed oscillations (see text).

surface the scattering angle θ is equal to the angle between the incident photon wavevector in the sample and the sample surface. This angle can be easily calculated by Snell's law. Given a strain wave propagating into the crystal, the scattered light undergoes a tiny Doppler-red-shift corresponding to the frequency of the moving sound wave, which can be detected by high-resolution Brillouin scattering experiments. [41,42]

Eq. (3) is a direct result of the *optical* Laue-condition $\vec{k}' - \vec{k} = \pm\vec{Q}$, (Fig. 3(b)) under quasi-elastic scattering conditions ($|\vec{k}'| \approx |\vec{k}|$), and is in fact Eq. (1) describing Brillouin scattering with $\vec{G} = 0$. For a fixed angle θ Eq. (3) implies that an optical photon with wavelength λ specifically scatters from phonons with the wavevector magnitude

$$Q(\lambda) = \frac{4\pi}{\lambda} n(\lambda) \cdot \sin \theta. \quad (4)$$

For $n(\lambda) = 1$ Eq. (4) defines the well known scattering vector in elastic X-ray scattering theory.

Up to now we have adopted a perspective which is suitable for conventional Brillouin scattering experiments detecting the frequency shift of a narrow-band-laser. In optical picosecond acoustics experiments a laser pulse excites a short bipolar strain pulse with a broad spectrum (Fig. 1, red line). The detection by a time-delayed laser pulse is explained as follows: A part of the supercontinuum probe pulse is diffracted by the refractive index modulation associated with the propagating sound pulse fulfilling Eq. (4) and interferes with the reflection of the probe pulse at the sample surface (Fig. 3(c)). The moving sound pulse leads to a phase change of the diffracted wave which depends on the pump-probe delay t . The resulting intensity of the interfering electric fields is proportional to $\cos(\omega_s t) = \cos(2\pi t/T_s)$ with the period

$$T_s = \frac{\lambda}{2v_s n(\lambda) \sin \theta}. \quad (5)$$

For normal incidence T_s corresponds to the time a soundwave with wavevector \vec{Q} perpendicular to the surface needs to propagate one half of the optical wavelength λ_m . Combining Eqs. (4) and (5) leads to $v_s \cdot Q = 2\pi/T_s = \omega_s$. Hence ω_s is the angular frequency of the phonon with the wavevector \vec{Q} . Such oscillations are in fact observed in all-optical reflectivity experiments [13,16] using a single optical pump pulse and an ultrashort broadband probe pulse. Figure 4(a) shows the recorded reflectivity change for the LSMO transducer on STO after subtraction of

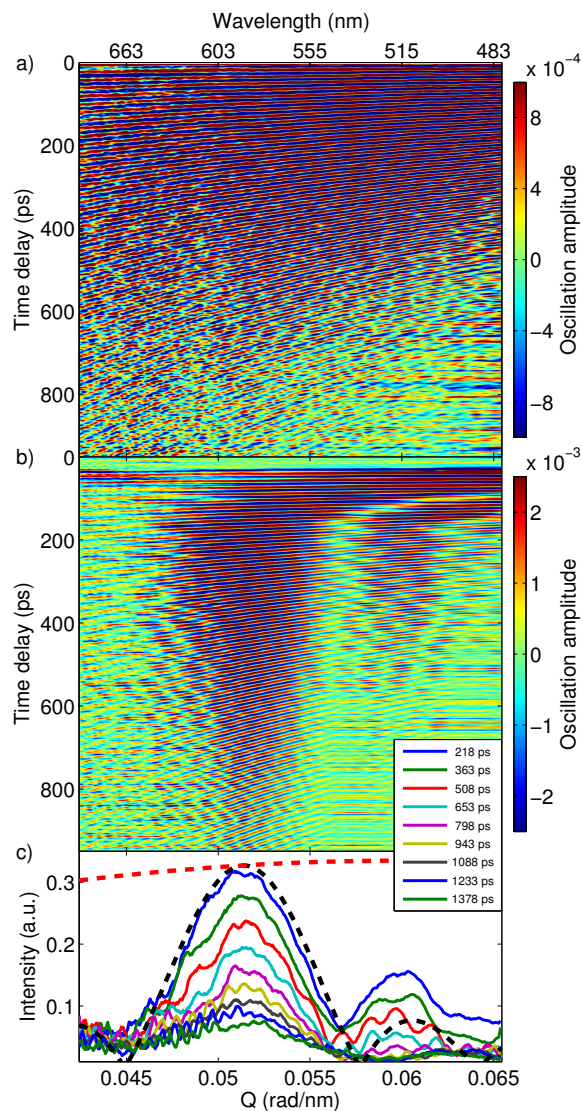


Fig. 4. **Experimental proof for the wavevector selectivity of supercontinuum probe pulses.** (a) Measured transient relative reflectivity change for single-pulse excitation as a function of the phonon wavevector given by Eq. (4). Slowly varying background is subtracted. (b) Same for an excitation with 8 pulses. (c) The dashed lines show the calculated spectral amplitude of the excited phonons for 1 (red dashed) and 8 (black dashed) excitations pulses (reproduced from Fig. 1). The solid lines show short-time Fourier transform data of Fig. 4(b). Each of the extracted datasets was multiplied with the probe wavelength to obtain a quantity proportional to the spectral amplitude of the coherent phonons.

a slowly varying electronic and thermal contribution to the signal. The observed oscillation period depends on the probe wavelength as predicted by Eq. (5) and extends across the entire visible spectrum according to the broad spectrum of the excited coherent phonons calculated to obtain the red line in Fig. 1. Here, Eq. (4) is applied to translate the optical probe wavelength λ into the phonon wavevector \vec{Q} .

6. Selectivity of the supercontinuum probe

Finally, we show that Brillouin scattering with broadband optical probe pulses not only has a mathematical one-to-one correspondence between the optical probe wavelength and a specific phonon with wavevector \vec{Q} (Eq. (4)) but that in fact individual wavevector components can be experimentally discriminated. Similar to the X-ray experiments shown in Fig. 2, we synthesized a monochromatic phonon via excitation of an LSMO transducer by a train of eight optical pump pulses ($\lambda = 800$ nm) with the pulse duration $\tau_{pulse} \sim 100$ fs and separation $\Delta T = 15.4$ ps. Figure 4(b) shows the relative reflectivity change of the sample. After $t \approx 150$ ps oscillations are mainly visible in the vicinity of $|\vec{Q}| = 0.05$ rad/nm. The black dashed line in Fig. 4(c), reproduced from Fig. 1, shows the idealized simulation of the coherent phonon spectrum in the substrate after 150 ps when all bipolar strain pulses have entered the substrate. The excellent agreement of the measured suppression of the reflectivity oscillations in certain wavelength regions of Fig. 4(b) with the simulated destructive interference in the phonon spectrum confirms both the wavevector-selective probing process and the shaping of quasi-monochromatic phonon wavepackets by tailored destructive interference. To support this argument we have extracted the spectral amplitude of oscillations observed in Fig. 4(b) by short-time Fourier-transform and multiplied the spectra by the wavelength of the probe light to get a quantity which is in first approximation proportional to the spectral amplitude of the occupied phonons. [7] The results plotted in Fig. 4(c) show good quantitative agreement of the measured spectra with the predicted spectrum (black dashed line). In particular, the measured spectral width of the main spectral component of the wavepacket exactly matches the prediction, demonstrating the simultaneous spatial and temporal resolution of the supercontinuum pump-probe setup. The higher amplitude of the secondary maximum is due to slight imperfections in the experimental optical pump pulse train, which leads to an imperfect destructive interference of phonon modes. Furthermore, Figure 4(c) directly measures the damping of the phonon amplitude in time. This is analogous to the measured phonon attenuation using UXRD (Fig. 2(c)). In particular, both experiments show that high-frequency components of the wavepackets undergo stronger damping.

Scattering experiments using synthesized monochromatic phonon wavepackets thus show directly that both UXRD and picosecond ultrasonics are wavevector-selective probes of ultrafast phonon dynamics, which are both described by Eq. (1). The difference of the two methods is that in the X-ray range we have selected the detected phonon wavevector \vec{Q} by tuning the Bragg angle, keeping the light wavelength fixed, whereas for the optical experiment we kept the angle of incidence fixed and measured a broad frequency range using a spectrometer. In principle, the experiments could also be carried out vice versa. More importantly, the absorption of the probe pulses is different. STO has essentially no optical absorption, while the penetration depth for hard X-rays is not larger than $10\mu\text{m}$. Generally, for very short sound wavelengths hard X-rays are definitely the only suitable choice, since the required VUV and XUV photons undergo very strong absorption.

7. Conclusions

In conclusion, we have given a unifying interpretation of ultrafast versions of Brillouin scattering in the ranges of optical and X-ray photon energies. We have synthesized large-amplitude quasi-monochromatic phonon wavepackets and proved that their spectrum and their anhar-

monic decay can be directly observed in both types of experiments. In particular, we showed that the optical supercontinuum is a direct, simultaneous and nonetheless selective real-time probe of the spectra composing a phonon wavepacket in bulk material. We confirmed this interpretation by comparison to UXRd experiments for which the direct access to the spectrum of the lattice strain is obvious. We think that this experimental confirmation will be essential for the interpretation of future experiments where wavevector-selective excitation and probing will be used to measure anharmonic and nonlinear phonon interactions in condensed matter. In particular, we envision experiments on nonlinear phononics as an analog of nonlinear optics, in which we observe sum and difference frequency mixing of synthesized phonons.

Acknowledgments

We thank M. Wulff and D. Kakhulin for their valuable contributions to the synchrotron experiments at the ESRF and I. Vrejoiu for sample growth. A.B. thanks the Leibnitz graduate school "Dynamics in new Light" for financial support. This research was made possible through the funding by BMBF via 05K10IP1.

**Detecting optically synthesized
quasi-monochromatic sub-terahertz
phonon wavepackets by ultrafast x-ray
diffraction**

M. Herzog, A. Bojahr, J. Goldshteyn, W. Leitenberger,
I. Vrejoiu, R. Shayduk, D. Khakhulin, M. Wulff,
R. Shayduk, P. Gaal and M. Bargheer.

Appl. Phys. Lett. **100**, 094101 (2012).

Detecting optically synthesized quasi-monochromatic sub-terahertz phonon wavepackets by ultrafast x-ray diffraction

M. Herzog,¹ A. Bojahr,¹ J. Goldshteyn,² W. Leitenberger,¹ I. Vrejoiu,³ D. Khakhulin,⁴ M. Wulff,⁴ R. Shayduk,² P. Gaal,¹ and M. Bargheer^{1,2,a)}

¹Institut für Physik und Astronomie, Universität Potsdam, Karl-Liebknecht-Str. 24-25, 14476 Potsdam, Germany

²Helmholtz-Zentrum Berlin für Materialien und Energie GmbH, Wilhelm-Conrad-Röntgen Campus, BESSY II, Albert-Einstein-Str. 15, 12489 Berlin, Germany

³Max-Planck-Institut für Mikrostrukturphysik, Weinberg 2, 06120 Halle, Germany

⁴European Synchrotron Radiation Facility (ESRF), 6 rue Jules Horowitz, 38000 Grenoble, France

(Received 10 January 2012; accepted 7 February 2012; published online 27 February 2012)

We excite an epitaxial SrRuO₃ thin film transducer by a pulse train of ultrashort laser pulses, launching coherent sound waves into the underlying SrTiO₃ substrate. Synchrotron-based x-ray diffraction (XRD) data exhibiting separated sidebands to the substrate peak evidence the excitation of a quasi-monochromatic phonon wavepacket with sub-THz central frequency. The frequency and bandwidth of this sound pulse can be controlled by the optical pulse train. We compare the experimental data to combined lattice dynamics and dynamical XRD simulations to verify the coherent phonon dynamics. In addition, we observe a lifetime of 130 ps of such sub-THz phonons in accordance with the theory. © 2012 American Institute of Physics. [<http://dx.doi.org/10.1063/1.3688492>]

Ultrafast x-ray diffraction (UXRD) is a powerful tool for monitoring atomic motion in solids on the related length and timescales. In principle, each displacement field within a crystal can be decomposed into discrete phonon modes of respective frequency ω and wavevector Q which are related by the phonon dispersion relation $\omega = \omega(Q)$. One key aspect of UXRD is the direct correspondence of a phonon-induced real-space periodicity $\lambda = 2\pi/Q$ within a host crystal of lattice spacing c and the finite diffraction intensity at wavevector transfer $q = |\mathbf{k}_{\text{in}} - \mathbf{k}_{\text{out}}| = G \pm Q$, where \mathbf{k}_{in} and \mathbf{k}_{out} are the incident and diffracted x-ray photon wavevectors, respectively, and $G = 2\pi/c$ is the reciprocal lattice vector of the host crystal.^{1,2} This relation is depicted in Fig. 1(a) for $G + Q$. Each phonon mode Q is, thus, responsible for x-rays diffracted into sharp sidebands of the main crystal Bragg reflection at $G \pm Q$ which oscillate at their respective eigenfrequency $\omega(Q)$. These features have been theoretically discussed by Larsson *et al.*²

Early UXRD experiments verified these relations by observing UXRD signals of longitudinal acoustic (LA) phonons in bulk crystals.¹⁻³ In these experiments, the intense and ultrashort laser pulses excite bipolar strain waves into the bulk crystal⁴ which have a broad phonon spectrum that accordingly generates contributions in a broad vicinity of the bulk Bragg reflection. The linear dispersion relation of LA phonons, $\omega = v_{\text{LA}}Q$, was verified by tuning q , where v_{LA} is the LA sound velocity.

For various physical and technical issues (such as phonon spectroscopy, phonon-phonon scattering, etc.), it is favorable to selectively generate high-frequency monochromatic phonon beams instead of spectrally broad pulses as in the first UXRD experiments. Several techniques have been developed, e.g., via thermomodulation⁵ or piezoelectric trans-

ducers.⁶ Roshchupkin and co-workers observed XRD sidebands due to continuous surface acoustic waves in langatate crystals.⁷ Acoustoelectrically amplified phonons below 10 GHz forming a continuous monochromatic bulk sound wave have also been detected by XRD.⁶ Solely optical techniques provide tunability of the phonon frequencies into the THz region. Optical multi-pulse excitation has been used to coherently control LA phonons in bulk InSb.⁸ Recently, high-frequency narrow-bandwidth tunable LA phonon pulses were coherently excited by optical pulse trains and subsequently verified by optical means.^{9,10} Alternatively, the single-pulse photoexcitation of semiconductor superlattices generates folded LA phonons.^{11,12} Due to coupling to the substrate, these folded phonons unfold into the substrate which results in similar phonon pulses as discussed here.¹³ Such unfolding could be monitored by UXRD; however, the corresponding weak signatures in the diffraction curves were mainly dominated by the strong superlattice Bragg peaks.¹⁴ Moreover,

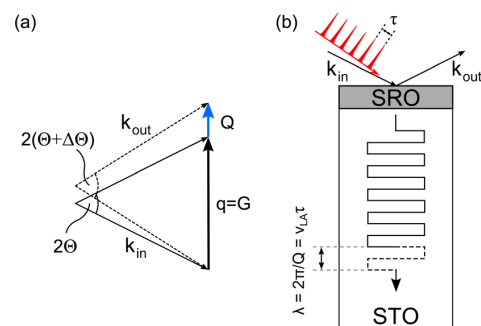


FIG. 1. (Color online) (a) Schematic representation of coherent XRD from a reciprocal lattice vector G (solid lines) and from an additional phonon of wavevector Q (dashed lines). The same process is possible for G and Q being antiparallel. (b) Schematic of the experiment. Each laser pulse launches a bipolar strain wave into the substrate (dashed line) resulting in a phonon wavepacket with central wavevector Q (dashed and solid line).

^{a)}Electronic mail: bargheer@uni-potsdam.de.

these unfolded phonon wavepackets have a fixed central frequency defined by the spatial superlattice period.^{13,14}

In this letter, we synthesized a quasi-monochromatic phonon pulse by excitation of a SrRuO₃ (SRO) thin film transducer epitaxially grown by pulsed laser deposition³² on a SrTiO₃ substrate¹⁵ with a train of ultrashort optical laser pulses (schematically shown in Fig. 1(b)). Relevant material properties of SRO and STO can be found in, e.g., Refs. 27, 28, 33, and 34. Each laser pulse impulsively launches a single spectrally broad bipolar strain pulse with high amplitude into the substrate (schematically depicted by the dashed line in Fig. 1(b)).¹⁶ The optical pulse train with pulse frequency $\nu = \tau^{-1}$ and N pulses thus synthesizes a coherent phonon wavepacket¹⁰ with wavevector $Q_p = 2\pi\nu/v_{LA}$, where v_{LA} is the LA sound velocity of the STO substrate. Using UXRD, we observe clear sidebands to the STO Bragg peak as the x-ray photons scatter from the monochromatic phonons according to $q = G + Q_p$. The selective excitation of coherent phonons with a specific Q_p allows us to directly monitor the 130 ps lifetime of these sub-THz phonons which undergo strong damping attributed to thermoelastic damping and Akhiezer's mechanism of relaxation damping.^{17–19} The central wavevector of the observed wavepacket can be controlled by the pulse repetition rate ν and the bandwidth is inversely proportional to N . By tuning ν , one can thus map out the LA phonon dispersion relation $\omega(Q)$.

The time-resolved XRD experiments were performed at the undulator beamline ID09B at the synchrotron source ESRF.²⁰ The general experimental setup working at 1 kHz repetition rate was described in Ref. 21. The storage ring was running in 16-bunch mode generating ≈ 100 ps x-ray pulses. We chose a photon energy of 12 keV for the experiments and utilized only one sample (cf. Ref. 21). The optical pulse train was produced by a mirror composed of four alternately stacked glass plates and spacer rings giving eight reflections from the air-glass interfaces. The plates and rings had a thickness of 710 μm and 1100 μm , respectively, corresponding to pulse spacing of $\tau \approx 7.2$ ps ($\nu \approx 140$ GHz) at normal incidence, which was verified by optical cross-correlation measurements. Due to the rather low reflectivity of the air-glass interfaces, the energy distribution within the pulse train was almost homogeneous. The integrated fluence at the sample was set to ≈ 44 mJ/cm², i.e., each pulse contributed a mean fluence of ≈ 5.5 mJ/cm².

The inset of Fig. 2(a) shows the static rocking curve around the (002) STO substrate Bragg peak from which we deduced a SRO layer thickness of ≈ 15.4 nm. The high-angle side of the STO substrate Bragg peak has very little contribution from the SRO layer which allows to observe the sidebands of the phonon wavepackets without any congestion from the top layer(s). This situation is even improved by the shift of the SRO peak towards lower angles due to the photoinduced thermal expansion. The robust perovskite oxide SRO has a fast electron-phonon coupling and is, thus, perfectly suited as a thin film transducer which can be triggered by strong laser-pulse excitation in order to generate phonon spectra with a high frequency cutoff.^{22–25}

Figure 2(a) shows the measured rocking curves in the vicinity of the (002) STO substrate Bragg peak before (open black diamonds) and 130 ps after (solid red bullets) the ar-

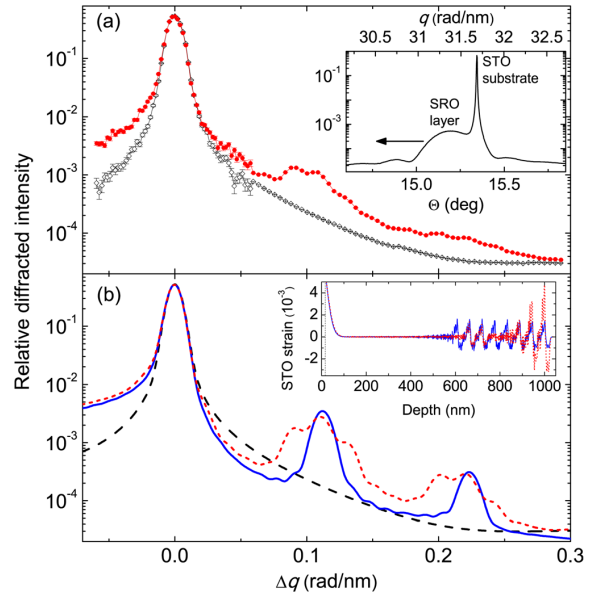


FIG. 2. (Color online) (a) Experimental rocking curves (measured piecewise) of the high-angle side of the STO substrate peak before (open black diamonds) and 130 ps after (solid red bullets) excitation by a pulse train with 7.2 ps pulse separation. Inset: static rocking curve measured with a high-resolution x-ray photodiode. The arrow indicates the shift of the SRO peak due to the photoinduced thermal expansion. (b) Simulations of the measured rocking curves without excitation (long-dashed black) and with excitation by a pulse train having a uniform (solid blue) and non-uniform (short-dashed red) pulse energy distribution. Inset: calculated strain pattern 130 ps after excitation with uniform (solid blue) and non-uniform (dashed red) pulse energy distribution.

rival of the first pump pulse of the pulse train. The rocking curve at positive time delay shows a distinct sideband evidencing the excitation of a coherent narrow-bandwidth phonon wavepacket with a central wavevector around $\Delta q = Q_p^{(1)} = 0.11$ nm⁻¹. Moreover, the excitation of the second harmonic around $\Delta q = Q_p^{(2)} = 0.22$ nm⁻¹ with much weaker amplitude can be inferred from Fig. 2. Although we observe clearly separated harmonics, the sidebands are rather broad and exhibit additional modulations. The comparatively large penetration depth of the 800 nm pump light in SRO ($\xi_{\text{SRO}} \approx 52$ nm) results in nearly homogeneous excitation of the thin film transducer.^{13,26} The individual bipolar strain pulses thus roughly have a rectangular and steplike shape and consequently higher harmonics of Q_p are generated. Since we have an independent measure of ν , the linear LA phonon dispersion relation readily yields $v_{LA} \approx 7.9$ nm/ps which perfectly agrees with the literature values.^{27,28}

In order to understand the experimental data in more detail, we utilized numerical model calculations to simulate the experiment. First, we use a linear-chain model of masses and springs to calculate the coherent lattice dynamics.¹³ The multiple pump pulse excitation necessitates the inclusion of heat diffusion into the simulation. The resulting spatio-temporal strain maps then serve as an input for dynamical XRD simulations to calculate the transient rocking curves.^{26,29} The simulated transient rocking curves are plotted in Fig. 2(b). We first assume a pulse train of 8 identical pulses with 7.2 ps pulse separation. The calculated strain field at 130 ps is shown in the inset of Fig. 2(b). The corresponding rocking

curve (solid blue) exhibits sharp Bragg peaks at the experimentally observed wavevector $\Delta q = 0.11 \text{ nm}^{-1}$ and its higher harmonics.

The experimental peak width is much broader than for the idealized simulation. This may originate from varying pulse energies at the probe area. For instance, a different pointing of the individual optical pump beams due to non-parallel glass plates of the mirror stack would generate different excitation densities at the fairly distant probe spot for each pulse. To account for such effects, we further assumed a non-uniform pump pulse energy distribution within the pulse train which results in the dashed red curve in Fig. 2. This rocking curve satisfactorily approximates the shape of the experimental data. The individual pulse energies are proportional to the corresponding amplitudes of the bipolar strain pulses plotted in the inset of Fig. 2(b). Thus, a controlled variation of the pulse energy distribution in principle allows to generate arbitrary phonon spectra in addition to the tunability of the central wavevector by the pulse frequency ν .

Finally, we analyze the time-dependence of the first-order sideband of the phonon wavepacket. For this, we evaluate the integrated intensity of the main part between $\Delta q = 0.08 \text{ rad/nm}$ and $\Delta q = 0.14 \text{ rad/nm}$ for each measured time delay. The result is given by the symbols in Fig. 3. We fit this transient by an exponential function which is set to zero before $t = 0$ and convoluted by a Gaussian representing the limited time-resolution. The solid black line in Fig. 3 shows the best fit from which we extract a decay time $\tau_{\text{data}} = 130 \pm 8 \text{ ps}$. If we perform an analogous evaluation on the simulated data, we obtain the dashed red line. Here, the decay time is $\tau_{\text{sim}} \approx 600 \text{ ps}$ which is essentially determined by (1) the x-ray absorption as the strain pulse propagates deeper into the substrate (absorption length at 12 keV in STO is $\approx 54 \mu\text{m}$) and (2) normal dispersion of the phonon wavepacket. Since our lattice dynamics model does not include anharmonic phonon interactions, τ_{sim} marks an upper limit. The fact that $\tau_{\text{data}} \ll \tau_{\text{sim}}$ thus implies a rather efficient attenuation of the phonon wavepacket. Combining τ_{sim} and theoretical estimations including Akhiezer's mechanism of relaxation damping^{17,18} and thermoelastic damping¹⁹ yields a decay time of $\approx 200 \text{ ps}$ which is close to our measured phonon lifetime. We also obtain very similar values ($\approx 130 \text{ ps}$)

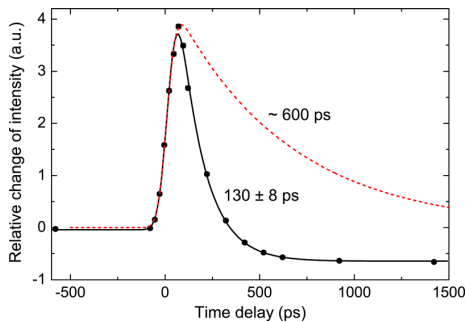


FIG. 3. (Color online) Time evolution of the integrated intensity of the 1st order sideband in Fig. 2(a) (black bullets) and the corresponding fit (solid black line). For comparison, we also show the corresponding transient obtained from the simulation which disregards anharmonic interactions in Fig. 2(b) (dashed red line).

by extrapolation of previously measured sub-GHz sound attenuation in STO (Refs. 30 and 31) according to $\tau_{\text{decay}} \sim \omega^{-2}$ given by Akhiezer's damping.¹⁷⁻¹⁹ More insight in the exact phonon attenuation dynamics could be gained by using shorter x-ray probe pulses since the observed phonon lifetime is close to the time-resolution of the experiment.

In conclusion, we presented UXRD data that evidence the efficient generation of quasi-monochromatic coherent LA phonon wavepackets at 140 GHz. We could explain and successfully simulate the corresponding sidebands of the STO substrate Bragg peak using a microscopic lattice dynamics model and dynamical XRD simulations. As the sidebands originate from a scattering of x-ray photons from selectively synthesized phonons with specific Q vector, the transient intensity of the sidebands directly measures the lifetime of these sub-THz LA phonons which is in accordance with theory and earlier acoustic experiments in the sub-GHz range. We believe that the combination of continuously tunable selective excitation of monochromatic phonon-pulses and UXRD will prove to be a versatile tool for investigation of sound attenuation and anharmonic phonon-phonon interactions in various materials with physically interesting coupling mechanisms at hypersonic frequencies.

We thank the BMBF for funding the project via Grant No. 05K10IP1 and the DFG via Grant No. BA2281/3-1.

- ¹D. A. Reis, M. F. DeCamp, P. H. Bucksbaum, R. Clarke, E. Dufresne, M. Hertlein, R. Merlin, R. Falcone, H. Kapteyn, M. M. Murnane *et al.*, *Phys. Rev. Lett.* **86**, 3072 (2001).
- ²J. Larsson, A. Allen, P. H. Bucksbaum, R. W. Falcone, A. Lindenberg, G. Naylor, T. Missalla, D. A. Reis, K. Scheidt, A. Sjögren *et al.*, *Appl. Phys. A* **75**, 467 (2002).
- ³C. Rose-Petruck, R. Jimenez, T. Guo, A. Cavalieri, C. W. Siders, F. Rksi, J. A. Squier, B. C. Walker, K. R. Wilson, and C. P. J. Barty, *Nature* **398**, 310 (1999).
- ⁴C. Thomsen, H. T. Grahn, H. J. Maris, and J. Tauc, *Phys. Rev. B* **34**, 4129 (1986).
- ⁵E. P. N. Damen, A. F. M. Arts, and H. W. de Wijn, *Phys. Rev. Lett.* **74**, 4249 (1995).
- ⁶S. D. LeRoux, R. Colella, and R. Bray, *Phys. Rev. Lett.* **35**, 230 (1975).
- ⁷D. Roshchupkin, A. Erko, L. Ortega, and D. Irzhak, *Appl. Phys. A* **94**, 477 (2009).
- ⁸O. Synnergren, T. N. Hansen, S. Canton, H. Enquist, P. Sondhaus, A. Srivastava, and J. Larsson, *Appl. Phys. Lett.* **90**, 171929 (2007).
- ⁹J. D. Choi, T. Feurer, M. Yamaguchi, B. Paxton, and K. A. Nelson, *Appl. Phys. Lett.* **87**, 081907 (2005).
- ¹⁰C. Klieber, E. Peronne, K. Katayama, J. Choi, M. Yamaguchi, T. Pezeril, and K. A. Nelson, *Appl. Phys. Lett.* **98**, 211908 (2011).
- ¹¹M. Bargheer, N. Zhavoronkov, Y. Gritsai, J. C. Woo, D. S. Kim, M. Woerner, and T. Elsaesser, *Science* **306**, 1771 (2004).
- ¹²P. Sondhaus, J. Larsson, M. Harbst, G. A. Naylor, A. Plech, K. Scheidt, O. Synnergren, M. Wulff, and J. S. Wark, *Phys. Rev. Lett.* **94**, 125509 (2005).
- ¹³M. Herzog, D. Schick, P. Gaal, R. Shayduk, C. v. Korff Schmising, and M. Bargheer, *Appl. Phys. A* **106**, 489 (2012).
- ¹⁴M. Trigo, Y. M. Sheu, D. A. Arms, J. Chen, S. Ghimire, R. S. Goldman, E. Landahl, R. Merlin, E. Peterson, M. Reason *et al.*, *Phys. Rev. Lett.* **101**, 025505 (2008).
- ¹⁵The sample was grown by pulsed laser deposition (Ref. 32) and included a protective coating in the form of a 1-2 nm STO capping layer.
- ¹⁶The epitaxial growth of the thin film transducer is not mandatory for generating the plane wave strain pulses. The almost perfectly matched acoustic impedances of SRO and STO ensure that there are no acoustic post-pulses and the amplitude of the strain pulses in the substrate is maximized (mass densities $\rho_{\text{SRO}} = 6.26 \text{ g/cm}^3$ and $\rho_{\text{STO}} = 5.12 \text{ g/cm}^3$, LA sound velocities $v_{\text{LA}}^{\text{SRO}} = 6312 \text{ m/s}$ and $v_{\text{LA}}^{\text{STO}} = 7876 \text{ m/s}$ from Refs. 27, 33, and 34). The impedance matching is required for the tunability of the central wavevector of the phonon wavepacket.

- ¹⁷T. O. Woodruff and H. Ehrenreich, *Phys. Rev.* **123**, 1553 (1961).
- ¹⁸A. Koreeda, T. Nagano, S. Ohno, and S. Saikan, *Phys. Rev. B* **73**, 024303 (2006).
- ¹⁹J. Y. Duquesne and B. Perrin, *Phys. Rev. B* **68**, 134205 (2003).
- ²⁰M. Wulff, A. Plech, L. Eybert, R. Randler, F. Schotte, and P. Anfinrud, *Faraday Discuss.* **122**, 13 (2003).
- ²¹H. A. Navirian, M. Herzog, J. Goldshteyn, W. Leitenberger, I. Vrejoiu, D. Khakhulin, M. Wulff, R. Shayduk, P. Gaal, and M. Bargheer, *J. Appl. Phys.* **109**, 126104 (2011).
- ²²C. von Korff Schmising, M. Bargheer, M. Kiel, N. Zhavoronkov, M. Woerner, T. Elsaesser, I. Vrejoiu, D. Hesse, and M. Alexe, *Appl. Phys. B* **88**, 1 (2007).
- ²³C. von Korff Schmising, A. Harpoeth, N. Zhavoronkov, Z. Ansari, C. Aku-Leh, M. Woerner, T. Elsaesser, M. Bargheer, M. Schmidbauer, I. Vrejoiu *et al.*, *Phys. Rev. B* **78**, 060404 (2008).
- ²⁴M. Herzog, W. Leitenberger, R. Shayduk, R. van der Veen, C. J. Milne, S. L. Johnson, I. Vrejoiu, M. Alexe, and D. Hesse, *Appl. Phys. Lett.* **96**, 161906 (2010).
- ²⁵C. von Korff Schmising, M. Bargheer, M. Kiel, N. Zhavoronkov, M. Woerner, T. Elsaesser, I. Vrejoiu, D. Hesse, and M. Alexe, *Phys. Rev. Lett.* **98**, 257601 (2007).
- ²⁶M. Herzog, D. Schick, W. Leitenberger, R. Shayduk, R. M. van der Veen, C. J. Milne, S. L. Johnson, I. Vrejoiu, and M. Bargheer, *New J. Phys.* **14**, 013004 (2012).
- ²⁷R. O. Bell and G. Rupprecht, *Phys. Rev.* **129**, 90 (1963).
- ²⁸Y. H. Ren, M. Trigo, R. Merlin, V. Adyam, and Q. Li, *Appl. Phys. Lett.* **90**, 251918 (2007).
- ²⁹S. A. Stepanov, E. A. Kondrashkina, R. Köhler, D. V. Novikov, G. Materlik, and S. M. Durbin, *Phys. Rev. B* **57**, 4829 (1998).
- ³⁰R. Nava, R. Callarotti, H. Ceva, and A. Martinet, *Phys. Lett. A* **28**, 456 (1968).
- ³¹R. Nava, R. Callarotti, H. Ceva, and A. Martinet, *Phys. Rev.* **188**, 1456 (1969).
- ³²I. Vrejoiu, G. Le Rhun, L. Pintilie, D. Hesse, M. Alexe, and U. Gösele, *Adv. Mater.* **18**, 1657 (2006).
- ³³S. Yamanaka, T. Maekawa, H. Muta, T. Matsuda, S. Kobayashi, and K. Kurosaki, *J. Solid State Chem.* **177**, 3484 (2004).
- ³⁴G. J. Fischer, Z. Wang, and S.-i. Karato, *Phys. Chem. Miner.* **20**, 97 (1993).

PAPER VI

Direct time-domain sampling of subterahertz coherent acoustic phonon spectra in SrTiO₃ using ultrafast x-ray diffraction

R. Shayduk, M. Herzog, A. Bojahr, D. Schick, P. Gaal,
W. Leitenberger, H. Navirian, M. Sander, J. Goldshteyn,
I. Vrejoiu and M. Bargheer.

Phys. Rev. B **87**, 184301 (2013).

Direct time-domain sampling of subterahertz coherent acoustic phonon spectra in SrTiO₃ using ultrafast x-ray diffraction

Roman Shayduk,^{1,*} Marc Herzog,² Andre Bojahr,² Daniel Schick,² Peter Gaal,¹ Wolfram Leitenberger,² Hengameh Navirian,² Mathias Sander,² Jevgenij Goldshteyn,¹ Ionela Vrejoiu,³ and Matias Bargheer^{1,2}

¹*Helmholtz-Zentrum Berlin für Materialien und Energie GmbH, Wilhelm-Conrad-Röntgen Campus, BESSY II, Albert-Einstein-Str. 15, 12489 Berlin, Germany*

²*Institut für Physik und Astronomie, Universität Potsdam, Karl-Liebknecht-Str. 24-25, 14476 Potsdam, Germany*

³*Max-Planck-Institut für Mikrostrukturphysik, Weinberg 2, D-06120 Halle, Germany*

(Received 18 December 2012; revised manuscript received 22 March 2013; published 7 May 2013)

We synthesize sub-THz longitudinal quasimonochromatic acoustic phonons in a SrTiO₃ single crystal using a SrRuO₃/SrTiO₃ superlattice as an optical-acoustic transducer. The generated acoustic phonon spectrum is determined using ultrafast x-ray diffraction. The analysis of the generated phonon spectrum in the time domain reveals a k -vector dependent phonon lifetime. It is observed that even at sub-THz frequencies the phonon lifetime agrees with the $1/\omega^2$ power law known from Akhiezer's model for hyper sound attenuation. The observed shift of the synthesized spectrum to the higher q is discussed in the framework of nonlinear effects appearing due to the high amplitude of the synthesized phonons.

DOI: [10.1103/PhysRevB.87.184301](https://doi.org/10.1103/PhysRevB.87.184301)

PACS number(s): 63.20.-e, 61.05.cp

I. INTRODUCTION

The increasing importance of coherent phonon spectroscopy in material science is related to the growing problem of heat dissipation in modern nanoscale devices. This problem is impossible to solve without detailed understanding of underlying phonon-phonon and phonon-electron interactions on the nanoscale. One of the methods to study these processes is coherent phonon spectroscopy, in which a particular phonon spectrum is excited coherently in the sample and detected optically. Research efforts in this direction resulted in significant progress in generation and detection of coherent phonons in various materials. The available phonon frequency has reached the THz acoustic limit¹ and basically the whole phonon frequency range nowadays could be excited coherently. However, convenient optical detection methods based on Raman^{2,3} or Brillouin⁴ scattering allow for the observation of phonons excited only in the vicinity of the Brillouin zone center. Therefore, sub-THz acoustic phonons could be accessed optically only in multilayer structures, in which the acoustic dispersion branch backfolds many times inside a mini-Brillouin zone of a multilayer.⁵ Modern progress in pulsed laser techniques as well as in multilayer fabrication has led to a set of successful experiments in which the coherent zone-folded superlattice phonons have been optically excited and detected.⁵⁻⁷ However, these optical methods are insensitive to the THz frequency phonons which have propagated into the bulk of the crystal due to the unfolding of the phonon dispersion curve. Convenient optical methods based on Brillouin scattering in this case have a detection limit in the 100 GHz range given by the wave vector magnitude of the optical light.^{8,9} Recently, ultrafast x-ray diffraction (UXRD) has become available to extend the accessible phonon frequency range to above 100 GHz. It has been used successfully to study both the time-domain structure of optically excited zone-folded coherent acoustic phonons in epitaxial multilayers,¹⁰ as well as to observe the propagation of unfolded phonons into the bulk.¹¹

In this paper we report our new UXRD experiments from coherent quasimonochromatic longitudinal acoustic phonons

in SrTiO₃ synthesized by fs-laser excitation of SrRuO₃/SrTiO₃ (SRO/STO) epitaxial multilayers. Using UXRD we determine the laser excited phonon spectrum in SrTiO₃ and monitor the modification of the spectrum in the time domain. The epitaxial multilayers were prepared using pulsed laser deposition.¹² The experiments are carried out at the BESSY EDR beamline using a unique setup for a 1 MHz repetition rate UXRD experiments.

The experiments are done in a traditional scheme which uses an optical delay line to change the time interval between the optical pump and the x-ray probe pulses. We use infrared optical pulses with the wavelength of 1.03 μm for pumping and 8 keV x-rays for probing the lattice dynamics. The important feature of this setup is the simultaneous acquisition of the x-ray photons scattered from the sample before and after the pumping optical pulse. This makes the x-ray intensity difference signal sensitive only to those changes in the crystal lattice which were exclusively initiated by the optical pulses. For further details we refer to a recent publication describing the setup.¹³

II. THEORY

A. Synthesis of quasimonochromatic coherent acoustic phonons

Recent studies showed that the optical excitation of a metal transducer by a sequence of ultrashort laser pulses is an efficient method to generate sub-THz quasimonochromatic longitudinal acoustic (LA) phonons.¹⁴⁻¹⁶ In essence, the repetitive generation of bipolar strain pulses by the laser-excited transducer¹⁷ forms a phonon wave packet of narrow spectral bandwidth propagating throughout the substrate. In this report we consider a different approach which uses a spatial repetition instead of a temporal one, i.e., the excitation of a periodic metal-dielectric multilayer (superlattice) with a single ultrashort laser pulse [see Fig. 1(a)]. This way the so-called superlattice phonon mode is excited,^{10,18-21} which subsequently unfolds into the substrate thereby forming LA phonon wave packets with similarly narrow spectral

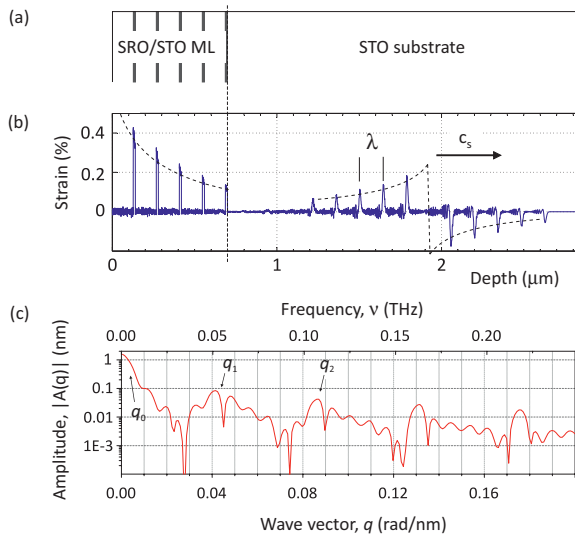


FIG. 1. (Color online) (a) Sketch of the five-period epitaxial SrRuO₃/SrTiO₃ multilayer on top of the SrTiO₃ substrate. (b) Calculated strain profile in the sample along the surface normal, taken at 250 ps after the multilayer excitation. (c) Calculated spectrum of the strain pulse in the wave vector and frequency domains induced by the optical excitation. The vertical scale stands for the excitation fluence of 6 mJ/cm² used in the experiment.

bandwidth.^{11,20} In most cases the laser-induced coherent lattice dynamics may be calculated using either a model of a continuous elastic medium¹⁷ or a linear-chain model (LCM) of masses and springs.²⁰ Here we employ the latter approach which will be more appropriate for short-period superlattices and automatically accounts for the acoustic phonon dispersion. The details of the numerical model can be found in Ref. 20. The excellent agreement of such a linear-chain model with related optical and UXRD experiments has been previously demonstrated for various sample structures.^{16,19–23}

Further we consider linear chain calculations for a five-period SRO/STO multilayer with the spatial period $D = 140$ nm which is schematically shown in Fig. 1(a). The structural parameters of the sample which are determined by static high-resolution x-ray diffraction (HRXRD)²⁴ are collected in Table I. In addition, the longitudinal sound velocities of the individual materials are shown.²⁵ The results of the linear-chain calculations using the parameters given in Table I and the experimental pump fluence of 6 mJ/cm² are shown in Figs. 1(b) and 1(c).

The graph in Fig. 1(b) shows the calculated one-dimensional strain profile in the sample 250 ps after the

TABLE I. Structural and mechanical properties employed in the calculations.

Material	Lattice constant	Thickness	Sound speed
Substrate STO	3.905 Å	10 μm	7.9 nm/ps
STO in ML	3.92 Å	127 nm	7.8 nm/ps
SRO in ML	3.95 Å	13 nm	6.3 nm/ps

excitation. Figure 1(c) plots the spectral amplitude of the linear-chain eigenvectors (normal modes) as a function of the eigenfrequency. This amplitude spectrum is solely determined by the initial conditions.²⁰ For the bulk STO substrate the eigenvectors are plane elastic waves with wave vector q satisfying the well-known dispersion relation of acoustic phonons.²⁶ As Fig. 1(b) illustrates, the optical excitation of the metal layers of the multilayer system results in the generation of a coherent strain wave packet propagating into the STO substrate at the longitudinal sound velocity.²⁰ The resulting wave packet inside the STO substrate attains the particular shape shown in Fig. 1(b), namely, five leading compression pulses and five trailing expansion pulses which are separated by $\lambda \approx 140$ nm, respectively. In other words, the metal/dielectric multilayer acts as the photoacoustic transducer synthesizing the coherent LA phonon wave packet in the STO substrate. The sharp static profile of the thermal strain inside the multilayer [see Fig. 1(b)] remains unchanged with time because the linear chain model neglects the effect of heat diffusion. The heat diffusion in multilayers is a complicated separate topic which lays out of the scope of this paper. In this paper we focus on the coherent lattice dynamics in the STO substrate which occur at a later timescale when the effect of heat diffusion within the multilayer does not play a role. For the detailed description of the wave packet strain profile and its generation we refer to our earlier works.²⁰

The calculated amplitude spectrum in Fig. 1(c) contains several equidistant peaks. The most pronounced peak at $q_0 = 0$ rad/nm is responsible for the overall bipolar shape of the wave packet.^{17,20} The width of the peak is determined by the total thickness of the multilayer ($\Delta q \approx \pi/5\lambda$). The peak around $q_1 = 2\pi/\lambda \approx 0.046$ rad/nm corresponds to the characteristic spatial period λ of the wave packet. The nonsinusoidal shape of the wave packet gives rise to the higher harmonics at integer multiples of q_1 .

Altogether, we find that using a periodic metal-dielectric multilayer as photoacoustic transducer we can generate LA phonon wave packets similar to the quasimonochromatic wave packets produced by multiple-pulse excitation of a thin metal film.^{14–16} In both cases the wave packets exhibit narrow spectral bandwidth and higher harmonics of lower amplitude.

B. Ultrafast x-ray diffraction from sub-THz elastic waves

The x-ray diffraction from crystals which are subject to a strong acoustic field is a well-established topic.^{27–29} However most of the previous studies deal with strain fields generated by surface acoustic wave (SAW) transducers. Such devices normally generate acoustic waves with wavelengths longer than either the x-ray extinction length or the x-ray coherence length. The x-ray diffraction from a crystal lattice perturbed by such waves results in modifications of the Bragg peak shape within the Darwin width or in the appearance of diffuse scattering contributions in the vicinity of the peak.^{30,31} The description of the x-ray scattering from such waves usually requires dynamical x-ray diffraction theory.

Here we consider quasimonochromatic coherent LA phonons which in fact are elastic waves at hypersonic frequencies. The corresponding wave vectors q are large enough to allow for coherent Bragg-like scattering of x rays

from the associated “moving gratings.” Due to the sufficiently high q vectors of the quasimonochromatic phonons the x-ray scattering contributes in the off-Bragg region in which the x-ray scattering efficiency from the bulk of the crystal is small. This allows us to probe the x rays exclusively scattered from the wave packet with only minor perturbation by the bulk-scattered x-ray wave field.

In this section we introduce the necessary theoretical basis which allows a thorough interpretation of the UXRD experiments. Since we intend to apply the following theory to study the laser-induced structural dynamics in one dimension we restrict ourselves to a one-dimensional formulation.

A plain elastic wave with wave vector q contributes to the scattered x-ray intensity if the x-ray scattering vector Q is given by

$$Q = G \pm q, \quad (1)$$

where G is a reciprocal lattice vector and $Q = |\mathbf{k} - \mathbf{k}_i|$ is the x-ray scattering vector.^{16,32-34}

From simulations of the scattered x-ray intensity using dynamical theory of x-ray diffraction one finds that the x-ray intensity scattered from the crystal perturbed by a bunch of elastic waves can be well described by the equation

$$\langle I_p(Q) \rangle_t = I_{up}(Q) + \alpha A(q)^2, \quad (2)$$

where $I_p(Q)$ and $I_{up}(Q)$ is the scattered x-ray intensity from the perturbed and unperturbed crystal, respectively. The angle brackets stand for time averaging. The function $A(q)$ is the spectral amplitude of the elastic wave with wave vector magnitude $q = |Q - G|$ and α is some constant. It is worth showing here that formula (2) is equivalent to the expression describing thermal diffuse scattering (TDS) from acoustic phonons.³⁵ To show this we need to relate the energy of a classical plane elastic wave in the crystal with the phonon population. The energy of plane elastic waves in the classical linear theory of elasticity is proportional to the squared product of the wave amplitude A and frequency ω

$$E(\omega) \propto A^2 \omega^2. \quad (3)$$

In a crystal lattice this corresponds to the energy of the corresponding vibrational normal mode which is associated with a single harmonic oscillator. According to quantum mechanics the energy of a harmonic oscillator with angular frequency ω is

$$E(\omega) = \hbar \omega \left(n + \frac{1}{2} \right), \quad (4)$$

where n is the excitation level. That is, the energy of the vibrational normal modes is quantized and n refers to the number of phonons in the crystal having the angular frequency ω . Therefore, the following relationship between the excited classical amplitude spectrum of elastic waves and the phonon population holds

$$A(q_i)^2 \propto \left(n(\omega_i) + \frac{1}{2} \right) / \omega_i \approx \frac{n(\omega_i)}{\omega_i}, \quad (5)$$

in which index i identifies the normal mode. The combination of Eqs. (2) and (5) yields

$$\langle I_p(Q) \rangle_t - I_{up}(Q) \propto \frac{n(Q - G)}{\omega(Q - G)}, \quad (6)$$

which is a one-dimensional equivalent of the relation for TDS derived by Warren.³⁵

We thus conclude that UXRD from a quasimonochromatic strain pulse directly measures the squared spectral amplitudes of the plane elastic waves constituting the strain pulse. As an example we consider the reciprocal lattice vector G_{002} of STO and rewrite Eqs. (2) and (6) into

$$A(q) \propto \sqrt{\langle I_p(G_{002} + q) \rangle_t - I_{up}(G_{002} + q)} \quad (7)$$

$$n(q) \propto \omega(q) (\langle I_p(G_{002} + q) \rangle_t - I_{up}(G_{002} + q)). \quad (8)$$

In the standard θ - 2θ geometry applied in our UXRD experiments, the magnitude of the phonon wave vector q is

$$q = \frac{4\pi}{\lambda_X} |\sin \theta - \sin \theta_0|, \quad (9)$$

where λ_X is the x-ray wavelength, θ is the x-ray incidence angle with respect to the sample surface [(001) crystallographic plane], and θ_0 is the Bragg angle.

To demonstrate that Eq. (7) is applicable to our case we compare the calculated amplitude spectrum of the laser-excited strain waves to the dynamical UXRD simulations from the same acoustically perturbed sample.¹⁹ The calculated spectrum for the laser fluence of 6 mJ/cm² is plotted in Fig. 2 as a red solid line. The dynamical UXRD calculations are performed for 200 time steps within the interval from 100 ps to 300 ps after the excitation and then time averaged. The blue symbols in Fig. 2 show the scaled time averaged square root of the intensity differences [cf. (7)] obtained from the dynamical UXRD calculations.

We see that the curves almost coincide although the fine structure of the UXRD-related curve (blue symbols) slightly

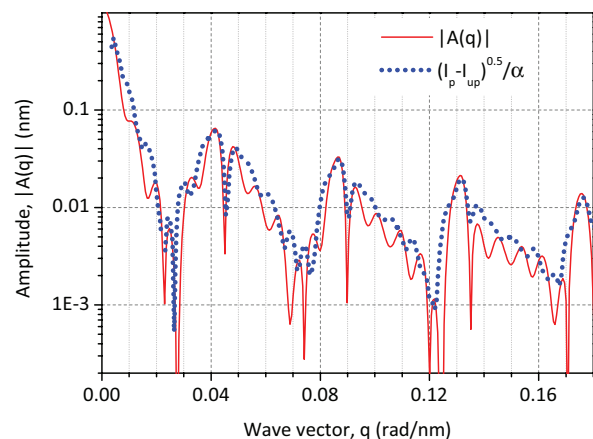


FIG. 2. (Color online) Comparison of the calculations of the spectral strain amplitudes of phonons with the corresponding x-ray intensity difference signal of perturbed-unperturbed structures. The red solid line indicates the calculated phonon spectrum in the sample in the q domain. The values in the vertical axis correspond to the phonon spectral amplitudes calculated for the excitation fluence of 6 mJ/cm². The blue bullets show the square root of the x-ray intensity difference signal calculated for the perturbed and unperturbed structures. The vertical scale factor for the UXRD signal is arbitrary.

deviates from the actual spectrum (red solid line). This is due to the fact that the scattered x-ray intensity from a propagating strain wave packet actually oscillates in the time domain at each fixed q vector with the frequency of the corresponding phonon mode. These oscillations were successfully observed in pioneering experiments with the advent of UXRD.^{32–34} The classical explanation for the oscillations is the interference of x rays scattered from a moving grating (elastic wave) and the x rays scattered from the static component of the crystal lattice. This is an x-ray analog of Brillouin oscillations in all-optical experiments.³⁶ In our case, as we can see, this interference is not very strong. Therefore, the shape of the blue curve slightly depends on the averaging time window. To eliminate these artifacts, the averaging time window should be either much longer than any phonon vibration period or we need to fit an integer number of vibrations for each q . The averaging over many vibrational periods is not possible in our case, because the actual phonon lifetime is only several vibration periods as we will see later.

To finish this section we briefly review the conditions at which the approximation (7) should be valid:

(i) The interatomic displacement in the strain wave is much less than the interatomic distance

$$|r_m - r_n| \ll_{m \neq n} |a(m - n)|, \quad (10)$$

in which a is the interatomic distance, and m and n are the index number of atoms. This is required by the perturbation theory of x rays scattered from a dynamical lattice.³⁵

(ii) The wave vector of a phonon is much smaller than any reciprocal lattice vector:

$$q \ll G. \quad (11)$$

This is necessary to avoid the signal overlap from the adjacent Bragg reflections of the crystal.

(iii) The wavelength of a phonon mode is much smaller than both the x-ray coherence and the x-ray extinction lengths:

$$q \gg \frac{1}{l}, \quad (12)$$

in which l is either x-ray coherence or x-ray extinction lengths, depending on which one is larger.

(iv) The x-ray intensity is time averaged over many vibrational periods.

III. EXPERIMENTAL RESULTS

We performed UXRD experiments on the laser-excited five-period SRO/STO multilayer with the structure parameters presented in Table I. In this section we present the experimental results which evidence the presence of a propagating quasimonochromatic LA phonon wave packet. We discuss the dynamics of the first- and second-order transient diffraction peaks and the corresponding dynamics of the strain pulse.

In the experiment we acquire the x-ray photons scattered from the sample 50 ns before each optical pulse and at a given probe delay after each optical pulse. The corresponding scattered x-ray intensities from the perturbed and unperturbed sample are thus defined as I_p and I_{up} , respectively. The time resolution of the experiments was 100 ps due to the limited

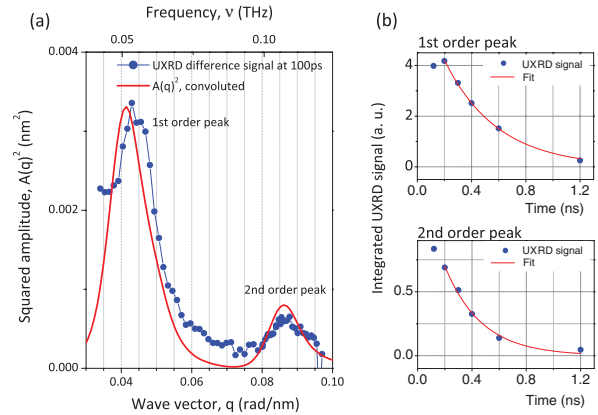


FIG. 3. (Color online) (a) The solid dots show the UXRD difference signal with an arbitrary vertical scale factor. Red is the calculated spectrum of the synthesized wave packet. (b) The integrated UXRD difference signal of the first two order phonon peaks as a function of time. The solid lines indicate the exponential fit.

x-ray pulse length, therefore the measured x-ray intensity is time averaged over multiple phonon vibrations.

Figure 3(a) shows the measured x-ray intensity difference signal $I_p - I_{up}$ (blue symbols) in the vicinity of the STO (002) Bragg peak (not visible) at 100 ps after the laser-pulse excitation. The experimental incidence angle θ has been converted into the phonon wave vector using Eq. (9). The vertical scale for the measured data is arbitrary. The UXRD data exhibit the first- and second-order spectral components of the synthesized quasimonochromatic phonon wave packet inside the STO substrate at wave vectors $q_1 \approx 0.045$ rad/nm and $q_2 \approx 0.09$ rad/nm, respectively. Given the longitudinal sound velocity in STO (cf. Table I), the linear phonon dispersion relation of acoustic phonons implies the corresponding hypersonic frequencies $\nu_1 \approx 55$ GHz and $\nu_2 \approx 110$ GHz. The nonvanishing contributions between the phonon peaks are due to the diffraction from the laser-heated multilayer. However, since the lattice constants throughout the multilayer are larger than that of the substrate (cf. Table I), the x-ray scattering from the multilayer is rather weak in this angular range. The red solid line in Fig. 3(a) shows the squared amplitude spectrum of the propagating sound wave as obtained from the linear-chain model. The shown spectrum includes the convolution with a Gaussian resolution function having a full width at half maximum (FWHM) of $15 \times 10^{-3} \text{ nm}^{-1}$ to fit the angular resolution of the UXRD experiment. The main contribution to the XRD peak broadening is due to the sample bending according to the stationary laser heat load.¹³ The UXRD signal shows very good agreement with the convoluted spectrum in terms of position, relative intensity and width of the first and second-order phonon peaks. This verifies the relation between the measured x-ray intensity and the amplitude spectrum of the coherent strain wave derived in Eq. (7).

In the following we discuss the intensity changes of the measured phonon peaks with time. During the first 100 ps after laser excitation the intensity of the phonon peaks builds up¹⁶ due to the unfolding of the initially excited superlattice phonon

TABLE II. Comparison of the experimentally observed UXRD intensity decay time τ_{exp} , the apparent decay time due to x-ray absorption τ_{abs} , and the derived phonon lifetime τ_{ph} for the first- and second-order phonon peaks. The corresponding standard deviations $\sigma_{\text{exp/abs}}$ are also shown.

q , rad/nm	τ_{abs} , ps	τ_{exp} , ps	τ_{ph} , ns
0.045	450	373 ± 12	2.2 ± 0.5
0.09	450	235 ± 30	0.49 ± 0.13

mode into the substrate.^{11,20} Subsequently, the integrated intensity of the phonon peaks decays exponentially as is evidenced by the blue symbols in Fig. 3(b). The red solid lines show fits according to the function

$$f(t) = \Delta I_0 e^{-\frac{t}{\tau_{\text{exp}}}}, \quad (13)$$

where the two fitting parameters ΔI_0 and τ_{exp} are the amplitude and decay time of the measured signal. The data points before 200 ps after the excitation were excluded from the fit since the wave packet may not yet be fully propagated from the multilayer to the substrate. The extracted decay times τ_{exp} and standard deviations σ_{exp} are shown in Table II.

There are two major reasons for the observed decrease of the UXRD peak intensities. First, the absorption of the x rays by the crystal reduces the sensitivity of the x rays to the wave packet as it propagates deeper into the substrate. Second, the dissipation of energy from the elastic wave due to the finite phonon lifetimes leads to a decay of the strain amplitude.

Considering the first reason, the decay time of the UXRD signal exclusively due to x-ray absorption is related to the x-ray absorption coefficient $\mu = 0.056 \mu\text{m}^{-1}$ by

$$\frac{1}{\tau_{\text{abs}}} = \frac{2\mu c_s}{\sin \theta} = \frac{8\pi\mu c_s}{Q\lambda_X}, \quad (14)$$

where $c_s = 7.9 \text{ nm/ps}$ is the longitudinal sound speed in the substrate.²⁵ The relative variation of the x-ray scattering vector Q during the presented UXRD experiments is 10^{-3} , which implies that τ_{abs} is virtually independent of the observed phonon wave vectors q . In the measured off-Bragg region the x-ray extinction due to dynamical x-ray diffraction is negligible, therefore only the angular independent x-ray absorption is relevant. Under the chosen experimental conditions we estimate a signal decay time of $\tau_{\text{abs}} \approx 466 \text{ ps}$ due to the x-ray absorption. Nevertheless, since this value is critical for the correct interpretation of the experimental data, we have performed dynamical XRD calculations based on results of the linear-chain lattice dynamics in harmonic approximation which excludes the effect of phonon damping.^{16,20} The simulations yield the q -independent value of $450 \pm 5 \text{ ps}$ for the decay constant due to x-ray absorption which we will use in the following.

Regarding the second reason for the decay of the UXRD phonon signals, we assume an exponential law for the decrease of the phonon population $n(q,t)$ and define the associated decay time τ_{ph} . According to Eq. (7) the corresponding intensity of the scattered x rays possesses the same decay constant. Therefore, the UXRD signal decay mechanisms

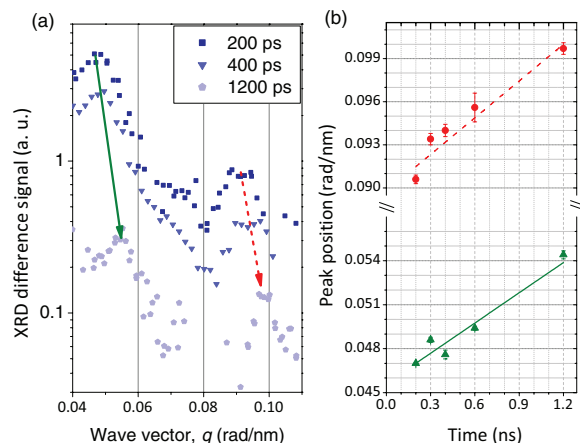


FIG. 4. (Color online) (a) Transient first- and second-order phonon diffraction peaks at various probe delays. The intensity decay due to sound attenuation is accompanied by a continuous shift to larger wave vectors as is indicated by the arrows. (b) First- and second-order peak position determined by Gaussian fits as a function of time delay. The solid lines show the linear fits to the experimental points.

introduce the relationship between the phonon lifetimes τ_{ph} , x-ray absorption time constant τ_{abs} , and the experimentally measured time constant τ_{exp} :

$$\frac{1}{\tau_{\text{exp}}} = \frac{1}{\tau_{\text{abs}}} + \frac{1}{\tau_{\text{ph}}}. \quad (15)$$

The phonon lifetimes τ_{ph} extracted from the UXRD experiments according to Eq. (15) are given in Table II for the wave vector magnitudes corresponding to the first- and second-order phonon peaks. The standard deviations σ_{ph} for the phonon lifetimes are calculated from the standard deviations σ_{exp} of the experimental time constants according to the error propagation relation.

The important observation is the fact that the determined lifetimes differ by a factor of ~ 4 whereas the related phonon wave vector differ by a factor of 2. In addition to the signal decay we see a gradual drift of the phonon peak position to higher values of q as the wave packet propagates. This is seen from Fig. 4(a), in which the phonon spectrum is shown for different time delays. In the following section we discuss the physical interpretation of the described observations.

IV. DISCUSSION

The central observation from the transient phonon-induced diffraction peaks presented in the previous section is the apparent quadratic decrease of the phonon lifetime with phonon wave vector q . This observation is in agreement with the $1/\omega^2$ law predicted by the Akhiezer's sound attenuation mechanism.³⁷

There are basically two theories which explain the attenuation of hypersonic waves in dielectric crystals due to incoherent anharmonic phonon-phonon scattering. These are

the Landau-Rumer theory³⁸ and the Akhiezer theory³⁷ which have different application limits:

$$\omega \ll \frac{1}{\tau_{\text{th}}} \quad \text{Akhiezer} \quad (16)$$

$$\omega \gg \frac{1}{\tau_{\text{th}}} \quad \text{Landau-Rumer}, \quad (17)$$

where ω is the angular frequency of the hypersonic wave and τ_{th} is the mean thermal phonon relaxation time. That is, in both cases the elastic energy of hypersonic waves decreases with time due to the interaction with incoherent thermal phonons. The mean thermal phonon relaxation time τ_{th} can be estimated from the thermal conductivity k , heat capacity C_V , average sound speed v_s , and mass density ρ by the relation²⁶

$$k = \frac{1}{3}\rho C_V v_s^2 \tau_{\text{th}}. \quad (18)$$

For STO at room temperature Eq. (18) yields $\tau_{\text{th}} \approx 0.26$ ps. The experiments are performed at room temperature. More precisely, the sample persisted at around 400 K during the actual measurements due to the thermal load from the laser.¹³ Condition (16) is fulfilled for this temperature range. That is, for the presented experiments Akhiezer's theory of relaxation damping could be applied, hereby explaining the observed ratio of the phonon lifetimes for the first- and second-order phonon diffraction peaks. However the UXRD data exhibit additional features which cannot be explained within Akhiezer's sound attenuation model. We extracted the transient peak positions by Gaussian fits to the data shown in Fig. 4(a), and the results are plotted as symbols in Fig. 4(b). The solid lines indicate linear fits to the phonon peak positions as a function of time. Clearly, a gradual shift of the first- and second-order spectral components to higher q values can be observed as the phonon wave packet propagates deeper into the STO substrate.

A recent study revealed the nonlinear propagation of large-amplitude sound wave packets in STO at room temperature.²² In addition to the Akhiezer-like attenuation of the coherent LA phonons the authors observed transient changes of the acoustic spectrum due to coherent anharmonic phonon-phonon scattering within the wave packet. The lattice anharmonicity gave rise to a strain-dependent longitudinal sound velocity. In particular, the sound velocity of compressive (tensile) parts of the wave packet was found to increase (decrease) with the strain amplitude. This effect led to an anomalous dispersion of the wave packet and the corresponding modification of the phonon spectrum.

Accordingly, we expect the first compressive half of the wave packet shown in Fig. 1(b) to propagate faster than the second tensile half. Moreover, the individual pulses inside the respective parts also exhibit different velocities due to the exponential amplitude distribution determined by the optical penetration of the pump light in SRO. For both the compressive and tensile parts of the strain pulse the spatial separation λ of the individual pulses of the wave packet is reduced as it propagates, i.e., the wavelength of both subpackets is decreased. This explains the observed shift of the phonon peaks to larger q values.

The presented UXRD data thus evidence the influence of two different effects on the propagation of LA phonon wave

packets generated by periodic multilayers. First, the inevitable attenuation of the wave packets by Akhiezer's relaxation damping and, second, the change of spatial and spectral shape of the wave packet by nonlinear sound propagation. Both effects influence the observed phonon lifetime, however, for a quantitative determination of the respective contributions additional measurements have to be performed. The results of our earlier all-optical experiments having much stronger excitation were successfully explained solely in the framework of nonlinear acoustics.²² We believe that at the presented experimental conditions the influences of both damping mechanisms, the nonlinear acoustic propagation and the Akhiezer's relaxation, are comparable.

UXRD has the advantage of measuring the lattice dynamics directly and quantitatively, i.e., the absolute amplitude of the lattice motion is determined. The wave vector range over which acoustic phonons in bulk material are accessible is very large. In particular resolving the second order phonon peak as presented in this paper or higher orders is possible. The extension of the UXRD detection of acoustic phonons in amorphous materials is challenging the available x-ray fluence, since the Bragg spots are dispersed in diffraction rings.

On the other hand all-optical picosecond acoustics,^{3,4,7,8,17} in principle, do not require crystalline materials and for transparent media, the propagation of strain pulses can be monitored over longer distances. With current technology femtosecond time resolution is standard in all-optical experiments, while it is still a challenge in x-ray technology, which was essentially resolved by free-electron lasers. High time-resolution permits the determination of the wave-vector-dependent sound velocity in addition to the damping time. We believe that the UXRD-based methods and the all-optical methods do not compete with each other but complete each other, together providing a more complete picture of the complex coherent phonon dynamics for a broader range of frequencies and wave vectors and for a broader class of materials and experimental conditions.

V. CONCLUSIONS

This report presents ultrafast x-ray diffraction (UXRD) studies on laser-excited periodic SrRuO₃/SrTiO₃ multilayers which are epitaxially grown on a SrTiO₃ substrate. The ultrafast heating of the metallic SrRuO₃ layers by ultrashort laser pulses generates coherent longitudinal acoustic phonons which eventually propagate into the substrate as a quasimonochromatic coherent LA phonon wave packet at hypersonic frequencies. We discussed the properties of such wave packets in detail and derived equations which show that UXRD is a powerful tool to measure the spectral phonon population and its dynamics. The presented UXRD data evidence the formation of a quasimonochromatic coherent phonon wave packet. We extracted the phonon lifetimes of the first- and second-order peaks of the phonon spectrum. The observed quadratic decrease of the phonon lifetime with increasing phonon wave vector q is in accordance with Akhiezer's mechanism of relaxation damping. Shifts of the peaks corresponding to the excited phonons to larger q values are interpreted as a

modification of the spatial shape profile due to the nonlinear wave propagation leading to a strain dependent sound velocity. This considerably modifies the observed phonon lifetimes. In essence, UXR provides a detailed and direct view on the complex nonlinear evolution of phonon-wave packets, including incoherent damping of the phonon amplitude by coupling to

other modes and specific coherent changes of the wave vector spectrum.

ACKNOWLEDGMENT

We thank the BMBF for funding via 05K 2012-OXIDE.

*roman.shayduk@helmholtz-berlin.de

¹A. Q. Wu and X. Xu, *Appl. Phys. Lett.* **90**, 251111 (2007).

²C. V. Raman and K. S. Krishnan, *Nature* **121**, 501 (1928).

³G. C. Cho, W. Kütt, and H. Kurz, *Phys. Rev. Lett.* **65**, 764 (1990).

⁴R. Y. Chiao, C. H. Townes, and B. P. Stoicheff, *Phys. Rev. Lett.* **12**, 592 (1964).

⁵C. Colvard, R. Merlin, M. V. Klein, and A. C. Gossard, *Phys. Rev. Lett.* **45**, 298 (1980).

⁶C. Colvard, T. A. Gant, M. V. Klein, R. Merlin, R. Fischer, H. Morkoc, and A. C. Gossard, *Phys. Rev. B* **31**, 2080 (1985).

⁷A. Bartels, Y. M. Sheu, D. A. Arms, J. Chen, S. Ghimire, R. S. Goldman, E. Landahl, R. Merlin, E. Peterson, M. Reason, and D. A. Reis, *Phys. Rev. Lett.* **101**, 025505 (2008).

⁸S. Brivio, D. Polli, A. Crespi, R. Osellame, G. Cerullo, and R. Bertacco, *Appl. Phys. Lett.* **98**, 211907 (2011).

⁹W. Kaiser and R. Zurek, *Phys. Lett.* **23**, 668 (1966).

¹⁰M. Bargheer, N. Zhavoronkov, Y. Gritsai, J. C. Woo, D. S. Kim, M. Woerner, and T. Elsaesser, *Science* **306**, 1771 (2004).

¹¹M. Trigo, Y. M. Sheu, D. A. Arms, J. Chen, S. Ghimire, R. S. Goldman, E. Landahl, R. Merlin, E. Peterson, M. Reason, and D. A. Reis, *Phys. Rev. Lett.* **101**, 025505 (2008).

¹²I. Vrejoiu, M. Alexe, D. Hesse, and U. Gösele, *Adv. Funct. Mater.* **18**, 3892 (2008).

¹³H. Navirian, R. Shayduk, W. Leitenberger, J. Goldshteyn, P. Gaal, and M. Bargheer, *Rev. Sci. Instrum.* **83**, 063303 (2012).

¹⁴J. D. Choi, T. Feurer, M. Yamaguchi, B. Paxton, and K. A. Nelson, *Appl. Phys. Lett.* **87**, 081907 (2005).

¹⁵C. Klieber, E. Peronne, K. Katayama, J. Choi, M. Yamaguchi, T. Pezeril, and K. A. Nelson, *Appl. Phys. Lett.* **98**, 211908 (2011).

¹⁶M. Herzog, A. Bojahr, J. Goldshteyn, W. Leitenberger, I. Vrejoiu, D. Khakhulin, M. Wulff, R. Shayduk, P. Gaal, and M. Bargheer, *Appl. Phys. Lett.* **100**, 094101 (2012).

¹⁷C. Thomsen, H. T. Grahn, H. J. Maris, and J. Tauc, *Phys. Rev. B* **34**, 4129 (1986).

¹⁸M. Herzog, W. Leitenberger, R. Shayduk, R. van der Veen, C. J. Milne, S. L. Johnson, I. Vrejoiu, M. Alexe, D. Hesse, and M. Bargheer, *Appl. Phys. Lett.* **96**, 161906 (2010).

¹⁹M. Herzog, D. Schick, W. Leitenberger, R. Shayduk, R. M. van der Veen, C. J. Milne, S. L. Johnson, I. Vrejoiu, and M. Bargheer, *New J. Phys.* **14**, 013004 (2012).

²⁰M. Herzog, D. Schick, P. Gaal, R. Shayduk, C. von Korff Schmising, and M. Bargheer, *Appl. Phys. A* **106**, 489 (2012).

²¹A. Bojahr, D. Schick, L. Maerten, M. Herzog, I. Vrejoiu, C. von Korff Schmising, C. J. Milne, S. L. Johnson, and M. Bargheer, *Phys. Rev. B* **85**, 224302 (2012).

²²A. Bojahr, M. Herzog, D. Schick, I. Vrejoiu, and M. Bargheer, *Phys. Rev. B* **86**, 144306 (2012).

²³P. Gaal, D. Schick, M. Herzog, A. Bojahr, R. Shayduk, J. Goldshteyn, H. A. Navirian, W. Leitenberger, I. Vrejoiu, D. Khakhulin, M. Wulff, and M. Bargheer, *Appl. Phys. Lett.* **101**, 243106 (2012).

²⁴R. Shayduk, H. A. Navirian, W. Leitenberger, J. Goldshteyn, I. Vrejoiu, M. Weinelt, P. Gaal, M. Herzog, C. von Korff Schmising, and M. Bargheer, *New J. Phys.* **13**, 093032 (2011).

²⁵R. O. Bell and G. Rupprecht, *Phys. Rev.* **129**, 90 (1963).

²⁶N. D. Ashcroft and N. W. Mermin, *Solid state physics*, 1st ed. (Saunders College, Fort Worth, 1976).

²⁷I. R. Entin, *Phys. Status Solidi A* **106**, 25 (1988).

²⁸W. Sauer, T. H. Metzger, J. Peisl, Y. Avrahami, and E. Zolotoyabko, *Physica B* **248**, 358 (1998).

²⁹E. Zolotoyabko and J. P. Quintana, *J. Synchrotron Radiat.* **9**, 60 (2002).

³⁰B. Sander, E. Zolotoyabko, and Y. Komem, *J. Phys. D: Appl. Phys.* **28**, A287 (1995).

³¹E. Zolotoyabko and I. Polikarpov, *J. Appl. Crystallogr.* **31**, 60 (1998).

³²A. M. Lindenberg, I. Kang, S. L. Johnson, T. Missalla, P. A. Heimann, Z. Chang, J. Larsson, P. H. Bucksbaum, H. C. Kapteyn, H. A. Padmore, R. W. Lee, J. S. Wark, and R. W. Falcone, *Phys. Rev. Lett.* **84**, 111 (2000).

³³D. A. Reis, M. F. DeCamp, P. H. Bucksbaum, R. Clarke, E. Dufresne, M. Hertlein, R. Merlin, R. Falcone, H. Kapteyn, M. M. Murnane, J. Larsson, T. Missalla, and J. S. Wark, *Phys. Rev. Lett.* **86**, 3072 (2001).

³⁴J. Larsson, A. Allen, P. H. Bucksbaum, R. W. Falcone, A. Lindenberg, G. Naylor, T. Missalla, D. A. Reis, K. Scheidt, A. Sjögren, P. Sondhaus, M. Wulff, and J. S. Wark, *Appl. Phys. A* **75**, 467 (2002).

³⁵B. E. Warren, *X-ray diffraction*, 2nd ed. (Dover Publications, INC., New York, 1990).

³⁶A. Bojahr, M. Herzog, L. Maerten, D. Schick, J. Goldshteyn, W. Leitenberger, R. Shayduk, P. Gaal, I. Vrejoiu, and M. Bargheer (unpublished).

³⁷A. I. Akhieser, Zhur. Eksp.: Teoret. Fiz. **8**, 1330 (1938).

³⁸L. D. Landau and G. Rumer, Phys. Z. Sovjetunion **11**, 8 (1937).

PAPER VII

Observing backfolded and unfolded acoustic phonons by broadband optical light scattering

L. Maerten, A. Bojahr and M. Bargheer.

Ultrasonics **56**, 148-152 (2015).



Contents lists available at ScienceDirect

Ultrasonics

journal homepage: www.elsevier.com/locate/ultras

Observing backfolded and unfolded acoustic phonons by broadband optical light scattering

L. Maerten^a, A. Bojahr^a, M. Bargheer^{a,b,*}^a Institut für Physik & Astronomie, Universität Potsdam, Karl-Liebknecht-Str. 24-25, 14476 Potsdam, Germany^b Helmholtz-Zentrum-Berlin für Energie und Materialforschung, Wilhelm-Conrad-Röntgen Campus, BESSY II, Albert-Einstein-Str. 15, 12489 Berlin, Germany

ARTICLE INFO

Article history:

Received 20 June 2014

Received in revised form 26 August 2014

Accepted 27 August 2014

Available online 10 September 2014

Keywords:

Phonon dispersion

Phonon backfolding

Time resolved Brillouin scattering

Superlattice

Broadband detection

ABSTRACT

We use broadband time domain Brillouin scattering to observe coherently generated phonon modes in bulk and nanolayered samples. We transform the measured transients into a frequency-wavevector diagram and compare the resulting dispersion relations to calculations. The detected oscillation amplitude depends on the occupation of phonon modes induced by the pump pulse. For nanolayered samples with an appropriately large period, the whole wavevector range of the Brillouin zone becomes observable by broadband optical light scattering. The backfolded modes vanish, when the excitation has passed the nanolayers and propagates through the substrate underneath.

© 2014 Elsevier B.V. All rights reserved.

1. Introduction

The advent of mode locked laser systems has lead to the exciting field of picosecond ultrasonics [1]. Coherently generated phonons can be studied using this powerful technique [1–4]. In contrast to frequency domain techniques, the spectral resolution of time domain scattering is only limited by the observed temporal range. The maximum frequency that can be resolved is limited by the temporal width of the excitation and probing pulses. The observable range of phonon wavevectors is primarily determined by the probe light spectrum [5]. The fraction of the Brillouin zone that can be covered by this spectrum, however, depends on the sample structure. In a superlattice, backfolding of phonon branches at the new Brillouin zone edge occurs due to the enlarged artificial unit cell and the thus narrower Brillouin zone. This backfolding of phonons has first been studied by Colvard et al. [6] using Raman scattering techniques and later also using time resolved methods [2–4,7]. More recent studies have concentrated on shaping the excitation profile [3,8–12], designing suitable superlattices for detection [9,13,14] and building phonon [15] and photon [8,16] cavities to enhance the generation and detection mechanisms [17]. The theoretical framework was given by Thomsen et al. [1] and extended to multilayer samples by Matsuda and Wright [18].

In this paper we report on measurements in which a metal film and metal-dielectric superlattices are used for the excitation of phonon dynamics in the samples. By means of broadband optical light scattering we detect a broad spectrum of the excited phonon modes simultaneously. We show, how the detected phonons determine the oscillatory features in transient optical reflectivity measurements: near zero wavevector modes lead to oscillations that are visible in all probe wavelength equally while the detection of larger wavevector modes lead to an oscillation frequency dependent on probe wavelength. In particular we discuss how the spatial period of a superlattice determines which fraction of the Brillouin zone becomes observable by optical light scattering. We show measurements, in which the whole wavevector range of the superlattice Brillouin zone is observed.

2. Experiment

In phonon-light scattering experiments, the energy of phonons is much smaller than the energy of the probing photons leading to the approximation, that the absolute of the incident photon wavevector k is approximately equal to the absolute of the scattered photon wavevector k' : $k \approx k'$. Let us consider energy and momentum conservation, as illustrated in Fig. 1(a). In the scattering event the momentum component of the photons perpendicular to the momentum of the phonon is unaltered. The parallel component $k \cos \theta$ is changed by addition (or subtraction) of the energy and momentum of a phonon. The energy and the parallel component

* Corresponding author at: Institut für Physik & Astronomie, Universität Potsdam, Karl-Liebknecht-Str. 24-25, 14476 Potsdam, Germany.

E-mail address: bargheer@uni-potsdam.de (M. Bargheer).

URL: <http://www.udkm.physik.uni-potsdam.de> (M. Bargheer).

<http://dx.doi.org/10.1016/j.ultras.2014.08.023>

0041-624X/© 2014 Elsevier B.V. All rights reserved.

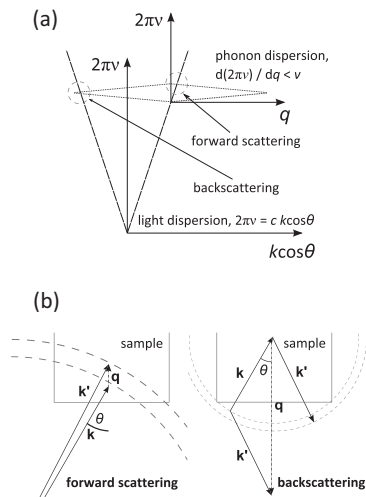


Fig. 1. (a) Illustration of energy and momentum conservation. A photon with given energy and momentum (dashed dispersion) can combine with a phonon (dotted dispersion, discussed in the next section) to form a new photon with approximately the same energy and momentum (forward scattering) or reversed momentum (backscattering). The energies are not drawn to scale, the light dispersion is much steeper in reality. (b) Illustration of momentum conservation and scattering geometry. In forward scattering the component of the incoming light parallel to the propagating phonon is nearly unaltered, in backscattering the component is reversed. The momenta are not drawn to scale. The changes in k and θ are not detectable in our experiment.

of the resulting photon must again fulfill the dispersion relation of light. Therefore, for a given photon there are two different solutions for the phonon involved (i. e. two intersection points in the figure) and thus two possible scattering regimes [19]. In the first regime the momentum of the scattering photon parallel to the travelling phonon is nearly unaltered (i.e. it is scattered in forward direction) and the transferred phonon momentum q is approximately zero:

$$q \approx 0 \quad (\text{forward scattering}) \quad (1)$$

The signature of this scattering regime is, that it occurs with approximately the same characteristic frequency for all photons independent of wavelength. It is usually detected in transmission geometry. We observe this type of scattering also in reflection geometry due to the reflection of the photons at different interfaces. In the second regime the momentum of the scattering photon parallel to the travelling phonon is reversed (i.e. it is scattered in backward direction) and the wavevector of the scattering phonon is thus given by:

$$q \approx 2k \cos \theta \quad (\text{backscattering}) \quad (2)$$

with internal angle of incidence with respect to the surface normal θ . Fig. 1(b) illustrates the vectorial nature of the momentum conservation for both scattering mechanisms: the photon momentum parallel to the phonon momentum is either reversed or nearly unchanged.

In time domain Brillouin scattering, the propagation of phonons that are coherently excited by a short pump pulse (excitation mechanism see below) are monitored by a delayed probe pulse. Instead of observing a spectral shift of the probe light as in ordinary (frequency domain) Brillouin scattering, we observe the frequency of the phonon in the time domain. Two effects modulate the light reflected from the sample by the frequency of the scattering phonons: one is, that the phonons present in the sample periodically

modulate the optical properties of the different layers leading to a periodic modulation of the reflection from each interface (this is presumably the dominant effect in the multilayers, where the optical properties of the individual layers differ) and the other one is that the light field that undergoes Brillouin scattering from a phonon interferes with a static reference of the probe light reflected from the sample surface and interfaces. In this latter case the relative phase of the interfering signals varies with the phase of the scattering phonon or equivalently, the distance the lattice distortion has propagated into the sample and thus with the time delay between the pump and probe pulses, leading to constructive or destructive interference (this is the effect in the substrate).

The modulation frequency is simply given by $v(q \approx 0)$ for forward scattering and $v(q = 2k \cos \theta)$ for backscattering. For a linear phonon dispersion $2\pi v = v \cdot q$, with sound velocity v , follows for backscattering:

$$v = v \cdot 2k \cos \theta / (2\pi) = v \cdot 2n(\lambda) \cos \theta / \lambda \quad (3)$$

with vacuum probe wavelength λ and refractive index $n(\lambda)$.

In this paper we show measurements on phonon dynamics in three different samples (compare Table 1): (a) a 37 nm ($\text{La}_{0.7}\text{Sr}_{0.3}$) MnO_3 (LSMO) transducer film on a SrTiO_3 (STO) substrate, (b) an $\text{LSMO}/(\text{Ba}_{0.7}\text{Sr}_{0.3})\text{TiO}_3$ (BST) superlattice with 15 double layers of 21 nm period and (c) a SrRuO_3 (SRO)/STO superlattice with 5 double layers of 140 nm period. The samples were prepared using pulsed laser deposition [20]. Sketches of the samples are shown in the upper insets of Fig. 2.

We use optical pump pulses with 800 nm wavelength and 120 fs pulse duration derived from an amplified Ti-Sa laser system at a repetition rate of 5 kHz to excite the absorbing layers (LSMO and SRO) with a fluence of a few tens of mJ/cm^2 . The rapid electron-phonon coupling and subsequent thermal expansion of the metal layers launches strain pulses into the material. In the case of a single metal film (sample (a)) on a transparent substrate, a bipolar strain pulse [1] is generated and propagates into the substrate (compare Fig. 2(a), lower inset, finite laser penetration depth neglected). Exciting a superlattice (samples (b) and (c)), a pulse train is generated. In this case left and right propagating strain fronts start from each metal-dielectric interface and lead to an oscillatory movement of the layers (standing wave). These strain pulses eventually propagate into the substrate where they build a train of strain pulses [12] (compare Fig. 2(c), lower inset, finite laser penetration depth neglected). The propagation of the coherently generated phonon pulses is monitored by a delayed probe pulse, which scatters from these phonons. In order to simultaneously probe several phonon wavevectors we generate a white light continuum in a sapphire disc which is detected in reflection geometry using a fibre-optic spectrometer for broadband detection [11,21].

In Fig. 2 we show colour plots of the wavelength dependent transient optical reflectivity for the three different samples. An instantaneous electronic response and slow thermalization effects have been subtracted. Sample (a) shows oscillations described by Eq. (3). In this sample, the single LSMO layer expands and launches a bipolar strain pulse (as depicted in the lower inset of Fig. 2(a)) into the STO substrate underneath. Because of good acoustic matching between layer and substrate, the strain wave has

Table 1
Details of selected samples. Acronyms: interlayer (IL), amount of double layers (# DL), thin film (TF), superlattice (SL).

Nr.	Type	Metal	Dielectric IL	# DL	Substrate
(a)	TF	LSMO, 37 nm			STO (100)
(b)	SL	LSMO, 7.3 nm	BST, 13.7 nm	15	STO (100)
(c)	SL	SRO, 13 nm	STO, 127 nm	5	STO (100)

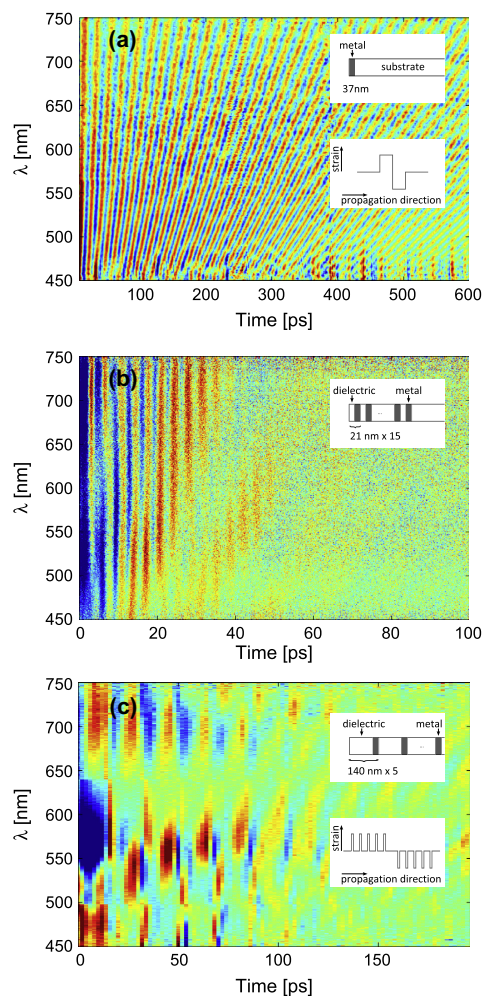


Fig. 2. Broadband transient reflectivity data at room temperature for different samples (colour code: $\Delta R/R_0$ [a.u.], slowly varying background subtracted): (a) thin LSMO film on bulk STO, (b) LSMO-BST superlattice with short period, (c) SRO-STO superlattice with long period, as depicted in the upper inset. In all graphs, the wavelength dependent oscillation period of the travelling phonon (seen via phonon backscattering) is clearly visible. Note that the time scales are different in each panel. In (b) and (c) the standing SL phonon showing a wavelength-independent oscillation frequency (via forward scattering) is also discernible. The lower insets in (a) and (c) show the excitation profiles. (For interpretation of the references to colour in this figure legend, the reader is referred to the web version of this article.)

completely entered the substrate when the strain front starting from the film-substrate interface has travelled once back and forth in the film. Thus after about $t = 2d_{\text{TF}}/v_{\text{LSMO}} \sim 12$ ps, where d_{TF} is the thickness of the film and v_{LSMO} is the sound velocity in the film (compare Table 2), there are no further coherent dynamics in the metal film. We have therefore cut off the first 12 ps from our data and only display the dynamics in the bulk STO underneath. For sample (b) in Fig. 2(b) we also observe the probe-wavelength dependent oscillations according to Eq. (3). Here, we focus on the first 100 ps of the dynamics, in which the excited pulse train is still present in the superlattice. In this comparatively short time window (compare: in Fig. 2(a), 600 ps are displayed), these appear as slow oscillations (10–20 ps, dependent on wavelength). In addition, we observe the λ -independent (forward scattering) signature

Table 2

Sound velocities employed in the calculations in nm/ps. v_b and v_c denote the average sound velocities in the superlattices [5] of samples (b) and (c).

$v_{\text{STO, layer}}$	v_{LSMO}	v_{BST}	v_{SRO}	$v_{\text{STO, substrate}}$	v_b	v_c
7.8	6.5	5.1	6.3	8	5.5	7.6

of the standing superlattice oscillation with period $\tau = d_{\text{SL}}/v_b \sim 3$ ps, with the appropriate period $d_{\text{SL}} = 21$ nm and average sound velocity in the superlattice $v_b \approx 5.5$ nm/ps. For sample (c) forward and backscattering signals have similar period. The sample is chosen such, that the energy of the standing superlattice phonon approximately coincides with the energy of the longitudinal acoustic phonon in the centre of the frequency window, where Brillouin scattering is observable for visible light. Thus, the λ -independent oscillation and the oscillation dependent on λ are superimposed, leading to the complicated picture in Fig. 2(c).

3. Theory

The dispersion relation of a superlattice can be calculated using the formula [22]

$$\cos(qd_{\text{SL}}) = \cos \left[2\pi v \left(\frac{d_1}{v_1} + \frac{d_2}{v_2} \right) \right] - \frac{1}{2} \left(\frac{|\rho_1 v_1 - \rho_2 v_2|}{(\rho_1 v_1 \rho_2 v_2)^{1/2}} \right)^2 \times \sin \left(\frac{2\pi v d_1}{v_1} \right) \sin \left(\frac{2\pi v d_2}{v_2} \right), \quad (4)$$

where d_1 and d_2 are the thicknesses of the individual layers with superlattice period $d_{\text{SL}} = d_1 + d_2$, v_1 and v_2 are the sound velocities and ρ_1 and ρ_2 the densities of materials 1 and 2. Since the cosine is a periodic function, its value does not change when multiples of 2π are added to the argument: $\cos(qd_{\text{SL}}) = \cos(qd_{\text{SL}} \pm n2\pi) = \cos((q \pm nG)d_{\text{SL}})$, with positive integer n . Furthermore the function is symmetric with respect to $q = 0$. In a simple picture, the size of the Brillouin zone extending originally to π/a , determined by the lattice constant a is reduced to π/d_{SL} when the larger period d_{SL} is introduced. Thus, points in the Brillouin zone beyond $q = \pi/d_{\text{SL}}$ can be displaced by multiples of the reciprocal lattice vector $G = 2\pi/d_{\text{SL}}$ in order to fit into the so called mini Brillouin zone. Graphically this means that the acoustic phonon branch is backfolded into the mini zone. Additionally, a gap in the dispersion curve opens at the edge of the mini zone, scaling with the acoustic mismatch of the materials [5]. When the acoustic mismatch is small, Eq. (4) simplifies to read

$$\cos(qd_{\text{SL}}) = \cos \left[2\pi v \left(\frac{d_1}{v_1} + \frac{d_2}{v_2} \right) \right], \quad (5)$$

where the energy gap can be neglected.

The dispersion curves of our samples calculated according to the parameters¹ in Tables 1 and 2, are shown in Fig. 3(a)–(c). In (a) the linear acoustic dispersion in bulk STO is displayed. The q -range accessible in our experiment via backscattering is indicated. In sample (b) the stacking of LSMO and BST layers with period d_{SL} leads to a reduction of the Brillouin zone and thus to the backfolding of the acoustic phonon branch. The frequency of the $q \approx 0$ superlattice phonon should be visible in all probe wavelengths via forward scattering and is therefore indicated as thin dashed line² although the q -value

¹ The parameters were checked by static X-ray diffraction.

² The maximum detected phonon frequency in our experiments here is $\nu \approx 0.25$ THz in forward scattering (compare Fig. 3(b), higher orders are too weakly excited). If the phonon dispersion is assumed to be flat at the intersection (compare Fig. 1(a)), the change in photon wavevector (and therefore q of the detected phonon) amounts to $0.006 \mu\text{m}^{-1}$ and is by far too small to be displayed in the graph. This underlines that $q \approx 0$ is a reasonable approximation for forward scattering in these experiments.

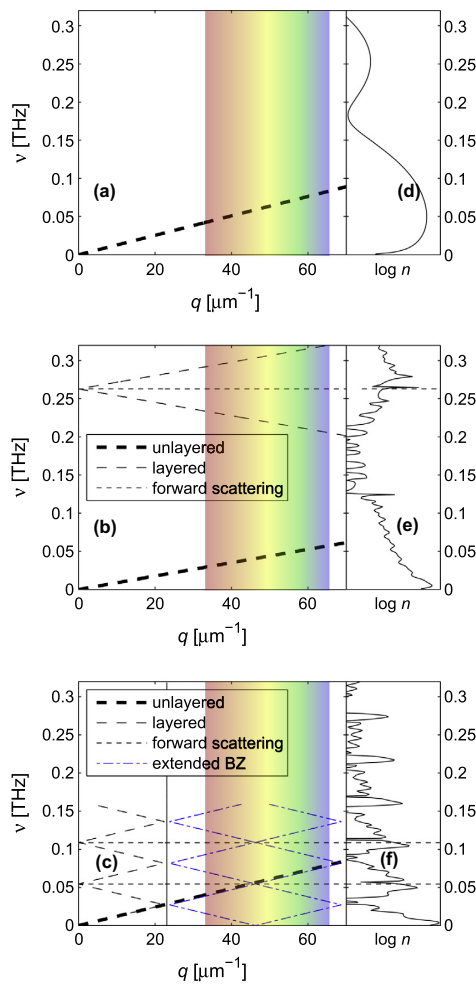


Fig. 3. (a)–(c) Calculated dispersion relations for the three samples according to Eq. (4). (a) Sample (a), unlayered, simple acoustic dispersion (black thick dashed line). (b) Sample (b), small period, the acoustic dispersion (black thick dashed line) is backfolded at the Brillouin zone edge $\pi/d_{\text{SL}} = 140 \mu\text{m}^{-1}$ (not shown), yielding the superlattice dispersion (black thin dashed line) with additional branches. The frequency of the $q \approx 0$ superlattice mode is indicated as thin dotted horizontal line (see main text). (c) Sample (c), the acoustic dispersion (black thick dashed line) is backfolded at the Brillouin zone edge $\pi/d_{\text{SL}} = 23 \mu\text{m}^{-1}$, yielding the SL-dispersion (black thin dashed line). The first zone scheme can be extended by adding a reciprocal lattice vector $G_{\text{SL}} = 2\pi/d_{\text{SL}}$, yielding the dispersion relation in the Brillouin zone (blue dash-dotted line). $q \approx 0$ superlattice mode again indicated as thin dotted horizontal line. The optically observable q -range in backscattering is highlighted in rainbow colours in each plot. (d)–(f) Corresponding occupation of the excited modes calculated in linear chain model. (For interpretation of the references to colour in this figure legend, the reader is referred to the web version of this article.)

on the axis only holds for phonons observed in backscattering. Fig. 3(c) shows the dispersion curve of the even larger superlattice (140 nm period) with yet smaller Brillouin zone. In this case, the q -range accessible to our probe technique via backscattering lies outside of the first Brillouin zone and we show an extended zone scheme, where multiples of the reciprocal lattice vector G_{SL} are added to each point in the mini zone. Again, the $q \approx 0$ phonon observable for all probe wavelengths is indicated as thin dashed line. In this superlattice, nearly the whole q -range of the original (reduced) Brillouin zone lies in the visible spectrum if a reciprocal lattice vector is added to

each point. This is possible if the detectable phonon bandwidth $\Delta q = q_{\text{min}} - q_{\text{max}}$ with q_{min} and q_{max} the minimum and maximum detectable phonon wavevector in backscattering, is at least the maximum wavevector in the Brillouin zone π/d_{SL} . If one octave is covered in probe bandwidth as approximately in our case: $q_{\text{max}} \approx 2q_{\text{min}}$, it follows that $\Delta q \approx q_{\text{min}}$. Thus, the whole q -range of the Brillouin zone can in principle be covered with one octave, if $q_{\text{min}} > \pi/d_{\text{SL}}$.

The occupation of each mode (i.e. the number of phonons in each mode) can be calculated analytically using a linear chain model [23,24]. We again chose the layer parameters according to Tables 1 and 2 and built a substrate composed of 5000 unit cells underneath. We assume an instantaneous heating and subsequent rapid expansion of the absorbing metal layers [24,25]. Since no anharmonic effects are included in the calculations the obtained results scale with the excitation fluence. The results for the samples are shown in Fig. 3(d)–(f). In (d), a broad spectrum of modes is excited around $q = 2\pi/d_{\text{TF}}$, with film thickness d_{TF} [11]. In the superlattices ((e) and (f)), modes around $q = G_{\text{SL}}$ are dominantly excited, which are backfolded to $q = 0$.

4. Discussion

Now we compare the calculations with our measurements. Fig. 4(a)–(c) shows temporal Fourier transforms of the original data in Fig. 2 as colour maps. The λ -axis has been converted to display the phonon wavevector $q = 4\pi n \cos(\theta)/\lambda$ for backscattering and the calculations are overlaid. Fig. 4(a) shows the linear acoustic dispersion in bulk STO. In Fig. 4(b) we observe the linear dispersion of the acoustic branch, traces of the first and second backfolded branch and the λ -independent signature of the $q \approx 0$ superlattice oscillation via forward scattering. Fig. 3(e) reveals why the wavelength independent oscillations dominate the signal: in this sample, the phonon modes that can be observed via backscattering are only weakly excited. Fig. 4(c) shows the diamond shape dispersion curve according to the extended zone scheme (compare Fig. 3(c)). Here, the forward scattering signal is nearly invisible. In the vicinity of the preferentially excited modes at $q = nG_{\text{SL}}$, many modes are populated that can be observed by the white light probe in backscattering and dominate the signal. When the phonon wavepacket has passed the superlattice (after $t \approx 2d_{\text{SL}}/v_c \approx 180$ ps) and travels into the substrate, the backfolded branches of the phonon dispersion unfold [12,26] and the usual acoustic dispersion in bulk STO (with slightly larger slope due to the larger sound velocity of $v_{\text{STO}} = 8$ nm/ps compared to $v_c = 7.6$ nm/ps that can be calculated for this superlattice) is retrieved, as shown in Fig. 5 for sample (c). The amplitude is now modulated by the wavevector selection rule $q = nG_{\text{SL}}$ in agreement with the simulations (Fig. 3(f)). The dispersion is identical to Fig. 4(a). The remaining discrepancies between theory and experiment, e.g. the intensity just below and above the first backfolded zone centre mode for sample (c), might be due to sample inhomogeneities particularly at the sample surface or anharmonicity effects that lead to changes in the spectrum of excited modes [11]. Additionally, the relative intensities of the frequencies in the Fourier transforms depend on the time window chosen for the transform and the high pass filtering that was performed in order to extract the oscillations. Furthermore, the intensity detected for each q -vector also depends on the dielectric function of the samples, how this changes with strain, and thus on the sample structure.

5. Summary

We have performed time resolved Brillouin scattering experiments on different nanolayered samples. We explained the temporal profiles and assigned their multiple features to Brillouin forward and backscattering processes. We extracted the dispersion

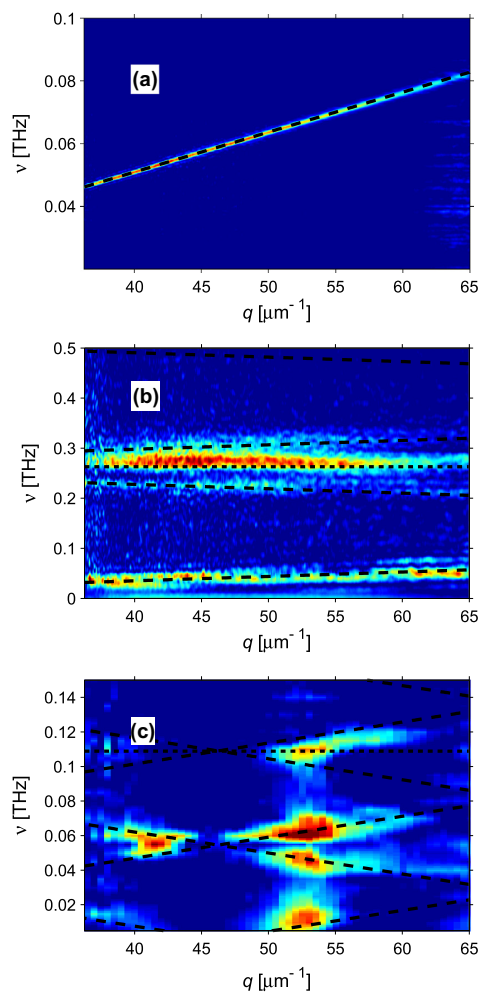


Fig. 4. Fourier transform of data in Fig. 2 for the three different samples. λ -axis has been converted to phonon wavevector for backscattering, calculations are overlaid. Colour code: Fourier amplitude [a.u.]. (For interpretation of the references to colour in this figure legend, the reader is referred to the web version of this article.)

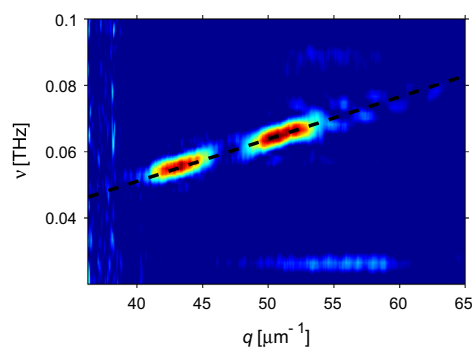


Fig. 5. Fourier transform of the first 1 ns transient reflectivity data from sample (c), where the first 150 ps have been cut out (temporal trace not shown), calculated dispersion overlaid. Colour code: Fourier amplitude [a.u.]. (For interpretation of the references to colour in this figure legend, the reader is referred to the web version of this article.)

relation of the observed phonons by Fourier transforming the temporal traces and compared these with theoretical calculations. In particular, we presented measurements on a sample, in which nearly the complete phonon wavevector range of the Brillouin zone is accessible to optical light scattering.

Acknowledgements

We thank I. Vrejoiu for providing the samples and the Leibniz Graduate School DinL for financial support.

References

- [1] C. Thomsen, H.T. Grahn, H.J. Maris, J. Tauc, *Phys. Rev. B* 34 (1986) 4129.
- [2] A. Yamamoto, T. Mishina, Y. Masumoto, M. Nakayama, *Phys. Rev. Lett.* 73 (1994) 740.
- [3] A. Bartels, T. Dekorsy, H. Kurz, K. Köhler, *Appl. Phys. Lett.* 72 (1998) 2844.
- [4] K. Mizoguchi, M. Hase, S. Nakashima, M. Nakayama, *Phys. Rev. B* 60 (1999) 8262. ISSN 0163-1829.
- [5] B. Jusserand, F. Alexandre, J. Dubard, D. Paquet, *Phys. Rev. B* 33 (1986) 2897.
- [6] C. Colvard, R. Merlin, M.V. Klein, A.C. Gossard, *Phys. Rev. Lett.* 45 (1980) 298.
- [7] A. Bartels, T. Dekorsy, H. Kurz, K. Köhler, *Phys. Rev. Lett.* 82 (1999) 1044. ISSN 0031-9007.
- [8] A. Huynh, B. Perrin, N. Lanzillotti-Kimura, B. Jusserand, A. Fainstein, A. Lemaitre, *Phys. Rev. B* 78 (2008) 233302. ISSN 1098-0121.
- [9] M.F. Pascual-Winter, A. Fainstein, B. Jusserand, B. Perrin, A. Lemaitre, *Appl. Phys. Lett.* 94 (2009) 103103 (pages 3).
- [10] M. Herzog, a. Bojahr, J. Goldshteyn, W. Leitenberger, I. Vrejoiu, D. Khakhulin, M. Wulff, R. Shayduk, P. Gaal, M. Bargheer, *Appl. Phys. Lett.* 100 (2012) 094101. ISSN 00036951.
- [11] A. Bojahr, M. Herzog, S. Mitzscherling, L. Maerten, D. Schick, J. Goldshteyn, W. Leitenberger, R. Shayduk, P. Gaal, M. Bargheer, *Opt. Express* 21 (2013) 21188.
- [12] R. Shayduk, M. Herzog, A. Bojahr, D. Schick, P. Gaal, W. Leitenberger, H. Navirian, M. Sander, J. Goldshteyn, I. Vrejoiu, et al., *Phys. Rev. B* 87 (2013) 184301.
- [13] M. Trigo, T.A. Eckhause, J.K. Wahlstrand, R. Merlin, M. Reason, R.S. Goldman, *Appl. Phys. Lett.* 91 (2007) 023115 (pages 3).
- [14] M.F. Pascual-Winter, A. Fainstein, B. Jusserand, B. Perrin, A. Lemaitre, *Phys. Rev. B* 85 (2012) 235443.
- [15] A. Huynh, N. Lanzillotti-Kimura, B. Jusserand, B. Perrin, A. Fainstein, M. Pascual-Winter, E. Peronne, A. Lemaitre, *Phys. Rev. Lett.* 97 (2006) 115502. ISSN 0031-9007.
- [16] N.D. Lanzillotti-Kimura, A. Fainstein, B. Perrin, B. Jusserand, *Phys. Rev. B* 84 (2011) 064307. ISSN 1098-0121.
- [17] N. Lanzillotti-Kimura, A. Fainstein, A. Huynh, B. Perrin, B. Jusserand, A. Miard, A. Lemaitre, *Phys. Rev. Lett.* 99 (2007) 217405. ISSN 0031-9007.
- [18] O. Matsuda, O.B. Wright, *J. Opt. Soc. Am. B* 19 (2002) 3028. ISSN 0740-3224.
- [19] B. Jusserand, D. Paquet, F. Mollot, F. Alexandre, G. Le Roux, *Phys. Rev. B* 35 (1987) 2808.
- [20] I. Vrejoiu, M. Alexe, D. Hesse, U. Gösele, *Adv. Funct. Mater.* 18 (2008) 3892. ISSN 1616-3028.
- [21] A. Bojahr, M. Herzog, D. Schick, I. Vrejoiu, M. Bargheer, *Phys. Rev. B* 86 (2012) 144306.
- [22] S.M. Rytov, *Akust. Zh.* 2 (1956) 71.
- [23] D. Schick, A. Bojahr, M. Herzog, C. von Korff Schmising, R. Shayduk, M. Bargheer, *Comput. Phys. Commun.* 185 (2014) 651. ISSN 0010-4655.
- [24] M. Herzog, D. Schick, P. Gaal, R. Shayduk, C. von Korff Schmising, M. Bargheer, *Appl. Phys. A* 106 (2012) 489. ISSN 0947-8396.
- [25] A. Bojahr, D. Schick, L. Maerten, M. Herzog, I. Vrejoiu, C. von Korff Schmising, C.J. Milne, S.L. Johnson, M. Bargheer, *Phys. Rev. B* 85 (2012) 224302.
- [26] M. Trigo, Y.M. Sheu, D.A. Arms, J. Chen, S. Ghimire, R.S. Goldman, E. Landahl, R. Merlin, E. Peterson, M. Reason, et al., *Phys. Rev. Lett.* 101 (2008) 025505.

PAPER VIII

Selective preparation and detection of phonon polariton wavepackets by stimulated Raman scattering

J. Goldshteyn, A. Bojahr, P. Gaal, D. Schick and
M. Bargheer.

Phys. Status Solidi B **251**, 821-828(2014).

Selective preparation and detection of phonon polariton wavepackets by stimulated Raman scattering

J. Goldshteyn^{1,2}, A. Bojhr², P. Gaal^{1,2}, D. Schick², and M. Bargheer^{*,1,2}

¹ Helmholtz-Zentrum-Berlin für Energie und Materialforschung, Wilhelm-Conrad-Röntgen Campus, BESSY II, Albert-Einstein-Str. 15, 12489 Berlin, Germany

² Institut für Physik & Astronomie, Universität Potsdam, Karl-Liebknecht-Str. 24–25, 14476 Potsdam, Germany

Received 5 August 2013, revised 1 November 2013, accepted 7 November 2013

Published online 12 December 2013

Keywords lithium niobate, polaritonics, phonon polariton, Raman scattering

*Corresponding author: e-mail bargheer@uni-potsdam.de, Phone: +49 331 977 4272, Fax: +49 331 977 5493

Wavevector-selective impulsive excitation of phonon-polaritons by a spectrally broad femtosecond transient grating produces wavepackets propagating in opposite directions. The photons in spectrally narrow probe pulses are scattered from these elementary excitations in lithium niobate (LiNbO₃). Both elastically and inelastically scattered photons are simultaneously detected in a spectrometer. The Stokes- and anti-Stokes

shifted probe pulses uniquely determine the propagation direction of the detected polariton wavepacket components and correspond to creation or annihilation of phonon-polaritons. Our experiments with spectrally broad pump and spectrally narrow probe pulses allows dissecting the four-wave-mixing process into two sequential stimulated Raman scattering events.

© 2013 WILEY-VCH Verlag GmbH & Co. KGaA, Weinheim

1 Introduction In ionic crystals, the coupling of transverse optical phonon modes and their electromagnetic dipole field results in a quasiparticle excitation called phonon polariton (PP) [1, 2]. First frequency domain observations of PP were made with forward Raman scattering in GaP and stimulated Stokes scattering in LiNbO₃ crystals [3, 4]. Femtosecond laser pulses permitted impulsive excitation of PPs and vibrational modes [5, 6].

For impulsive generation of PP the pulse duration of the excitation laser has to be shorter than the polariton oscillation period. Consequently the spectral width $\Delta\lambda$ of the excitation laser pulses with carrier wavelength λ is large enough to cover the angular frequency ω_{pp} of the PP: $\Delta\lambda/\lambda^2 > \omega_{pp}/2\pi c$. For low frequency PP the quasi-particle is essentially light like and propagates at the velocity c/n_{THz} of far infrared light with the appropriate refractive index n_{THz} . The generation mechanism is described as the nonlinear optical process of difference frequency generation (DFG). For high frequency PP the quasiparticle is essentially phonon like, i.e., it corresponds to a Raman- and infrared active optical lattice vibration. Near the transverse phonon resonance, the oscillation of the ionic lattice gains importance in the contribution to the nonlinear susceptibility [7–9]. In this case the excitation

process is described in terms of impulsive stimulated Raman scattering (ISRS) [10]. In both cases energy and momentum conservation rules apply for three participating particles [11]. The dispersion relation (introductory review [12]) sets the group velocity of the quasiparticle, which identifies it as light- or phonon-like. In the intermediate region the PP is a quasiparticle associated with a light field as well as strong optical lattice vibrations which propagate as a coupled entity through the crystal at light-like speeds [13]. The PP field can also be described as far-infrared Cherenkov radiation [7, 14]. Several research groups focused on the coherent excitation of PP wave packets [13–17]. Excitation by a single laser pulse supports PP generation with wavevectors limited not only by the laser pulse bandwidth $\Delta\lambda$ but also by the convergence angle of the focused light. A wavevector selective excitation of PP is achieved by two noncollinear laser pulses which write a transient polarization grating into the sample. The complex polariton dispersion including the damping rate was measured in the time domain [18]. The most common setup uses a boxcar geometry in which a probe laser pulse is diffracted from the transient PP grating, where the diffracted intensity depends on the time delay τ between the two pump pulses and the probe pulse [5]. The Nelson group

explored coherent control of the excited PPs in time and space by advanced laser shaping techniques [19]. The propagation of PP can be visualized by ultrafast time resolved phase-contrast microscopy (Schlieren-Imaging) [20], where the movies show the wavelike behavior of PP such as interference, focusing, diffraction, etc. [12, 21]. Moreover, PP can be used for efficient generation of tunable narrow-band terahertz light pulses [22].

Generally the entire process of polariton generation and probing in a boxcar geometry is described as a single coherent process of four-wave mixing (4WM). The process can essentially be viewed as a transient grating composed of PPs, which are impulsively generated by the interference of two pump pulses at $\tau = 0$ and the detection by impulsive stimulated Raman scattering at later time τ , where the stimulation is given by the light field associated with the PP. Despite the general acceptance of this interpretation, there only exist experiments where all pump and probe pulses are either spectrally broad and temporally short [17, 23] or temporally long and spectrally narrow [4, 24]. In the former case the dynamics can be resolved with high time resolution, but the expected frequency shifts by the inelastic (Raman) light scattering with creation or annihilation of PPs remains unresolved due to the large bandwidth $\Delta\lambda$ of the probe pulses. The spectrally narrow pulses used to confirm the spectral shifts [4, 24] but see the rapid propagation and decay of the PP indirectly as contributions to the linewidth.

In this paper, we use ultrashort light pulses to impulsively excite PP with a wavevector selected by the angle Θ between the two pump pulses. The excitation is probed with a narrow band probe pulse which can resolve the Raman shifts on the one hand, but with a pulse duration short enough to follow the propagation and damping of the PP on the other hand. This approach helps clarifying that the four wave mixing experiment consists in fact of an inelastic scattering of pump photons which impulsively excite phonon-polaritons and a stimulated scattering of probe photons from this elementary excitation, which leads to annihilation or creation of PP. Left- and right propagating PP are uniquely identified by the Raman probe event, since they undergo only Stokes or anti-Stokes scattering. The frequencies $\omega_{pp}/2\pi$ and wavevectors q_{pp} of the right and left propagating PP are directly determined with a high precision and the dispersion relation $\omega_{pp}(q)$ of the lower polariton branch of LiNbO₃ is mapped out to larger q_{pp} values. We discuss that the wavelength resolved detection of the diffracted light leads to an interference of elastically scattered and inelastically diffracted light, which gives rise to oscillations in the time domain data.

2 Method and idea We perform degenerate 4WM experiments on PPs in LiNbO₃ in the boxcar geometry depicted in Fig. 1. A Ti:sapphire amplifier laser system provides FWHM = 60 fs pulses with a repetition rate of 1 kHz at a central wavelength of 800 nm. Two pump pulses (≈ 20 mW) with wavevectors \mathbf{k}_1 and \mathbf{k}_2 excite a transient grating composed of PPs. A third optical pulse, \mathbf{k}_3 , is diffracted by this grating into the direction \mathbf{k}_4 , where it is detected. The polar-

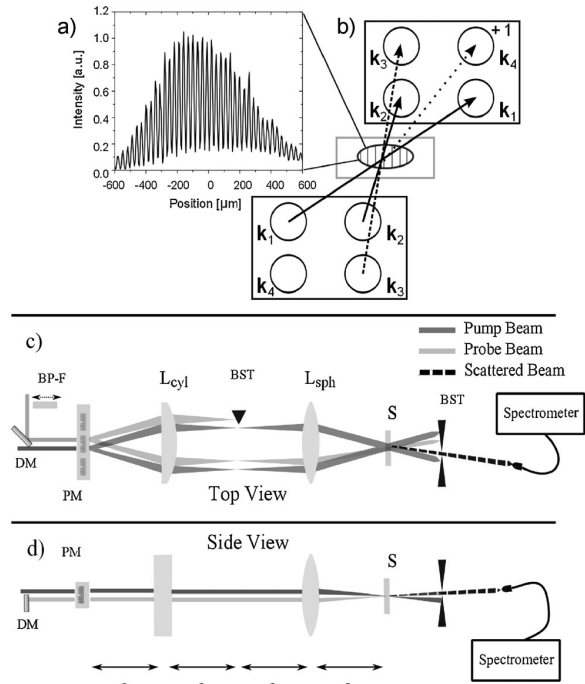


Figure 1 (a) Intensity profile detected on a CCD camera at the sample position when both pump pulses (\mathbf{k}_1 and \mathbf{k}_2) interfere under an angle of $\Theta = 1.5^\circ$, given by the focal length of the spherical and cylindrical lens and the spatial period of the phase mask Λ_G . The observed fringe period measures the component of the excited PP $q_{||} = q_G$ parallel to the crystal surface. (b) Schematic illustration of the boxcar arrangement for four-wave mixing (4WM). Two laser beams \mathbf{k}_1 and \mathbf{k}_2 intersect in a transparent sample to create a transient spatial modulation of the refractive index. A delayed third beam \mathbf{k}_3 is diffracted into the direction \mathbf{k}_4 . (c) Top view of the 4WM setup. The probe beam is displaced for clarity. Used abbreviations: BP-F, bandpass filter; BST, beam stop; DM, D-shape mirror; L, lens; PM, phase mask; S, sample. (d) Side view of the same setup.

ization of all three beams is set parallel to the ferroelectric axis of the crystal. We excite and probe the lowest A₁ transverse optical mode of the lattice [25]. We use the optical setup introduced by the Nelson group [26], in which a transmission grating phase mask is imaged onto the sample by a spherical and a cylindrical lens, as shown in Fig. 1c. The pump laser pulse is split into a +1st and -1st diffraction order at the phase mask transmission grating, giving rise to the two pump-pulses with wavevectors \mathbf{k}_1 and \mathbf{k}_2 . This creates a transient excitation grating in the sample with an ellipsoidal cross section as shown in Fig. 1. If we replace the sample by a CCD camera, we can record the interference fringes (Fig. 1a) with the transient grating period [27]

$$\lambda_{ig} = \frac{\lambda}{2 \sin(\Theta_{\text{air}}/2)}, \quad (1)$$

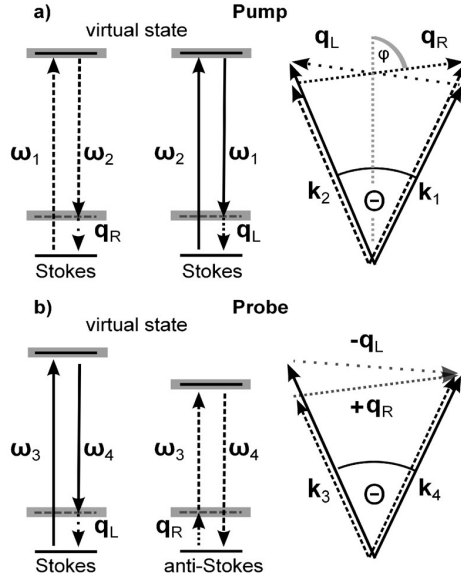


Figure 2 (a) Energy level and momentum conservation diagrams considered in the impulsive generation of PP. Two counter-propagating PPs q_R and q_L are excited within the bandwidth of the laser pulses by ISRS. (b) The probe process is sensitive to the light scattered from left and right propagating PP. The spectrometer position selects the direction k_4 along which light is detected and the spectrometer pixel fixes the wavevector magnitude $|k_4|$ of the detected light.

where λ is the wavelength of the excitation pulses and Θ_{air} is the intersection angle in air.

A time-delayed probe pulse derived from the same laser is sent through the same transmission grating slightly below the pump pulse and is imaged onto the sample in the same way. However, the beam along k_4 is blocked and only k_3 is sent onto the sample, where it is diffracted into the k_4 direction towards the detector, yielding a nearly background-free signal. We have implemented two modifications of the original setup [26]: The detecting photodiode is replaced by a fiber-optic spectrometer, which spectrally resolves the light waves emitted from the sample into the k_4 direction with a resolution of about 0.2 nm. In addition we can insert a band-pass filter into the probe beam to cut down the bandwidth of the probe pulse from 30 to 2 nm (centered at 795 nm), which increases the pulse duration from 60 to 610 fs, as measured by transient grating FROG [11].

This setup using narrow band probe pulses together with a spectrometer which permits the time-resolved detection of the frequency shift induced by the Stokes and anti-Stokes Raman scattering events, and guarantees an unambiguous discussion and interpretation of the processes involved. The time resolution remains sufficient to measure the damping of the PPs.

Figure 2 summarizes how we analyze the 4WM process in terms of two sequential Raman scattering events, one for exciting PP and one for probing them. We first discuss

the excitation of PP (Fig. 2a), for which the Stokes scattering describing creation of PPs is the dominant Raman process.¹ Hence, if $|k_1| > |k_2|$ a right-propagating PP with wavevector q_R is created, whereas the generation of a left-propagating polariton q_L requires $|k_1| < |k_2|$ (see Fig. 2a). Since both pump-pulses possess the same frequency spectrum, both processes are equally likely. The directions of the pump photon momenta are fixed by the parallel-beam geometry with minimal angular divergence in the plane of the optical table resulting from the combination of a cylindrical and a spherical lens [26]. The energy- and momentum conservation of the Raman scattering event therefore lead to PPs propagating in exactly two directions, to the right and the left with a small component into the sample. The wavevector is selected by the angle Θ between the crossed laser beams [3] in the medium, which can be calculated from Snell's law. The magnitude of the wavevector is calculated using the law of cosine in the wavevector diagram (Fig. 2):

$$q_{\text{pp}} = \frac{n}{c_0} \sqrt{\omega_1^2 + \omega_2^2 - 2\omega_1\omega_2 \cos(\Theta)}, \quad (2)$$

where n is in our case the extraordinary refractive index, ω_1 and ω_2 are the angular frequencies of the first and second beam, and c_0 is the speed of light in vacuum. The angular frequency ω_{pp} of the excited PP satisfies the conservation of energy $\omega_{\text{pp}} = |\omega_1 - \omega_2|$. The relative bandwidth of the PPs is given by the relative bandwidth of the laser pulses: $\frac{\Delta\omega_{\text{pp}}}{\omega_{\text{pp}}} \approx \frac{\Delta\omega_{\text{pp}}}{q_{\text{pp}}} \approx 3\%$. The magnitude of the excited wavevectors $q_{\text{pp}} \pm \Delta q_{\text{pp}}$ and the corresponding frequencies $\omega_{\text{pp}} \pm \Delta\omega_{\text{pp}}$ are set by the transmission phase mask grating [26]. This choice also determines the angle φ with respect to the bisector of incident laser beams, at which the polaritons travel into the sample.

$$\cos(\varphi) = \frac{nv_{\text{pp}}}{c_0} \cos\left(\frac{\Theta}{2}\right) = \frac{n\omega_{\text{pp}}}{c_0 q_{\text{pp}}} \cos\left(\frac{\Theta}{2}\right), \quad (3)$$

where v_{pp} is the phase velocity of the PP. Because of this angle φ , the wavelength λ_{pp} of the PPs is few percent smaller than the transient grating λ_{tg} written by the laser pulses [28, 29].

In the probe process both Stokes and anti-Stokes processes are relevant, since the pump-pulses lead to a considerable population of the two well-defined modes. The boxcar setup is highly symmetric, however, by blocking k_4 , we break this symmetry. Therefore panel 2b only discusses the situations, where only k_3 is impinging on the sample. In the Stokes scattering process this incoming photon with frequency ω_3 is inelastically scattered from the left-propagating PP q_L under the stimulated emission of a red shifted photon with frequency ω_4 and an additional PP with wavevector q_L . Anti-Stokes scattering in this geometry leads to annihilation of a right-propagating PP q_R under the emission of a blue-shifted photon with ω_4 . Figure 2b shows these two

¹At room temperature, PP modes in the THz frequency range have only small thermal occupation numbers.

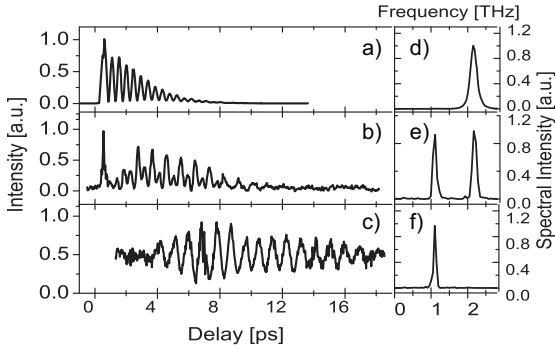


Figure 3 (a) Transient 4WM signals for excitation of PPs with wavevector magnitude $q = 1050 \text{ cm}^{-1}$ in a standard boxcar configuration, where pump and probe overlap, all pulses are short and spectrally broad. The signals are integrated over the spectrum. (b) Same, but with the probe spot displaced by $350 \mu\text{m}$ to the left side. (c) Same, but with the probe spot displaced by $750 \mu\text{m}$ to the left side. (d–f) Corresponding Fourier analysis of all three data sets is presented in (d)–(f).

processes, which contribute to the signal detected in \mathbf{k}_4 direction on a certain pixel of the detecting spectrometer, i.e., for a fixed wavevector magnitude $|\mathbf{k}_4|$. For a different pixel on the spectrometer the schematic is simply scaled, reconfirming that all PP have a wavevector parallel to either \mathbf{q}_L or \mathbf{q}_R . If we would choose \mathbf{k}_4 as the probe beam with finite bandwidth and detect with the spectrometer in \mathbf{k}_3 direction, the roles of created or annihilated PPs would switch.

In the Section 4, we analyze the intensity at each spectrometer pixel given by the interference of photons generated in the two processes with the weak contribution of light elastically scattered by impurities. We show how the delay dependence of the observed signal emerges from the phase shifts accumulated for a certain time-delay after the pump pulse. First we describe and qualitatively discuss experimental observations justifying this description.

3 Experimental results In Fig. 3, we examine the propagation of PPs with a wavevector magnitude of $q = 1050 \text{ cm}^{-1}$ by probing in different spatial regions near the elliptical excitation spot ($70 \mu\text{m} \times 800 \mu\text{m}$). Figure 3a shows transient 4WM data, where the pump and probe pulses spatially overlap. The signal oscillates at $2(\omega_{pp}/2\pi) = 2.2 \text{ THz}$, which is attributed to the fact that the transient grating is a standing wave composed of two counter propagating polariton waves (see Section 4) [30]. The signal decay can be partially ascribed to the propagation of the PPs out of the probed region and partially to coupling with phonon-modes. The ratio of the signal maximum and the scattering background for $\tau < 0$ is $I_{\text{max}}/I_s = 400$. For Fig. 3c the probe is displaced by $750 \mu\text{m}$ to be essentially separated from the excitation region. Now the signal is modulated at the fundamental polariton frequency $\omega_{pp}/2\pi = 1.1 \text{ THz}$, and we attribute this to the fact that the probe pulse can only be scattered by the left propagating PP [31]. In this case

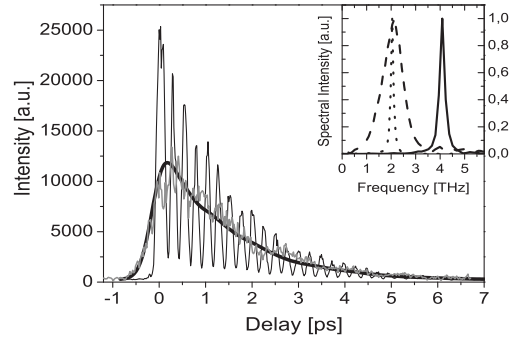


Figure 4 Transient 4WM data from LiNbO_3 (thin black line) for the selected wavevector magnitude $q = 2090 \text{ cm}^{-1}$ with short and spectrally broad pump and probe pulses. The spectrally integrated intensity detected at the spectrometer oscillates at twice the frequency of the PP $2\omega_{pp}/2\pi$ (see text). The thick black line shows the same signal when only the probe pulse is spectrally narrowed to 2 nm which leads to a probe pulse duration of 610 fs . For comparison, the thick gray line shows a convolution of the signal with spectrally broad probe with a Gaussian function with temporal width of $\text{FWHM} = 610 \text{ fs}$. Inset: Normalized power spectrum (black solid line) as obtained after Fourier analysis of the oscillating 4WM data and the same spectrum scaled by a factor of two (black dotted line). It shows the same central frequency as the anti-Stokes spectrum shift (black dashed line) as it is detected on the spectrometer for narrow band widths probe pulses.

$I_{\text{max}}/I_s = 2$. In the intermediate regime (Fig. 3b), where the probe is displaced by $350 \mu\text{m}$, the signal level is still low, with $I_{\text{max}}/I_s = 3$. We observe both frequencies $\omega_{pp}/2\pi$ and $2(\omega_{pp}/2\pi)$ and attribute this to the left propagating PP moving through the observation spot whereas the right propagating PP only leaves this region. Panels 3d–f show the according Fourier spectra.

The use of short probe pulses allows us to resolve the fast lattice dynamics in the time domain. The oscillation frequency and PP damping time are well accessible. Consequently, the dispersion relation of the quasiparticle could be determined. However, the broad spectrum of the probe pulses prevents the direct detection of the inelastic nature of the Raman interaction, because the associated shift is much smaller than the bandwidth of the probe pulse. In order to directly observe the Stokes- and anti-Stokes shifted Raman scattering contributions, we narrowed the probe spectrum down to 2 nm . In principle, one could use radiation with even better monochromatization at the expense of time resolution and efficiency. Here we chose a compromise that still permits the measurement of decay times.

The effect of narrowing the probe spectrum is exemplified for a typical measurement with perfect spatial overlap of pump and probe in Fig. 4 for a somewhat larger wavevector magnitude $q = 2090 \text{ cm}^{-1}$. For $\tau < 0$ negligible intensity I_s of light is diffracted or scattered into the detector. As discussed above, for $\tau > 0$ the measured intensity oscillates at twice the frequency of the PPs $2(\omega_{pp}/2\pi)$ imprinted into the sample and decays as the polaritons propagate out of the

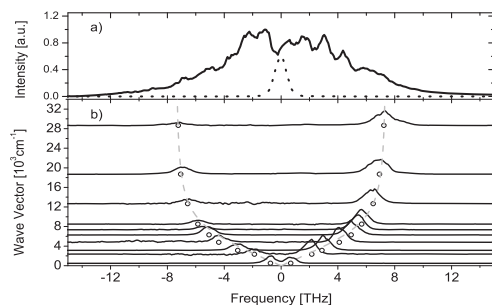


Figure 5 (a) Spectra of pump (solid line) and probe pulses (dotted line). (b) Solid lines show intensities of the spectra observed along k_4 , when the PP wavevector is tuned to the wavenumber indicated by the intersection with the left axis. The maxima of these spectra are indicated as open circles in the $\omega(q_{pp})$ plot. The calculated dispersion relation of PPs in LiNbO₃ is shown by the gray dashed lines. The parameters are taken from Ref. [25].

probed area and are damped by coupling to other modes [18, 30]. The Fourier transform of the signal in the inset of Fig. 4 peaks at 4 THz. We compare this result to a measurement, where the spectrum of the probe pulse was cut down to 2 nm. The signal decay (black line) is identical to the one observed with short pulses, convoluted with a Gaussian function with the temporal duration $\tau_{\text{pulse}} = 610$ fs of the spectrally narrow pulse (thick gray line). On the spectrometer the probe pulse is clearly shifted by $\Delta\omega = \pm|\omega_4 - \omega_3| = 2$ THz. The anti-Stokes case (positive shift) is indicated in the inset of Fig. 4. The comparison experimentally proves that the signal oscillates at $2(\omega_{pp}/2\pi)$ for broadband probe pulses. The price for the higher spectral resolution, is a smeared out signal rise at $\tau = 0$ which is now limited by the probe pulse duration.

Panel 5b summarizes the detected spectrometer signal including Stokes and anti-Stokes shifted signal components for polariton gratings tuned to different wavevectors q_{pp} by tuning the intersection angle Θ according to Eq. (2). The peak position of the measured Raman shift $\omega_{pp}/2\pi$ as a function of q_{pp} represents the dispersion relation of PPs in LiNbO₃. The dashed line is the calculated phonon polariton dispersion. The data show an excellent agreement with the theory. The measurement of the PP dispersion relation is extended to higher wavevectors. Figure 5a compares the bandwidth of the pump pulses (solid lines) to the bandwidth of the probe pulses. We emphasize that the signal contribution without frequency shift, i.e., elastic light scattering, is negligible.

In order to directly identify the propagating PPs, we repeat the narrow probe band experiments with a probe beam spatially displaced to the left. For reduced damping and longer propagation lengths we choose a small wavevector $q_{pp} = 700$ cm⁻¹ of the transient grating. In addition we minimize the probed region by a knife-edge which blocks the flank of the probe pulse overlapping with the pump region.

We look at left-propagating PP q_L . The probe pulse enters along k_3 and the detector is in k_4 direction. In Fig. 6a we reproduce the vector diagram from Fig. 2b consistent with

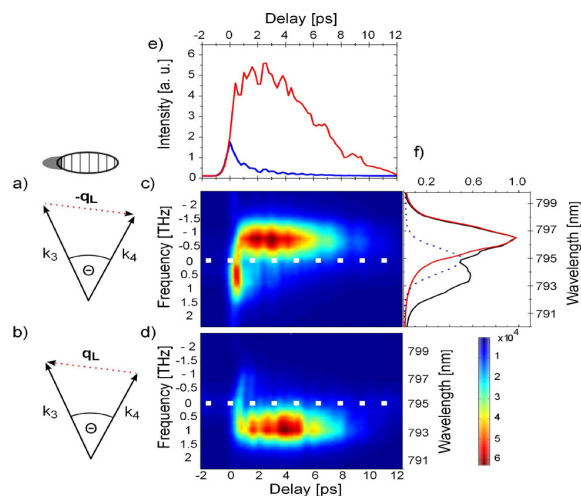


Figure 6 Detection of left propagating PP. The probe spot is displaced by 500 μm and is spatially cut to prevent any overlap of pump and probe areas. (a) Wavevector diagram for the case of Stokes scattering from q_L , when k_3 is the incoming light and the spectrometer detects light along k_4 . (b) Same for anti-Stokes scattering, however, now with incoming light along k_4 and detection along k_3 . (c) Transient Stokes lines indicating the creation of left propagating PP with a wavevector magnitude of $|q_L| = 750$ cm⁻¹. The dashed line shows the unshifted probe spectrum. (d) Same for anti-Stokes scattering with annihilation of the PP. (e) Transients of Stokes (red line) and anti-Stokes light (blue line) determined from data set shown in (c) and integrated over wavelengths around $\lambda = 797$ nm and $\lambda = 793$ nm respectively. (f) Light spectrum around $\tau = 0$ ps (black line) indicates scattering from left and right propagating PP. For later times (3.8–7.8 ps) the spectrum (red line) shows only Stokes scattering.

energy and momentum conservation in this case, i.e., only a Stokes scattering accompanied by the creation of an additional polariton q_L is allowed. The contour plot in Fig. 6c verifies this. In fact, the cross sections in Fig. 6f shows that immediately after pumping there are still small contributions of an anti-Stokes scattering from right-propagating q_R . The cross sections for $\tau > 3$ ps, however, exclusively show Stokes scattering from q_L . The time-dependence of the Stokes (red) and anti-Stokes (blue) signal depicted in Fig. 6e shows a sharp rise of both signals limited by the probe pulse duration. The blue signal associated with the right-propagating polariton q_R immediately fades out according to the damping and direction of propagation. In contrast, the red signal keeps rising as the polariton q_L moves more and more into the probe region before it finally decays due to damping.

To verify our interpretation that Stokes and anti-Stokes scattering can clearly distinguish q_R and q_L , we exchange the roles of k_3 and k_4 by shining only k_4 on the same probe spot and detecting in k_3 direction. Now the vector diagram in panel 6b shows the only detected scattering process, which is anti-Stokes scattering with annihilation of a PP q_L . This is confirmed by the experimental spectrum.

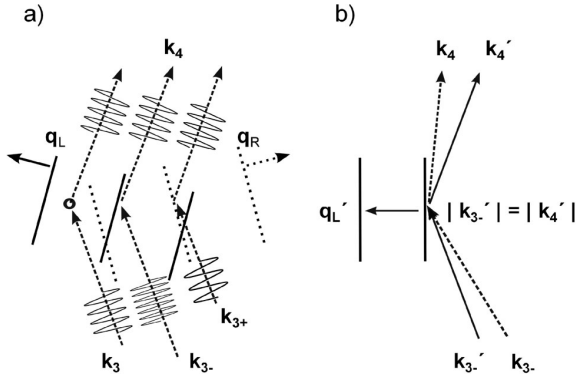


Figure 7 (a) Visualization of the three components of light fields that contribute to the signal intensity on a certain pixel of the spectrometer which detects light along a fixed direction of \mathbf{k}_4 . The spectrometer pixel selects $|\mathbf{k}_4|$. Incoming wavevectors along \mathbf{k}_3 have different magnitude (wavelength). (b) Geometric representation of the diffraction from the PP grating in the laboratory frame (dashed vectors) and in the frame of reference co-propagating with the PP at relativistic velocities (solid vectors) [32].

4 Discussion Up to now we have qualitatively discussed the measured data, demonstrating that the narrow-band probe pulses can uniquely identify left- and right-propagating polaritons via the red or blue shift they induce in a Raman scattering event. In this section, we lay out the mathematical background for describing the Raman-scattering probe process which detects the excited PPs [30], when the scattered radiation is spectrally resolved by a monochromator. In particular we quantitatively explain the oscillation periods and damping constants observed in the experimental data (Figs. 3 and 4) and show how the narrow-band experiments are explained in the same mathematical framework. We again choose the incoming light field E_3 to have a wavevector parallel to \mathbf{k}_3 and record the scattered light field E_4 in the \mathbf{k}_4 direction. We distinguish three contributions: $E_4 = E_+ + E_- + E_{el}$, where E_+ and E_- are the components inelastically scattered from PPs (anti-Stokes and Stokes) whereas E_{el} corresponds to light elastically scattered by the sample, e.g., from inhomogeneities.

Figure 7a visualizes the origin of the three signal contributions. Since the monochromator spectrally resolves the detected light field, each pixel coherently adds up three contributions yielding the same frequency ω_4 . They originate either from the incoming frequency component $\omega_{3,el}$ for the field E_{el} which is elastically scattered or from ω_{3-} for the field E_- which is Stokes scattered by a PP with frequency ω_{pp} , or from ω_{3+} for the field E_+ which is anti-Stokes scattered.² This implies $\omega_{3\pm} \pm \omega_{pp} = \omega_4$ and $\omega_{3,el} = \omega_4$. From the discussion above we know that E_+ leads to annihilation of right-propagating polaritons and E_- to the creation of a left-propagating polariton, where the Raman probe processes are stimulated by the polaritons which were previously excited

²As a good approximation we assume that $\omega_{pp} = \omega_{pp+} = \omega_{pp-}$.

by Raman pump pulses along \mathbf{k}_1 and \mathbf{k}_2 . These inelastic scattering processes can be described as a Bragg diffraction from a moving grating where the frequency shift is explained by the optical Doppler effect [32]. Unlike acoustic Bragg gratings the high velocity of the PP and the correspondingly large Raman shift lead to the situation, where the Bragg diffraction is not symmetric with respect to the PP wavefronts. Figure 7b shows for the case of a left-propagating PP, how the incoming and inelastically scattered wavevectors have to be transformed in the frame of reference co-propagating with the PP at relativistic speed. In this frame of reference the Bragg scattering is elastic (the grating is not moving) and hence symmetric. Each scattering event can be analyzed in its appropriate co-propagating frame of reference, since phase differences are invariant under Lorentz transformations and hence the explanation will hold in the laboratory frame [33]. We have discussed this relativistic transformation here, in order to emphasize, that despite the asymmetric scattering, the phases of the scattered waves are the same, irrespective of the position in the sample, where the scattering takes place. This is evident for symmetric Bragg diffraction.

We now discuss how the delay τ of the optical pulse exciting the PP and the optical pulse probing the PP give rise to the observed signals by changing the relative phase of the contributing signals. We define the phases of the spectral components of the incoming light fields $E_3(\omega_4)$, $E_3(\omega_{3-} = \omega_4 + \omega_{pp})$, and $E_3(\omega_{3+} = \omega_4 - \omega_{pp})$, to be $\phi_{3,el}(0)$, $\phi_{3-}(0)$, and $\phi_{3+}(0)$ for $\tau = 0$, respectively. The relative phases of the incoming spectral light components are fixed. The inelastically scattered light fields detected on a pixel of the spectrometer observing in the direction \mathbf{k}_4 are

$$E_{\pm} = \pm E_{\pm 0} e^{-\gamma\tau} e^{i(\omega_4 t + \phi_{4\pm}(\tau))}, \quad (4)$$

where $E_{\pm 0}$ quantifies the inelastic scattering efficiency and $e^{-\gamma\tau}$ describes the reduction of the scattered light field due to the damping of the PPs. $\phi_{4\pm}(\tau)$ is the phase of the scattered light fields. The elastically scattered contribution is

$$E_{el} = E_{el0} e^{i(\omega_4 t + \phi_{4,el})} \quad (5)$$

with E_{el0} and $\phi_{4,el}$ quantifying the efficiency and phase of elastic scattering, e.g., from impurities. When the pump pulse is delayed with respect to the probe by τ , the polariton wavefronts advance by $|r_{\pm}| = v_{pp}\tau = \omega_{pp}/q_{pp}\tau$ in the directions of the polariton propagation $\mathbf{q}_{R/L}$. The phase of the scattered light wave is shifted to

$$\phi_{4\pm}(\tau) = (\mathbf{r}_{\pm} \cdot \mathbf{k}_{3\pm} - \mathbf{r}_{\pm} \cdot \mathbf{k}_4) = \pm\omega_{pp}\tau, \quad (6)$$

where the second equality holds according to the wavevector matching $(\mathbf{k}_4 - \mathbf{k}_{3+}) = \mathbf{q}_R$, $-(\mathbf{k}_4 - \mathbf{k}_{3-}) = \mathbf{q}_L$ and the phase velocity $v_{pp} = \omega_{pp}/q_{pp}$ of the PP. The phase $\phi_{4,el}$ of the elastically scattered light is unaffected by τ .

In general, the intensity detected on a pixel of the spectrometer,

$$I \sim |E_+ + E_- + E_{el}|^2, \quad (7)$$

depends on τ via the phases $\phi_{4\pm}$ and ϕ_{el} of the scattered light fields.

(A) If we now investigate the experimentally detected signal from Fig. 4a we may assume $E_{el} \ll E_{\pm}$, since the signal intensity for $\tau < 0$ ps, which represents the elastically scattered light, is very small. The detected light field intensity on a pixel now is only given by the interference of E_+ and E_- :

$$I \sim |E_+ + E_-|^2 = E_{\pm 0}^2 e^{-2\gamma\tau} |e^{i(\omega_4 t)}|^2 |e^{i\phi_{4+}(\tau)} - e^{i\phi_{4-}(\tau)}|^2. \quad (8)$$

The intensity decays with twice the damping rate of the PPs. For delays $\tau \gg 1/\gamma$ the intensity decays back to the time independent background given by the weak elastically scattered light field $E_{el,0}$. The term oscillating with the detected light frequency ω_4 is a pure phase factor dropping out in the intensity measurement and the last contribution gives rise to the oscillation of the signal with twice the polariton frequency:

$$I \sim (1 - \cos(2\omega_{pp}\tau)) e^{-2\gamma\tau}. \quad (9)$$

This fully and quantitatively explains the observations in Fig. 3a.

(B) If the probe pulse samples a region of the sample that can only be reached by left-propagating PPs, as depicted in Fig. 3c), we can neglect E_+ which originates from the right propagating polaritons. For larger wavevectors the strong polariton damping leads to rapid decrease of E_- as well, so that it becomes comparable to the elastically scattered light field: $E_- \approx E_{el}$. Now the detected intensity shows interference of elastically and inelastically scattered light, notably leading to the same light frequency ω_4 after the scattering.

$$I \sim |E_- + E_{el}|^2 = |E_{-0} e^{-\gamma\tau + i\phi_{4-}(\tau)} - E_{el,0} e^{i\phi_{4,el}(\tau)}|^2. \quad (10)$$

This weak signal oscillates at the fundamental frequency ω_{pp} around the intensity level given by the elastically scattered light field $E_{el,0}$ and an inelastic scattering term which is damped at the rate 2γ :

$$I \sim E_{el,0}^2 + E_{-0}^2 e^{-2\gamma\tau} - 2E_{el,0}E_{-0} e^{-\gamma\tau} \cos(\omega_{pp}\tau + \phi_{4,el}). \quad (11)$$

Unlike case (A) the oscillation amplitude decays with the damping rate γ of the PPs (not with 2γ), in full accord with Fig. 3c. The relative intensity of the E_{el} and E_{\pm} determines the relative oscillation amplitude. Intermediate cases like in Fig. 3b are explained analogously. Generally the interference of the two inelastic contributions E_{\pm} on the detector gives

rise to oscillations at $2\omega_{pp}$, whereas the interference of one inelastic contribution with E_{el} yields oscillations at ω_{pp} , even when the position of the probe pulse perfectly overlaps with the pump. However, if the two interfering light fields have very different intensities, the signal modulation is very weak.

For the narrow band probe pulses the situation is different. Not only are the probe pulses too long to resolve the beating. More importantly, the probe spectrum is so narrow that for all except for the smallest wavevector polaritons in Fig. 5 the inelastically scattered probe pulses do neither overlap with each other nor with the unshifted probe spectrum. The time dependence of such signals for perfectly overlapping pump and probe is plotted as a black solid line in Fig. 4. The signal shows no oscillatory signature and exhibits the double damping rate 2γ . Since the three signal contributions E_{\pm} and E_{el} are detected by separate pixels of the spectrometer, they do not interfere and Eq. (8) must be modified:

$$I_{\pm} \sim E_{\pm 0}^2 e^{-2\gamma\tau} |e^{i\omega_4 t}|^2 |e^{i\phi_{4\pm}}|^2 = E_{\pm 0}^2 e^{-2\gamma\tau}. \quad (12)$$

Now the delay τ only enters into the decay since the absolute magnitude of the phase factors is unity.

5 Conclusions In conclusion, we have shown that the 4WM experiments on PP can be regarded as two sequential processes: The first is an excitation of PPs by impulsive stimulated Raman scattering and difference frequency mixing, where both processes imply the same energy and momentum conservation rules. The second process, namely the probe process contains the same physics. Here the PP wave itself leads to stimulated emission of the inelastically scattered photon. We have shown that left and right propagating PP can be distinguished by observing the sign of the frequency shift: Stokes and Anti-Stokes scattering. Technically, the dispersion relation of PPs, e.g., in Lithium Niobate are measured to higher wavevectors and we showed that narrowing down the spectrum of the probe pulse only allows detecting the frequency shifts connected with the Raman scattering directly. We believe that our findings shed new light on four wave mixing experiments on PPs and may help to design new fundamental and applied experiments in the field of polaritonics.

Acknowledgements We are grateful to K.A. Nelson for providing phase masks for the experiments and for sharing the experimental know-how. A.B. thanks the graduate school DiNL of the Leibnitz society for financial support.

References

- [1] C. Kittel, Introduction to Solid State Physics, seventh ed. (Wiley, New York, 1996).
- [2] R. Loudon, Adv. Phys. **13**(52), 423–482 (1964).
- [3] C. H. Henry and J. J. Hopfield, Phys. Rev. Lett. **15**, 964–966 (1965).
- [4] J. M. Yarborough, S. S. Sussman, H. E. Purhoff, R. H. Pantell, and B. C. Johnson, Appl. Phys. Lett. **15**(3), 102–105 (1969).
- [5] L. Dhar, J. A. Rogers, and K. A. Nelson, Chem. Rev. **94**(1), 157–193 (1994).

- [6] R. Merlin, *Solid State Commun.* **102**(2–3), 207–220 (1997).
- [7] J. K. Wahlstrand and R. Merlin, *Phys. Rev. B* **68**, 054301 (2003).
- [8] W. L. Faust and C. H. Henry, *Phys. Rev. Lett.* **17**, 1265–1268 (1966).
- [9] J. Hebling, K. L. Yeh, M. C. Hoffmann, B. Bartal, and K. A. Nelson, *J. Opt. Soc. Am. B* **25**(7), B6–B19 (2008).
- [10] Y. X. Yan and K. A. Nelson, *J. Chem. Phys.* **87**(11), 6240–6256 (1987).
- [11] J.-C. Diels and W. Rudolph, *Ultrashort Laser Pulse Phenomena: Fundamentals, Techniques and Applications on a Femtosecond Time Scale*, second ed. (Academic Press, San Diego, 2006).
- [12] T. Feurer, N. S. Stoyanov, D. W. Ward, J. C. Vaughan, E. R. Statz, and K. A. Nelson, *Annu. Rev. Mater. Res.* **37**(1), 317–350 (2007).
- [13] T. P. Dougherty, G. P. Wiederrecht, and K. A. Nelson, *J. Opt. Soc. Am. B* **9**(12), 2179–2189 (1992).
- [14] K. P. Cheung and D. H. Auston, *Phys. Rev. Lett.* **55**, 2152–2155 (1985).
- [15] G. M. Gale, F. Vallée, and C. Flytzanis, *Phys. Rev. Lett.* **57**, 1867–1870 (1986).
- [16] J. Etchepare, G. Grillon, A. Antonetti, J. C. Loulergue, M. D. Fontana, and G. E. Kugel, *Phys. Rev. B* **41**, 12362–12365 (1990).
- [17] P. C. M. Planken, L. D. Noordam, J. T. M. Kennis, and A. Lagendijk, *Phys. Rev. B* **45**, 7106–7114 (1992).
- [18] G. P. Wiederrecht, T. P. Dougherty, L. Dhar, K. A. Nelson, D. E. Leaird, and A. M. Weiner, *Phys. Rev. B* **51**, 916–931 (1995).
- [19] T. Feurer, J. C. Vaughan, and K. A. Nelson, *Science* **299**(5605), 374–377 (2003).
- [20] R. M. Koehl, S. Adachi, and K. A. Nelson, *J. Phys. Chem. A* **103**(49), 10260–10267 (1999).
- [21] C. A. Werley, K. A. Nelson, and C. R. Tait, *Am. J. Phys.* **80**(1), 72–81 (2012).
- [22] A. Stepanov, J. Hebling, and J. Kuhl, *Opt. Express* **12**(19), 4650–4658 (2004).
- [23] D. P. Kien, J. C. Loulergue, and J. Etchepare, *Opt. Commun.* **101**(1–2), 53–59 (1993).
- [24] U. T. Schwarz and M. Maier, *Phys. Rev. B* **58**, 766–775 (1998).
- [25] A. S. Barker and R. Loudon, *Phys. Rev.* **158**, 433–445 (1967).
- [26] A. A. Maznev, K. A. Nelson, and J. A. Rogers, *Opt. Lett.* **23**(16), 1319–1321 (1998).
- [27] H. J. Eichler, P. Günter, and D. W. Pohl, *Laser Induced Dynamic Gratings*, Springer Series in Optical Sciences, Vol. 50 (Springer, Berlin, 1986).
- [28] C. J. Brennan, *Femtosecond wavevector overtone spectroscopy of anharmonic lattice dynamics in ferroelectric crystals*, Thesis, MIT (1997).
- [29] J. Hebling, *Phys. Rev. B* **65**, 092301 (2002).
- [30] T. F. Crimmins, N. S. Stoyanov, and K. A. Nelson, *J. Chem. Phys.* **117**(6), 2882–2896 (2002).
- [31] H. J. Bakker, S. Hunsche, and H. Kurz, *Phys. Rev. B* **48**, 13524–13537 (1993).
- [32] V. N. Mahajan and J. D. Gaskill, *J. Appl. Phys.* **45**(6), 2799–2800 (1974).
- [33] J. D. Jackson, *Classical Electrodynamics*, third ed. (Wiley, New York, 1999).

PAPER IX

Normalization schemes for ultrafast x-ray diffraction using a table-top laser-driven plasma source

D. Schick, A. Bojahr, M. Herzog, C. von Korff Schmising,
R. Shayduk, W. Leitenberger, P. Gaal and M. Bargheer.
Rev. Sci. Instrum. **83**, 025104 (2012).

Normalization schemes for ultrafast x-ray diffraction using a table-top laser-driven plasma source

D. Schick,¹ A. Bojahr,¹ M. Herzog,¹ C. von Korff Schmising,² R. Shayduk,³ W. Leitenberger,³ P. Gaal,³ and M. Bargheer^{3,a)}

¹*Institut für Physik & Astronomie, Universität Potsdam, Karl-Liebknecht-Str. 24-25, 14476 Potsdam, Germany*

²*Institut für Optik und Atomare Physik, Technische Universität Berlin, Straße des 17. Juni 135, 10623 Berlin, Germany*

³*Helmholtz Zentrum Berlin, Albert-Einstein-Strasse 15, 12489 Berlin, Germany*

(Received 1 November 2011; accepted 10 January 2012; published online 7 February 2012)

We present an experimental setup of a laser-driven x-ray plasma source for femtosecond x-ray diffraction. Different normalization schemes accounting for x-ray source intensity fluctuations are discussed in detail. We apply these schemes to measure the temporal evolution of Bragg peak intensities of perovskite superlattices after ultrafast laser excitation. © 2012 American Institute of Physics. [doi:10.1063/1.3681254]

I. INTRODUCTION

Ultrafast x-ray diffraction (UXRD) allows for tracking atomic motion on its specific time scale in various physical, chemical, and biological processes.^{1–3} In most UXRD experiments the pump-probe scheme is employed, in which the sample is excited repetitively by an ultrafast stimulus, e.g., a fs laser pulse, and is probed subsequently at different time delays between pump and probe pulses.

Besides accelerator-based x-ray sources with fs time resolution,^{4–7} laser-driven plasma x-ray sources (PXS) proved to be a practical alternative for UXRD experiments with no beamtime limitation, relatively low costs for build-up and maintenance as well as an intrinsic synchronisation between the optical pump and x-ray probe pulses.⁸ In conventional x-ray tubes electrons are accelerated onto a metal target to generate characteristic line emission (K-shell ionization and recombination) and a broad bremsstrahlung background. This process can also be driven efficiently by focusing an intense laser pulse of more than 10^{16} W cm⁻² onto a metal target. Under proper conditions free electrons are generated and instantaneously accelerated back into the metal by the next half-cycle of the laser's electric field.^{9–15} The released x-ray pulses typically have a duration of a few hundred fs which is generally determined by the interaction time of the electrons with the metallic target.

Even though sources working at kilohertz repetition rate offer a relatively high flux of up to 3×10^6 ph/s on the sample using x-ray optics^{16,17} long integration times are necessary to acquire a sufficient signal-to-noise ratio (SNR) in most UXRD experiments. Moreover, large intensity fluctuations of PXS sources, compared to conventional x-ray tubes, call for advanced normalization schemes.

In this review we present a brief description of the new UXRD setup at the University of Potsdam. On the example of ultrafast Bragg peak intensity oscillations of two perovskite superlattices we discuss different normalization approaches and their experimental applicability. In particular, we intro-

duce a rapid scanning technique adapted from all-optical experiments as well as a scheme which utilizes the single reflection of a Montel x-ray optic to measure the incoming x-ray flux directly.

II. SYSTEM CHARACTERISTICS

In recent years, different designs of laser-driven plasma x-ray sources have been successfully applied to numerous UXRD experiments.^{18–21} The PXS setup at the University of Potsdam is a further development of the system introduced in Ref. 22. In addition to its excellent degree of automation and stability as well as its high standard of radiation safety, the setup can be employed in various x-ray diffraction and reflection geometries.^{23–25}

The PXS is driven by a two-stage Ti:sapphire amplifier (Legend Duo, COHERENT) working at 1 kHz repetition rate with a center wavelength of 800 nm and a pulse energy of 8 mJ compressed into a pulse duration of 40 fs. The laser beam is split into a main part of 80% for the x-ray generation and the remaining pulse energy is guided via a motorized mechanical delay line to excite the sample at a defined time before the probing x-ray pulse. The laser plasma is generated on a copper tape running in an evacuated interaction chamber, which can be moved within the fixed focal plane of the laser, perpendicular to the spooling direction of the tape. Thereby one can write multiple tracks onto one tape prolonging the measurement time up to 10 h. Both the entrance and exit window of the vacuum chamber are protected by plastic tapes which catch most of the copper debris that is ejected by the laser plasma. The generated x-ray pulses (dominantly characteristic Cu K_α and K_β lines) are collected, focused, and monochromatized to only Cu K_α energies by a Montel multilayer optic (INCOATEC) with a convergence of 0.3° and a focal spot size of only 200–300 μm FWHM at a distance $d = 1000$ mm from the source. The selected x-ray optic is adapted to the experimental needs which specify the energy bandwidth, angular distribution, and spot size of the x-rays at the sample. In most of our experiments

^{a)}Electronic mail: bargheer@uni-potsdam.de.

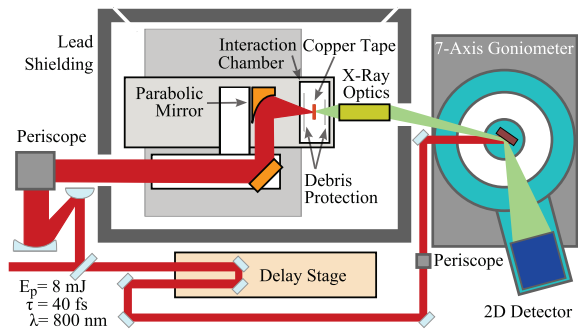


FIG. 1. (Color online) The laser is focused onto a copper tape inside a vacuum chamber to generate fs x-ray pulses. Both copper tape and plastic debris-protection tapes run perpendicular to the plane of drawing. To write new tracks on the copper band, the entire vacuum chamber is translated. The x-rays are collected, monochromatized, and focused onto the sample by a multilayer Montel optic. The diffracted x-rays are detected by a fast read-out CMOS 2D camera.

on epitaxial thin films and multilayers a symmetric θ - 2θ geometry is applied. Here, the sample is placed in the x-ray focal plane to reduce time smearing effects due to a generally inevitable non-collinearity between laser pump and x-ray probe beam and to probe a homogeneously excited part of the sample. The x-ray detector can be easily exchanged, but we commonly use a fast read-out CMOS 2D camera (Pilatus 100 k, DECTRIS) to record diffracted x-ray photons. The complete setup is sketched in Fig. 1.

The performance of the PXS can be characterized by three main parameters: pulse length, photon flux, and intensity stability. Since there is no detector that is fast enough to measure the duration of ultrashort x-ray pulses directly we rely on several successful experiments in our and other groups^{21,25} which evidence the sub-ps temporal resolution of PXS machines.

The x-ray flux can be improved by an increase of the laser intensity on the metal target, but only up to a certain saturation limit.^{10,12} From there on a further increase of the x-ray flux can be achieved by a larger interaction volume of the laser-produced electrons with the target, e.g., by larger foci, which will increase the x-ray source size in return. At very high laser intensities in the relativistic limit the efficiency rises again, however, at the expense of a high background of high energetic radiation. For our setup we achieved nearly 10^{11} ph/s with Cu K_α energy in the full solid angle of 4π under optimal conditions. Only 5×10^5 ph/s of the total flux are focused onto the sample using the Montel x-ray optic at a normal performance. Thus, the number of diffracted photons per pulse for a typical Bragg peak with 1% peak reflectivity is well below ten for our system. Consequently, we are within the single photon counting regime for each detector pixel, because the divergence of the diffracted x-rays yields 10–100 illuminated pixels on the detector area depending on the exact sample-detector-position.

Of course, the optimal performance of the PXS requires extensive tuning of all mechanical and optical components. Although we benefit heavily from the engineering knowledge and skills which are included in the commercial and semi-commercial components of our setup, we cannot avoid all me-

chanical and optical instabilities which cause x-ray intensity fluctuations on several time scales. In general, we distinguish short-term fluctuations and long term drifts. The latter ones occur within minutes up to hours and can be explained by contamination of the PXS interaction chamber by copper debris, side shifts of the copper tape, and also by the increasing roughness of the copper tape after writing multiple tracks with the laser onto it. These long-term drifts can result in intensity changes and jumps of up to 50% and are not periodic in time.

Short-term fluctuations include all intensity instabilities typically within a few seconds down to pulse-to-pulse fluctuations. They are caused by the driving laser, unstable optical components but mainly by the position instabilities of the spooled copper tape with respect to the laser focus as well as target material inhomogeneities. Under certain conditions (which we usually avoid) very large intensity bursts can be observed in the integrated energy range from 1–100 keV, which may be assigned to electron beam generation²⁶ and the subsequent bremsstrahlung creation in the surrounding aluminium and lead walls of the vacuum chamber. These fluctuations can be easily suppressed by any type of monochromator in the setup, such as a Montel optic.

III. NORMALIZATION SCHEMES

As already described above only a few photons per pulse are diffracted in a typical UXRD experiment. In order to measure temporal intensity changes of only a few percent with a sufficient SNR it is necessary to accumulate thousands up to millions of diffracted x-ray pulses over minutes and hours of measurement time. In general, the short-term fluctuations of the incoming x-ray flux increase the statistical error of the recorded signal. A reliable normalization technique can help to cancel the contribution of the intensity fluctuations to the signal and to minimize the necessary averaging time. Normalization is definitely mandatory in case of long-term drifts, which describe the changing mean value of the fluctuating x-ray intensity over absolute measurement time t . Because of the non-periodic behaviour in time of these drifts it is not easy to average them out. Hence, the measured signal would mainly represent the intensity drift of the source rather than the response of the sample under investigation if no normalization is applied.

We choose two superlattice (SL) samples in order to evaluate different normalization approaches. These artificial heterostructures consist of N_{SL} epitaxially grown double layers made of a metallic and insulating perovskite material. The spatial period $d_{SL} = d_{metal} + d_{insulator}$ of a double layer leads to SL Bragg peaks at multiple integers of the reciprocal SL vector $g_{SL} = 2\pi/d_{SL}$ where we adapt the enumeration of the SL peaks from Ref. 27. In the UXRD experiments an 800 nm fs-pulse excites the sample, but is only absorbed in the metallic layers of the SL and thus induces a periodic stress profile.^{28,29} As a result, a coherent longitudinal phonon mode is excited which corresponds to an anti-phase oscillation of the individual layer thicknesses in each double layer. These structural dynamics lead to a periodic intensity change of most SL Bragg peaks. For many superlattice peaks the intensity of the x-ray Bragg reflection is proportional to the

amplitude of the superlattice phonon (i.e., expansion of the metallic layers and compression of the dielectric layers in between), since the contribution of the two layer materials to the structure factor of the reflections is varied linearly. In some cases this x-ray interference leads to additional modulation as for the peak SL+1 in Figs. 5 and 7 making the response even faster.³⁰ For both samples studied in this paper, the signal can be well approximated by a cosine-like oscillation due to the quasi-instantaneous stress. The oscillations are exponentially damped as the energy stored in the superlattice phonons propagates into the substrate.²⁹ Since in the current paper we only use the fast response for a demonstration of the setup, we refrain from further discussion of the physics and settle for observing the good applicability of the fit function. The according oscillation period of the coherent phonon mode is given by the double layer period d_{SL} and the material-specific sound velocities and is only a few ps for the considered samples. Thus, we can prove the sub-ps temporal resolution of the PXS. In order to observe the coherent phonon oscillation of the SL the integrated intensity of the diffracted x-rays $R(\tau)$ from a single SL Bragg peak has to be measured for different time delays τ . In analogy to all-optical pump-probe experiments we refer to $R(\tau)$ as transient x-ray reflectivity.

In the experiment the measured signal $S(\tau, t)$ also depends on the absolute time t because of the fluctuations and drifts of the incoming intensity $I(t)$:

$$S(\tau, t) = R(\tau) I(t).$$

In order to extract the reflectivity $R(\tau)$ from the real signal a normalization scheme must provide a measure which is proportional to $I(t)$ and at the same time independent of the delay τ . Obviously, this can be achieved by an additional detector that monitors only $I(t)$. For the observation of structure factor changes of a Bragg reflection we are only interested in the relative reflectivity change

$$\frac{S(\tau, t) - S_0(t)}{S_0(t)} = \frac{[R(\tau) - R_0] I(t)}{R_0 I(t)} = \frac{\Delta R(\tau)}{R_0},$$

where $R_0 = R(\tau < 0)$ denotes the unpumped reflectivity and $S_0(t) = S(\tau < 0, t)$ the measured unpumped signal. Here the incoming intensity $I(t)$ cancels out if $S(\tau, t)$ and $S_0(t)$ can be measured simultaneously or within a sufficiently small time interval Δt in which $I(t)$ can be assumed to be constant, e.g., for Δt smaller than long-term drifts of the x-ray source, and hence a direct measure of $I(t)$ is not necessary.

However, the applicability of a certain normalization method can be limited by various factors such as the x-ray diffraction geometry or the investigated sample itself. In the upcoming paragraphs we describe general approaches for normalization and give examples of their implementation from our and other groups.

A. Low-repetition rate normalization

The first SL sample consists of 11 double layers made of 7.9 nm metallic SrRuO₃ (SRO) and 14.9 nm dielectric SrTiO₃ (STO) epitaxially grown on a SRO buffer layer and a STO substrate by pulsed laser deposition.³¹ This sample was already studied intensively^{29,32,33} and has a SL phonon

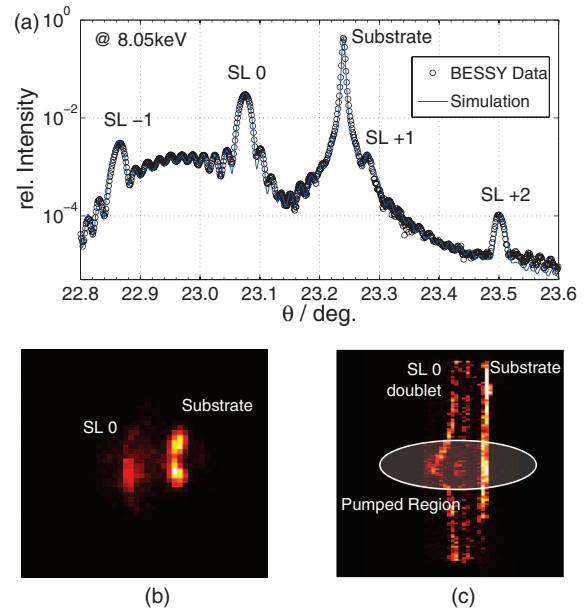


FIG. 2. (Color online) (a) The θ - 2θ diffraction scan of the STO/SRO SL features the sharp and intense STO substrate Bragg peak as well as several SL Bragg peaks. The experimental 2D diffraction patterns of the 0th SL Bragg peak are shown in two configurations. (b) The sample is placed in the focus of the Montel x-ray optic. (c) The sample is illuminated by the direct PXS emission without x-ray optics. The 0th SL Bragg peak appears as a $K_{\alpha 1, \alpha 2}$ doublet. The $K_{\alpha 2}$ Bragg reflection of the substrate is not within the divergence of the x-rays on the sample.

oscillation period of 3.2 ps, which can be derived most easily from the transient reflectivity change of the 0th SL Bragg peak. The θ - 2θ diffraction curve of the STO/SRO SL is shown in Fig. 2(a). It was measured at the energy-dispersive reflectometry (EDR) beamline of the storage ring BESSY II of the Helmholtz-Zentrum Berlin at a photon energy of 8.82 keV. For better comparison with the PXS data the θ -axis of the diffraction curve was rescaled for the Cu K_{α} energy of 8.05 keV.

PXS driven UXRD experiments generally feature a rather large angular distribution of the incoming x-ray beam because of the used focussing x-ray optics or, in case of no optics, because of the divergence of the nearly point-like x-ray emission from the laser plasma. Thus, it is favourable to use 2D x-ray cameras, or at least 1D arrays, in order to record the available angular information of the diffracted photons. In case of a diode-like point detector angular information or even the total information of the diffracted intensity, which misses the angular acceptance of the detector, is lost. Unfortunately, typical CCD x-ray cameras have a very low frame rate because of their long dead-time up to several seconds, which is mainly due to their long read-out time. Accordingly, the integration time for a single diffraction image should be well above 1 min in order to have a sufficiently high duty cycle of the detector. Otherwise a large fraction of the precious diffracted x-ray photons cannot be detected. The drawback of slow frame rates can be balanced by taking advantage of the large number of CCD pixels in order to record simultaneously the signal and normalization with the same CCD camera.²¹

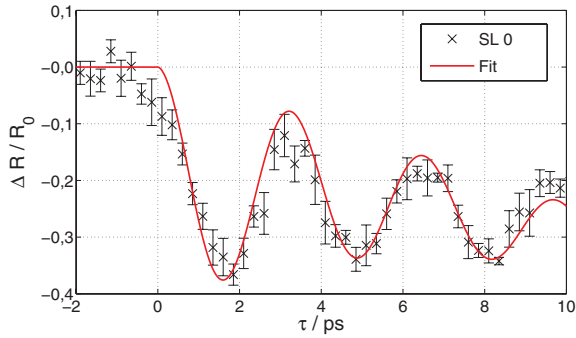


FIG. 3. (Color online) The relative reflectivity $\Delta R/R_0$ of the 0th SL Bragg peak of the SRO/STO SL was measured with the substrate normalization scheme. The error bars are determined by averaging 10 independent delay scans.

As it can be seen from Fig. 2(a) the angular separation between the 0th SL peak and the STO substrate peak is smaller than 0.3° . Thus, it is possible to record both peaks simultaneously within the convergence of our Montel optic, see Fig. 2(b). The same situation can be achieved without the use of an x-ray optics, where the divergence on the sample depends on its distance to the x-ray source. In the latter case, see Fig. 2(c), the sample is completely illuminated by the direct PXS emission. Within the collected angular range the 0th SL peak is visible as a $K_{\alpha 1, \alpha 2}$ doublet, whereas the $K_{\alpha 2}$ contribution of the strong substrate is cut off by the finite size of the sample.

The dielectric STO substrate is not optically excited by the 800 nm pump pulse. For delays larger than the time for sound propagation through the thin SL layers (in our case $\tau > 35$ ps) propagating sound waves originating from within the SL influence the structure of the STO substrate.^{29,34} Within this defined delay window the substrate peak reflectivity R_{sub} is constant. Consequently, the recorded signal of the substrate peak $S_{\text{sub}}(t)$ only depends on the absolute time t and can thus be utilized as a measure of the incoming intensity $I(t)$. Here we directly benefit from the large detector area, since no additional hardware is required to employ this normalization scheme. The data shown in Fig. 3 were obtained with this substrate normalization scheme while the sample was placed in the direct emission of the PXS without x-ray optics. Due to the repetition of the complete delay scan for several times we are able to plot also statistical error bars. The substrate normalization scheme strongly depends on the sample and the available angular distribution of the incoming x-rays. Furthermore, this method cannot be applied for large delays because of the transient change of the substrate reflectivity.

A more generally applicable normalization scheme is already indicated in Fig. 2(c) where the sample is placed in the direct PXS emission without x-ray optics. For a sufficiently large x-ray spot size on the sample also each point in the diffraction pattern originates from a different position on the sample. If the pumped region is smaller than the probe area on the sample also the diffraction pattern will contain a pumped and unpumped region. This situation can also be achieved with x-ray optics, but here the sample should be placed out of the x-ray focal plane in order to superimpose both areas more

easily. In this pumped-unpumped normalization scheme the transient signal $S(\tau, t)$ and the unpumped signal $S_0(t)$ can be measured simultaneously with the same CCD camera. We can apply this scheme as a normalization to determine the transient reflectivity change $\Delta R(\tau)/R_0$ for any crystalline sample.

However, a large fraction of the photons diffracted by the 0th SL Bragg peak does not contribute to the transient reflectivity $R(\tau)$. Moreover, the excitation on the sample is very inhomogeneous, as it is indicated by the curvature of the SL peak in Fig. 2(c). Another drawback of this scheme is the rather large x-ray footprint on the sample, which gives rise to an undesired time smearing and also maps different positions of the sample at once, which may be problematic for low-quality samples that lack lateral homogeneity.

For this specific STO/SRO SL sample the substrate normalization scheme is preferable compared to the pumped-unpumped method, because the SNR mainly depends on the total number of recorded photons, meaning the sum of photons contributing to the signal and to the normalization. This number is much higher for the intense substrate reflection. However, both normalization schemes can be applied in the so-called low-repetition rate regime for slow detectors without the need of additional hardware. It is even possible to apply both methods with or without x-ray optics, although one should prefer the use of the Montel x-ray optic because of the higher flux on the sample and the smaller x-ray energy bandwidth.

B. High-repetition rate normalization

The following normalization schemes are applied to a similar SL sample. This SL is made of 15 double layers of which each consist of 7.3 nm metallic $(\text{La}_{0.7}\text{Sr}_{0.3})\text{MnO}_3$ (LSMO) and 13.7 nm ferroelectric $(\text{Ba}_{0.7}\text{Sr}_{0.3})\text{TiO}_3$ (BST). Again the SL is grown epitaxially on a STO substrate. The $\theta-2\theta$ diffraction curve is shown in Fig. 4 and was again measured at the EDR beamline of the storage ring BESSY II of the Helmholtz-Zentrum Berlin.³⁵ The ultrafast response of this SL to an 800 nm fs pump pulse is very similar to the STO/SRO SL discussed above but with a slightly different period of the coherent SL phonon oscillation of 3.8 ps.

A common procedure to reduce statistical errors in a pump-probe experiment is increasing the repetition rate of the measurement. A well-known high-repetition rate

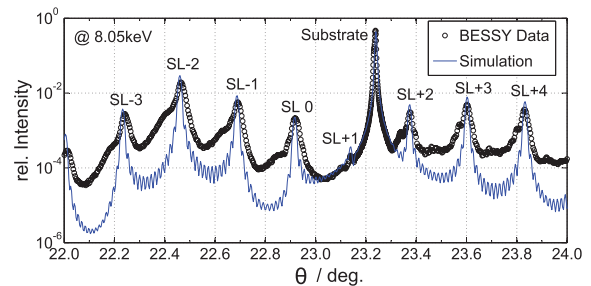


FIG. 4. (Color online) Several orders of SL Bragg peaks as well as an intense substrate Bragg peak are observable in the $\theta-2\theta$ scan of the LSMO/BST SL sample.

normalization scheme from all-optical experiments is chopping. Here the pump beam is periodically blocked in order to record the signal $S(\tau, t)$ and the unpumped signal $S_0(t)$ subsequently within a short time interval $\Delta t = 1/f_{\text{chop}}$ where f_{chop} is the chopping frequency. In this case half of the diffracted photons contribute to the signal and the other half to the normalization. If Δt is shorter than the time scale of long term drifts we can assume $I(t) = I(t + \Delta t)$ to be constant within this interval neglecting short-term fluctuations. Hence, we can apply this scheme to measure the relative reflectivity change $\Delta R(\tau)/R_0$. If Δt is even shorter than most of the characteristic short-term fluctuations of the PXS, chopping can also drastically reduce these sources of noise. Ideally, this requires a shot-to-shot temporal resolution of the x-ray camera. Because area detectors with kHz readout frequencies are just becoming available we have not implemented the chopping scheme, yet.

A very elegant way of normalization is again adapted from all-optical experiments and referred to as the rapid scanning method.³⁶ As the name suggests the complete delay range of interest of a pump-probe experiment is scanned very rapidly within a time interval Δt in which the incoming intensity $I(t)$ can again assumed to be constant. Thus, a single scan has to be faster than the time scale on which long-term drifts occur. It is not possible to scan the complete delay in a time shorter than all short-term fluctuations ($\Delta t < 5$ ms). Several of these fast delay scans are averaged to decrease the statistical errors caused by the fluctuations of the incoming intensity. With the rapid scanning method all diffracted photons contribute directly to the signal and no intensity is lost for normalization.

Similar to the chopping technique, the performance of rapid scanning is mainly limited by the frame rate of the x-ray detector and additionally by the speed of the delay stage. A complete delay scan has to be faster than the long-term drifts of the PXS which occur typically on the time scale of minutes. Hence, we do not have to utilize the Pilatus' full frame rate of up to 200 Hz but can work within a more easily controllable regime of ~ 1 Hz frame rate in order to scan a typical number of 50 delays well within 1 min of scan time.

A measurement of reflectivity oscillation for different SL Bragg peaks of the LSMO/BST SL is depicted in Fig. 5. The data were recorded with a frame rate of 2 Hz of the Pilatus camera and the complete scan was repeated up to 40 times.

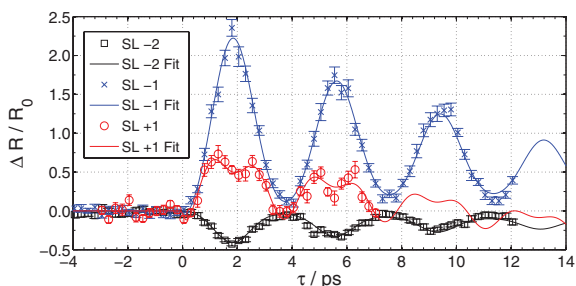


FIG. 5. (Color online) The rapid scanning technique was applied to measure the relative reflectivity $\Delta R/R_0$ of the SL-2, SL-1, and SL+1 Bragg peaks of the LSMO/BST SL. The data for each SL peak was accumulated within ~ 20 min per curve averaging over 40 complete delay scans with a frame rate of 2 Hz.

The total integration time per curve was ~ 20 min and we achieved an average relative error for all data points of 5.3%.

Rapid scanning provides a normalization without measuring the incoming intensity $I(t)$ directly. It is not capable of reducing short-term fluctuations in our implementation but can only average them out. This normalization technique is universally applicable. However, fast read-out x-ray detectors are the key part of this high-repetition normalization scheme, since one complete delay scan must be finished faster than the time scale of long-term fluctuations.

C. Direct normalization

In order to provide a sample-independent and direct measure of the incoming intensity $I(t)$ an additional detector is required. This detector then has to measure the PXS flux between source and sample ideally with the same frame rate as the x-ray camera records the diffraction signal. X-ray sensitive diodes are generally fast enough for this purpose and have a sufficiently high quantum efficiency to record also low x-ray intensities. Since the integrated intensity over the whole PXS spectrum is not proportional to the intensity of the characteristic x-ray emission lines used in the diffraction experiments, it is necessary to monitor the x-ray flux behind a monochromator or with an according energy-dispersive detector.³⁷ One usually has to bypass some fraction of the incoming x-ray beam onto the normalization detector which will reduce the flux on the sample accordingly. Such direct normalization schemes were already implemented, e.g., by placing an ionization chamber³⁸ or a thin diamond beam splitter²⁴ into the incoming x-ray beam.

In our setup the Montel x-ray optic acts as a monochromator since it transmits only the Cu K_α energies which are then diffracted from the sample. A detailed description of Montel optics can be found in the literature.^{16,39} The divergent emission of the source is focused in two dimensions by two sequential reflections from elliptically bent multilayer mirrors. The transmission profile of the optic shown in the inset of Fig. 6 reveals that in addition to this monochromatic focal region F there are two regions S which are produced by x-rays undergoing only a single reflection from one multilayer mirror. This radiation is monochromatic as well, and we can assume a linear relation between the intensity in the S regions and in the focus F. In a typical diffraction experiment the two S-beams do not hit the sample and are therefore useless. In our case we use an x-ray diode (CRYSTAL PHOTONICS) to monitor the x-ray flux in one of the S regions to have a direct and proportional measure of the monochromatic incoming intensity $I(t)$.

In order to verify the applicability of this normalization scheme we measured the direct intensity of the Montel focus F with the Pilatus camera in single-photon-counting mode and the intensity of a single reflection S with the x-ray diode simultaneously. The ratio of the diode and the Pilatus signal shown as red line in Fig. 6 proves the linear relation between the two signals. Accordingly, the normalized signal contains much less short-term fluctuations as compared to the original intensity which improves the SNR for UXR experiments drastically. For very large fluctuations and drifts of about 50%

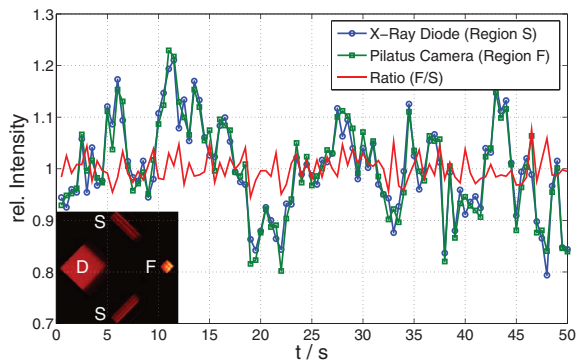


FIG. 6. (Color online) The focus F of the Montel optic was measured with the Pilatus camera (green square) simultaneously with the intensity of a single reflection S of the Montel optic by an x-ray diode (blue circle). The ratio of the Pilatus and diode signal (red line) features much less fluctuations than the original data. The transmission profile of the Montel optic is shown in the inset, where the direct transmission of the Montel optic is labelled as D.

of the PXS intensity a slight nonlinearity of the x-ray diode signal causes deviations of the normalized signal. This nonlinearity is most likely caused by an electronic offset of the diode itself and may be reduced by a suitable calibration routine. The direct normalization scheme reduces short-term fluctuations but cannot completely cancel large long-term drifts because of the diode's nonlinearity. Therefore, we combine this method with the rapid scanning technique to improve the SNR even further.

We apply this combination of diode-normalization and rapid scanning again for the measurement of SL Bragg peak oscillations of the LSMO/BST SL (Fig. 7). In comparison with the data shown in Fig. 5 the average relative error for each data point is further reduced to 4.6% although the total integration time per curve is reduced to only 10 min. This normalization scheme requires extensive technical efforts such as high-repetition x-ray cameras and an additional x-ray diode as well as an x-ray optic. On the other hand, this combined normalization technique is independent of the investigated sample and does not decrease the number of photons which account for the diffraction signal.

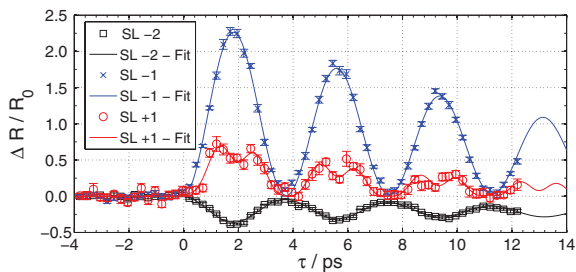


FIG. 7. (Color online) The reflectivity oscillations of three different SL Bragg peaks of a LSMO/BST SL were measured with a combination of the x-ray diode normalization and rapid scanning. The frame rate of the Pilatus was 1 Hz and each curve was obtained within a total integration time of ~ 10 min.

IV. CONCLUSIONS AND OUTLOOK

Even though PXS sources operated at kHz repetition rate are easy to use and feature high stability, advanced normalization schemes are necessary to achieve a sufficient SNR in UXRD experiments. Here we presented a detailed overview of low- and high-repetition rate normalization techniques as well as a diode-based direct normalization scheme utilizing the specific transmission profile of a Montel x-ray optic. With the combination of the direct intensity normalization and the rapid scanning we could drastically reduce short-term fluctuations and cancel long term drifts of the PXS, respectively. With the diode normalization scheme it is also possible to record time-resolved θ - 2θ scans over an angular range much larger than the divergence of the x-ray optics. Thereby not only peak intensity but also the position, width and shape of a Bragg peak can be precisely observed on an ultrafast time scale.

ACKNOWLEDGMENTS

We gratefully acknowledge the financial support by the BMBF via Grant No. 03WKP03A and the Deutsche Forschungsgemeinschaft (DFG) (Grant No. BA2281/3-1). We thank Dr. Ionela Vrejoiu for fruitful discussions and for providing the samples experimentally investigated.

- ¹A. Rousse, C. Rischel, and J.-C. Gauthier, *Rev. Mod. Phys.* **73**, 17 (2001).
- ²M. Bargheer, N. Zhavoronkov, M. Woerner, and T. Elsaesser, *ChemPhysChem* **7**, 783 (2006).
- ³M. Chergui and A. H. Zewail, *ChemPhysChem* **10**, 28 (2009).
- ⁴R. W. Schoenlein, S. Chattopadhyay, H. H. W. Chong, T. E. Glover, P. A. Heimann, C. V. Shank, A. A. Zholents, and M. S. Zolotarev, *Science* **287**, 2237 (2000).
- ⁵K. Hollnack, S. Khan, R. Mitzner, and T. Quast, *Phys. Rev. Lett.* **96**, 054801 (2006).
- ⁶P. Beaud, S. L. Johnson, A. Streun, R. Abela, D. Abramsohn, D. Grolimund, F. S. Krasniqi, T. Schmidt, V. Schlott, and G. Ingold, *Phys. Rev. Lett.* **99**, 174801 (2007).
- ⁷B. McNeil, *Nat. Photonics* **3**, 375 (2009).
- ⁸A. L. Cavalieri, D. M. Fritz, S. H. Lee, P. H. Bucksbaum, D. A. Reis, J. Rudati, D. M. Mills, P. H. Fuoss, G. B. Stephenson, C. C. Kao, D. P. Siddons, D. P. Lowney, A. G. MacPhee, D. Weinstein, R. W. Falcone, R. Pahl, J. Als-Nielsen, C. Blome, S. Diusterer, R. Ischebeck, H. Schlarb, H. Schulte-Schrepping, T. Tschentscher, J. Schneider, O. Hignette, F. Sette, and K. Sokolowski-Tinten, *Phys. Rev. Lett.* **94**, 114801 (2005).
- ⁹F. Brunel, *Phys. Rev. Lett.* **59**, 52 (1987).
- ¹⁰C. Reich, P. Gibbon, I. Uschmann, and E. Förster, *Phys. Rev. Lett.* **84**, 4846 (2000).
- ¹¹A. Cavalleri, C. W. Siders, F. L.H. Brown, D. M. Leitner, C. Tóth, J. A. Squier, C. P. J. Barty, K. R. Wilson, K. Sokolowski-Tinten, M. Horn von Hoegen, D. von der Linde, and M. Kammler, *Phys. Rev. Lett.* **85**, 586 (2000).
- ¹²F. Ewald, H. Schwoerer, and R. Sauerbrey, *Europhys. Lett.* **60**, 710 (2002).
- ¹³W. Krueer, *The Physics of Laserplasma Interactions* (Westview, New York, 2003).
- ¹⁴W. Lu, M. Nicoul, U. Shymanovich, A. Tarasevitch, P. Zhou, K. Sokolowski-Tinten, D. von der Linde, M. Mašek, P. Gibbon, and U. Teubner, *Phys. Rev. E* **80**, 026404 (2009).
- ¹⁵M. Nicoul, U. Shymanovich, A. Tarasevitch, D. von der Linde, and K. Sokolowski-Tinten, *Appl. Phys. Lett.* **98**, 191902 (2011).
- ¹⁶M. Bargheer, N. Zhavoronkov, R. Bruch, H. Legall, H. Stiel, M. Woerner, and T. Elsaesser, *App. Phys. B: Lasers Opt.* **80**, 715 (2005).
- ¹⁷N. Zhavoronkov, Y. Gritsai, M. Bargheer, M. Woerner, T. Elsaesser, F. Zamponi, I. Uschmann, and E. Förster, *Opt. Lett.* **30**, 1737 (2005).
- ¹⁸C. Rose-Petrucci, R. Jimenez, T. Guo, A. Cavalleri, C. W. Siders, F. Rksi, J. A. Squier, B. C. Walker, K. R. Wilson, and C. P. J. Barty, *Nature (London)* **398**, 310 (1999).

- ¹⁹K. Sokolowski-Tinten, C. Blome, J. Blums, A. Cavalleri, C. Dietrich, A. Tarasevitch, I. Uschmann, E. Forster, M. Kammiller, M. Horn-von Hoegen, and D. von der Linde, *Nature (London)* **422**, 287 (2003).
- ²⁰C. von Korff Schmising, M. Bargheer, M. Kiel, N. Zhavoronkov, M. Woerner, T. Elsaesser, I. Vrejoiu, D. Hesse, and M. Alexe, *Phys. Rev. Lett.* **98**, 257601 (2007).
- ²¹M. Bargheer, N. Zhavoronkov, Y. Gritsai, J. C. Woo, D. S. Kim, M. Woerner, and T. Elsaesser, *Science* **306**, 1771 (2004).
- ²²F. Zamponi, Z. Ansari, C. von Korff Schmising, P. Rothhardt, N. Zhavoronkov, M. Woerner, T. Elsaesser, M. Bargheer, T. Trobitzsch-Ryll, and M. Haschke, *Appl. Phys. A: Mater. Sci. Process.* **96**, 51 (2009).
- ²³*Time-Resolved X-Ray Scattering*, edited by K.-T. Tsen, J.-J. Song, M. Betz, and A. Y. Elezzabi (SPIE, Bellingham, Washington, 2011), Vol. 7937.
- ²⁴B. Freyer, J. Stingl, F. Zamponi, M. Woerner, and T. Elsaesser, *Opt. Express* **19**, 15506 (2011).
- ²⁵F. Zamponi, Z. Ansari, M. Woerner, and T. Elsaesser, *Opt. Express* **18**, 947 (2010).
- ²⁶J. Uhlig, C. G. Wahlström, M. Walczak, V. Sundström, and W. Fullagar, *Laser Part. Beams* **29**, 415 (2011).
- ²⁷G. Bauer, *Optical Characterization of Epitaxial Semiconductor Layers* (Springer-Verlag, Berlin, 1996).
- ²⁸M. Woerner, C. von Korff Schmising, M. Bargheer, N. Zhavoronkov, I. Vrejoiu, D. Hesse, M. Alexe, and T. Elsaesser, *Appl. Phys. A: Mater. Sci. Process.* **96**, 83 (2009).
- ²⁹M. Herzog, D. Schick, P. Gaal, R. Shayduk, C. von Korff Schmising, and M. Bargheer, *Appl. Phys. A* **1** (2011).
- ³⁰M. Herzog, D. Schick, W. Leitenberger, R. Shayduk, R. M. van der Veen, C. J. Milne, S. L. Johnson, I. Vrejoiu, and M. Bargheer, *New J. Phys.* **14**, 013004 (2012).
- ³¹I. Vrejoiu, G. Le Rhun, L. Pintilie, D. Hesse, M. Alexe, and U. Gösele, *Adv. Mater.* **18**, 1657 (2006).
- ³²C. von Korff Schmising, M. Bargheer, M. Kiel, N. Zhavoronkov, M. Woerner, T. Elsaesser, I. Vrejoiu, D. Hesse, and M. Alexe, *App. Phys. B* **88**, 1 (2007).
- ³³M. Herzog, W. Leitenberger, R. Shayduk, R. van der Veen, C. J. Milne, S. L. Johnson, I. Vrejoiu, M. Alexe, and D. Hesse, *Appl. Phys. Lett.* **96**, 161906 (2010).
- ³⁴C. von Korff Schmising, M. Bargheer, M. Kiel, N. Zhavoronkov, M. Woerner, T. Elsaesser, I. Vrejoiu, D. Hesse, and M. Alexe, *Phys. Rev. B* **73**, 212202 (2006).
- ³⁵In the simulation we assume a perfect sample structure. Accordingly, only the positions and amplitudes of the SL Bragg peaks are predicted correctly.
- ³⁶G. C. Cho, W. Kütt, and H. Kurz, *Phys. Rev. Lett.* **65**, 764 (1990).
- ³⁷M. Silies, H. Witte, S. Linden, J. Kutzner, I. Uschmann, E. Förster, and H. Zacharias, *Appl. Phys. A: Mater. Sci. Process.* **96**, 59 (2009).
- ³⁸K. Sokolowski-Tinten, private communication (2011).
- ³⁹U. Shymanovich, M. Nicoul, K. Sokolowski-Tinten, A. Tarasevitch, C. Michaelsen, and D. von der Linde, *Appl. Phys. B: Lasers Opt.* **92**, 493 (2008).

PAPER X

Ultrafast reciprocal-space mapping with a convergent beam

D. Schick, R. Shayduk, A. Bojahr, M. Herzog,
C. von Korff Schmising, P. Gaal and M. Bargheer.

J. Appl. Cryst. **46**, 1372-1377 (2013).

research papers

Journal of
Applied
Crystallography

ISSN 0021-8898

Received 24 May 2013

Accepted 19 July 2013

Ultrafast reciprocal-space mapping with a convergent beam

Daniel Schick,^a Roman Shayduk,^d André Bojahr,^a Marc Herzog,^{a,b} Clemens von Korff Schmising,^c Peter Gaal^d and Matias Bargheer^{a,d*}

^aInstitut für Physik und Astronomie, Universität Potsdam, Karl-Liebknecht-Strasse 24–25, 14476 Potsdam, Germany, ^bAbteilung Physikalische Chemie, Fritz-Haber-Institut der Max-Planck-Gesellschaft, Faradayweg 4–6, 14195 Berlin, Germany, ^dHelmholtz-Zentrum Berlin für Materialien und Energie GmbH, Wilhelm-Conrad-Röntgen Campus, BESSY II, Albert-Einstein-Strasse 15, 12489 Berlin, Germany, and ^cInstitut für Optik und Atomare Physik, Technische Universität Berlin, Strasse des 17 Juni 135, 10623 Berlin, Germany. Correspondence e-mail: bargheer@uni-potsdam.de

A diffractometer setup is presented, based on a laser-driven plasma X-ray source for reciprocal-space mapping with femtosecond temporal resolution. In order to map out the reciprocal space, an X-ray optic with a convergent beam is used with an X-ray area detector to detect symmetrically and asymmetrically diffracted X-ray photons simultaneously. The setup is particularly suited for measuring thin films or imperfect bulk samples with broad rocking curves. For quasi-perfect crystalline samples with insignificant in-plane Bragg peak broadening, the measured reciprocal-space maps can be corrected for the known resolution function of the diffractometer in order to achieve high-resolution rocking curves with improved data quality. In this case, the resolution of the diffractometer is not limited by the convergence of the incoming X-ray beam but is solely determined by its energy bandwidth.

© 2013 International Union of Crystallography
Printed in Singapore – all rights reserved

1. Introduction

Reciprocal-space mapping (RSM) has been established as a powerful tool for the nondestructive structural analysis of thin films and heterostructures (Bauer *et al.*, 1995; Fewster, 1997; Bowen & Tanner, 1998; Holy *et al.*, 1999). In addition to the intense specular Bragg reflections, the surrounding diffuse scattering covered by RSM gives access to microscopic information on strain states, dislocations and mosaicity, as well as the shape and size of the coherently scattering domain. The common drawback of RSM experiments is the need for time-consuming mesh scans in order to map out the reciprocal space in two or even three dimensions.

So far, high-resolution RSM has been precluded from time-resolved diffractometry such as *in situ* or pump–probe X-ray diffraction (XRD), either because of the too long integration time for a single reciprocal-space map or because of the required long-term stability, respectively. Owing to the availability of modern position-sensitive X-ray detectors (PSDs) with low noise and large dynamic range, several new diffractometer setups for RSM have been implemented (Kinne *et al.*, 1998; Mudie *et al.*, 2004; Masson *et al.*, 2005; Mariager *et al.*, 2009). In these high-speed RSM setups, the analysing part of the diffractometer has been replaced by a PSD in order to record symmetrically and asymmetrically diffracted X-rays simultaneously, resulting in a considerable decrease in the total measurement time. Compared with a conventional high-resolution diffractometer, the resolution in reciprocal space of the above-mentioned high-speed RSM

setups is limited by the PSD used, which defines the analyser acceptance by its pixel size and distance from the sample, while the monochromator settings are unchanged. Recent high-speed *in situ* RSM experiments during molecular beam epitaxy by Hu *et al.* (2012) proved the power of this new method.

In this contribution, we present a detailed characterization of a diffractometer for time-resolved RSM utilizing a laser-driven plasma X-ray source (PXS) providing femtosecond (fs) temporal resolution in a pump–probe scheme. The low photon flux at such exceptionally short pulse sources requires the collection of as many photons as possible. Accordingly, the resolution function of the PXS diffractometer is dominated by the convergent incoming X-rays, including Cu $K\alpha_1$ and $K\alpha_2$ energies, in contrast with other high-speed RSM setups.

In the first part, we will derive the resolution function of the ultrafast reciprocal-space mapping (URSM) setup in order to prove its applicability for the multidimensional structural analysis of thin films and heterostructures. As an example of a time-resolved URSM experiment, we present data from a double-layer structure made up of a ferroelectric $\text{PbZr}_{0.2}\text{Ti}_{0.8}\text{O}_3$ (PZT) layer grown on a metallic SrRuO_3 (SRO) layer on top of a dielectric SrTiO_3 (STO) substrate, which exhibits in- and out-of-plane lattice dynamics on a picosecond (ps) timescale after photo-excitation (Schick *et al.*, 2013). For laterally nearly perfect samples, the resolution function of the URSM setup dominates the in-plane broadening of the reciprocal lattice points (RLPs), and no lateral structural infor-

mation is resolvable by RSM. In order to access only the out-of-plane structural information we can correct the URSM data for the known resolution function of the setup, in order to collect one-dimensional time-resolved XRD data with high resolution and increased data quality compared with conventional XRD. The resolution of such rocking curves is no longer limited by the convergence of the incoming X-ray beam but solely by its energy bandwidth.

2. Experimental setup

The hardware constituting the experimental setup of the PXS has been described recently (Zamponi *et al.*, 2009; Schick *et al.*, 2012). In short, we use a two-stage Ti:sapphire amplifier operating at a repetition rate of 1 kHz with a centre wavelength of 800 nm and a pulse energy of 8 mJ compressed into a pulse of 40 fs duration to generate X-ray pulses (predominantly characteristic Cu $K\alpha$ and $K\beta$ lines) by focusing the main part (80%) of the laser light onto a moving copper tape in a vacuum chamber. The emitted X-ray bursts are further collected, focused and monochromated to only Cu $K\alpha$ energies ($E_{K\alpha_1} = 8047$ eV, $E_{K\alpha_2} = 8027$ eV, $\Delta E/E \simeq 0.25\%$) by a Montel multilayer optic with a convergence of $\Delta\omega = 0.3^\circ$ (full width at half-maximum, FWHM) in both dimensions and a focal spot size of only 200–300 μm (FWHM) at a distance $d = 1000$ mm from the source. From the maximum X-ray flux of approximately 5×10^5 photons s^{-1} , the brilliance B of the X-ray focus can be estimated as

$$B = 1.1 \times 10^5 \frac{\text{photons}}{\text{s mm}^2 \text{ mrad}^2 0.1\% \text{ BW}}, \quad (1)$$

which is much lower than for standard X-ray tubes (BW denotes bandwidth). However, considering the PXS pulse length of only 200 fs, the resulting peak brilliance per pulse becomes

$$B_{\text{peak}} = 5.7 \times 10^{14} \frac{\text{photons}}{\text{s mm}^2 \text{ mrad}^2 0.1\% \text{ BW}}. \quad (2)$$

Owing to the limited photon flux of the PXS, it is not reasonable to increase the brilliance of the source by additional monochromators and/or collimators since time-resolved experiments require high counting statistics.

The remaining 20% of the optical laser light is used to excite the sample. The relative timing of the optical pump pulses to the X-ray probe pulses is set by a mechanical delay stage and is inherently jitter free. The temporal information is extracted by performing XRD scans for different delays between optical pump pulses and X-ray probe pulses.

The sample is mounted in the centre of a two-circle goniometer which is placed in the focal plane of the X-ray optics. Thus, the X-ray footprint on the sample is minimized in order to reduce time-smearing effects due to the inevitable non-collinearity between laser pump and X-ray probe beam, and in order to probe a homogeneously excited part of the sample. The fast read-out CMOS (complementary metal-oxide semiconductor) two-dimensional X-ray detector is mounted on the outer circle of the goniometer at a distance of approximately

700 mm from the centre. The pixel size of the detector is approximately 200 μm in both dimensions, resulting in an angular acceptance in the scattering plane for each pixel of $\Delta\theta = 0.016^\circ$.

In order to account for both long- and short-term fluctuations, the PXS intensity is monitored directly by recording the unused intensity of a single reflection of our Montel X-ray optic with an integrating fast X-ray diode (Schick *et al.*, 2012). The nonlinear dependence between the diode response and the number of X-ray photons at the focus have been calibrated to determine the absolute number of X-ray photons per second at the focus during real experiments. Accordingly, the recorded rocking scans/RSM reflect the absolute diffracted intensity of the investigated sample.

3. Resolution area

Here, we discuss the resolution of the URSM setup, which is given by the smallest volume element in reciprocal space that is resolved by the X-ray diffractometer. Since we are carrying out only two-dimensional RSM, this volume element is reduced to an area and we can integrate the diffracted intensity on the two-dimensional detector along the dimension that is normal to the diffraction plane during the actual XRD scans. Accordingly, it would be sufficient to use a one-dimensional pixel array with a large pixel height to detect the diffracted X-rays. Knowledge of the resolution area is essential for the applicability of the diffractometer setup, since it determines the structural details of a sample which can be identified by RSM.

We carried out an $\omega/2\theta$ scan with the area detector in order to measure symmetric Bragg reflections with the URSM setup (see Fig. 1). The $\omega/2\theta$ scan ($\omega = \theta$) corresponds to a scan along q_z in reciprocal space (inset in Fig. 1). However, the PSD records symmetrically and asymmetrically diffracted photons at the same time, which corresponds to a scan of the detector angle θ at a fixed incoming angle ω (2θ scan). Accordingly, we can assign an angle θ to each individual pixel column of the PSD for a fixed ω , if the centre column of the region of interest (ROI) on the PSD is always at $\theta = \omega$. The angles of the surrounding pixel columns at position x (positive integer) follow from

$$\theta(x) = \Delta\theta(x - x_c) + \omega, \quad (3)$$

where x_c is the position of the central pixel column in the ROI and $\Delta\theta$ is the angular acceptance of each pixel column.

The diffracted intensities measured in (ω, θ) space can be converted into q space by the following coordinate transformation (Holy *et al.*, 1999):

$$\mathbf{q} = \begin{pmatrix} q_x \\ q_z \end{pmatrix} = k \begin{pmatrix} \cos\theta - \cos\omega \\ \sin\omega + \sin\theta \end{pmatrix}, \quad (4)$$

where $k = 2\pi/\lambda$ is the magnitude of the incoming and outgoing X-ray wavevectors, since only elastic diffraction is considered; λ is the wavelength of the radiation. The resolution area of the diffractometer depends on various parameters but we discuss only the most prominent ones here. We can neglect any

research papers

broadening on the reciprocal-space map due to a finite X-ray spot size on the sample, since we use a convergent beam with the sample in the focus of the X-ray beam path, and hence the X-ray footprint is comparable to the size of the individual pixels of the PSD. We consider the convergence of the incoming X-rays $\Delta\omega$, the acceptance of the detector pixels $\Delta\theta$ and the wavevector spread due to the energy bandwidth of the X-ray photons $\Delta k/k = \Delta E/E$ as sources of instrumental broadening. As a linear approximation, both the magnitude and direction of the instrumental broadening in q space can be determined by the partial derivative of \mathbf{q} multiplied by the change in the deviating parameter:

$$\Delta \mathbf{q}_\omega = \frac{\partial \mathbf{q}}{\partial \omega} \Delta \omega = \begin{pmatrix} \sin \omega \\ \cos \omega \end{pmatrix} k \omega \Delta \omega, \quad (5)$$

$$\Delta \mathbf{q}_\theta = \frac{\partial \mathbf{q}}{\partial \theta} \Delta \theta = \begin{pmatrix} -\sin \theta \\ \cos \theta \end{pmatrix} k \theta \Delta \theta, \quad (6)$$

$$\Delta \mathbf{q}_k = \frac{\partial \mathbf{q}}{\partial k} \Delta k = \begin{pmatrix} \cos \theta - \cos \omega \\ \sin \omega + \sin \theta \end{pmatrix} \Delta k. \quad (7)$$

For a symmetric Bragg reflection, the inclination of $\Delta \mathbf{q}_\omega$ with respect to the q_z axis is ω . This is referred to as the monochromator streak (Holy *et al.*, 1999). The so-called analyser

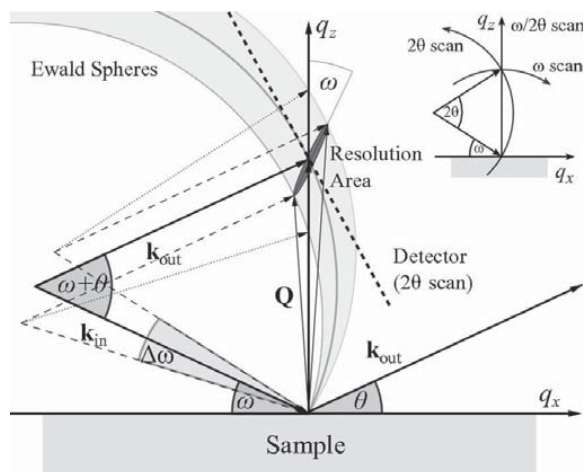


Figure 1 The reciprocal-space coordinate system (q_x, q_z) of the sample. The angles between the sample surface and the incoming and outgoing X-rays, \mathbf{k}_{in} and \mathbf{k}_{out} , are denoted ω and θ , respectively. Owing to the convergence $\Delta\omega$ of \mathbf{k}_{in} , a range of nonconcentric Ewald circles is illuminated simultaneously (dotted lines). The angle-resolving detector is represented as a tangent at the intersection of an Ewald circle and the q_z axis (thick dashed line). The resolution is dominated by the convergence $\Delta\omega$ and we neglect the acceptance of the detector pixels $\Delta\theta \rightarrow 0$ here (see text). A pixel at a fixed angle θ then integrates over the resolution area, which is inclined by ω with respect to the q_z axis. The thin dashed lines are parallel to \mathbf{k}_{out} (fixed θ) but originate at different \mathbf{k}_{in} vectors, determined by the convergence $\Delta\omega$. The energy spread leads to a broadening along q_z . The resolution area is approximated as an ellipsoid, assuming a Gaussian distribution of $\Delta\omega$ and ΔE . The inset shows the different scan types for RSM: the $\omega/2\theta$ scan goes along the q_z axis, the ω scan is approximately parallel to the q_x axis and the 2θ scan goes along the Ewald circle.

streak originates from $\Delta \mathbf{q}_\omega$ and is inclined by $\omega \simeq \theta$ in the opposite direction. Since the magnitude of $\Delta \mathbf{q}_\omega$ is approximately 20 times larger than the magnitude of $\Delta \mathbf{q}_\theta$ for the URSM setup, we neglect the latter in the following discussion. Fig. 1 shows the graphical analogue of the theoretical derivation of the instrumental broadening of the URSM setup. Owing to the convergence $\Delta\omega$ of the incoming X-rays \mathbf{k}_{in} , a distribution of nonconcentric Ewald circles is illuminated in reciprocal space. A single detector pixel at a fixed angle θ with an infinitesimally small acceptance $\Delta\theta \rightarrow 0$ integrates the diffracted intensity along the vector $|\Delta \mathbf{q}_\omega|$, which is constructed by a parallel translation of \mathbf{k}_{out} to the origins of all incident \mathbf{k}_{in} (thin dashed lines in Fig. 1). This resolution streak is inclined by ω with respect to the q_z axis (monochromator streak). The energy spread of the incoming X-rays leads to an additional broadening along q_z , which is approximated as an ellipsoidal resolution area in Fig. 1 for a Gaussian distribution of $\Delta\omega$ and ΔE .

The resolution function of the URSM setup can be determined experimentally by measuring the reciprocal-space map around an RLP of an almost perfect bulk crystal. The measured data correspond to a convolution of the resolution function with the RLP, which can be approximated as a δ function for the case of a perfect bulk crystal. Fig. 2(a) shows the experimental reciprocal-space map of the (002) Bragg

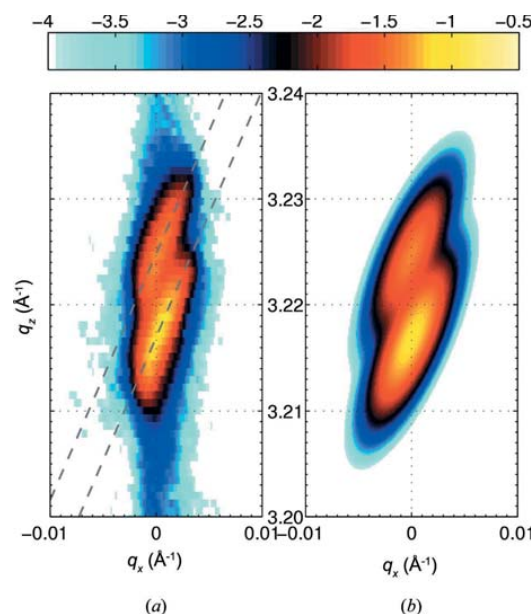


Figure 2 (a) The measured reciprocal-space map of the (002) Bragg reflection of a nearly perfect STO substrate. The data are plotted with equidistant axes and reveal the resolution area of the time-resolved RSM setup. The inclination of the resolution area with respect to the q_z axis is ω and is represented by the grey dashed lines. The peak doubling and the broadening along q_z are caused by the Cu $K\alpha$ doublet and the natural line width of each $K\alpha$ line, respectively. (b) The theoretical resolution area at $\omega = 23.23^\circ$ is plotted, accounting for the convergence $\Delta\omega$ and the energy bandwidth of the incoming X-rays \mathbf{k}_{in} . Broadening due to the finite acceptance of the detector is neglected here.

reflection of a nearly perfect STO substrate. The inclination of the resolution area with respect to the q_z axis can be determined as $\omega = 23.23^\circ$, which is represented by the grey dashed lines. The doubling of the RLP originates from the Cu $K\alpha$ doublet and corresponds to a separation of approximately $\Delta q_z = k\Delta E/E \simeq 0.01 \text{ \AA}^{-1}$. The broadening along q_z is caused by the natural line width of each $K\alpha$ line, which is approximately 2 eV (Krause & Oliver, 1979). The diffuse background along the q_z axis indicates the crystal truncation rod of the substrate. In Fig. 2(b), the theoretical resolution area of the URSM setup is plotted, which is derived from equations (5)–(7). The resolution area is approximated as two two-dimensional Gaussian functions with one main axis along $\Delta \mathbf{q}_\omega$. The intensities are normalized to the maximum of the experimental data shown in Fig. 2(a), and the ratio of the maxima of the two Gaussians equals the intensity ratio of the Cu $K\alpha_1$ and $K\alpha_2$ lines. The good agreement between the experimentally determined and theoretically derived resolution functions of the URSM setup allows one to distinguish between instrumental and structural broadening of RLPs in actual time-resolved RSM experiments. Furthermore, neglecting additional sources of instrumental broadening proved to be valid.

4. Time-resolved reciprocal-space mapping

In order to prove the applicability of the diffractometer setup for time-resolved RSM, we have chosen an epitaxial thin-film

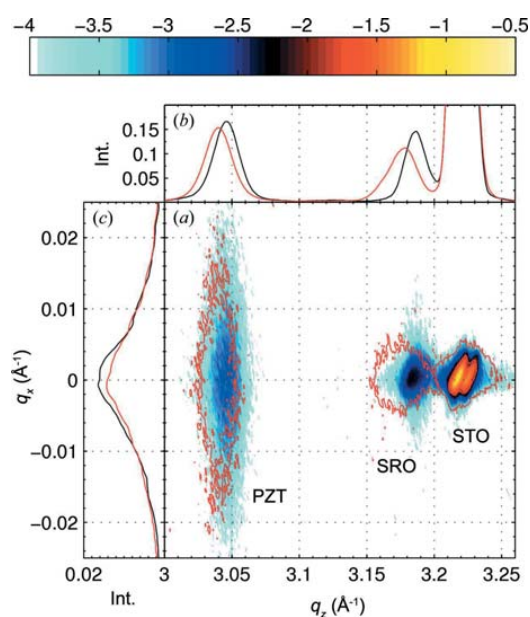


Figure 3
(a) The measured reciprocal-space map of the (002) Bragg reflections of the PZT/SRO double layer on an STO substrate. The red contour lines (constant reflectivity of $10^{-3.5}$) and the red lines in parts (b) and (c) indicate the changed RSM at a delay of $t = 75 \text{ ps}$ after excitation of the sample with an 800 nm femtosecond laser pulse. (b), (c) Integrated reciprocal-space maps over the q_x and q_z dimension, respectively. In (c), the integration is carried out only over the q_z range of the PZT peak.

sample that consists of a ferroelectric PZT layer and a metallic SRO transducer layer which were grown onto an STO substrate by pulsed laser deposition (Vrejoiu *et al.*, 2006). From the detailed characterization of the sample by transmission electron microscopy (TEM) and static XRD, we derived layer thicknesses of $d_{\text{PZT}} = 207 \text{ nm}$ and $d_{\text{SRO}} = 147 \text{ nm}$, and average lattice constants normal to the sample surface of $c_{\text{PZT}} = 4.130 \text{ \AA}$, $c_{\text{SRO}} = 3.948 \text{ \AA}$ and $c_{\text{STO}} = 3.905 \text{ \AA}$ (Schick *et al.*, 2013). The ferroelectric PZT layer exhibits large defects such as threading and misfit dislocations, due to the intrinsic domain formation of this material. This gives rise to structural in-plane broadening of the corresponding RLP.

The resulting time-resolved reciprocal-space map is depicted in Fig. 3 and features the dominant broadening of the PZT RLP along q_x . The broadening of the SRO and STO RLPs is dominated by the resolution area of the diffractometer, which is indicated by their size and inclination. The SRO RLP also features a slight diffuse broadening in the q_x dimension due to its lower crystal quality compared with the STO substrate. The adoption of the high-speed RSM technique allows one to measure a time-resolved reciprocal-space map within minutes, providing good photon statistics. For the femtosecond variant of RSM at PXS machines this is particularly important, because the reciprocal-space maps for different time delays after excitation have to be compared, and long-term drifts of the setup are often inevitable. The unpumped data set shown in Fig. 3 was recorded within 30 min. The red contour lines at a constant reflectivity of $10^{-3.5}$ in Fig. 3(a), and the red lines in Figs. 3(b) and 3(c), show the result of the RSM probing 75 ps after excitation of the sample with an 800 nm femtosecond laser pulse. The changes in the positions and widths of the material-specific Bragg peaks in the reciprocal-space map can be analysed in order to study the photoinduced in- and out-of-plane lattice dynamics with femtosecond temporal resolution (Schick *et al.*, 2013).

5. Rocking scans

For laterally nearly perfect crystalline samples, the structural Bragg peak broadening in-plane is well below the resolution of our URSM setup. As an example, we show the URSM data of a superlattice (SL) in Fig. 4(a). The SL is composed of 15 double layers, each consisting of 7.3 nm metallic ($\text{La}_{0.7}\text{Sr}_{0.3}\text{MnO}_3$ (LSMO) and 13.7 nm ferroelectric ($\text{Ba}_{0.7}\text{Sr}_{0.3}\text{TiO}_3$ (BST)). The SL is grown epitaxially on an STO substrate with very high crystalline quality. Here, we wish to derive a means of benefitting from the URSM setup for such highly perfect crystalline samples. Since we cannot resolve the in-plane Bragg peak broadening for this sample, we are limited to out-of-plane structural information, which can be achieved by standard rocking scans ($\omega/2\theta$ scan for symmetric Bragg reflection). Thus, it would be sufficient to use a one-dimensional point detector in the diffractometer setup. The corresponding rocking curve for a point detector with a large acceptance $\Delta\theta \gg \Delta\omega$ is plotted in Fig. 4(c) as a red line (the data are imitated by integrating the original data from the PSD detector along the scattering plane). The rocking curve

research papers

exhibits good statistics, since nearly all diffracted photons are collected by the detector, but the resolution of the individual Bragg peaks is very low because $\Delta\mathbf{q}_\theta$ can no longer be neglected. Accordingly, all peaks are broadened and no Cu $K\alpha$ doublet is observed.

If we use a point detector with the same acceptance $\Delta\theta$ as for a single pixel of the PSD, *e.g.* by the use of slits, we obtain a much higher resolution of the rocking curve, shown as a blue line in Fig. 4(c). This plot is equivalent to a cut along q_x of the data shown in Fig. 4(a). However, since we discriminate all asymmetrically diffracted X-ray photons with this slit setup, the counting statistic of the resulting rocking curve is approximately 14% that of the large-aperture detector (red line) and is thus not applicable for time-resolved experiments with PXS machines.

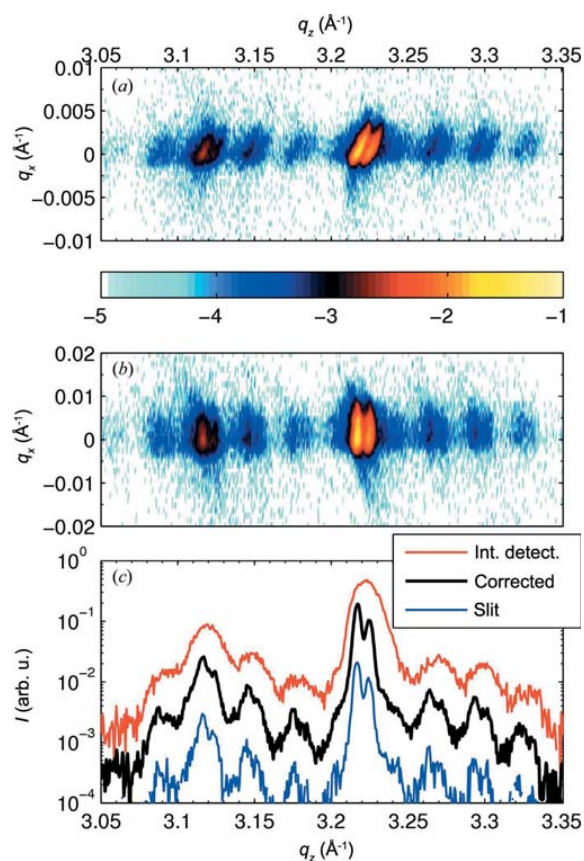


Figure 4
(a) (Original) reciprocal-space map for the BST/LSMO SL on an STO substrate, revealing several SL reflections and the most intense STO substrate (002) reflection. (b) (Corrected) reciprocal-space map after translational/rotational transformation. (c) The red curve imitates a measurement using a large point detector with an acceptance $\Delta\theta$ much larger than the convergence $\Delta\omega$. The blue curve imitates the use of a slit in front of a point detector $\Delta\theta \rightarrow 0$, *i.e.* a cut at $q_x = 0$ from (a). The black curve is the integration over the complete q_x range of the corrected data shown in (b). The curves are offset in intensity for better visualization.

Since we know that the broadening of the RLP for such highly perfect samples originates primarily from the resolution function of the URSM setup, we can correct the data accordingly. By rotating each ellipsoidal RLP that intersects the q_z axis at $q_z = 2k \sin \omega$ by an angle of $\gamma = (90^\circ - \omega)$, we can assign all asymmetrically diffracted X-ray photons to the correct q_z value of the symmetric RLP by integrating over the q_x axis. The coordinate transformation is derived in Appendix A and the result is shown in Fig. 4(b), where all RLPs are now aligned parallel to the q_x axis. The integration of these corrected data along q_x is shown as a black curve in Fig. 4(c) and combines the high resolution of the slit-like blue curve and the good statistics of the large-aperture-like red curve.

6. Conclusions

The implementation of the high-speed RSM technique using position-sensitive X-ray detectors allows the implementation of time-resolved RSM at PXS setups. The instrumental and structural broadening of the URSM can be distinguished by the inclination and width of the measured RLPs. The method has been applied to study the in- and out-of-plane lattice dynamics in a ferroelectric thin film after photoexcitation on a picosecond timescale (Schick *et al.*, 2013). For nearly perfect crystalline samples, the experimental routine can be applied with an adapted data-processing routine in order to correct the measured RLPs for the known resolution function of the diffractometer. This procedure allows for the recording of high-resolution rocking curves without discriminating diffracted X-rays, since the resolution is no longer limited by the convergence of the incoming X-ray beam, but solely by its energy bandwidth.

APPENDIX A
Resolution area correction

Fig. 5 sketches the RLP in the reciprocal-space map for a highly perfect crystalline sample, so the RLP is primarily broadened by the resolution area of the URSM setup. As was derived in §3, the ellipsoidal RLP is inclined by ω with respect

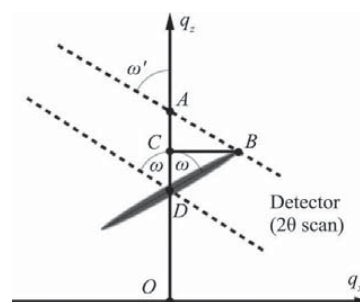


Figure 5
The ellipsoidal RLP is inclined by ω and intersects the q_z axis at point D. The intensity along the ellipsoidal RLP, *e.g.* at point B, is recorded for an incoming angle ω' at a pixel at $\theta' \neq \omega'$.

to the q_z axis when the intersection of the RLP with the q_z axis is at the point $D = (0, 2k \sin \omega)$. In order to correct the data for the resolution function of the diffractometer, one has to rotate the ellipsoidal RLP around the point D by an angle of $\gamma = (90^\circ - \omega)$. For any point B along the RLP, this is done by translating point B by the vector $-\mathbf{OD}$, in order subsequently to rotate B counterclockwise by γ around the origin O of the coordinate system, and translating it back by the vector \mathbf{OD} .

However, the intensity at point B is measured at an incoming angle ω' with a pixel at an angle $\theta' \neq \omega'$. Thus, it is nontrivial to determine the coordinates of the corresponding intersection point $D(\omega)$ from the point $B(\omega', \theta')$. If $\omega' \simeq \omega$, which holds for a small convergence $\Delta\omega$, one can approximate that $\overline{DC} = \overline{CA}$ and one can derive the q_z coordinate of point D as

$$D_z = \overline{OA} - 2\overline{CA} = 2(B_z - k \sin \omega'), \quad (8)$$

where B_z is the q_z coordinate of the point $B(\omega', \theta')$ given by the general transformation $\mathbf{q}(\omega, \theta)$ into q space, cf. equation (4).

The complete coordinate transformation for the correction of the URSM data for laterally nearly perfect samples can then be written in matrix form as a combination of translation and rotation:

$$\begin{aligned} \mathbf{q}_c &= \mathbf{R} \cdot [\mathbf{q}(\omega, \theta) - \mathbf{OD}] + \mathbf{OD} \\ &= \begin{pmatrix} \cos \gamma & -\sin \gamma \\ \sin \gamma & \cos \gamma \end{pmatrix} \cdot \left[\mathbf{q}(\omega, \theta) - \begin{pmatrix} 0 \\ D_z \end{pmatrix} \right] + \begin{pmatrix} 0 \\ D_z \end{pmatrix}, \quad (9) \end{aligned}$$

where \mathbf{R} is a rotation matrix.

The authors gratefully acknowledge financial support by the BMBF via grant No. 03WKP03A and by the Leibniz Graduate

School 'Dynamics in New Light' (DinL). We thank Dr Ionela Vrejoiu for fruitful discussions and for providing the experimental samples.

References

- Bauer, G., Li, J. & Koppensteiner, E. (1995). *J. Cryst. Growth*, **157**, 61–67.
- Bowen, D. K. & Tanner, B. K. (1998). *High-resolution X-ray Diffractometry and Topography*. London: Taylor and Francis.
- Fewster, P. F. (1997). *Crit. Rev. Solid State Mater. Sci.* **22**, 69–110.
- Holy, V., Pietsch, U. & Baumbach, T. (1999). *High-resolution X-ray Scattering from Thin Films and Multilayers*. Springer Tracts in Modern Physics, Vol. 149. Heidelberg: Springer.
- Hu, W., Suzuki, H., Sasaki, T., Kozu, M. & Takahashi, M. (2012). *J. Appl. Cryst.* **45**, 1046–1053.
- Kinne, A., Thoms, M., Röss, H. R., Gerhard, T., Ehinger, M., Faschinger, W. & Landwehr, G. (1998). *J. Appl. Cryst.* **31**, 446–452.
- Krause, M. O. & Oliver, J. H. (1979). *J. Phys. Chem. Ref. Data*, **8**, 329–338.
- Mariager, S. O., Lauridsen, S. L., Dohn, A., Bovet, N., Sørensen, C. B., Schlepütz, C. M., Willmott, P. R. & Feidenhans'l, R. (2009). *J. Appl. Cryst.* **42**, 369–375.
- Masson, O., Boule, A., Guinebretière, R., Lecomte, A. & Dauger, A. (2005). *Rev. Sci. Instrum.* **76**, 063912.
- Mudie, S. T., Pavlov, K. M., Morgan, M. J., Hester, J. R., Tabuchi, M. & Takeda, Y. (2004). *J. Synchrotron Rad.* **11**, 406–413.
- Schick, D., Bojahr, A., Herzog, M., Gaal, P., Vrejoiu, I. & Bargheer, M. (2013). *Phys. Rev. Lett.* **110**, 095502.
- Schick, D., Bojahr, A., Herzog, M., von Korff Schmising, C., Shayduk, R., Leitenberger, W., Gaal, P. & Bargheer, M. (2012). *Rev. Sci. Instrum.* **83**, 025104.
- Vrejoiu, I., Le Rhun, G., Zakharov, N. D., Hesse, D., Pintilie, L. & Alexe, M. (2006). *Philos. Mag.* **86**, 4477–4486.
- Zamponi, F., Ansari, Z., von Korff Schmising, C., Rothhardt, P., Zhavoronkov, N., Woerner, M., Elsaesser, T., Bargheer, M., Trobitzsch-Ryll, T. & Haschke, M. (2009). *Appl. Phys. A*, **96**, 51–58.

PAPER XI

Time-domain sampling of x-ray pulses using an ultrafast sample response

P. Gaal D. Schick, M. Herzog, A. Bojahr, R. Shayduk ,
J. Goldshteyn, H. Navirian, W. Leitenberger, I. Vrejoiu,
D. Khakhulin, M. Wulff, and M. Bargheer.

Appl. Phys. Lett. **101**, 243106 (2012).

Time-domain sampling of x-ray pulses using an ultrafast sample response

P. Gaal,^{1,a)} D. Schick,² M. Herzog,² A. Bojahr,² R. Shayduk,¹ J. Goldshteyn,²
H. A. Navirian,² W. Leitenberger,² I. Vrejoiu,³ D. Khakhulin,⁴ M. Wulff,⁴ and M. Bargheer^{1,2}

¹Helmholtz-Zentrum Berlin für Materialien und Energie GmbH, Wilhelm-Conrad-Röntgen Campus,

BESSY II, Albert-Einstein-Str. 15, 12489 Berlin, Germany

²Institut für Physik und Astronomie, Universität Potsdam, Karl-Liebknecht-Str. 24-25, 14476 Potsdam, Germany

³Max-Planck-Institut für Mikrostrukturphysik, Weinberg 2, 06120 Halle, Germany

⁴European Synchrotron Radiation Facility (ESRF), 6 rue Jules Horowitz, 38000 Grenoble, France

(Received 18 September 2012; accepted 19 November 2012; published online 10 December 2012)

We employ the ultrafast response of a 15.4 nm thin SrRuO₃ layer grown epitaxially on a SrTiO₃ substrate to perform time-domain sampling of an x-ray pulse emitted from a synchrotron storage ring. Excitation of the sample with an ultrashort laser pulse triggers coherent expansion and compression waves in the thin layer, which turn the diffraction efficiency on and off at a fixed Bragg angle during 5 ps. This is significantly shorter than the duration of the synchrotron x-ray pulse of 100 ps. Cross-correlation measurements of the ultrafast sample response and the synchrotron x-ray pulse allow to reconstruct the x-ray pulse shape. © 2012 American Institute of Physics. [<http://dx.doi.org/10.1063/1.4769828>]

Ultrafast x-ray diffraction (UXRD) performed at synchrotron sources is an ideal tool for detecting atomic motion in solids, due to the large brilliance and stability of these sources.^{1,2} In particular, the utilization of nanostructured samples, which are excited and measured in a pump-probe scheme, has led to a deeper understanding of the propagation of coherent acoustic sound waves in layered structures.³ In this way, coherent optical superlattice phonons, which correspond to back-folded acoustic phonons have been excited and studied in detail.^{4,5} Such systems show modulations of superlattice Bragg peaks on a picosecond (ps) timescale⁶ and may eventually lead to the development of new devices such as an ultrafast x-ray switch.^{7,8} On a more fundamental level, it has been shown recently that thin layer transducers can be used to excite quasi-monochromatic strain waves, which allow for studying coherent acoustic phonon dynamics.⁹ In typical pump-probe measurements, a sample is excited by an ultrafast laser and subsequently probed by a time-delayed ultrashort probe pulse. For each time delay τ , a snapshot of the sample is recorded. However, the complete dynamics in the sample can only be reconstructed through a series of snapshots if the probe pulses are at least twice as short as the inverse of the highest frequency that is contained in the sample response. In general, a pump-probe signal I_{pp} corresponds to a cross-correlation measurement of the delayed probe pulse $P(t + \tau)$ with the time-dependent response of the sample $S(t)$.¹⁰

$$I_{pp}(\tau) = \int_{-\infty}^{\infty} dt \cdot S(t)P(t + \tau). \quad (1)$$

In the limit of infinitely short probe pulses $P(t) \rightarrow \delta(t)$, the pump-probe signal directly yields the sample response $S(t)$. Therefore, a good knowledge of the temporal structure of the probe pulse is crucial for a correct analysis of the data

obtained in a pump-probe scheme. X-ray pulses generated at synchrotron sources are typically characterized by streak camera measurements, which can provide time-resolutions below 1 ps.^{11,12}

In this letter, we present a cross-correlation measurement of a 100 ps x-ray probe pulse delivered by a synchrotron storage ring and the ultrafast response of a laser excited sample. The idea of the experiment together with the experimental setup is explained in Figures 1(a) and 1(b), respectively. An x-ray probe pulse (black), delivered from the ESRF storage ring is diffracted by a sample (red) exhibiting a dynamic response upon excitation, which is much shorter than the duration of the probe pulse. The sample dynamics is such that it turns the x-ray diffraction (XRD) efficiency on and off on an ultrafast timescale. The transient shown in red in Figure 1(a) is a simulation of the x-ray response of the actual structure that was used in the experiment and which is described below. By delaying the optical excitation pulse against the x-ray probe pulse, different sections of the latter are diffracted. The black transient in Figure 1(a) shows the x-ray probe pulse as determined by streak camera measurements.¹⁴ The ESRF x-ray pulse shows a slight asymmetry. Due to the finite diffraction efficiency of the unexcited sample, a fraction of the x-ray probe pulse is also diffracted when the sample is not excited. We call this fraction the diffraction background. Figure 1(b) shows the experimental setup. Time-resolved measurements were done at the undulator beamline ID09B at ESRF. A general description of the setup can be found in Ref. 13. The storage ring was running in 16-bunch mode¹⁵ delivering monochromatized x-ray pulses at an energy of 12 keV and a duration of 90-120 ps, depending on the charge of the electron bunch. The beamline is equipped with a commercial laser system (Coherent Legend), which yields 800 nm optical pulses with an energy of 1.5 mJ and a duration of 600 fs at a repetition rate of 1 kHz.

In the following, we characterize our sample and explain the nature of the ultrafast response that is later applied to

^{a)}Electronic mail: peter.gaal@helmholtz-berlin.de.

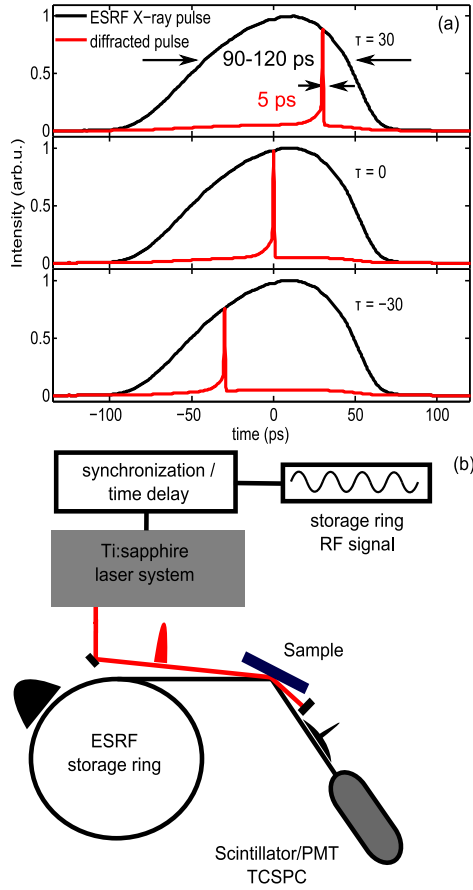


FIG. 1. (a) Cross-correlation of an ultrafast sample response against a 100 ps x-ray probe pulse. The calculated sample diffraction efficiency is modulated by optical excitation of the sample at different delay times τ . Since the sample dynamics last for roughly 5 ps, it is much shorter than the x-ray pulse. (b) Experimental setup at ID09B at the ESRF storage ring (for details see Ref. 13): A Ti:sapphire laser is synchronized to the RF signal from the storage ring. The synchronization allows to delay the laser pulse against the x-ray probe pulse with ps resolution. Diffracted x-ray photons from the sample are captured in a combined scintillator/photomultiplier (PMT) detector and counted in a time-correlated single-photon-counting (TCSPC) module.

sample the synchrotron x-ray pulse. For the cross-correlation measurement, we used a $d = 15.4$ nm thin layer of metallic SrRuO₃ (SRO) grown epitaxially on an SrTiO₃ (STO) substrate. The relevant parameters of these materials are well known.^{16–19} While the SRO layer is opaque for the optical pump light, the STO substrate is transparent. Therefore, energy from the pump pulse is only deposited in the thin layer. Figure 2(a) shows a measurement of the ultrafast sample dynamics upon excitation with a 800 nm optical pump pulse of a duration of 50 fs. The measurement was performed at the plasma X-ray source (PXS) at University of Potsdam which delivers x-ray pulses of ≈ 150 fs duration at the characteristic copper K_α energy of 8.047 keV.^{20,21} The pump fluence was set to 30 mJ/cm². The θ -axis in Figure 2(a) has been converted to match the measurements from ESRF. Upon optical excitation, the layer peak shifts to

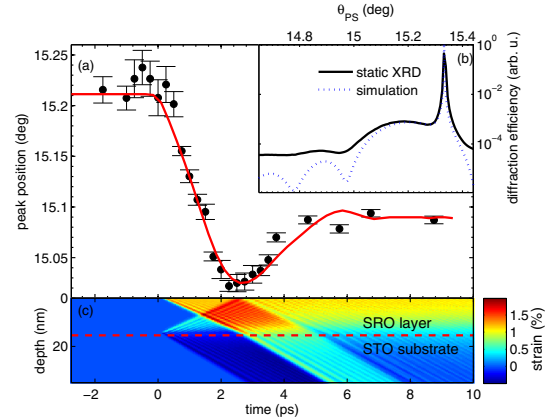


FIG. 2. (a) Measurement (black dots) and simulation (red solid line) of the center of mass shift of the SRO layer peak upon excitation with an ultrashort optical pump pulse. The measurement is performed at the PXS at University of Potsdam. (b) Measurement (black solid line) and simulation (blue dotted line) of the static x-ray diffraction curve of a 15.4 nm thin SRO layer grown epitaxially on an STO substrate. (c) Simulation using a masses and springs model of the coherent phonon dynamics upon impulsive optical excitation of the SRO layer.

smaller angles and reaches a minimum angle of $\theta = 15.02^\circ$ after 2.5 ps. At later times, the peak shifts back to a quasi-stationary position around an angle of 15.1° . This position is reached at a delay of 5 ps. The timescale of the peakshift results from the ratio of the sample thickness and the velocity of sound in the sample. The sample thickness of 15.4 nm represents a good trade-off between the duration of coherent phonon propagation and diffraction efficiency from the SRO layer. Figure 2(b) shows a static XRD measurement of the structure. The STO substrate peak appears at an angle of 15.33° . Due to the small layer thickness, the layer peak has a width of 0.12° . The dynamics in the sample, which leads to the observed peak shift, is illustrated in Figure 2(c). This graph shows a simulation using a masses and springs model,²² which accounts for coherent phonon propagation and for heat diffusion from the excited layer to the substrate. Optical excitation triggers coherent expansion waves which are launched at the layer-substrate and layer-air interface, respectively, and propagate into the SRO layer. The lattice expansion is shown in red colors. At the same time, a compression wave, which is shown in dark blue colors, is launched at the layer-substrate interface. This compression wave directly propagates into the substrate. At a delay of roughly 1.3 ps, the layer peak shifts across the angle of the quasi-stationary peak position. The reason is the interference of the excited strain waves from both interfaces, as shown in Figure 2(c). The maximum shift occurs at 2.5 ps, when both expansion waves have propagated through the layer. While the strain wave that was launched at the sample surface now propagates into the substrate, the other strain wave is reflected at the sample surface and propagates back through the layer. Reflection at the surface also converts the expansion wave into a compression wave. Therefore, the layer peak position is shifted to larger θ -angles for delays larger than 2.5 ps. The quasi-stationary peak position is reached,

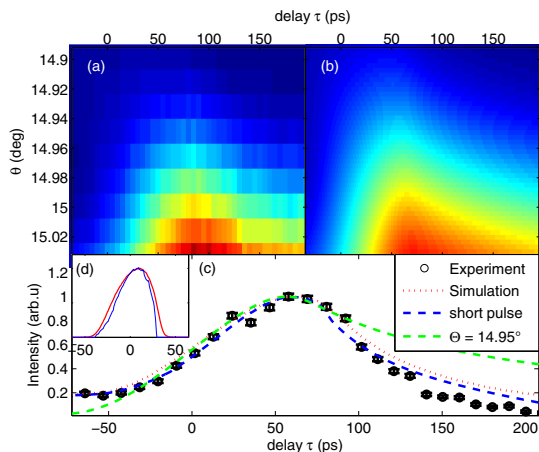


FIG. 3. (a) Two-dimensional measurement of the cross-correlation between the x-ray pulse from ESRF and the optically excited sample. The temporal delay is plotted against the x-axis, the y-axis corresponds to the Bragg angle of the sample. The diffracted intensity is coded in colors. The duration of the measured dynamics increases for larger Bragg angles. (b) Simulated cross-correlation (same axis as (a)). The probe pulse employed for this simulation is shown in the red solid line in (d). (c) Transient diffraction data (black diamonds) measured at a Bragg angle of 14.9° . The dashed and dotted lines are calculated transient signals assuming an ESRF probe pulses shape that was extracted by a deconvolution of the data (blue) and measured by a streak camera (red). The green dashed transient was calculated by setting $\theta = 14.95^\circ$ at the sample. The temporal resolution is reduced as a result of a thermal peak shift of the excited layer. (d) ESRF x-ray pulse shapes used for the calculations. The color code corresponds to (c).

when both strain waves have propagated into the substrate. The layer peak relaxes to its equilibrium position via heat diffusion from the hot layer to the substrate. This process is much slower than the coherent phonon dynamics and occurs on a nanosecond timescale.²³ Hence, after the layer peak has shifted to its quasi-stationary position, the diffraction efficiency is constant on the timescale of the incident x-ray pulse. Due to the constructive interference of both expansion waves, there is an angular range, where the peak shift is governed exclusively by the propagation of coherent phonons in the sample. Therefore, in the appropriate angular range, the sample shows a modulation of its x-ray diffraction efficiency which lasts for only 5 ps. We exploit this feature as an ultrafast probe of the x-ray pulse from the synchrotron.

Measurements of the cross-correlation signal between the ESRF x-ray pulse and the ultrafast sample response are shown in Figure 3(a) for Bragg angles from 14.89° to 15.03° . The excitation fluence was set to 15 mJ/cm^2 . Since the duration of the optical pulse is 600 fs, which is significantly faster than the propagation time of the coherent phonons through the layer, it can be omitted in the analysis of the correlation signal. Figure 3(b) shows a simulation in the same angular range that reproduces the measurement. A cut along the delay time axis is shown in Figure 3(c) for a Bragg angle of 14.9° . The measured transient has a full width at half maximum (FWHM) duration of 100 ps. Together with the experimental data, we plot a calculated pump-probe signal that was obtained by cross-correlating the simulated sample response with an ESRF probe pulse. The simulation shown in the red dotted line was

obtained by using the ESRF pulse profile as measured by a streak camera. It is shown in Figure 1(a) and in the red solid line in Figure 3(d), respectively. This pulse has a FWHM duration of ≈ 100 ps. The blue solid line in Figure 3(d) shows the shape of the ESRF x-ray pulse as extracted from a deconvolution of the simulated sample response out of the measured data. The data have been slightly smoothed for that procedure. This pulse, which has a FWHM duration of 85 ps, was used to calculate the blue dashed transient shown in Figure 3(c). It yields an even better representation of the data compared to the red transient that was calculated using the measured ESRF pulse. This concurs with the observations from previous experiments at the ID09B beamline at ESRF, which indicate a pulse length of the order of 80 ps in 16-bunch mode. Hence, the determination of the x-ray pulse length using our cross-correlation technique seems to characterize the x-ray pulse more accurately than the streak-camera measurement.

The green transient in Figure 3(c) shows a measurement where the Bragg-angle on the sample was set to $\theta = 14.95^\circ$. The slow decay at positive pump-probe delays stems from thermal relaxation from the excited layer to the substrate and the subsequent shift of the layer peak to larger angles. This effect deteriorates the temporal resolution in the cross-correlation measurement. Note that the rising edge coincides with the red and blue curves, since in all cases the rise of the pump-probe signal is determined by coherent phonon dynamics. However, the relative background at negative delays of the green dashed line in Figure 3(c) appears smaller compared to the other transients. This results from the fact that the diffraction background at negative delays is constant for all Bragg-angles, while the peak diffraction increases for increasing θ -angles of the sample.

In conclusion, we performed a time-domain sampling measurement of a 100 ps x-ray probe pulse using the ultrafast response of a laser-excited thin SRO film grown on an STO substrate. Excitation of the film with an ultrashort optical pulse triggers the propagation of coherent phonons, which modulate the diffraction efficiency in the sample. Already 5 ps after optical excitation, the sample reaches a quasi-equilibrium state that is stable for the remaining duration of the incident x-ray pulse. Our experiment is easy to reproduce and may be used for efficient time-zero determination and for measuring the shape of the x-ray probe pulse.

We thank the BMBF for funding the project via 05K10IP1.

¹M. F. DeCamp, D. A. Reis, D. M. Fritz, P. H. Bucksbaum, E. M. Dufresne, and R. Clarke, *J. Synchrotron Radiat.* **12**(2), 177–192 (2005).

²J. Larsson, P. A. Heimann, A. M. Lindenberg, P. J. Schuck, P. H. Bucksbaum, R. W. Lee, H. A. Padmore, J. S. Wark, and R. W. Falcone, *Appl. Phys. A: Mater. Sci. Process.* **66**, 587–591 (1998).

³D. A. Reis, M. F. DeCamp, P. H. Bucksbaum, R. Clarke, E. Dufresne, M. Hertlein, R. Merlin, R. Falcone, H. Kapteyn, M. M. Murnane, J. Larsson, T. Missalla, and J. S. Wark, *Phys. Rev. Lett.* **86**(14), 3072–3075 (2001).

⁴M. Trigo, Y. M. Sheu, D. A. Arms, J. Chen, S. Ghimire, R. S. Goldman, E. Landahl, R. Merlin, E. Peterson, M. Reason, and D. A. Reis, *Phys. Rev. Lett.* **101**(2), 025505 (2008).

⁵M. Herzog, D. Schick, W. Leitenberger, R. Shayduk, R. M. van der Veen, C. J. Milne, S. L. Johnson, I. Vrejoiu, and M. Bargheer, *New J. Phys.* **14**(1), 013004 (2012).

⁶M. Herzog, W. Leitenberger, R. Shayduk, R. van der Veen, C. J. Milne, S. L. Johnson, I. Vrejoiu, M. Alexe, D. Hesse, and M. Bargheer, *Appl. Phys. Lett.* **96**(16), 161906 (2010).

- ⁷P. H. Bucksbaum and R. Merlin, *Solid State Commun.* **111**, 535 (1999).
- ⁸J. M. H. Sheppard, P. Sondhauss, R. Merlin, P. H. Bucksbaum, R. W. Lee, and J. S. Wark, *Solid State Commun.* **136**, 181 (2005).
- ⁹M. Herzog, A. Bojahr, J. Goldshteyn, W. Leitenberger, I. Vrejoiu, D. Khakhulin, M. Wulff, R. Shayduk, P. Gaal, and M. Bargheer, *Appl. Phys. Lett.* **100**(9), 094101 (2012).
- ¹⁰S. Mukamel, “Principles of Nonlinear Optical Spectroscopy” (Oxford University Press, New York, 1995).
- ¹¹H. Enquist, H. Navirian, R. Nueske, C. von Korff Schmising, A. Jurgilaitis, M. Herzog, M. Bargheer, P. Sondhauss, and J. Larsson, *Opt. Lett.* **35**(19), 3219–3221 (2010).
- ¹²Z. Chang, A. Rundquist, J. Zhou, M. M. Murnane, H. C. Kapteyn, X. Liu, B. Shan, J. Liu, L. Niu, M. Gong, and X. Zhang, *Appl. Phys. Lett.* **69**, 133 (1996).
- ¹³H. A. Navirian, M. Herzog, J. Goldshteyn, W. Leitenberger, I. Vrejoiu, D. Khakhulin, M. Wulff, R. Shayduk, P. Gaal, and M. Bargheer, *J. Appl. Phys.* **109**(12), 126104 (2011).
- ¹⁴S. Anfinrud, P. A. Srajer, V. Moffat, K. Schotte, F. Techert, and M. Wulff, “Third-Generation Hard X-ray Synchrotron Radiation Sources. Source Properties, Optics, and Experimental Techniques” (John Wiley & Sons, Inc., 2002).
- ¹⁵M. Cammarata, L. Eybert, F. Ewald, W. Reichenbach, M. Wulff, P. Anfinrud, F. Schotte, A. Plech, Q. Kong, M. Lorenc, B. Lindenau, J. Rübiger, and S. Polachowski, *Rev. Sci. Instrum.* **80**(1), 015101 (2009).
- ¹⁶R. O. Bell and G. Rupprecht, *Phys. Rev.* **129**, 90–94 (1963).
- ¹⁷Y. H. Ren, M. Trigo, R. Merlin, V. Adyam, and Q. Li, *Appl. Phys. Lett.* **90**, 251918 (2007).
- ¹⁸S. Yamanaka, T. Maekawa, H. Muta, T. Matsuda, S. Kobayashi, and K. Kurosaki, *J. Solid State Chem.* **177**(10), 3484–3489 (2004).
- ¹⁹G. J. Fischer, Z. Wang, and S.-I. Karato, *Phys. Chem. Miner.* **20**, 97–103 (1993).
- ²⁰D. Schick, A. Bojahr, M. Herzog, C. von Korff Schmising, R. Shayduk, W. Leitenberger, P. Gaal, and M. Bargheer, *Rev. Sci. Instrum.* **83**(2), 025104 (2012).
- ²¹F. Zamponi, Z. Ansari, C. von Korff Schmising, P. Rothhardt, N. Zhavoronkov, M. Woerner, T. Elsaesser, M. Bargheer, T. Trobitzsch-Ryll, and M. Haschke, *Appl. Phys. A* **96**(1), 51–58 (2009).
- ²²M. Herzog, D. Schick, P. Gaal, R. Shayduk, C. von Korff Schmising, and M. Bargheer, *Appl. Phys. A* **106**(3), 489–499 (2012).
- ²³R. Shayduk, H. A. Navirian, W. Leitenberger, J. Goldshteyn, I. Vrejoiu, M. Weinelt, P. Gaal, M. Herzog, C. von Korff Schmising, and M. Bargheer, *New J. Phys.* **13**(9), 093032 (2011).

PAPER XII

Ultrafast switching of hard X-rays

P. Gaal D. Schick, M. Herzog, A. Bojahr, R. Shayduk ,
J. Goldshteyn, W. Leitenberger, I. Vrejoiu, D. Khakhulin,
M. Wulff, and M. Bargheer.

J. Synchrotron Rad. **21**, 380-385 (2014).

research papers

Journal of
Synchrotron
Radiation

ISSN 1600-5775

Received 3 September 2013
Accepted 22 November 2013

Ultrafast switching of hard X-rays

Peter Gaal,^{a*} Daniel Schick,^b Marc Herzog,^b André Bojahr,^b Roman Shayduk,^a Jevgeni Goldshteyn,^b Wolfram Leitenberger,^b Ionela Vrejoiu,^c Dmitry Khakhulin,^d Michael Wulff^d and Matias Bargheer^{a,b}

^aHelmholtz-Zentrum Berlin für Materialien und Energie GmbH, Wilhelm-Conrad-Röntgen Campus, BESSY II, Albert-Einstein-Strasse 15, 12489 Berlin, Germany, ^bInstitut für Physik und Astronomie, Universität Potsdam, Karl-Liebknecht-Strasse 24-25, 14476 Potsdam, Germany, ^cMax-Planck-Institut für Mikrostrukturphysik, Weinberg 2, 06120 Halle, Germany, and ^dEuropean Synchrotron Radiation Facility (ESRF), 6 rue Jules Horowitz, 38000 Grenoble, France.

*E-mail: peter.gaal@helmholtz-berlin.de

A new concept for shortening hard X-ray pulses emitted from a third-generation synchrotron source down to few picoseconds is presented. The device, called the PicoSwitch, exploits the dynamics of coherent acoustic phonons in a photo-excited thin film. A characterization of the structure demonstrates switching times of ≤ 5 ps and a peak reflectivity of $\sim 10^{-3}$. The device is tested in a real synchrotron-based pump-probe experiment and reveals features of coherent phonon propagation in a second thin film sample, thus demonstrating the potential to significantly improve the temporal resolution at existing synchrotron facilities.

Keywords: ultrafast X-ray diffraction; thin film; coherent phonons; X-ray switching; pulse shortening; optical pump X-ray probe; time-resolved.

© 2014 International Union of Crystallography

1. Introduction

Ultrafast structural dynamics can be monitored by time-resolved X-ray techniques, provided that the probing X-ray pulse is sufficiently short (Bargheer *et al.*, 2006; Rousse *et al.*, 2001). Unfortunately, large-scale facilities like synchrotrons, which offer the best experimental conditions in terms of stability, tunability and brilliance, typically do not deliver pulses shorter than 100 ps. An exception is the so-called low- α mode (Abo-Bakr *et al.*, 2002), where the synchrotron is able to generate pulses as short as 5 ps. However, the low- α mode is only available for a few weeks per year, since it reduces the X-ray intensity at all beamlines connected to the storage ring. To date, various schemes exist that can manipulate or resolve the time structure of a synchrotron X-ray pulse. All of them are indirect in the sense that they do not act on the X-ray pulse itself. Either the electron bunch in the storage ring is manipulated [e.g. femtoslicing (Schoenlein *et al.*, 2000; Beaud *et al.*, 2007) or orbit deflection using RF cavities (Zholents *et al.*, 1999)], or electrons generated in photocathodes are used to spatially map the temporal structure of the synchrotron pulse on a screen (Enquist *et al.*, 2010; Chang *et al.*, 1996). The highest temporal resolution at synchrotron sources is obtained by using electron slicing schemes, which leads to 150 fs pulses (Schoenlein *et al.*, 2000; Beaud *et al.*, 2007). However, these schemes result in a rather low photon flux. Highly improved experimental conditions are found at new facilities like free-electron-laser (FEL) sources (Emma *et al.*, 2010; Pile, 2011;

Geloni *et al.*, 2010). However, the large demand for ultrashort, brilliant and stable X-ray pulses from the ultrafast community is not yet satisfied.

Several early attempts were made to manipulate the time structure of the synchrotron X-ray pulse directly. Early experiments reported switching of hard X-rays resulting in pulses of 100 ps duration and more (Wark *et al.*, 1989; Zolotoyabko & Quintana, 2004; Allam, 1970; Grigoriev *et al.*, 2006; Navirian *et al.*, 2011). A promising concept is based on optical phonons (Bucksbaum & Merlin, 1999); however, this could not yet be realised experimentally (Sheppard *et al.*, 2005). A modified approach exploiting zone-folded acoustic phonons in a superlattice (Herzog *et al.*, 2010) demonstrated a modulation of the switching-contrast ratio of $\Delta R/R = 24.1$ during 1 ps. However, the first modulation maximum is followed by several post-pulses that result from the generation of multiple sound waves at interfaces between the superlattice layers. This leads to a significant protraction of the switching time.

Here we present a new concept that builds on the experience of previous approaches. We excite coherent strain waves in a thin metallic oxide film in order to modify the diffraction efficiency of the structure at a fixed Bragg angle on a picosecond time scale. An exemplary gate is shown in Fig. 1. A good switch provides short rise and fall times t_r and t_f and a short on-time ΔT . Also the diffraction efficiency before (η_0) and after (η_∞) the switching should be low, whereas it should be high in the on-state (η_{\max}). This automatically increases the switching contrast C_0 and C_∞ . The contrast is defined as $C_i =$

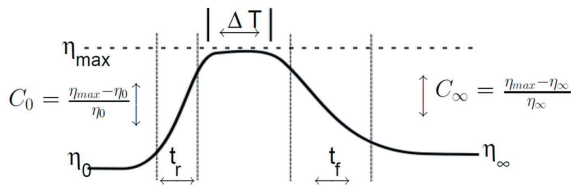


Figure 1
Gate parameters defining the performance of an X-ray switch: turn-on time ΔT , rise- and fall-time t_r and t_f , respectively, diffraction efficiency before (η_0), during (η_{\max}) and after (η_∞) switching and contrast before (C_0) and after (C_∞) switching.

$(\eta_{\max} - \eta_i) / \eta_i$ ($i = 0, \infty$). After introducing the experimental method of ultrafast X-ray diffraction (UXRD) in the next section, we present a full characterization of the PicoSwitch both experimentally and theoretically in §3. In §4 we apply our approach to a real synchrotron-based ultrafast pump-probe experiment. Results of this experiment are discussed in §5.

2. Experimental set-ups

We performed UXRD experiments at the Plasma X-ray Source (PXS) (Schick *et al.*, 2012, 2013) at the University of Potsdam and at the ID09B beamline at the European Synchrotron Radiation Facility (ESRF) in Grenoble, France. Schematics of the set-ups are shown in Figs. 2(a) and 2(b), respectively. A high-power laser yielding ultrashort laser pulses is employed to excite the sample and the PicoSwitch, respectively. At the University of Potsdam we use a commercial Coherent Legend Duo system which provides optical pulses ($\lambda = 800$ nm, pulse energy = 8 mJ) with a duration of 40 fs at a repetition rate of 1 kHz. For X-ray generation, the laser pulses are focused onto a copper target in a vacuum chamber. The target is wrapped on a system of

spools together with debris protection tape. Interaction of the highly intense laser pulses with the copper target leads to the emission of characteristic Cu K_α X-ray ($E = 8.047$ keV) bursts of 150 fs duration (Schick *et al.*, 2012; Zamponi *et al.*, 2009). The temporal delay between optical pump and X-ray probe pulses is realised by a mechanical delay stage. Since the X-ray probe pulse is generated by the same laser as the pump beam, both are perfectly synchronized. X-ray photons, which are emitted in a solid angle of 4π , are collected using a Montel X-ray focusing mirror having an image ratio of 1:7. The mirror is mounted 875 mm from the sample. The 4π emission angle, the energy bandwidth and the focal distance reduce the angular resolution to approximately 0.1° in a diffraction experiment in convergence correction mode (Schick *et al.*, 2013), as indicated by the gray shaded area in Figs. 4(d) and 4(e). Reflected X-ray photons from the sample are detected with a CMOS hybrid-pixel area detector (Dectris Pilatus 100K).

For the experiments at the ID09B beamline at the ESRF the storage ring was running in 16-bunch mode, delivering monochromated X-ray pulses at an energy of 12 keV and a duration of 90–120 ps (Cammarata *et al.*, 2009). The beamline is equipped with a commercial laser system (Coherent Legend) which yields 800 nm optical pulses with an energy of 1.5 mJ and a duration of 600 fs at a repetition rate of 1 kHz. The laser oscillator was electronically phase-locked to the synchrotron repetition rate, which allows for timing the delay t between the amplified optical and X-ray pulses with an accuracy of better than 5 ps. This is significantly shorter than the X-ray pulse duration. The gated probe pulse reflected by the PicoSwitch is inherently synchronized to the pump laser after switching. For the second optical path, a mechanical delay stage has been introduced to realise the pump-probe delay τ . X-ray photons have been detected with a plastic scintillator (BC408, Saint-Gobain) attached to a Hamamatsu

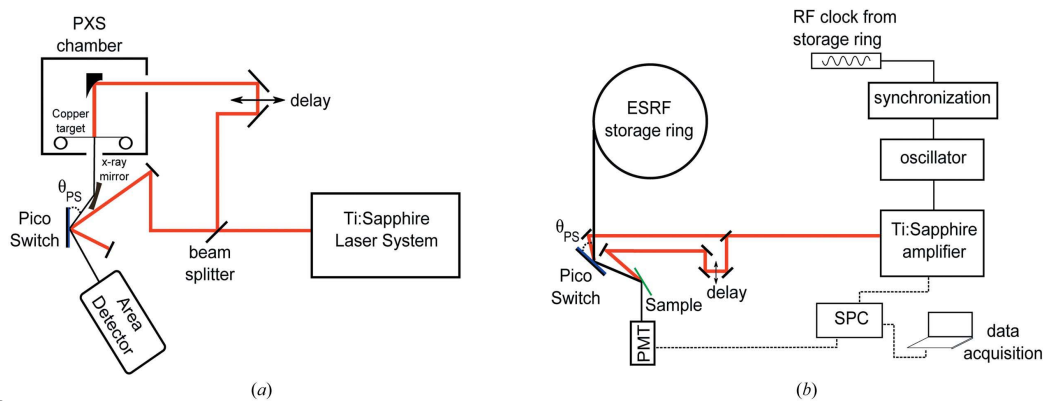


Figure 2
(a) Typical UXRD set-up. The PXS at the University of Potsdam delivers 150 fs X-ray pulses at an energy of 8.047 keV. A detailed description of the PXS is given by Schick *et al.* (2012) and Zamponi *et al.* (2009). Laser parameters are: pulse energy 8 mJ, pulse duration 40 fs and repetition rate 1 kHz. The pump fluence was set to 30 mJ cm^{-2} . (b) Synchrotron-based pump-probe experiment. A Ti:sapphire laser system (Coherent Legend) is synchronized to the repetition rate of the ESRF storage ring with an accuracy of ≤ 5 ps between the X-ray and laser pulses. Laser parameters are: pulse energy 1.5 mJ, pulse duration 600 fs and repetition rate 1 kHz. The pump-probe scheme is shown in Fig. 4(a) in detail. X-ray photons diffracted from the sample are captured in a photomultiplier (PMT) and counted in a single-photon-counting (SPC) unit.

research papers

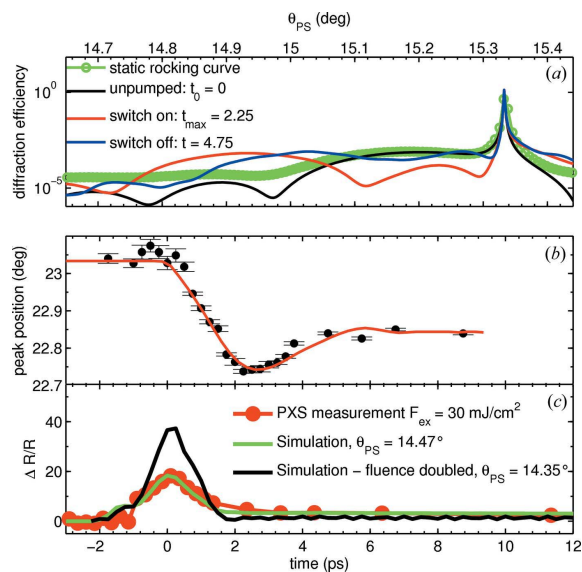


Figure 3 Characterization of the PicoSwitch. (a) Green: measured diffraction curve of the PicoSwitch. The data were recorded at the ID09B beamline at ESRF at an X-ray energy of 12 keV. Black: simulation of the unexcited structure; red: simulation for maximum layer expansion 2.25 ps after optical excitation; blue: simulation at $t = 4.75$ ps after optical excitation. At this delay all coherent sound waves have propagated into the substrate. (b) Ultrafast shift of the layer peak measured at the PXS at the University of Potsdam with an X-ray energy of 8.047 keV. The red curve shows a simulation of the coherent phonon dynamics. (c) Measurement (red bullets) and simulations (green and black solid lines) of the PicoSwitch. The measurement was performed at the Plasma X-ray Source (PXS) at the University of Potsdam. The simulation (green line) shows excellent agreement with the measured data. A larger contrast and switching efficiency is predicted for higher pump fluences (black line). The angle θ_{PS} is the X-ray diffraction angle as defined in Fig. 2(a).

photomultiplier tube (H7422). The detector signal was fed to a single-photon-counting unit controlled by computer.

It is important to note that the different X-ray energies used during the PXS and the ESRF experiments lead to two different angular ranges in the diffraction data presented in this contribution. We preserved the original angular scales to clearly distinguish the different experiments. The X-ray response of the sample is essentially the same for both X-ray energies used in the experiments. All diffraction data shown were recorded on the (002) reflection of SrTiO₃ (STO) (substrate peak) and SrRuO₃ (SRO) (layer peak). At an X-ray energy of 12 keV, the maximum of the (002) reflection of SRO appears at 15.2° (Fig. 3a). These data were recorded at the ESRF. At an X-ray energy of 8.047 keV, the SRO layer peak appears at 23.03° (Fig. 3b). These data were recorded at the PXS at the University of Potsdam.

3. PicoSwitch characterization

The PicoSwitch consists of a thin SRO layer with a thickness of $d_{SRO} = 15.4$ nm which was epitaxially grown on an STO substrate (Vrejoiu *et al.*, 2006). A static $\theta/2\theta$ scan recorded at

the ID09B beamline at the ESRF is shown by the green line in Fig. 3(a). Note in particular that the peak reflectivity of the (002) SRO reflection at X-ray energies from 8 keV to 12 keV is $\sim 10^{-3}$. This corresponds to the highest achievable diffraction efficiency in the on-state, as defined in Fig. 1. The black line is a simulation of the diffraction profile from the structure using dynamic diffraction theory (Als-Nielsen, 2011).

To record the ultrafast response of the PicoSwitch to the optical excitation, we resort to the UXRD set-up at the PXS at the University of Potsdam (Schick *et al.*, 2012). Fig. 3(b) shows the shift of the SRO layer peak as a function of the delay after excitation of the PicoSwitch with an ultrashort 800 nm pump pulse. The interpretation of coherent phonon dynamics of an excited layer is straightforward (Sokolowski-Tinten *et al.*, 2001) and the red solid line shows a simulation using a linear-chain model (Herzog *et al.*, 2012b). Excitation of the PicoSwitch with an ultrashort optical pulse launches coherent expansion waves starting at the air/SRO and SRO/STO interfaces through the SRO layer, shifting the layer Bragg peak to lower angles. The expansion waves propagate at the sound velocity in SRO of $v_{SRO} = 6.3$ nm ps⁻¹ (Herzog *et al.*, 2012a; Schick *et al.*, 2014). Reflection of the strain wave at the surface converts the expansion that was launched at the SRO/STO interface into a compression wave, which propagates back through the layer and into the substrate, thus shifting the Bragg peak back to about two-thirds compared with the maximum expansion. Due to the perfect matching of the acoustic impedances of SRO and STO (Herzog *et al.*, 2012a), there is no reflection at the interface. The coherent dynamics in the SRO film last for $\tau_{switch} = 2d_{SRO}/v_{SRO} \leq 5$ ps, *i.e.* the time it takes for the strain waves to propagate back and forth through the layer. For later times the peak position is given by the remaining heat expansion, and heat conduction cools the layer on a nanosecond timescale (Shayduk *et al.*, 2011). Hence, there is an angular range, which extends from 22.85° to 22.75° in Fig. 3(b), where the ultrafast coherent phonon propagation is responsible for the rise and fall of the diffraction efficiency. This range can be exploited for ultrafast X-ray switching. For the experiments conducted at the ESRF at an X-ray photon energy of 12 keV, this angular range extends from 14.9° to 14.75° (Fig. 3a). In order to quantitatively compare the experimental signal with theory we feed the spatio-temporal strain map calculated in a linear-chain model into a simulation of the dynamical X-ray diffraction, yielding the X-ray response of the PicoSwitch $R(t, \theta)$ (Herzog *et al.*, 2012b; Schick *et al.*, 2014). The result shows excellent agreement with the measured dynamics of the peak shift demonstrated in Fig. 3(b) and the corresponding intensity change plotted in Fig. 3(c) when keeping the angle of the PicoSwitch fixed. Fig. 3(a) shows the simulations in a broader angular range for an X-ray energy of 12 keV. The red curve represents a simulated rocking curve at a time delay of 2.25 ps after excitation. At this moment the thin SRO layer is maximally expanded. The blue curve, which is simulated for a delay of 4.74 ps, depicts the situation where the coherent compression wave has propagated into the substrate and thus terminates the coherent dynamics in the PicoSwitch.

4. Synchrotron-based pump–probe experiment

Now we apply the PicoSwitch, which was characterized in the previous section by simulations and measurements at the University of Potsdam, to a real synchrotron-based pump–probe experiment in order to study the impulsive expansion of a photo-excited metallic layer. These experiments were performed at the ID09B beamline at ESRF. The output of a Ti:sapphire laser amplifier is split into two beams in order to pump the PicoSwitch and the sample separately with delays t and τ , respectively. The pump fluence was set to 15 mJ cm^{-2} on both the PicoSwitch and the sample. A detailed schematic of the experimental set-up is shown in Figs. 4(a) and 2(b). The electronic delay t is set so that the diffraction efficiency of the

switch is turned on and off approximately when the maximum of the 100 ps X-ray pulse from the synchrotron impinges on the PicoSwitch. It is held constant during the experiment. The X-ray flux incident on the PicoSwitch was $3.4 \times 10^{10} \text{ photons s}^{-1}$. The pump–probe delay τ shifts the optical pump pulse for the sample against the shortened X-ray pulse. The sample under investigation was a 70 nm metallic SRO layer grown on an STO substrate (Vrejoiu *et al.*, 2006). The dynamics in the sample can be understood in the framework of coherent phonon propagation as described before. We employ this structure as a reference to test the achievable time resolution with the gated X-ray probe pulse. The diffraction angle of the sample θ_s is set to the maximum of the SRO layer peak. After excitation of the sample with the incident optical pulse, the

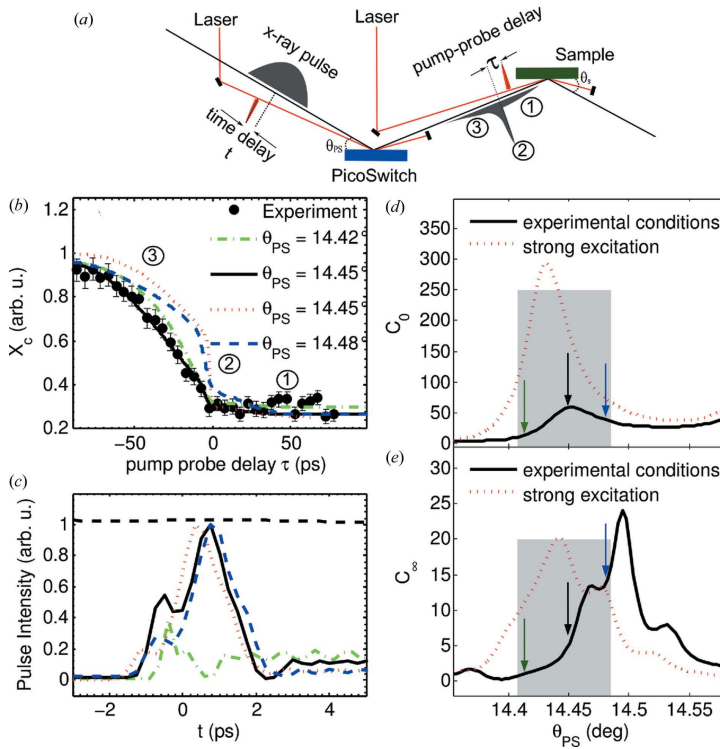


Figure 4 Synchrotron-based time-resolved experiment. (a) Sketch of the experimental set-up showing the fixed timing t of laser and X-ray pulses and the pump–probe delay τ . If the optical excitation pulse arrives earlier at the sample than the gated section of the X-ray probe pulse, the pump–probe delay τ is positive. The probe pulse is divided into three sections: leading edge (1), ultrafast gate (2) and trailing edge (3). (b) Measured (black dots) and simulated (green dash-dotted, black solid, blue dashed and red dotted lines) pump–probe correlation signal X_c . The error bars indicate a confidence interval of $\pm 32\%$. The simulations were obtained using equation (1). The angle θ_{PS} is color-coded. All simulations are for the fluence $F = 15 \text{ mJ cm}^{-2}$ used in the experiment. Only the red dotted curve is simulated for an optimized fluence of 20 mJ cm^{-2} . (c) Shortened X-ray probe pulses for different incident angles on the PicoSwitch color-coded as in (b). The black dashed line is the original X-ray probe pulse. (d) Simulated initial (C_0) and (e) final (C_∞) contrast as defined in Fig. 1 for different Bragg angles on the PicoSwitch. The black solid lines show simulations for a pump fluence of 15 mJ cm^{-2} . The red dotted lines show a contrast for stronger excitation with a fluence of 20 mJ cm^{-2} . The colored vertical arrows mark the angles where the probe pulses in (b) and (c) were calculated. The gray shaded area marks the angular resolution of the PXS measurement.

diffracted intensity decreases with a decay time of 4.5 ps, comparable with the duration of the gated X-ray pulse. Hence, the sample response is essentially a step function. Fig. 4(b) shows the measured relative change of the diffracted X-ray intensity (black bullets) as a function of the pump–probe delay τ . The green dash-dotted, black solid, red dotted and blue dashed lines represent simulations of the X-ray response assuming the simulated shortened probe pulses depicted in Fig. 4(c) with the same color code. The shape of the switched pulse is determined by the Bragg angle θ_{PS} chosen on the PicoSwitch and by the pump fluence. The simulated signals plotted as lines in Fig. 4(b) depict the normalized correlation of the sample X-ray response $R(t)$ at the fixed angle θ_s with the shortened probe pulse $P(t, \theta_{PS})$ for various diffraction angles θ_{PS} of the PicoSwitch,

$$X_c(\tau, \theta_{PS}) = \frac{\int_{-\infty}^{\infty} P(t, \theta_{PS}) R(\tau + t) dt}{\int_{-\infty}^{\infty} P(t, \theta_{PS}) R(-\infty) dt}. \quad (1)$$

5. Discussion

In the following we explain the impact of different probe pulse shapes on the measured signal. For a better understanding we divide the gated probe pulse shown in Fig. 4(a) into three sections: (1) and (3) are determined by the initial and final contrast C_0 and C_∞ , respectively, while (2) represents the ultrafast gate from the PicoSwitch. Figs. 4(b)–4(e) present the main results of the synchrotron-based optical-pump–X-ray-probe experiment with the shortened X-ray probe pulse. Experimental data are presented in Fig. 4(b) (black bullets).

Figs. 4(d) and 4(e) show the angle dependence of the initial and final contrast ratio C_0

research papers

and C_∞ , respectively. The angles θ_{PS} used in the simulations shown in Figs. 4(b) and 4(c) are marked by color-coded arrows. The black solid line is calculated for a pump fluence of 15 mJ cm^{-2} ; the red dotted line shows the contrast for a fluence of 20 mJ cm^{-2} . Note that features appearing in X_c at positive pump-probe delays stem from badly suppressed background photons in the leading edge of the probe pulse marked (1) in Fig. 4(a). Features at negative τ originate from the trailing edge of the probe pulse, which is marked (3) and is determined by the thermal relaxation of the PicoSwitch after optical pumping (Shayduk *et al.*, 2011). The sharp drop in X_c , which is observed in the red, blue and black simulation in Fig. 4(b), is caused by the short and intense section of the probe pulse and is marked (2).

Our experimental data are best reproduced by the simulation shown by the black solid line in Fig. 4(b). It shows a rather slow initial decay (3) and it is flat after the gated probe pulse (1), *i.e.* for positive τ . This indicates a large initial contrast C_0 , which is marked by the black arrow in Fig. 4(d). The sharp drop from $X_c = 0.4$ to $X_c = 0.25$ at $\tau = 0$ ps indicates the response to the ultrafast switching (2).

The simulation for larger θ_{PS} (blue dashed line) shows a lower initial and higher final contrast, leading to deviations from the observed correlation (black bullets). The dash-dotted green line shows a case where both the initial and final contrast C_0 and C_∞ are lower. The dash-dotted green probe pulse in Fig. 4(c) shows almost no ultrafast switching characteristics. Instead, the contrast ratio changes abruptly from C_0 to C_∞ . Hence, the ultrafast feature at $\tau = 0$ ps disappears and in addition there are deviations from the measured signal at negative τ . The best simulated performance could be obtained by increasing the pump fluence, as shown by the red dotted line in Figs. 4(b) and 4(c). Due to limited beam time, a corresponding measurement could not be realised. In essence, Fig. 4 shows that we have performed an ultrafast X-ray diffraction experiment with a synchrotron probe pulse which was shortened to approximately 2 ps as indicated in Fig. 4(c) by the black line.

For an optimized performance in future applications the PicoSwitch must be pumped with about 33% higher optical pump fluence. The simulation shown by the red dotted line in Figs. 4(b) and 4(c) demonstrates an increased initial and final contrast at the θ_{PS} chosen in the experiment. This parameter setting on the PicoSwitch would result in a correlation signal X_c shown by the red dotted line in Fig. 4(b). The corresponding probe pulse is shown in Fig. 4(c). The essential difference from the pulse used in the experiment is the higher contrast. The switching time is identical. For comparison, the X-ray flux of the gated pulse incident on the sample as well as the relative proportions of the sections (1)–(3) according to Fig. 4(a) are listed in Table 1.

While the PicoSwitch already allows for a significant reduction of the X-ray pulse duration, it still requires further development. In particular, the contrast ratio needs improvement in order to sufficiently suppress background photons that are reflected by the PicoSwitch in the off-state. As shown in Figs. 4(c) and 4(d), the contrast can be optimized

Table 1

X-ray flux (photons s^{-1}) and relative proportions according to Fig. 4(a) of the gated X-ray pulse for the simulations shown in Fig. 4(b).

	X-ray flux	(1)	(2)	(3)
Black solid	0.15×10^6	8%	22%	70%
Blue dashed	0.18×10^6	22%	38%	40%
Red dotted	2.8×10^6	7%	48%	45%

through the diffraction angle on the PicoSwitch and through the excitation fluence on the device. The main impediment to increasing the contrast is the lattice expansion due to laser heating of the device. Hence, the final contrast C_∞ is the limiting parameter. The contrast can be improved by changing the PicoSwitch structure from a thin film to a heterostructured multilayer. In such a structure one layer could be employed for the generation of a coherent expansion and compression wave that would propagate into neighboring layers. There, the central angle of the Bragg reflection would be shifted according to the modification of the lattice spacing, allowing for the same type of switching as was demonstrated in our experiment. Since the propagation of the strain wave occurs significantly faster than thermal diffusion, the switching would be almost free of thermal background distortion.

However, our experiment shows that the PicoSwitch is suitable for generating probe pulses that are capable of resolving ultrafast dynamics on a few-picosecond timescale. We would like to point out that the PicoSwitch can sustain even higher fluences up to 40 mJ cm^{-2} without degradation. The generated X-ray pulses are limited in duration to a few picoseconds and are therefore longer than the pulses obtained through slicing of the electron bunch. The achievable photon flux is comparable. However, the PicoSwitch experiment is significantly easier to implement. The temporal stability and angular resolution of the gated X-rays are determined by the synchrotron source. This is a significant advantage compared with laser plasma sources, such as the PXS at the University of Potsdam. We think that the PicoSwitch could be employed to improve the performance of synchrotron sources for time-resolved experiments in the future.

6. Conclusion

In conclusion, we have characterized and applied an ultrafast X-ray switch for gating synchrotron X-ray pulses on picosecond timescales. The shape of the shortened pulse can be adjusted by selecting the Bragg angle on the switch and by tuning the pump fluence. The switching relies on coherent phonon dynamics which modulate the diffraction efficiency. The rise and fall times t_r and t_f are determined by the layer thickness and the speed of sound in the material. We demonstrated a high switching contrast with a maximum diffraction efficiency of $\eta_{\text{max}} \simeq 10^{-3}$. The structure allows for repetitive switching and no long-term degradation effects have yet been observed. Hence, the device is suited for permanent installation in time-resolved beamline set-ups. The applicability of the PicoSwitch was demonstrated in a synchrotron-

based pump–probe experiment where we measured coherent lattice dynamics in a nanostructured sample with picosecond resolution.

We thank the BMBF for funding the project via 05K10IP1.

References

- Abo-Bakr, M., Feikes, J., Hollmack, K., Wüstefeld, G. & Hübers, H. W. (2002). *Phys. Rev. Lett.* **88**, 254801.
- Allam, D. (1970). *J. Phys. E*, **3**, 1022.
- Als-Nielsen, J. (2011). *Elements of Modern X-ray Physics*, 2nd ed. New York: John Wiley and Sons.
- Bargheer, M., Zhavoronkov, N., Woerner, M. & Elsaesser, T. (2006). *ChemPhysChem*, **7**, 783–792.
- Beaud, P., Johnson, S. L., Streun, A., Abela, R., Abramsohn, D., Grolimund, D., Krasniqi, F., Schmidt, T., Schlott, V. & Ingold, G. (2007). *Phys. Rev. Lett.* **99**, 174801.
- Bucksbaum, P. H. & Merlin, R. (1999). *Solid State Commun.* **111**, 535–539.
- Cammarata, M., Eybert, L., Ewald, F., Reichenbach, W., Wulff, M., Anfinrud, P., Schotte, F., Plech, A., Kong, Q., Lorenc, M., Lindenau, B., Rübiger, J. & Polachowski, S. (2009). *Rev. Sci. Instrum.* **80**, 015101.
- Chang, Z., Rundquist, A., Zhou, J., Murnane, M. M., Kapteyn, H. C., Liu, X., Shan, B., Liu, J., Niu, L., Gong, M. & Zhang, X. (1996). *Appl. Phys. Lett.* **69**, 133–135.
- Emma, P. et al. (2010). *Nat. Photon.* **4**, 641–647.
- Enquist, H., Navirian, H., Nüske, R., von Korff Schmising, C., Jurgilaitis, A., Herzog, M., Bargheer, M., Sondhauss, P. & Larsson, J. (2010). *Opt. Lett.* **35**, 3219–3221.
- Geloni, G., Saldin, E., Samoylova, L., Schneidmiller, E., Sinn, H., Tschentscher, T. & Yurkov, M. (2010). *New J. Phys.* **12**, 035021.
- Grigoriev, A., Do, D.-H., Kim, D. M., Eom, C.-B., Evans, P. G., Adams, B. & Dufresne, E. M. (2006). *Appl. Phys. Lett.* **89**, 021109.
- Herzog, M., Bojahr, A., Goldshteyn, J., Leitenberger, W., Vrejoiu, I., Khakhulin, D., Wulff, M., Shayduk, R., Gaal, P. & Bargheer, M. (2012a). *Appl. Phys. Lett.* **100**, 094101.
- Herzog, M., Leitenberger, W., Shayduk, R., van der Veen, R., Milne, C. J., Johnson, S. L., Vrejoiu, I., Alexe, M., Hesse, D. & Bargheer, M. (2010). *Appl. Phys. Lett.* **96**, 161906.
- Herzog, M., Schick, D., Gaal, P., Shayduk, R., von Korff Schmising, C. & Bargheer, M. (2012b). *Appl. Phys. A*, **106**, 489–499.
- Navirian, H. A., Herzog, M., Goldshteyn, J., Leitenberger, W., Vrejoiu, I., Khakhulin, D., Wulff, M., Shayduk, R., Gaal, P. & Bargheer, M. (2011). *J. Appl. Phys.* **109**, 126104.
- Pile, D. (2011). *Nat. Photon.* **5**, 456–457.
- Rousse, A., Rischel, C. & Gauthier, J.-C. (2001). *Rev. Mod. Phys.* **73**, 17–31.
- Schick, D., Bojahr, A., Herzog, M., von Korff Schmising, C., Shayduk, R. & Bargheer, M. (2014). *Comput. Phys. Commun.* **185**, 651–660.
- Schick, D., Bojahr, A., Herzog, M., von Korff Schmising, C., Shayduk, R., Leitenberger, W., Gaal, P. & Bargheer, M. (2012). *Rev. Sci. Instrum.* **83**, 025104.
- Schick, D., Shayduk, R., Bojahr, A., Herzog, M., von Korff Schmising, C., Gaal, P. & Bargheer, M. (2013). *J. Appl. Cryst.* **46**, 1372–1377.
- Schoenlein, R. W., Chattopadhyay, S., Chong, H. H., Glover, T. E., Heimann, P. A., Shank, C. V., Zholents, A. A. & Zolotorev, M. S. (2000). *Science*, **287**, 2237–2240.
- Shayduk, R., Navirian, H. A., Leitenberger, W., Goldshteyn, J., Vrejoiu, I., Weinelt, M., Gaal, P., Herzog, M., von Korff Schmising, C. & Bargheer, M. (2011). *New J. Phys.* **13**, 093032.
- Sheppard, J. M. H., Sondhauss, P., Merlin, R., Bucksbaum, P. H., Lee, R. W. & Wark, J. S. (2005). *Solid State Commun.* **136**, 181–185.
- Sokolowski-Tinten, K., Horn von Hoegen, M., von der Linde, D., Cavalleri, A., Siders, C. W., Brown, F. L. H., Leitner, D. M., Toth, C., Squier, J. A., Barty, C. P. J., R., Wilson, K. R. & Kammler, M. (2001). *J. Phys. IV*, **11**, Pr2-473–Pr2-477.
- Vrejoiu, I., Le Rhun, G., Pintilie, L., Hesse, D., Alexe, M. & Gösele, U. (2006). *Adv. Mater.* **18**, 1657–1661.
- Wark, J. S., Whitlock, R. R., Hauer, A. A., Swain, J. E. & Solone, P. J. (1989). *Phys. Rev. B*, **40**, 5705–5714.
- Zamponi, F., Ansari, Z., von Korff Schmising, C., Rothhardt, P., Zhavoronkov, N., Woerner, M., Elsaesser, T., Bargheer, M., Trobitsch-Ryll, T. & Haschke, M. (2009). *Appl. Phys. A*, **96**, 51–58.
- Zholents, A., Heimann, P., Zolotorev, M. & Byrd, J. (1999). *Nucl. Instrum. Methods Phys. Res. A*, **425**, 385–389.
- Zolotoyabko, E. & Quintana, J. P. (2004). *Rev. Sci. Instrum.* **75**, 699–708.

PAPER XIII

Second Harmonic Generation of Nanometric Phonon Wave Packets

A. Bojahr, M. Roessle, P. Gaal, W. Leitenberger, P. Pudell,
M. Reinhard, A. von Reppert, M. Sander and M. Bargheer.
Phys. Rev. Lett. **115**, 195502 (2015).

Second Harmonic Generation of Nanoscale Phonon Wave Packets

A. Bojahr,¹ M. Gohlke,¹ W. Leitenberger,¹ J. Pudell,¹ M. Reinhardt,² A. von Reppert,¹ M. Roessle,¹
M. Sander,¹ P. Gaal,² and M. Bargheer^{1,2,*}

¹*Institut für Physik and Astronomie, Universität Potsdam, Karl-Liebknecht-Strasse 24-25, 14476 Potsdam, Germany*

²*Helmholtz Zentrum Berlin, Albert-Einstein-Strasse 15, 12489 Berlin, Germany*

(Received 1 June 2015; published 5 November 2015)

Phonons are often regarded as delocalized quasiparticles with certain energy and momentum. The anharmonic interaction of phonons determines macroscopic properties of the solid, such as thermal expansion or thermal conductivity, and a detailed understanding becomes increasingly important for functional nanostructures. Although phonon-phonon scattering processes depicted in simple wave-vector diagrams are the basis of theories describing these macroscopic phenomena, experiments directly accessing these coupling channels are scarce. We synthesize monochromatic acoustic phonon wave packets with only a few cycles to introduce nonlinear phononics as the acoustic counterpart to nonlinear optics. Control of the wave vector, bandwidth, and consequently spatial extent of the phonon wave packets allows us to observe nonlinear phonon interaction, in particular, second harmonic generation, in real time by wave-vector-sensitive Brillouin scattering with x-rays and optical photons.

DOI: [10.1103/PhysRevLett.115.195502](https://doi.org/10.1103/PhysRevLett.115.195502)

PACS numbers: 62.25.-g, 63.20.-e, 78.20.hc, 78.47.J-

Basic physics lectures introduce phonons as uncoupled quanta of the lattice excitation, i.e., delocalized quasiparticles with certain energy and momentum. The low-temperature heat capacity of insulators and blackbody radiation are fundamental macroscopic consequences of quantum mechanics. Anharmonic effects are introduced to discuss heat expansion and thermal transport, where only thermally activated phonons contribute to these phenomena. Typically, theory averages over thermally excited quantum states before properties of the “mean heat carrying phonon” are compared to macroscopic measurements like the temperature of a solid. Our Letter shows a route towards detailed experimental information on mode-specific nonlinear interactions. This will facilitate fundamental tests of the theory avoiding the calculation of thermal averages, which inevitably obscure the full information.

Such progress is of high relevance for the “hot topic” of heat transport manipulation in nanostructures which is driven by the enormous size reduction of integrated circuits [1–6] and the field of thermoelectrics. Recent work aims at improving the conversion of waste heat into usable energy by tailored phonon-phonon interaction processes [7–9]. Nonlinear effects have been predicted to yield efficient thermal diodes [10]. Only in a few cases has the full phonon dispersion relation including the linewidth (inverse lifetime) been measured by inelastic scattering [11–13], and at low wave vectors the instrumental resolution currently sets limits. Linewidth measurements yield mode-averaged dissipation, but experimental knowledge about the dominant coupled modes is unavailable. The free-electron lasers hold great promise to access the coupling in the femtosecond time domain using diffuse scattering and inelastic x-ray scattering [14,15]. Recently, the coupling of terahertz excited optical phonons with other optical phonons was

observed and presented as one example of nonlinear phonon interactions [16].

Nonlinear phononics as discussed here shows many analogies to nonlinear photonics in transparent media where high electromagnetic wave fields yield nonlinear polarizations. These processes are described by interacting photons that fulfill momentum and energy conservation. The description of these optical phenomena is robust and extremely well tested by an enormous number of experiments such as sum- and difference-frequency generation or four-wave mixing. The first analogous experiments on nonlinear phononics date back to the 1960s, when collisions of two ultrasound beams were studied in real time and space [17]. These experiments somewhat resembled nonlinear optics before the utilization of the laser. The required interaction volume was in the centimeter range, and the time resolution was limited by the 10 MHz ultrasound frequency. The phonon analogue of optical supercontinuum generation by femtosecond lasers was studied in seminal picosecond-ultrasonics experiments on the self-steepening of the strain-pulse fronts [18,19] which finally lead to acoustic solitons [20–22]. In these experiments, the excitation of nanometric strain waves was not wave-vector specific. Recent progress in the creation and detection of gigahertz and terahertz phonon wave packets also known as hypersonic strain waves makes them a perfect test ground to investigate phonon-phonon interaction processes on the nanoscale [23].

In this work, we combine the selective excitation of longitudinal acoustic phonon wave packets with time-resolved variants of x-ray and broadband Brillouin scattering [23] to investigate the nonlinear interaction of phonons with a specific wave vector. The experiments provide a high temporal and spatial resolution for observing phonon dynamics in real time over a broad range of wave vectors which

correspond to the nanometer length scale. As the basic example of nonlinear phononics, we shaped giant and ultrashort phonon wave packets with well-defined momenta and observed the generation of their second harmonic (SH).

To create such giant amplitude strain waves, ultrashort laser pulses excite a metallic strontium ruthenate (SRO) film deposited on a bulk strontium titanate (STO) substrate, a system where we know the first-order lattice anharmonicity [19] and where the acoustic impedances of the thin film and substrate are nearly matched [24]. The metal film expansion induced by each laser pulse launches a bipolar strain pulse into STO [24]. A train of several laser pulses [Fig. 1(b)] with a defined temporal delay τ creates a phonon wave packet with a fundamental frequency of $\Omega = 2\pi/\tau$ [23,25,26]. If the laser-pulse train is composed of femtosecond pulses (blue lines in Fig. 1), the phonon wave packet exhibits

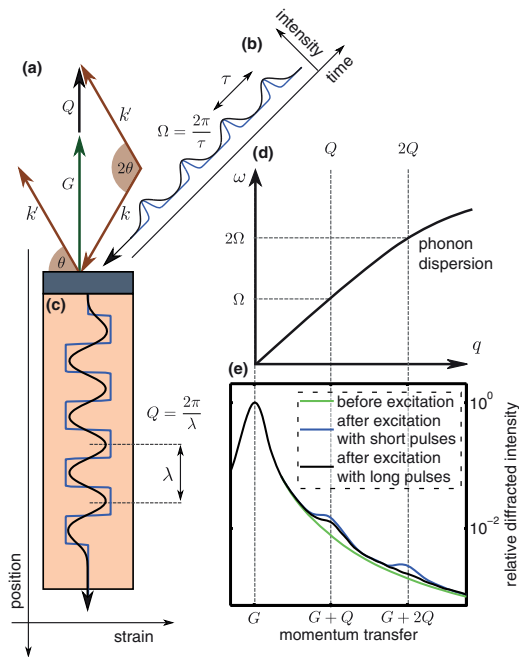


FIG. 1 (color). Preparation and observation of phonon wave packets. (a) X-rays with wave vector k are scattered (k') by the reciprocal lattice vector G plus a phonon with wave vector Q . (b) A metal film is excited by a laser-pulse train with short (blue) and long (black) pulses. (c) Short pulses excite phonon wave packets at the fundamental and higher harmonics [rectangular wave packet (blue)]. Excitation with long pulses suppresses higher harmonics and generates a sinusoidal wave (black). (d) The phonon dispersion relation connects the central frequency $\Omega = 2\pi/\tau$ of the excited phonon wave packet with its corresponding wave vector $Q = 2\pi/\lambda$. (e) Experimental data of ultrafast x-ray diffraction from the unexcited sample shows the (002) substrate reflection (green). After excitation with short pulses (blue), peaks at $G \pm Q$ and $G \pm 2Q$ occur. These peaks originate from inelastic scattering by the induced phonon wave packet. For longer pump pulses (black), the scattering at $G \pm 2Q$ is suppressed. This evidences that a narrow band phonon wave packet without its higher harmonics was excited.

several sharp strain fronts [Fig. 1(c)], corresponding to the excitation of higher harmonics $n \cdot \Omega$. These harmonics are identified in ultrafast x-ray diffraction (UXRD) experiments from their wave vector Q according to the dispersion relation of longitudinal phonons [$\omega = v_L q$, plotted in Fig. 1(d)]. For small wave vectors, $v_L(q)$ is a constant describing the longitudinal sound velocity. The UXRD data in Fig. 1(e) were obtained with an ultrathin SRO transducer layer ($d = 15$ nm). The green curve displays the relative diffraction intensity before the four pump pulses ($\tau = 11$ ps) reach the sample. The peak at G corresponds to the reciprocal lattice vector (002) of the STO substrate. When the 100 ps x-ray pulse was probing the sample shortly after the generation of the wave packet, additional diffraction intensity at $G \pm n \cdot Q = n \cdot 0.071 \text{ nm}^{-1}$ was detected (blue curve). The diffraction intensity is a direct measure of the spectral energy distribution of the imprinted coherent phonon modes [27]. When we increased the width of the pump pulses from $\Delta\tau_{\text{FWHM}} = 0.9$ to 3.4 ps, the diffraction of higher orders of Q was suppressed and we observed only the additional scattering from $G \pm Q$ (black curve) as suggested by the wave vector diagram in Fig. 1(a). High-frequency components of an oscillator can be excited only by stimuli which contain these frequencies.

To demonstrate second harmonic generation (SHG) of monochromatic phonon wave packets, we repeated the UXRD experiment with a 70 nm SRO transducer, which absorbs more optical energy. We used only two long laser pulses ($\tau = 17.7$ ps and $\Delta\tau_{\text{FWHM}} = 5.3$ ps) while keeping the total incident laser fluence constant. This doubles the local atomic displacement and quadruples the acoustic energy density $\mathcal{E} = E/V$ of the wave packet in the volume V —defined by the beam area and the length of the wave packet. This increased the up-conversion efficiency of phonons at the expense of monochromaticity according to the higher wave packet localization in space.

Figure 2(a) shows the fundamental phonon peak around $Q = 0.044 \text{ nm}^{-1}$ which was observed in the UXRD experiment when the x-rays probed the sample immediately after excitation. For time delays around 200 ps, a tiny peak at $2Q = 0.088 \text{ nm}^{-1}$ occurred. This rising SH is enhanced in Fig. 2(b), where the measured diffraction signal is multiplied by q^2 for better visibility. Figure 2(c) quantifies the transient change of the peak area Σ_i in the vicinity of 0.044 and 0.088 nm^{-1} [28]. $\Sigma_i \sim \mathcal{E}_i$ is proportional to the energy density $\mathcal{E}_i \sim \int \rho_E(q, t) dq$ of the phonons around $q = iQ$, obtained from integrating the spectral energy density $\rho_E(q, t)$ over the bandwidth of the fundamental ($i = 1$) and the SH ($i = 2$), respectively [27].

The signal Σ_1 of the excited fundamental mode (red diamonds) increased immediately after excitation, followed by a nearly exponential decay. Σ_2 describing the SH (cyan dots) was delayed by approximately 200 ps. Thus, the SH was not directly excited by the laser pulses but was only generated by the propagation of phonons in the anharmonic lattice of STO. The delay was longer than the 100 ps time

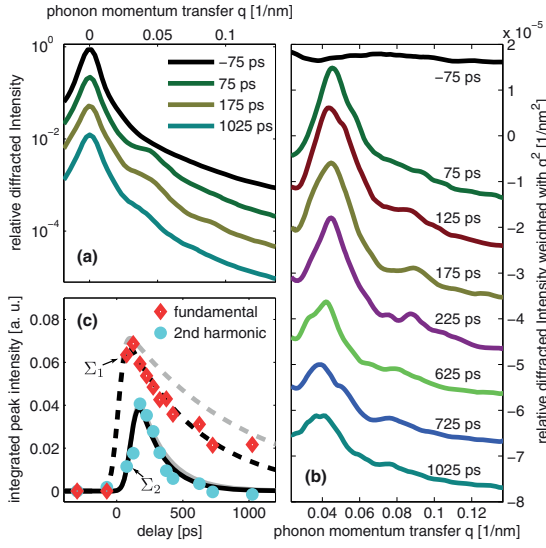


FIG. 2 (color). Transient x-ray diffraction from photoexcited phonons and their SH. (a) X-ray diffraction signals around the (002) lattice plane of the STO substrate. (b) Diffraction signals on the right shoulder of the STO substrate peak weighted by q^2 for better visualization. The peak around $Q = 0.044 \text{ nm}^{-1}$ after time zero reflects the optically excited coherent phonon wave packet with the central wave vector Q . After a delay of 200 ps, additional diffraction intensity around $2Q$ heralds the SH of Q generated via anharmonic phonon-phonon interaction. (c) The gray (black) lines quantify the transient change of the integrated peak intensities of the fundamental and its second harmonic with (and without) a correction for the x-ray absorption.

resolution of this synchrotron experiment [37] and is a direct evidence for the SHG of phonons. Although the SH is continuously generated, it reaches its maximum very fast, since the damping of phonons scales with the square of the frequency.

The SH phonons damped out faster than the fundamental as expected for the frequency dependence of the damping rate $\Gamma \sim \omega^2$ [27]. The gray lines in Fig. 2(c) show the damping of both phonons corrected for effects of x-ray absorption in STO [27]. The corrected exponential decay times for the fundamental and the SH are 1056 and 300 ps, respectively, in good agreement with the literature values [27,38].

To confirm our result and to explore the SHG of phonons in the same sample in more detail, we performed broadband time-domain Brillouin-scattering (TDBS) experiments, which measure a substantial fraction of the phonon spectrum from 0.035 to 0.06 nm^{-1} in STO [23]. We set the pulse separation to $\tau = 30$ ps to let the SH phonon emerge at $2Q = 0.052 \text{ nm}^{-1}$, in the center of the spectrum accessible by TDBS. The black line in Fig. 3(a) shows the time-dependent optical reflectivity change at $\lambda = 580$ nm which corresponds to this wave vector. The reflectivity increases in two steps from the two-pulse heating of SRO. We define the time zero as 7.5 ps after the maximum of the second pump pulse, confirmed by optical cross-correlation. The amplitude

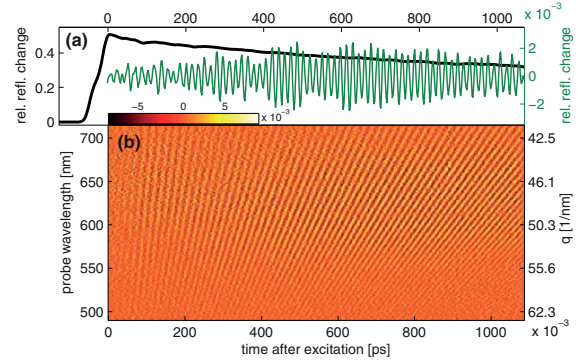


FIG. 3 (color). SHG of phonons observed by TDBS. (a) Transient relative reflectivity change at 580 nm (black line). The stepwise increase indicates the laser excitation of the metal film terminating at $t = 0$. Superimposed reflectivity oscillations (green line) originate from the SH phonons. The oscillation amplitude grows with the number of phonons up-converted to their SH. (b) Measured reflectivity oscillations across the white light probe spectrum. For each wavelength, the oscillation amplitude measures the occupation of a certain phonon q .

of the small superimposed oscillations with the phonon period 2Ω are a measure of how many second-harmonic phonons are present in the sample [23,39]. The rising oscillation amplitude indicates the nonlinear phonon interaction generating the SH of Q . The green line in Fig. 3(a) shows almost no SH phonons just after the two pump pulses with a pulse width of $\Delta\tau_{\text{FWHM}} = 15$ ps. The maximum number of these phonons is observed after approximately 600 ps. In the UXRD data of Fig. 2(c), the maximum is observed earlier, because the phonons with larger wave vector $Q = 0.088 \text{ nm}^{-1}$ suffer a much stronger damping.

The broadband detection scheme allowed us to evaluate the spectral content of this SH phonon wave packet even more precisely. The relatively broad wave vector spectrum that extends over a large fraction of the visible range [Fig. 3(b)] results from the spatial confinement of the excited strain wave to two oscillation cycles [23]. We extracted the oscillation amplitude $a(q, t)$ of the relative reflectivity change as a function of the time delay for each probe wavelength λ corresponding to the different wave vectors q which compose the wave packet in the vicinity of $2Q$ [28–36,40].

In these experiments, the spectral energy density of the acoustic wave packet $\rho_E(q, t)$ is proportional [39] to the square of the reflectivity modulations $a(q, t)^2$ divided by q^2 : $\rho_E \sim a(q, t)^2/q^2$. The experimentally derived energy proportional quantity $a(q, t)^2/q^2$ is plotted in Fig. 4(a) as contour lines and compared to the transiently changing spectral energy density $\rho_E(q, t)$ calculated on the basis of a Fermi-Pasta-Ulam (FPU) α - β chain with an empirical damping term. The FPU chain is widely used in theory to investigate phonons in the nonlinear lattice as well as heat transport in 1D [41–44]. In fact, we simulated a chain of oscillators with masses describing SRO and STO

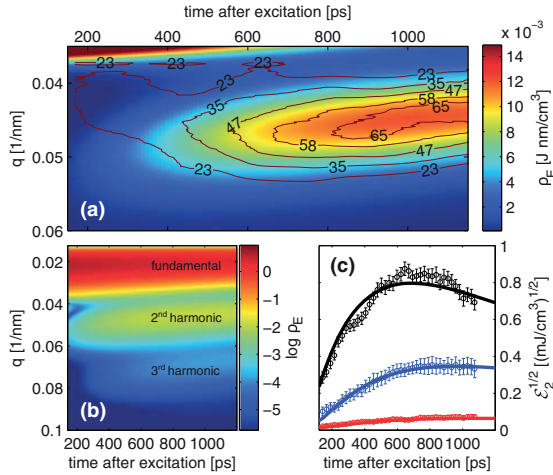


FIG. 4 (color). Comparing SHG experiments to the theory. (a) The color code shows the calculated transient change of the spectral energy density ρ_E around the SH of the excited phonons. The square of the measured relative reflectivity oscillation amplitude divided by q^2 in units of 10^{-7} nm^{-2} is overlaid as contour lines. (b) Calculated ρ_E over a broader range of wave vectors in the log scale. The photoexcited fundamental is transformed into the second and third harmonics. (c) visualizes the measured transient energy density change of the SH for different initial energy densities \mathcal{E}_1 (red = 13, blue = 67, and black = 235 mJ/cm^3) of the wave packet and compares this with theoretical calculations (solid lines). The wave vector for the highest energy density was $q = 0.03 \text{ nm}^{-1}$, somewhat larger than the $q = 0.025 \text{ nm}^{-1}$.

unit cells connected by anharmonic springs, where the second-order elastic constants along the [001] direction were derived from the speed of sound determined by time-resolved measurements [19,24,28]. From the comparison of the experimental data to the simulation, we found a third-order elastic constant describing the lattice anharmonicity in STO $C_{111} = -3.9 \times 10^{12} \text{ N/m}^2$ consistent with single-pulse time-resolved Brillouin scattering experiments [19]. It is 20% smaller than the value measured by megahertz acoustics at a frequency which is 3 orders of magnitude smaller [45]. In the calculation, the first few oscillators representing the opaque SRO film experience quasi-instantaneous [46] forces which describe the ultrafast heating by the two laser pulses. The force amplitude is known from previous UXRD measurements of the ultrafast lattice dynamics of SRO films [24].

Figure 4(b) shows $\rho_E(q, t)$ on a logarithmic scale over a broader wave vector range. The fundamental mode at 0.025 nm^{-1} is indeed excited at $t = 0 \text{ ps}$, and subsequently phonons at the second and third harmonics are generated. The second harmonic is generated earlier than the third harmonic. This is an intrinsic feature of this linear chain calculation. By considering only the third order of the lattice potential as the nonlinear term, only three phonon

processes are allowed [47,48], and the third harmonic can only be generated via two sequential scattering processes. By observing the very weak third-harmonic generation, one could get information about the importance of higher orders of the lattice potential.

A pronounced feature of the measured data is the slow shift of the spectral distribution towards smaller wave vectors. The physical origin is uncovered by the simulations which show that the compressive strain front travels faster than the expansive strain. Since the wave packet contains only two strain cycles, this leads to a slightly increasing central wavelength of the wave packet [19,28]. This effect is much less pronounced for wave packets with more cycles.

Finally, the solid lines in Fig. 4(c) show the square root of the energy density \mathcal{E}_2 of the generated SH as a function of time for three different initial energy densities \mathcal{E}_1 of the excited fundamental mode. The initial linear increase and the linear dependence $\sqrt{\mathcal{E}_2} \sim \mathcal{E}_1$ are characteristic for this second-order nonlinear process of sum frequency generation or three-phonon scattering in general [48]. The corresponding experimental data obtained from integrating $a(q, t)^2/q^2$ over the same wave vector range show excellent agreement. Both the experimental and simulated energy density in Fig. 4(c) take into account that, for the same total energy deposited, the energy density is larger for higher wave vectors. To achieve the highest energy density, it was necessary to increase the wave vector to $q = 0.03 \text{ nm}^{-1}$ in order to avoid multishot damage of the sample.

Conclusion.—With the generation of the SH of a certain well-defined phonon wave packet, we have demonstrated a first conceptually simple experiment that monitors an elementary process of nanoscale nonlinear phononics in real time. The observed damping of the fundamental and SH to other modes is proportional to the square of the wave vector. We strongly believe that these experiments stimulate a series of new experiments ranging from simple extensions such as difference-frequency mixing to more complex experiments which are analogs of four-wave mixing, well known in experimental photonics. Future investigations may address the coupling of optical phonons to acoustic phonons and extend the phase-matching considerations by including also transverse polarisation of phonons and by going to larger wave vectors where the dispersion relation is bending over. Improvements of the signal-to-noise ratio may eventually permit studies on the single quantum level. A similar stimulus may be expected for theory. The Fermi-Pasta-Ulam chain can well predict effects related to longitudinal phonons. Modeling anharmonic phonon propagation and interaction in three dimensions including longitudinal and transverse phonon polarization in detail remains a major challenge. Exploring the physical nature of phonon damping processes and describing soft mode behavior in the vicinity of structural phase transitions by simulations and analytical theories can now be compared in detail to experimental results on a microscopic level.

We thank the BMBF for funding via 05K13IPA and 05K12IP1. A.B. thanks the Leibnitz Graduate School “Dynamics in new Light.” We thank Ionela Vrejoiu for preparing the samples as well as Michael Wulff and Dmitry Khakhulin for their invaluable support at the beam line ID9 at the ESRF.

*bargheer@uni-potsdam.de

<http://www.udkm.physik.uni-potsdam.de>

- [1] M. E. Siemens, Q. Li, R. Yang, K. A. Nelson, E. H. Anderson, M. M. Murnane, and H. C. Kapteyn, *Nat. Mater.* **9**, 26 (2010).
- [2] M. N. Luckyanova, J. Garg, K. Esfarjani, A. Jandl, M. T. Bulsara, A. J. Schmidt, A. J. Minnich, S. Chen, M. S. Dresselhaus, Z. Ren, E. A. Fitzgerald, and G. Chen, *Science* **338**, 936 (2012).
- [3] N. Li, J. Ren, L. Wang, G. Zhang, P. Hänggi, and B. Li, *Rev. Mod. Phys.* **84**, 1045 (2012).
- [4] M.-H. Bae, Z. Li, Z. Aksamija, P. N. Martin, F. Xiong, Z.-Y. Ong, I. Knezevic, and E. Pop, *Nat. Commun.* **4**, 1734 (2013).
- [5] M. Maldovan, *Phys. Rev. Lett.* **110**, 025902 (2013).
- [6] J. Ravichandran, A. K. Yadav, R. Cheaito, P. B. Rossen, A. Soukiasian, S. J. Suresha, J. C. Duda, B. M. Foley, C.-H. Lee, Y. Zhu, A. W. Lichtenberger, J. E. Moore, D. A. Muller, D. G. Schlom, P. E. Hopkins, A. Majumdar, R. Ramesh, and M. A. Zurbuchen, *Nat. Mater.* **13**, 168 (2014).
- [7] R. Venkatasubramanian, E. Siivola, T. Colpitts, and B. O’Quinn, *Nature (London)* **413**, 597 (2001).
- [8] B. Poudel, Q. Hao, Y. Ma, Y. Lan, A. Minnich, B. Yu, X. Yan, D. Wang, A. Muto, D. Vashaee, X. Chen, J. Liu, M. S. Dresselhaus, G. Chen, and Z. Ren, *Science* **320**, 634 (2008).
- [9] K. Biswas, J. He, I. D. Blum, C.-I. Wu, T. P. Hogan, D. N. Seidman, V. P. Dravid, and M. G. Kanatzidis, *Nature (London)* **489**, 414 (2012).
- [10] B. Li, L. Wang, and G. Casati, *Phys. Rev. Lett.* **93**, 184301 (2004).
- [11] A. Shukla, M. Calandra, M. d’Astuto, M. Lazzeri, F. Mauri, C. Bellin, M. Krisch, J. Karpinski, S. M. Kazakov, J. Jun, D. Daghero, and K. Parlinski, *Phys. Rev. Lett.* **90**, 095506 (2003).
- [12] O. Delaire, J. Ma, K. Marty, A. F. May, M. A. McGuire, M.-H. Du, D. J. Singh, A. Podlesnyak, G. Ehlers, M. D. Lumsden, and B. C. Sales, *Nat. Mater.* **10**, 614 (2011).
- [13] J. W. L. Pang, W. J. L. Buyers, A. Chernatynskiy, M. D. Lumsden, B. C. Larson, and S. R. Phillpot, *Phys. Rev. Lett.* **110**, 157401 (2013).
- [14] J. Chen, M. Trigo, S. Fahy, D. Murray, Y. M. Sheu, T. Graber, R. Henning, Y. J. Chien, C. Uher, and D. A. Reis, *Appl. Phys. Lett.* **102**, 181903 (2013).
- [15] M. Trigo, M. Fuchs, J. Chen, M. P. Jiang, M. Cammarata, S. Fahy, D. M. Fritz, K. Gaffney, S. Ghimire, A. Higginbotham, S. L. Johnson, M. E. Kozina, J. Larsson, H. Lemke, A. M. Lindenberg, G. Ndabashimiye, F. Quirin, K. Sokolowski-Tinten, C. Uher, G. Wang *et al.*, *Nat. Phys.* **9**, 790 (2013).
- [16] M. Först, C. Manzoni, S. Kaiser, Y. Tomioka, Y. Tokura, R. Merlin, and A. Cavalleri, *Nat. Phys.* **7**, 854 (2011).
- [17] F. Rollins, *Appl. Phys. Lett.* **2**, 147 (1963).
- [18] P. J. S. van Capel and J. I. Dijkhuis, *Appl. Phys. Lett.* **88**, 151910 (2006).
- [19] A. Bojahr, M. Herzog, D. Schick, I. Vrejoiu, and M. Bargheer, *Phys. Rev. B* **86**, 144306 (2012).
- [20] O. L. Muskens and J. I. Dijkhuis, *Phys. Rev. Lett.* **89**, 285504 (2002).
- [21] W. Singhsomroje and H. J. Maris, *Phys. Rev. B* **69**, 174303 (2004).
- [22] E. Péronne and B. Perrin, *Ultrasonics* **44**, e1203 (2006).
- [23] A. Bojahr, M. Herzog, S. Mitzscherling, L. Maerten, D. Schick, J. Goldshteyn, W. Leitenberger, R. Shayduk, P. Gaal, and M. Bargheer, *Opt. Express* **21**, 21188 (2013).
- [24] D. Schick, M. Herzog, A. Bojahr, W. Leitenberger, A. Hertwig, R. Shayduk, and M. Bargheer, *Struct. Dyn.* **1**, 064501 (2014).
- [25] C. Klieber, E. Peronne, K. Katayama, J. Choi, M. Yamaguchi, T. Pezeril, and K. A. Nelson, *Appl. Phys. Lett.* **98**, 211908 (2011).
- [26] M. Herzog, A. Bojahr, J. Goldshteyn, W. Leitenberger, I. Vrejoiu, D. Khakhulin, M. Wulff, R. Shayduk, P. Gaal, and M. Bargheer, *Appl. Phys. Lett.* **100**, 094101 (2012).
- [27] R. Shayduk, M. Herzog, A. Bojahr, D. Schick, P. Gaal, W. Leitenberger, H. Navirian, M. Sander, J. Goldshteyn, I. Vrejoiu, and M. Bargheer, *Phys. Rev. B* **87**, 184301 (2013).
- [28] See Supplemental Material at <http://link.aps.org/supplemental/10.1103/PhysRevLett.115.195502> for details of the experimental setups, the data analysis and theory, which includes Refs. [29–36].
- [29] N. Li and B. Li, *Europhys. Lett.* **78**, 34001 (2007).
- [30] C. Alabiso, M. Casartelli, and P. Marenzoni, *J. Stat. Phys.* **79**, 451 (1995).
- [31] J. Liu, S. Liu, N. Li, B. Li, and C. Wu, *Phys. Rev. E* **91**, 042910 (2015).
- [32] C. Herring, *Phys. Rev.* **95**, 954 (1954).
- [33] H. J. Maris, *Phys. Acoust.* **8**, 279 (1971).
- [34] H. Y. Hao and H. J. Maris, *Phys. Rev. B* **64**, 064302 (2001).
- [35] A. N. Cleland, *Foundations of Nanomechanics: From Solid-State Theory to Device Applications*, Advanced Texts in Physics and Astronomy (Springer, Berlin, 2003).
- [36] G. P. Berman and F. M. Izrailev, *Chaos* **15**, 015104 (2005).
- [37] P. Gaal, D. Schick, M. Herzog, A. Bojahr, R. Shayduk, J. Goldshteyn, H. A. Navirian, W. Leitenberger, I. Vrejoiu, D. Khakhulin, M. Wulff, and M. Bargheer, *J. Synchrotron Radiat.* **21**, 380 (2014).
- [38] L. Maerten, A. Bojahr, M. Gohlke, M. Rössle, and M. Bargheer, *Phys. Rev. Lett.* **114**, 047401 (2015).
- [39] C. Thomsen, H. T. Grahm, H. J. Maris, and J. Tauc, *Phys. Rev. B* **34**, 4129 (1986).
- [40] M. Bradler, P. Baum, and E. Riedle, *Appl. Phys. B* **97**, 561 (2009).
- [41] S. Lepri, R. Livi, and A. Politi, *Phys. Rev. Lett.* **78**, 1896 (1997).
- [42] B. Gershgorin, Y. V. Lvov, and D. Cai, *Phys. Rev. Lett.* **95**, 264302 (2005).
- [43] N. Li, P. Tong, and B. Li, *Europhys. Lett.* **75**, 49 (2006).
- [44] S. Liu, J. Liu, P. Hänggi, C. Wu, and B. Li, *Phys. Rev. B* **90**, 174304 (2014).
- [45] E. L. Meeks and R. T. Arnold, *Phys. Rev. B* **1**, 982 (1970).
- [46] A. Bojahr, D. Schick, L. Maerten, M. Herzog, I. Vrejoiu, C. von Korff Schmising, C. J. Milne, S. L. Johnson, and M. Bargheer, *Phys. Rev. B* **85**, 224302 (2012).
- [47] R. L. Bivins, N. Metropolis, and J. R. Pasta, *J. Comput. Phys.* **12**, 65 (1973).
- [48] D. Sholl, *Phys. Lett. A* **149**, 253 (1990).

PAPER XIV

Calibrated real-time detection of nonlinearly propagating strain waves

A. Bojahr, M. Herzog, D. Schick, I. Vrejoiu and
M. Bargheer.

Phys. Rev. B **86**, 144306 (2012).

Calibrated real-time detection of nonlinearly propagating strain wavesAndré Bojahr,¹ Marc Herzog,¹ Daniel Schick,¹ Ionela Vrejoiu,² and Matias Bargheer^{1,3,*}¹*Institute of Physics and Astronomy, University of Potsdam, Karl-Liebknecht-Strasse 24-25, 14476 Potsdam, Germany*²*Max-Planck-Institut für Mikrostrukturphysik, Weinberg 2, 06120 Halle, Germany*³*Helmholtz Zentrum Berlin, Albert-Einstein-Str. 15, 12489 Berlin, Germany*

(Received 19 July 2012; revised manuscript received 2 October 2012; published 24 October 2012)

Epitaxially grown metallic oxide transducers support the generation of ultrashort strain pulses in SrTiO₃ (STO) with high amplitudes up to 0.5%. The strain amplitudes are calibrated by real-time measurements of the lattice deformation using ultrafast x-ray diffraction. We determine the speed at which the strain fronts propagate by broadband picosecond ultrasonics and conclude that, above a strain level of approx. 0.2%, the compressive and tensile strain components travel at considerably different sound velocities, indicating nonlinear wave behavior. Simulations based on an anharmonic linear-chain model are in excellent accord with the experimental findings and show how the spectrum of coherent phonon modes changes with time.

DOI: [10.1103/PhysRevB.86.144306](https://doi.org/10.1103/PhysRevB.86.144306)

PACS number(s): 43.35.+d, 43.25.+y, 61.05.cp, 63.20.kg

Acoustic wave propagation and the deformation of solids are usually analyzed within the approximation of harmonic interatomic potentials leading to the concept of decoupled acoustic phonons including their dispersion relation which is nearly linear for small wave vectors k_P . An anharmonicity must be introduced into the interaction potential in order to describe deformation under very high stress. But also small-phonon-amplitude phenomena are connected to phonon-phonon interaction processes, such as heat expansion and heat conduction.¹ For the material investigated in this paper, SrTiO₃ (STO), all these properties have been studied in detail, since STO is the generic dielectric (quantum paraelectric) perovskite oxide with a variety of interesting properties near its structural phase transition at 105 K. The elastic constants were determined by ultrasound measurements,² the damping of acoustic phonons was investigated by the linewidth of Brillouin scattering³ and apparent deviations of the acoustic dispersion were discussed in the context of picosecond ultrasonics measurements.⁴ Recently ultrafast x-ray diffraction (UXRD) was used to accurately measure the propagation and decay of quasimonochromatic strain pulses in STO.⁵ In general, UXRD data yield unambiguous information on the ultrafast lattice response, which is helpful for the interpretation of optical pump-probe investigations concerning complex problems in solids.⁶⁻⁸

In theory, the changes in the occupation of phonon modes are described as phonon damping due to scattering from defects or anharmonic interaction with thermally activated phonons.⁹⁻¹² For high strain amplitudes also interactions among coherent phonons are possible, which leads to a shape change of coherent phonon pulses. In particular, the self-steepening of strain pulses in sapphire giving rise to N-waves, shock waves, and soliton pulse trains were measured after a long propagation length of more than one hundred microns.¹³⁻¹⁶ These solitons were observed at low temperatures where phonon damping is weak and were discussed by nonlinear wave equations.¹⁶⁻¹⁸

In this paper we investigate the nonlinear propagation of giant longitudinal acoustic (LA) bipolar strain pulses in SrTiO₃. We calibrate the strain amplitude by UXRD and show how the mode spectrum constituting the wave changes

as a function of time. Simulations based on an anharmonic linear-chain model yield excellent agreement with ultrashort broadband optical reflectivity measurements and show that compressive strain components propagate faster than tensile strain components. The dependence of the sound velocity on the strain gives rise to a self-steepening of the strain fronts. We analyze the experiments in a linear-chain model with atomic resolution, although for the presented results a continuum model would also be applicable. There are several advantages of this approach and the discussion of sound waves in terms of phonons. First we anticipate experiments for very high wave vectors approaching the Brillouin zone boundary. At a temperature of 110 K, STO undergoes an antiferrodistortive phase transition connected to an optical phonon mode which softens near the zone boundary.¹⁹ For connecting the nonlinear parameters derived in the present paper with the physics near the phase transition our approach will be very helpful. Finally, ultrafast x-ray diffraction naturally supports simulations with unit cell accuracy, and we show in Eq. (1) that in our picosecond ultrasonics experiments the different wavelengths of the reflected photons are sensitive to particular wave vectors of phonons.

We use an epitaxially grown La_{0.7}Sr_{0.3}MnO₃ (LSMO) transducer film on a SrTiO₃ (001) substrate, fabricated by pulsed-laser deposition. The red symbols in Fig. 1(a) show a θ - 2θ scan of the sample recorded at the energy dispersive reflectometer (EDR) beamline of the synchrotron BESSYII of the Helmholtz-Zentrum-Berlin. The bright substrate peak at $\theta = 23.25^\circ$ is cut off to show the less intense layer peak (LSMO) at 23.58° more clearly. The excellent agreement with the simulation (black solid line) confirms the crystalline perfection of the epitaxial film with a thickness of $d_{\text{LSMO}} = 36$ nm, which is very robust against high excitation densities and supports high strain amplitudes. To calibrate the amplitude of the strain wave we measure the expansion of the metallic layer via the shift of the x-ray diffraction signal [Figs. 1(b) and 1(c)] after optical excitation by 50 fs laser pulses around 800 nm wavelength with a fluence of 20 mJ/cm². To probe the structural dynamics we use an x-ray plasma source which provides jitter-free x-ray pulses with a duration of approximately 200 fs.²⁰ The transient angular shift $\Delta\theta$ of the

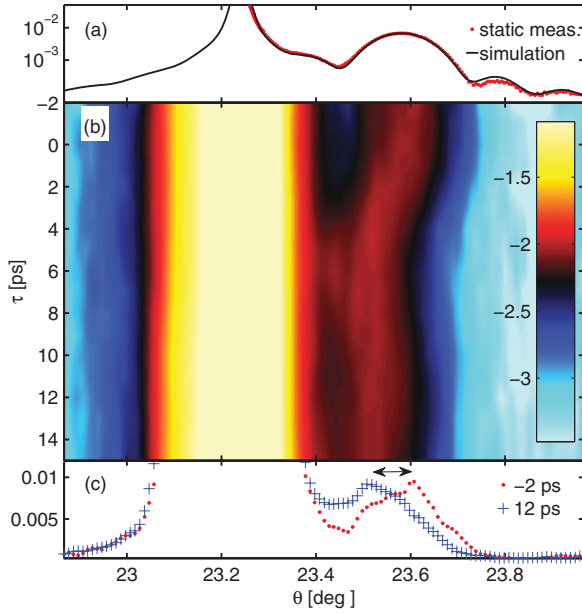


FIG. 1. (Color online) (a) Static θ - 2θ scan of the (002) peaks of the LSMO-STO sample showing a weak and broad layer (LSMO) peak and a much brighter and narrower STO substrate peak. (b) Transient UXRD signal after pumping with a laser pulse. The layer peak shifts to smaller angles indicating the expansion of LSMO within 6 ps (logarithmic color code). (c) Two cuts of panel (b) with pump-probe delays -2 ps (before pumping) and 12 ps (when the strain pulse has left the layer).

LSMO Bragg peak can be read from Fig. 1(b) for time delays up to 15 ps. The shift is connected to the layer strain ϵ by Bragg's law. Figure 1(c) shows the diffraction curve for a time delay of 12 ps yielding an induced LSMO strain of $\epsilon = 0.2\%$.

The observed time dependence of the LSMO Bragg peak can be understood as follows:^{21,22} The absorbed pump pulse induces a quasi-instantaneous thermal stress which is unbalanced at the layer boundaries. This leads to two strain fronts which propagate away from the air-LSMO and LSMO-STO interfaces eventually building up a bipolar strain pulse in the STO substrate.²³ The maximum expansion occurs at $T = d_{\text{LSMO}}/v_{\text{LSMO}} = 6$ ps after the excitation, when the expansion waves starting from the surface and the interface have traveled through the film at the velocity of sound in LSMO, v_{LSMO} .²⁴ After 12 ps the coherent strain wave has completely left the LSMO layer and entered the STO substrate. Reflections of the sound wave at the interface with good acoustic impedance matching can be neglected.^{21,24,25}

In previous experiments we confirmed that the layer strain depends linearly on the excitation fluence²⁶ and that the corresponding bipolar strain wave propagates into the STO substrate.²¹ Hence we conclude a calibration factor of 0.01% LSMO strain per 1 mJ/cm² fluence. The strain amplitude of the bipolar pulse in the STO is half of the LSMO strain after 12 ps weighted with the ratio of the layer and substrate sound

velocities which considers the bipolar pulse stretching in the STO.^{21,24,25}

Having calibrated the amplitude of the lattice response, we follow the propagation of the bipolar strain pulse by optical pump-probe measurements. The setup is very similar to the broadband picosecond ultrasonics setup reported by Pontecorvo *et al.*²⁷ We split the 800 nm laser light into two parts. The intense part is used to pump the sample with fluences ranging from 14 to 47 mJ/cm² and the smaller part is focused into a sapphire plate to generate a white light supercontinuum pulse. This spectrally broad light pulse ranging from 470 to 700 nm is reflected from the sample under an angle $\alpha = 45^\circ$ with respect to the surface normal. We measured the relative transient reflectivity change $\Delta R/R_0$ of the sample for four different fluences at pump-probe delays up to 1 ns with a resolution of 1 ps. Figure 2 shows the response of the sample after correction for the chirp of the white light probe pulse and after subtraction of the slowly varying background which is associated with the transient heat in the LSMO film. Figure 2(a) shows the relative change of reflectivity for the lowest fluence (14 mJ/cm²) and Fig. 2(b) shows the same for the highest fluence (47 mJ/cm²).

All measurements show pronounced oscillations which exhibit a period increasing with the probe wavelength λ . At high fluences we additionally observe a wavelength-dependent beating of these oscillations. The oscillations can be understood as an interference of the light wave reflected by the sample surface with the light wave reflected due to

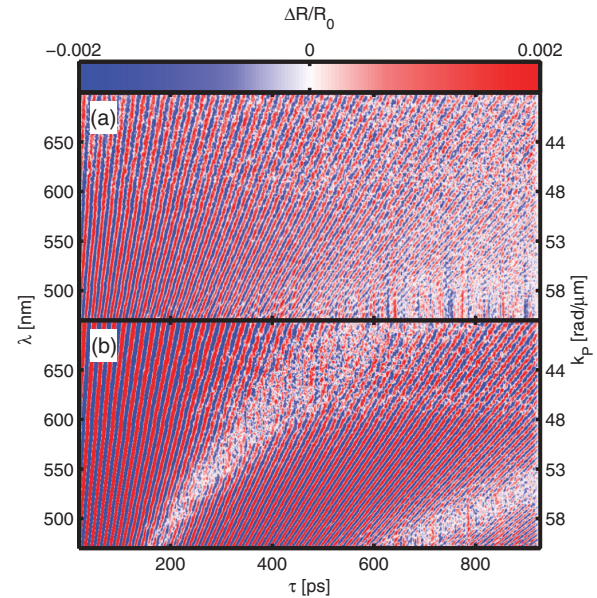


FIG. 2. (Color) Relative optical reflectivity change of the LSMO-STO sample for a pump fluence of (a) 14 mJ/cm² and (b) 47 mJ/cm². The low-frequency background was subtracted by high pass filtering. The probe pulse wavelength is given by λ (left axis). Both measurements show oscillations which are attributed to Brillouin backscattering of a photon from a phonon with wave vector k_p (right axis). For strong excitation conditions (b) we observe a beating in these oscillations.

the refractive index change induced by the propagating strain wave.²³

In order to explain how a photon with wave vector k_L is selectively probing a certain phonon with wave vector k_P , we describe the propagating wave front as a superposition of longitudinal acoustic (LA) phonons with wave vector k_P . Then the “reflection” of the probe light from the strain pulse can be understood as Brillouin backscattering of optical light with wave vector k_L . Therefore, such oscillations are often denoted as “Brillouin oscillations” in the literature.²⁸ The observed frequency ω_P of the signal oscillation corresponds to the eigenfrequency of the LA phonon with wavevector k_P . According to energy and momentum conservation the latter is related to the probe wavelength λ by the Brillouin backscattering condition

$$k_P = 2k_L^\perp = \frac{4\pi}{\lambda} n(\lambda) \cos(\beta), \quad (1)$$

where k_L^\perp is the internal optical wave vector component along the surface normal and $n(\lambda)$ is the refractive index of STO which is taken from the literature.²⁹ The internal angle β is related to α by Snell’s law. Equation (1) implies that the probe wavelength is specific for a certain wave vector of LA phonons. The amplitude of oscillations at each wavelength λ and time interval is a measure of the phonon amplitude of a specific phonon wave vector k_P . The beating observed in Fig. 2(b) is therefore interpreted as a change of the phonon spectrum in time. In particular, the beat node indicates the absence of a certain wave vector k_P at a certain time delay after excitation. This will be discussed in the context of Fig. 4.

Now we discuss how to derive the sound velocity from the measured data shown in Figs. 2(a) and 2(b). The linear dispersion relation of acoustic phonons near the Brillouin zone center is given by $\omega_P(\lambda)/k_P = v_s$ and thus relates the observed oscillation frequency $\omega_P(\lambda)$ to the speed of sound v_s for the LA phonons in STO:

$$v_s = \frac{\omega_P(\lambda)\lambda}{4\pi n(\lambda) \cos(\beta)}. \quad (2)$$

We then calculate the fast Fourier transform $I(\omega_P, \lambda)$ along the time axis for each probe wavelength λ . This yields a relation between λ and the related oscillation frequencies $\omega_P(\lambda)$, which implies a dependence of the sound velocity v_s on the phonon wave vector k_P according to the Brillouin backscattering condition. We use Eq. (2) as a coordinate transformation $v_s(\omega_P(\lambda), \lambda)$ which transforms our Fourier-transformed data into a wavelength-dependent sound velocity distribution $I(v_s, \lambda)$. By integration of the calculated result over all wavelengths we obtain Fig. 3, which shows the measured sound velocity distributions for different photoinduced LSMO strains calibrated by the results of the UXRD measurement. At low strain (0.14%) we observe a single peak around 8 nm/ps which is in a good agreement with the known sound velocity of the LA phonons in STO.²⁵ This peak validates the linear dispersion at low fluence. A nonlinear dispersion (k_P -dependent sound velocity) would lead to a broadened distribution.

However, with increasing strain amplitude we find a splitting in the sound velocity distribution. This implies that, for large strains, the speed of sound depends on the strain

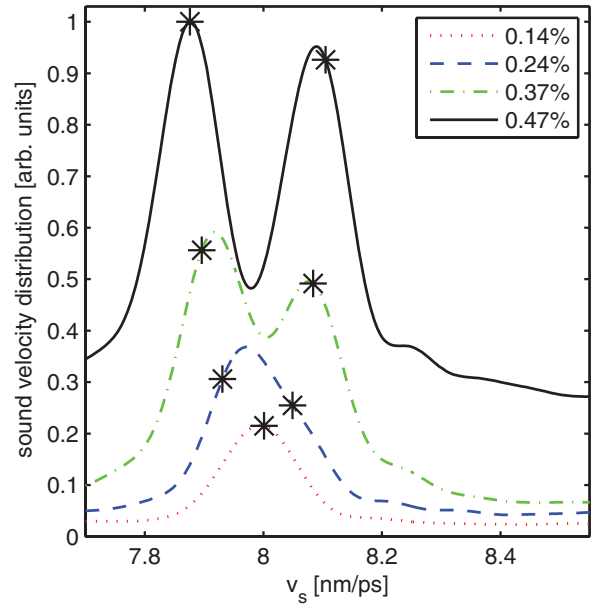


FIG. 3. (Color online) Measured sound velocity distribution of the induced strain pulse in STO. The different pump fluences were calibrated with the UXRD measurement to the resulting induced strains of the LSMO layer which is directly linked to the strain amplitude of the bipolar strain pulse in the STO. The narrow distribution for 0.14% strain implies that the entire strain pulse essentially propagates with a speed around 8 nm/ps. With increasing strain amplitude the sound velocity distribution gets broader and eventually a double-peak distribution is established. At high excitation levels different parts of the strain pulse propagate with different velocities. The stars indicate the sound velocities of the self-steepened sound pulses simulated in Fig. 4(a).

amplitude. The strain amplitude itself modulates the sound velocity of the medium.

To verify these assignments and to understand the underlying excited phonon spectrum, we simulate the lattice dynamics in a linear-chain model which was successfully tested against UXRD data in several cases.^{21,30} In addition to the model proposed in Ref. 21, we introduce an anharmonic potential between adjacent oscillators in order to describe the nonlinear wave propagation. Moreover, we add an empirical phonon damping term proportional to the velocity difference of adjacent oscillators. Mathematically the system is described by N coupled oscillators where each oscillator describes one lattice plane (half unit cell) of the LSMO thin film or the STO substrate. The set of N coupled second-order ordinary differential equations is

$$m_i \ddot{x}_i = k_M(\Delta_i - \Delta_{i-1}) + a_M(\Delta_i^2 - \Delta_{i-1}^2) + m_i \gamma_M(\dot{\Delta}_i - \dot{\Delta}_{i-1}) + F_i(t), \quad (3)$$

where $\Delta_i = x_{i+1} - x_i$ and $i = 2, \dots, N-1$. The potential is nearly harmonic with a small cubic term. This leads to the linear and parabolic force terms in the coupling force of Eq. (3), where m_i is the mass of the oscillator, k_M is the spring constant, a_M is the anharmonicity parameter, and γ_M is a material specific damping constant.^{31,32} At the interface

of LSMO and STO the differential equation is asymmetric, since k_M , a_M , and γ_M cannot be factored out as in Eq. (3). The first and the last oscillator have no opponent. This defines the boundary condition. We used $N = 48182$ oscillators, i.e., the first $9.4 \mu\text{m}$ of the STO substrate are included in the lattice dynamics simulations.

The elastic properties of LSMO and STO were taken from the literature.^{24,25} For the anharmonicity of STO we made a first approximation from the hydrostatic pressure dependence of the elastic constants, which leads directly to a qualitative agreement.² We then varied the anharmonicity of STO and LSMO to find quantitative agreement of the theory with the experimental data. The final value of the anharmonicity of STO reads $1.8 \times 10^{13} \text{ kg s}^{-2} \text{ m}^{-1}$, which is only 10% smaller than the first guess. The anharmonicity in the LSMO transducer film has only little influence on the dynamics because of the short propagation length. For this we finally used a value of $3 \times 10^{13} \text{ kg s}^{-2} \text{ m}^{-1}$. For the damping parameter γ_i we used a value which yields good agreement for phonon damping in STO observed by UXRD.⁵

$F_i(t)$ describes the driving force of the oscillators due to the optical excitation process. We assume an instantaneous force step $F_i(t)$ at time zero according to the strong electron-phonon coupling in the metallic oxides.⁸ The spatial excitation profile $F_i(t)$ follows an exponential decay determined by the penetration depth of the optical pump light. Accordingly, deeper-lying unit cells exhibit less expansion.²¹

Figure 4(a) shows the simulated strain profile for different times after excitation of the sample with the smallest (black line) and largest (blue line) strain amplitude in the copropagating frame of reference. The center of the bipolar pulse which has a strain level close to zero propagates with the normal speed of sound, which is only valid in the harmonic approximation. In the regions with high amplitude the strain modulates the elastic constants. This nonlinear interaction between the masses changes the shape of the bipolar pulse, in particular leading to a self-steepening pulse front and tail. The tensile part is slower and the compressive part is faster than the sound velocity v_s of the harmonic linear chain. The speed of the pulse front propagation is read from the simulation and indicated in Fig. 3 as stars. The good agreement verifies the interpretation of the measured splitting of the sound velocity distribution.

For further comparison to the measurement and to interpret the impact of the anharmonic interaction on the classical decoupled oscillators called phonons, we analyze the simulated strain profiles in Fig. 4(a) by calculating the Fourier amplitudes $A(k_p, t)$ of sinusoidal waves composing the wave packet for each time delay t . This is essentially an amplitude of phonons (decoupled modes) which describes the wave packet. For better comparison to the experimental observable we plot A/λ in Fig. 4(c), because for a transparent medium the reflectivity modulations scale inversely with λ according to equations (35–38) in the seminal paper of Thomsen *et al.*²³ The distribution of coherently excited phonons rapidly shifts to smaller k_p vectors.

Figure 4(b) shows the amplitude of the measured Brillouin oscillations [Fig. 2(b)], which is proportional to the phonon amplitude of the phonon with wave vector k_p .²³ During the time sequence 240, 320, and 410 ps the first minimum of

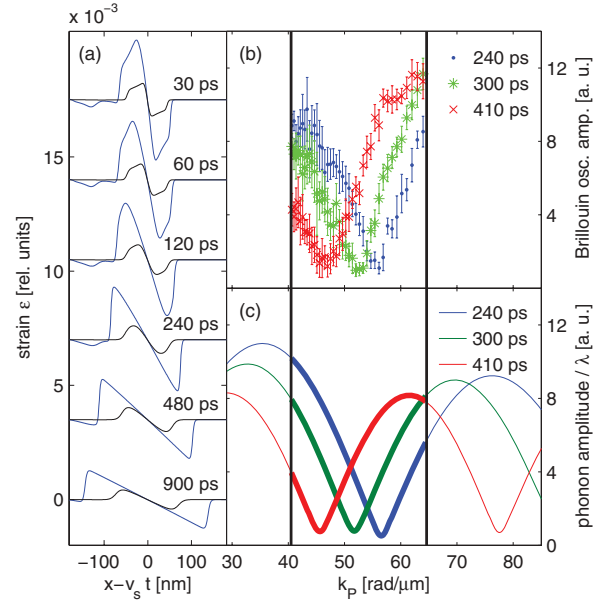


FIG. 4. (Color) (a) Spatial profile of the bipolar strain pulse in the STO for different propagation times in a frame of reference propagating with the speed of sound v_s , for high amplitude (blue line, 0.47% strain) and low amplitude (black line, 0.14% strain). For large amplitude, the tensile part of the pulse propagates with subsonic speed and the compressive part propagates with supersonic speed indicated by the stars in Fig. 3. (b) Measured amplitude of oscillations for each wavelength connected to the wave vectors by the Brillouin backscattering condition. The region between the vertical black lines indicates the wave vectors that can be accessed by the optical white light. (c) Phonon amplitude divided by the wavelength λ (see text) as a function of wave vector calculated from Fourier transforms of the simulated strain profile, showing good agreement with the measurement in panel (b).

the phonon amplitude is moving through the experimental window of observation given by the Brillouin backscattering condition [Eq. (2)]. These minima represent the fact that, at a certain point in time, these phonons are not occupied. This is the fundamental interpretation of the beating of the measured oscillations. The simulation reproduces also the second measured amplitude minimum [Fig. 2(b)], which moves into the observed wavelength range about 700 ps after excitation (not shown).

We now discuss the physics behind the anharmonic linear-chain model leading to the excellent agreement of theory and experiment. Deformations are only reversible if they are infinitely slow and if the thermodynamic system is in equilibrium at any time. This is not the case for phonons which have a finite oscillation period. The phonon has to damp out because of the intrinsic irreversibility of the oscillation. In other words, the coherent phonon amplitude goes down by dissipating energy to the heat bath.^{5,9–12} In our model we consider this fact by the hydrodynamic damping term γ_M in the second line of Eq. (3).

The force term to second order in strain [a_M in Eq. (3)] is given by the anharmonic interactions of atoms which

contribute only for large strain amplitudes. The set of differential equations [Eq. (3)] can be approximated by a Korteweg–de Vries–Burgers equation (KdVB) if the phonon wavelength is much larger than the lattice constant.³³ This is advantageous to find asymptotic solutions such as solitons. Our approach is useful for the calculation of solutions with certain excitation conditions and for considering acoustic mismatches of different materials. We can account for dispersion higher than third order and compute solutions with phonon wavelengths close to the lattice constant.

In conclusion, we determined the transient phonon spectra of nonlinearly propagating strain pulses in strontium titanate

by transient reflectivity measurements for different fluences, which are experimentally calibrated by time-resolved x-ray diffraction. An anharmonic linear-chain model with phonon damping reproduces the measured spectra in a quantitative way and verifies the interpretation of the transient reflectivity measurements. The anharmonicity thus changes the phonon occupation in time and leads to compressive and tensile strain fronts traveling at 1% faster and slower speed, respectively.

We thank the DFG for supporting the project via BA 2281/3-1 and SFB 762.

*bargheer@uni-potsdam.de

¹N. D. Ashcroft, Neil W. Mermin, *Solid State Physics*, 1st ed. (Saunders College, Fort Worth, 1976).

²A. G. Beattie and G. A. Samara, *J. Appl. Phys.* **42**, 2376 (1971).

³A. Koreeda, T. Nagano, S. Ohno, and S. Saikan, *Phys. Rev. B* **73**, 024303 (2006).

⁴S. Brivio, D. Polli, A. Crespi, R. Osellame, G. Cerullo, and R. Bertacco, *Appl. Phys. Lett.* **98**, 211907 (2011); A. Devos, Y.-C. Wen, P.-A. Mante, and C.-K. Sun, *ibid.* **100**, 206101 (2012); S. Brivio, D. Polli, A. Crespi, R. Osellame, G. Cerullo, and R. Bertacco, *ibid.* **100**, 206102 (2012).

⁵M. Herzog, A. Bojahr, J. Goldshsteyn, W. Leitenberger, I. Vrejoiu, D. Khakulin, M. Wulff, R. Shayduk, P. Gaal, and M. Bargheer, *Appl. Phys. Lett.* **100**, 094101 (2012).

⁶K. G. Nakamura, S. Ishii, S. Ishitsu, M. Shiokawa, H. Takahashi, K. Dharmalingam, J. Irisawa, Y. Hironaka, K. Ishioka, and M. Kitajima, *Appl. Phys. Lett.* **93**, 061905 (2008).

⁷C. von Korff Schmising, A. Harpoeth, N. Zhavoronkov, Z. Ansari, C. Aku-Leh, M. Woerner, T. Elsaesser, M. Bargheer, M. Schmidbauer, I. Vrejoiu *et al.*, *Phys. Rev. B* **78**, 060404 (2008).

⁸A. Bojahr, D. Schick, L. Maerten, M. Herzog, I. Vrejoiu, C. von Korff Schmising, C. J. Milne, S. L. Johnson, and M. Bargheer, *Phys. Rev. B* **85**, 224302 (2012).

⁹A. Akhiezer, *J. Phys. (USSR)* **1**, 277 (1939).

¹⁰H. J. Maris, *Phil. Mag.* **12**, 89 (1965).

¹¹W. Chen, H. J. Maris, Z. R. Wasilewski, and S.-i. Tamura, *Philos. Mag.* **70**, 687 (1994).

¹²B. C. Daly, K. Kang, Y. Wang, and D. G. Cahill, *Phys. Rev. B* **80**, 174112 (2009).

¹³P. J. S. van Capel and J. I. Dijkhuis, *Appl. Phys. Lett.* **88**, 151910 (2006).

¹⁴P. J. S. van Capel, H. P. Porte, G. van der Star, and J. I. Dijkhuis, *J. Phys.: Conf. Ser.* **92**, 012092 (2007).

¹⁵O. L. Muskens and J. I. Dijkhuis, *Phys. Rev. Lett.* **89**, 285504 (2002).

¹⁶P. J. S. van Capel and J. I. Dijkhuis, *Phys. Rev. B* **81**, 144106 (2010).

¹⁷H. Y. Hao and H. J. Maris, *Phys. Rev. B* **64**, 064302 (2001).

¹⁸H. J. Maris and S. Tamura, *Phys. Rev. B* **84**, 024301 (2011).

¹⁹G. Shirane and Y. Yamada, *Phys. Rev.* **177**, 858 (1969).

²⁰D. Schick, A. Bojahr, M. Herzog, C. von Korff Schmising, R. Shayduk, W. Leitenberger, P. Gaal, and M. Bargheer, *Rev. Sci. Instrum.* **83**, 025104 (2011).

²¹M. Herzog, D. Schick, P. Gaal, R. Shayduk, C. von Korff Schmising, and M. Bargheer, *Appl. Phys. A* **106**, 489 (2012).

²²K. Sokolowski-Tinten, C. Blome, C. Dietrich, A. Tarasevitch, M. Horn von Hoegen, D. von der Linde, A. Cavalleri, J. Squier, and M. Kammler, *Phys. Rev. Lett.* **87**, 225701 (2001).

²³C. Thomsen, H. T. Grahn, H. J. Maris, and J. Tauc, *Phys. Rev. B* **34**, 4129 (1986).

²⁴Y. H. Ren, M. Trigo, R. Merlin, V. Adyam, and Q. Li, *Appl. Phys. Lett.* **90**, 251918 (2007).

²⁵R. O. Bell and G. Rupprecht, *Phys. Rev.* **129**, 90 (1963).

²⁶M. Woerner, C. von Korff Schmising, M. Bargheer, N. Zhavoronkov, I. Vrejoiu, D. Hesse, M. Alexe, and T. Elsaesser, *Appl. Phys. A* **96**, 83 (2009).

²⁷E. Pontecorvo, M. Ortolani, D. Polli, M. Ferretti, G. Ruocco, G. Cerullo, and T. Scopigno, *APPLAB* **98**, 011901 (2011).

²⁸H. Ogi, T. Shagawa, N. Nakamura, M. Hirao, H. Odaka, and N. Kihara, *Phys. Rev. B* **78**, 134204 (2008).

²⁹M. Cardona, *Phys. Rev.* **140**, A651 (1965).

³⁰M. Herzog, D. Schick, W. Leitenberger, R. Shayduk, R. M. van der Veen, C. J. Milne, S. L. Johnson, I. Vrejoiu, and M. Bargheer, *New J. Phys.* **14**, 013004 (2012).

³¹L. D. Landau and E. M. Lifshitz, *Course of Theoretical Physics, Theory of Elasticity* (Pergamon Pr., London, 1986), Vol. 7.

³²E. Arévalo, Y. Gaididei, and F. G. Mertens, *Eur. Phys. J. B* **27**, 63 (2002).

³³E. Arévalo, F. G. Mertens, Y. Gaididei, and A. R. Bishop, *Phys. Rev. E* **67**, 016610 (2003).

PAPER XV

Coupling of GHz Phonons to Ferroelastic Domain Walls in SrTiO₃

L. Mearten, A. Bojahr, M. Gohlke, M. Roessle and
M. Bargheer.

Phys. Rev. Lett. **114**, 047401 (2015).

Coupling of GHz Phonons to Ferroelastic Domain Walls in SrTiO₃

L. Maerten,¹ A. Bojahr,¹ M. Gohlke,¹ M. Rössle,¹ and M. Bargheer^{1,2,*}

¹*Institut für Physik & Astronomie, Universität Potsdam, Karl-Liebknecht-Strasse 24-25, 14476 Potsdam, Germany*

²*Helmholtz-Zentrum-Berlin für Energie und Materialforschung, Wilhelm-Conrad-Röntgen Campus, BESSY II, Albert-Einstein-Strasse 15, 12489 Berlin, Germany*

(Received 1 November 2013; published 28 January 2015)

We study the linear and nonlinear acoustic response of SrTiO₃ across its ferroelastic transition at $T_a = 105$ K by time domain Brillouin scattering. Above T_a we observe that for a strain amplitude of $\sim 0.18\%$ the sound velocity for compressive strain exceeds the tensile strain velocity by 3%. Below T_a we find a giant slowing down of the sound velocity by 12% and attribute this to the coupling of GHz phonons to ferroelastic twin domain walls. We propose a new mechanism for this coupling on the ultrafast time scale, providing an important new test ground for theories used to simulate atomic motion in domain forming crystals.

DOI: 10.1103/PhysRevLett.114.047401

PACS numbers: 78.35.+c, 62.25.Fg, 63.20.Ry, 78.20.hc

SrTiO₃ (STO) is a dielectric perovskite which exhibits quantum paraelectric behavior at low temperatures [1]. It is widely used as a substrate material for the growth of perovskite thin films, e.g., to create novel nanoelectronic phenomena and applications. Hence, understanding the dynamics of the domain pattern in the substrate is crucial [2,3]. The various structural phase transitions and the domain pattern of STO have been subject to extensive research [4–12]. The elastic behavior of STO has been studied since the 1960s [13–16] and has recently attracted attention due to the observation of a very high mobility of domain walls in the antiferrodistortive phase [5,17].

STO undergoes an antiferrodistortive phase transition at $T_a = 105$ K, where the oxygen octahedra in adjacent unit cells rotate against each other around one of the cubic axes [18]. This motion is described by a triply degenerate optical zone edge mode, which softens towards the phase transition [11,19]. It is accompanied by a doubling of the unit cell and a small tetragonal elongation of the c axis oriented parallel to the rotational axis of the octahedra [4,11]. Domains are formed with the elongated axis oriented in one of the three possible directions. The formation of these so-called twin domains can be suppressed by external pressure [17,20], is altered near the crystal surface [12], and is strongly influenced by the presence of a surface layer [10]. The coupling of acoustic phonons to the soft optic mode leads to an anomaly in the acoustic properties [13,21] of the material and to an increased dissipation at the phase transition [15,16,22]. The induced softening of the acoustic modes at the transition is superimposed by an even larger softening below T_a that can be attributed to the coupling of phonons to domain walls between areas of differently oriented c axes (twin walls) and has been termed superelastic behavior [17]. This additional softening is minimized, when the domain formation is reduced, for example by external pressure [17,20]. The data compilation by

Carpenter shows a large variation of the sound velocity below T_a [9]. However, all data obtained by Brillouin scattering, i.e., experiments sensitive to GHz phonons, show only the small drop in sound velocity at T_a that is attributed to the coupling to the soft mode [22–24].

In this Letter we study the elastic behavior of STO by time domain Brillouin scattering (TDBS) [25]. We start in the regime of linear response and extend our measurements into the regime of nonlinear sound propagation. The amplitude of the strain pulses is calibrated using ultrafast x-ray diffraction (UXRD) [26,27]. When the hypersound strain amplitude exceeds $\sim 0.1\%$, we observe a giant reduction of the sound velocity below T_a , similar to the superelastic behavior observed for low frequency strain. This was previously thought to be impossible for GHz frequencies [17,28,29]. Our experiments suggest that this phenomenon occurs for GHz sound only when the strain amplitude is large enough to establish a new mechanism for coupling to the twin walls. It is enabled when the transient unit cell deformation exceeds the tetragonal distortion. We argue that under these conditions the velocity of the domain wall motion approaches the sound velocity and that the relevant time scale enabling full superelastic behavior is determined by the time $\tau = D/v_s$ it takes lattice deformations to propagate through the average size D of the domains at the speed of sound v_s .

We use optical pump pulses with a wavelength of 800 nm and 120 fs pulse duration at a repetition rate of 5 kHz to excite few nanometer thick metal transducer films on STO substrates. We use excitation fluences in the range between 15 and 45 mJ/cm². The rapid expansion of the metal film launches bipolar strain pulses into the STO which are probed by TDBS: an ultrashort white light continuum pulse generated in a sapphire disc is reflected from the sample and spectrally resolved by a fiber-optic spectrometer for broadband detection [25,26]. This method

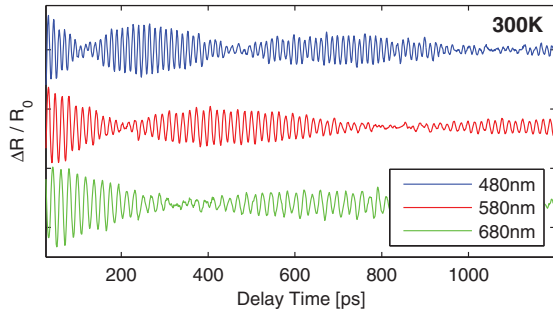


FIG. 1 (color). Transient reflectivity change at room temperature for high excitation fluences, plotted for different probe wavelengths. The curves are shifted vertically for clarity.

relies on the interference of the probe light reflected from the sample surface with a component reflected from the traveling strain pulse. Constructive interference is given when the optical path difference between the interfering light beams amounts to integer multiples of the light wavelength. This leads to a transient reflectivity signal which oscillates at the frequency

$$\nu(\lambda) = v_s 2n(\lambda) \cos(\beta)/\lambda, \quad (1)$$

where λ is the probe wavelength, β is the internal angle of incidence with respect to the surface normal, and $n(\lambda)$ the wavelength dependent refractive index extracted from the literature [30]. The measured oscillation frequency $\nu(\lambda)$ is equal to the frequency $\nu_{\text{ph}}(k_{\text{ph}})$ of the observed phonon with wave vector $k_{\text{ph}} = 2\pi/\lambda_{\text{ph}} = 2\pi 2n(\lambda) \cos(\beta)/\lambda$, for which the Brillouin backscattering condition is fulfilled [25]. Here, λ_{ph} is the wavelength of the detected phonon. The sample is mounted in a closed cycle refrigerator allowing for a temperature dependent series of measurements.

We mainly discuss experimental data obtained from a 37 nm thick (La_{0.7}Sr_{0.3})MnO₃ (LSMO) transducer grown by pulsed laser deposition onto a single-crystalline (100)-STO substrate (CrysTec, Berlin, miscut angle of 0.1°) [31]. Several similar samples have been measured in order to verify the conclusions, as will be discussed in the text below. Figure 1 shows high fluence data for three selected probe wavelengths at room temperature. The raw data are cut shortly after the fast electronic response at $t = 0$ and a slowly varying background is subtracted. The remaining signal oscillates at the frequency given by Eq. (1). In addition, the signal oscillations are modulated by a slow beating

$$\nu_{\text{beating}} = \Delta v_s 2n(\lambda) \cos(\beta)/\lambda, \quad (2)$$

which can be attributed to the difference Δv_s of the sound velocities present in the material [26]. In this case, for large

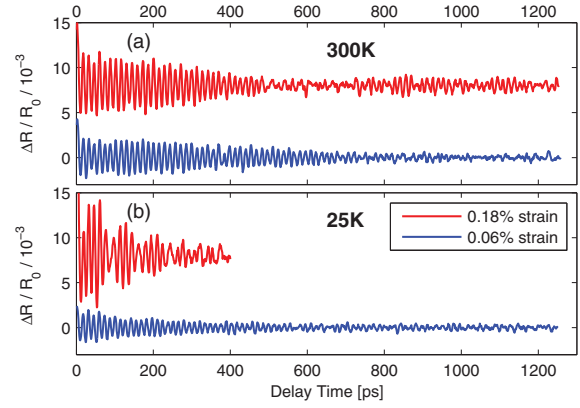


FIG. 2 (color). Transient reflectivity traces for (a) $T = 300$ K and (b) $T = 25$ K and two different strain amplitudes evaluated at $\lambda = 528$ nm ($\nu = 71$ GHz). The curves are shifted vertically for clarity.

amplitude strain in STO at room temperature, the sound velocity for compressive strain is larger than that for tensile strain. This is supported by calculations using an anharmonic linear chain model [26] and by UXRD experiments using acoustic pulse trains [32]. In Fig. 2 the beating is only present for large strain amplitudes (red curves). In the linear regime (low fluence, blue curves), we obtain a single Brillouin oscillation frequency $\nu(\lambda)$, i.e., a single value for the sound velocity. The amplitude of the generated sound pulse in STO has been calibrated by measuring the maximum expansion of the LSMO film after 6 ps using UXRD with 200 fs time resolution [26]. The strain amplitude in the STO amounts to half of the maximum strain in the LSMO weighted by the ratio of the sound velocities [13,26,33]. Figure 2(a) shows two measurements at room temperature. Figure 2(b) shows the same traces for $T = 25$ K, which look similar to the room temperature data for small strain amplitudes. The beating frequency for high excitation, however, is strongly temperature dependent. Additionally, we note that in the high excitation regime the oscillations are damped out comparatively fast. The Fourier transform of the signal yields the oscillation frequencies from which the sound velocity can be computed according to Eq. (1). The result is a velocity distribution [26], which reflects the fact that for large amplitude waves, compressive and tensile strains propagate at different sound velocities [32,34]. We extract the sound velocities for all temperatures at small and large strain levels. Figure 3(a) shows the sound velocity distribution for high excitation at four different temperatures computed from the signal at $\lambda = 528$ nm ($\nu \approx 70$ GHz). Figure 3(b) collects the maxima of the sound velocity distributions for low (open circles) and high (full circles) excitation as a function of temperature. In the linear regime, a sudden softening at the phase transition is observed in quantitative agreement with the literature

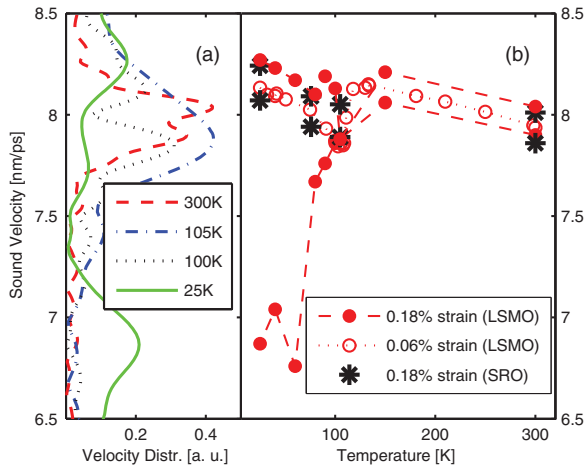


FIG. 3 (color). (a) Sound velocity distribution extracted from the Fourier transform of the transient reflectivity data shown in Fig. 2, for 0.18% strain amplitude in STO at selected temperatures generated by excitation of an LSMO transducer. (b) Extracted maxima from panel (a) as a function of temperature. Red open and full circles: sound velocities in STO for the LSMO transducer; black stars: sound velocities in STO for the SRO transducer. For strain amplitude refer to legend.

[14,22]. This softening close to the phase transition originates from the coupling of the strain wave to the soft mode describing the structural phase transition at T_a [9]. In the nonlinear regime and at temperatures above T_a we observe a temperature independent, symmetric splitting, which can be explained by the anharmonicity of the interatomic potential, as discussed in detail for the room temperature data [26]. Below T_a a giant reduction of the sound velocity is observed that exceeds the symmetric splitting and cannot only be explained by anharmonicity [35–37]. This reduction is comparable to the superelastic softening of the elastic constants in STO which has so far only been found for lower frequency phonons in the Hz to MHz regime and is attributed to the coupling of phonons to (twin) domain walls [5,17,20,28,29]. It is accompanied by an increased damping, which is observed for the low T high fluence data in Fig. 2. The scattering of the data at low T in Fig. 3 might be due to additional phase transitions discussed in the literature [4,5,17].

We confirm that the giant softening for large amplitude GHz strain waves originates from the coupling to twin walls by repeating the experiments for similar samples with different epitaxial strain conditions: we used two STO samples with 15 nm and 70 nm thick SrRuO₃ (SRO) transducer films and 20, 37, and 90 nm thick LSMO films. SRO transducers lead to a tensile strain at the interface, and therefore to a compressive out-of-plane strain in the STO substrate material. This suppresses the formation of domains with the elongated tetragonal c axis parallel to the direction of the strain pulse traveling perpendicular to

the surface in a similar way [38] as observed for static external stress [17,20,39].

In contrast, x-ray diffraction measurements on STO with a thin YBa₂Cu₃O₇ top layer prove that a transducer with a smaller lattice constant, such as LSMO, leads to mixed domains with the c axis aligned either parallel or perpendicular to the surface within the first micrometers of the STO substrate [10]. Indeed, all samples with LSMO transducers show a giant softening due to the interactions with the twin walls, while samples with SRO transducers should not. Low fluence TDBS data for the samples with SRO transducers (not shown) yield sound velocities in agreement with LSMO transducers for small strain levels [open symbols in Fig. 3(a)]. For large strain amplitudes the data obtained from SRO transducers (black stars in Fig. 3) are in accord with the results for LSMO transducers only for temperatures above T_a . Below T_a the sound velocity exhibits the same small but symmetric splitting of the sound velocities observed above T_a . These experiments with SRO transducers show that the alignment of the long c axis relative to the sample surface also removes the coupling of large amplitude GHz strain to the domain walls. The measurements with LSMO samples of different thicknesses (20 and 90 nm) confirm the results for the 37 nm LSMO film reported above.

Figure 4(a) visualizes a twin wall in STO according to the literature [2,3]. The shaded grey area visualizes the stress in the crystal in the vicinity of a kink in the wall as observed in simulations [7,8]. In the following we call the region on the upper left side of the domain wall A where the long c axis is perpendicular to \mathbf{k}_{ph} . The region on the lower right with the c axis oriented along \mathbf{k}_{ph} is addressed as B . For a slow and small expansion of the crystal, the domain wall travels by moving the kink parallel to the wall along the thin black arrow [7,17]. This increases domains with the c axis along \mathbf{k}_{ph} and decreases region A . In total, the crystal is expanded more along \mathbf{k}_{ph} than without domain wall motion. The crystal appears to be softer; i.e., it has a reduced sound velocity. This process requires a contraction of the crystal perpendicular to the applied stress by the Poisson effect and additionally due to the decreasing number of unit cells with the long c axis perpendicular to the stress. For a homogeneous expansion over the diameter $d_L = 100 \mu\text{m}$, given by the laser excited area, the in-plane contraction would take place on a time scale exceeding $\tau \sim d_L/v_s \sim 12 \text{ ns}$, determined by the time it takes to relax the strain at the sound velocity v_s . This restricts the superelastic regime to the 80 MHz range on a $100 \mu\text{m}$ length scale. For GHz phonons or picosecond strain pulses in the linear regime, twin wall motion is fully suppressed [28,29].

In the nonlinear regime we propose the following mechanism: The transducer with thickness d generates strain waves with wave vector \mathbf{k}_{ph} perpendicular to the sample surface. The fundamental wavelength

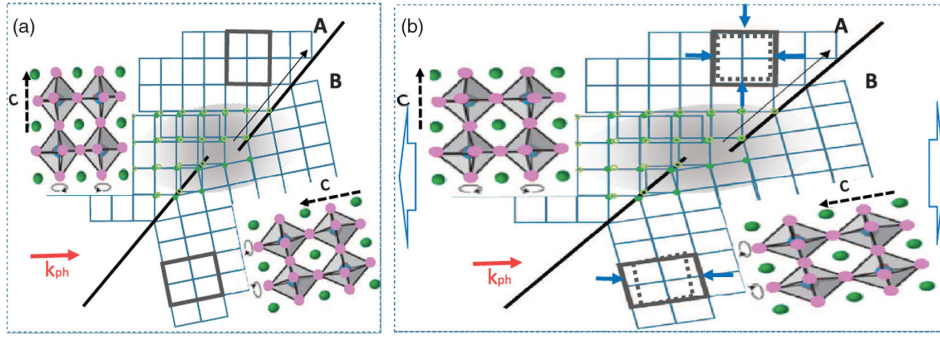


FIG. 4 (color). (a) Schematic of the STO crystal in the tetragonal phase near a kink in a twin wall according to literature [2,3,7,8]. Tetragonal distortion and twinning angle are exaggerated. The shaded grey region highlights the strain field near the kink. (a) Black line: twin wall with kink. Grey rectangles: unit cells of tetragonal phase. Details of these unit cells are shown with oxygen octahedra as enlarged insets. For slow vertical expansion the kink would move along the thin black arrow. (b) Snapshot for ultrafast uniaxial expansive strain along \mathbf{k}_{ph} with amplitude exceeding the original tetragonal distortion (see text). No contraction perpendicular to \mathbf{k}_{ph} can occur for this time scale. Blue narrow arrows: compressive forces that counteract the external uniaxial expansion.

$\lambda_{\text{ph}} = 2\pi/k_{\text{ph}} \leq 2d$ of the strain wave is limited by the thickness d or the optical penetration depth ξ of the exciting light in the transducer. The strain fronts are plane waves since the spot size of the exciting laser light $d_L = 100 \mu\text{m} \gg d$. We first discuss the effect on twin wall motion induced by the expansive part of the bipolar strain pulse. Strain with an amplitude (here 0.18%) much larger than the tetragonal distortion [4,18] ($[c-a]/a = 5 \times 10^{-4}$) leads to expanded tetragonal unit cells [40] in region A with the longer unit cell axis now parallel to \mathbf{k}_{ph} , as schematically shown by the solid grey rectangle in Fig. 4(b). These expanded unit cells in A want to contract in all three dimensions in order to recover their original volume (dotted grey rectangle). Within the domains, all stresses are balanced by adjacent unit cells. In region B the unit cells feel compressive stress (blue arrows) only along \mathbf{k}_{ph} . Thus, at the domain wall the stress perpendicular to \mathbf{k}_{ph} is unbalanced and leads to a motion of the domain wall and the connected strain fields such that region B increases. The reverse effect would be expected for the compressive part of the strain pulse. However, since space is required for the atoms at the domain boundary to rearrange, the coupling is mainly observed for tensile strain.

Figure 4(b) suggests complex microscopic dynamics. The moving domain walls do not separate domains in their equilibrium structure, but rather domains of the crystal with tetragonal nonequilibrium strain. The increased damping and the superelastic effect are intimately connected to propagation of nonequilibrium strain fields around kinks in the twin walls. The importance of lattice inhomogeneities for the propagation of strain waves is emphasized in related experiments: in ferroelectric $\text{Pb}(\text{Zr}_{0.2}\text{Ti}_{0.8})\text{O}_3$ we have observed by UXRD that the sign, amplitude, and frequency of the strain pulses alter the interaction with domain boundaries and dislocations [41]. Similar dependences on the frequency and amplitude of the applied strains

are reported for the velocity of ferroelastic [42] and ferroelectric [43] domain wall motion.

The considerable additional softening at 70 GHz indicates that the twin walls propagate a substantial fraction of the domain size [6] $D \sim 100 \text{ nm}$ within a half period τ of the sound wave. Therefore, the domain wall velocity must be on the order of the sound velocity. Computer simulations on the terahertz time scale have indicated kink-propagation velocities exceeding the sound velocity [8]. Our 12% reduction in sound velocity for 70 GHz large amplitude strain compares to a 50% reduction of the Young's modulus measured at 10 Hz [17]; i.e., we observe about half the softening effect.

In summary, we have performed time domain Brillouin-scattering experiments and measured the sound velocity in STO at different temperatures for various strain amplitudes. In the nonlinear regime of $\sim 0.18\%$ strain the sound velocity of compressive strain exceeds the velocity for tensile strain by 3% for temperatures above $T_a = 105 \text{ K}$. Below T_a a substantial softening of 12% is observed, which is attributed to a coupling of the GHz longitudinal phonons to twin domain walls. This behavior is observed for transient strains exceeding the tetragonal distortion in the low temperature phase, suggesting a different mechanism inducing the domain wall motion than for lower, Hz to MHz frequency sound. Our observations highlight the importance of understanding the coupling of strain waves to domain walls in domain forming samples. Our UXRD calibrated measurements provide a good testing ground for simulations attempting to predict the domain dynamics accompanying structural phase transitions in complex oxides.

We thank I. Vrejoiu and D. Schlom for providing the samples. We acknowledge the financial support by the Leibniz Graduate school DinL and the BMBF via 05K2012-OXIDE.

- *bargheer@uni-potsdam.de; www.udkm.physik.uni-potsdam.de.
- [1] K. A. Müller and H. Burkard, *Phys. Rev. B* **19**, 3593 (1979).
 - [2] M. Honig, J. A. Sulpizio, J. Drori, A. Joshua, E. Zeldov, S. Ilani, and W. Schranz, *Nat. Mater.* **12**, 1112 (2013).
 - [3] B. Kalisky *et al.*, *Nat. Mater.* **12**, 1091 (2013).
 - [4] F. W. Lytle, *J. Appl. Phys.* **35**, 2212 (1964).
 - [5] J. F. Scott, E. K. H. Salje, and M. A. Carpenter, *Phys. Rev. Lett.* **109**, 187601 (2012).
 - [6] J. Chrosch and E. K. H. Salje, *J. Phys. Condens. Matter* **10**, 2817 (1998).
 - [7] E. K. H. Salje, X. Ding, Z. Zhao, T. Lookman, and A. Saxena, *Phys. Rev. B* **83**, 104109 (2011).
 - [8] E. Salje, Z. Zhao, X. Ding, and J. Sun, *Am. Mineral.* **98**, 1449 (2013).
 - [9] M. A. Carpenter, *Am. Mineral.* **92**, 309 (2007).
 - [10] R. Loetzsch, A. Lübcke, I. Uschmann, E. Foerster, V. Grosse, M. Thuerk, T. Koettig, F. Schmidl, and P. Seidel, *Appl. Phys. Lett.* **96**, 071901 (2010).
 - [11] G. Shirane and Y. Yamada, *Phys. Rev.* **177**, 858 (1969).
 - [12] Z. Salman, M. Smadella, W. A. MacFarlane, B. D. Patterson, P. R. Willmott, K. H. Chow, M. D. Hossain, H. Saadaoui, D. Wang, and R. F. Kiefl, *Phys. Rev. B* **83**, 224112 (2011).
 - [13] R. O. Bell and G. Rupprecht, *Phys. Rev.* **129**, 90 (1963).
 - [14] W. Kaiser and R. Zurek, *Phys. Lett.* **23**, 668 (1966).
 - [15] R. Nava, R. Callarotti, H. Ceva, and A. Martinet, *Phys. Rev.* **188**, 1456 (1969).
 - [16] B. Berre, K. Fossheim, and K. A. Müller, *Phys. Rev. Lett.* **23**, 589 (1969).
 - [17] A. V. Kityk, W. Schranz, P. Sondergeld, D. Havlik, E. K. H. Salje, and J. F. Scott, *Phys. Rev. B* **61**, 946 (2000).
 - [18] H. Unoki and T. Sakudo, *J. Phys. Soc. Jpn.* **23**, 546 (1967).
 - [19] T. Kohmoto, K. Tada, T. Moriyasu, and Y. Fukuda, *Phys. Rev. B* **74**, 064303 (2006).
 - [20] K. Fossheim and B. Berre, *Phys. Rev. B* **5**, 3292 (1972).
 - [21] P. A. Fleury, *J. Acoust. Soc. Am.* **49**, 1041 (1971).
 - [22] A. Nagakubo, A. Yamamoto, K. Tanigaki, H. Ogi, N. Nakamura, and M. Hirao, *Jpn. J. Appl. Phys.* **51**, 07GA09 (2012).
 - [23] M. Yamaguchi, T. Yagi, Y. Tsujimi, H. Hasebe, R. Wang, and M. Itoh, *Phys. Rev. B* **65**, 172102 (2002).
 - [24] B. Hehlen, Z. Kallassy, and E. Courtens, *Ferroelectrics* **183**, 265 (1996).
 - [25] A. Bojahr, M. Herzog, S. Mitzscherling, L. Maerten, D. Schick, J. Goldshteyn, W. Leitenberger, R. Shayduk, P. Gaal, and M. Bargheer, *Opt. Express* **21**, 21188 (2013).
 - [26] A. Bojahr, M. Herzog, D. Schick, I. Vrejoiu, and M. Bargheer, *Phys. Rev. B* **86**, 144306 (2012).
 - [27] D. Schick, A. Bojahr, M. Herzog, C. von Korff Schmising, R. Shayduk, W. Leitenberger, P. Gaal, and M. Bargheer, *Rev. Sci. Instrum.* **83**, 025104 (2012).
 - [28] W. Schranz, *Phys. Rev. B* **83**, 094120 (2011).
 - [29] W. Schranz, H. Kabelka, and A. Tröster, *Ferroelectrics* **426**, 242 (2012).
 - [30] M. Cardona, *Phys. Rev.* **140**, A651 (1965).
 - [31] I. Vrejoiu, M. Ziese, A. Setzer, P. D. Esquinazi, B. I. Birajdar, A. Lotnyk, M. Alexe, and D. Hesse, *Appl. Phys. Lett.* **92**, 152506 (2008).
 - [32] R. Shayduk *et al.*, *Phys. Rev. B* **87**, 184301 (2013).
 - [33] Y. H. Ren, M. Trigo, R. Merlin, V. Adyam, and Q. Li, *Appl. Phys. Lett.* **90**, 0251918 (2007).
 - [34] O. L. Muskens and J. I. Dijkhuis, *Phys. Rev. Lett.* **89**, 285504 (2002).
 - [35] A. Hachemi, H. Hachemi, A. Ferhat-Hamida, and L. Louail, *Phys. Scr.* **82**, 025602 (2010).
 - [36] K. S. Viswanathan and B. Subramanyam, *Pramana J. Phys.* **42**, 175 (1994).
 - [37] See Supplemental Material at <http://link.aps.org/supplemental/10.1103/PhysRevLett.114.047401> for fluence dependent measurements and further discussion.
 - [38] The lattice mismatch between SRO and STO amounts to 6×10^{-3} . A uniaxial pressure of 1 MPa, which reduces the superelastic effect by several tens of percent [17], corresponds at room temperature [13] to an induced strain of 3×10^{-6} and is hence orders of magnitude larger than the lattice mismatch in our experiment.
 - [39] T. S. Chang, J. F. Holzrichter, G. F. Imbusch, and A. L. Schawlow, *Appl. Phys. Lett.* **17**, 254 (1970).
 - [40] The memory of the original *c*-axis orientation is rapidly lost since the thermal oxygen octahedra-tilt motion is fast compared to the duration of the passing strain pulse [19].
 - [41] D. Schick, A. Bojahr, M. Herzog, P. Gaal, I. Vrejoiu, and M. Bargheer, *Phys. Rev. Lett.* **110**, 095502 (2013).
 - [42] R. J. Harrison, S. A. T. Redfern, and E. K. H. Salje, *Phys. Rev. B* **69**, 144101 (2004).
 - [43] S. Lisenkov, I. Ponomareva, and L. Bellaiche, *Phys. Rev. B* **79**, 024101 (2009).

PAPER XVI

Following Strain-Induced Mosaicity Changes of Ferroelectric Thin Films by Ultrafast Reciprocal Space Mapping

D. Schick, A. Bojahr, M. Herzog, I. Vrejoiu and
M. Bargheer.

Phys. Rev. Lett. **110**, 095502 (2013).

Following Strain-Induced Mosaicity Changes of Ferroelectric Thin Films by Ultrafast Reciprocal Space Mapping

D. Schick,¹ A. Bojahr,¹ M. Herzog,¹ P. Gaal,² I. Vrejoiu,³ and M. Bargheer^{1,2,*}

¹*Institut für Physik und Astronomie, Universität Potsdam, Karl-Liebknecht-Straße 24-25, 14476 Potsdam, Germany*

²*Helmholtz-Zentrum Berlin für Materialien und Energie GmbH, Wilhelm-Conrad-Röntgen Campus, BESSY II, Albert-Einstein-Straße 15, 12489 Berlin, Germany*

³*Max-Planck-Institut für Mikrostrukturphysik, Weinberg 2, 06120 Halle, Germany*

(Received 24 October 2012; revised manuscript received 14 January 2013; published 26 February 2013)

We investigate coherent phonon propagation in a thin film of ferroelectric $\text{PbZr}_{0.2}\text{Ti}_{0.8}\text{O}_3$ (PZT) by ultrafast x-ray diffraction experiments, which are analyzed as time-resolved reciprocal space mapping in order to observe the in- and out-of-plane structural dynamics, simultaneously. The mosaic structure of the PZT leads to a coupling of the excited out-of-plane expansion to in-plane lattice dynamics on a picosecond time scale, which is not observed for out-of-plane compression.

DOI: [10.1103/PhysRevLett.110.095502](https://doi.org/10.1103/PhysRevLett.110.095502)

PACS numbers: 61.72.Hh, 07.85.Jy, 61.05.cp, 63.22.Np

Oxides are attractive constituents of future nanoelectronic devices because of their broad spectrum of outstanding physical properties, such as ferroelectricity and ferromagnetism, and owing to the progress made in the fabrication of high quality epitaxial heterostructures [1]. Epitaxial strain engineering and the careful choice of mechanical and electrical boundary conditions enable a direct influence on these functionalities [2–6]. Structural defects and nanoscale inhomogeneities, such as dislocations and domains, typically affect the properties of functional oxides and have been extensively studied by experiment and theory [7,8]. Ultrafast x-ray diffraction (UXRD) emerged as a powerful tool to observe lattice motion in real time [9–11] and has provided a deeper insight in the structure-property relations of functional oxides on ultrashort time scales. Recent femtosecond x-ray scattering experiments on ferroelectric oxides showed that electron screening induces an ultrafast piezoelectric response of the lattice [12] and that in turn, the deformation leads to a change of the polarization [13]. However, these experiments were conducted on rather perfect epitaxial crystals. The influence of nanodomains has been considered in experiments on transient phases [14], but the role of static structural defects remained unexplored on such an ultrafast time scale.

Here, we exemplify how ultrafast reciprocal space mapping (URSM) using a laser-based plasma x-ray source yields direct additional information on the reversible in-plane structure dynamics in a ferroelectric perovskite $\text{PbZr}_{0.2}\text{Ti}_{0.8}\text{O}_3$ (PZT) film which is solely induced by the existence of dislocations typical of such materials. In particular, the width of the PZT Bragg reflection reports that tensile out-of-plane strain leads to drastically increased damping. The energy dissipates into in-plane strain which is evidenced by the in-plane component of the reciprocal space map. Our results indicate that in mismatched epitaxial films of oxide materials, with their high

susceptibility to the formation of domains and dislocations, in-plane phenomena emerge on a hundred picosecond time scale. URSM yields the relevant information on lateral lattice dynamics in such materials in which nanoscale inhomogeneities inherently broaden the peaks in reciprocal space. It is important to realize that such inhomogeneities are a natural paradigm in oxides originating from competing phases with similar free energy rather than a result of imperfect crystal growth [7]. A better understanding of such time-domain effects in novel functional oxide materials will be important for studying the influence of structural defects on the ultrafast response of collective phenomena, such as piezoelectricity.

As a typical structure, we grew a ferroelectric layer of PZT and a metallic SrRuO_3 (SRO) electrode layer onto an SrTiO_3 (STO) substrate by pulsed laser deposition (PLD) [15]. The transmission electron micrograph (TEM) image [Fig. 1(a)] shows layer thicknesses of $d_{\text{PZT}} = 207$ nm and $d_{\text{SRO}} = 147$ nm, respectively. The average lattice

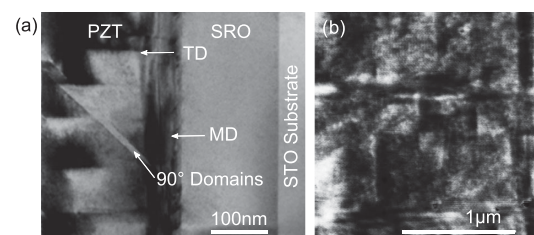


FIG. 1. TEM and AFM images of the PZT-SRO double layer grown onto an STO substrate by PLD. (a) The cross section TEM micrograph reveals that a minority of 90° a -domains are embedded in the matrix of the c -axis grown tetragonal PZT film, as proved by the AFM topography image in (b) as well. Misfit dislocations (MD) and threading dislocations (TD) formed at the SRO-PZT interface and across the PZT film account for the lateral inhomogeneity on a sub-100 nm length scale.

constants normal to the sample surface derived from static x-ray diffraction are $c_{\text{PZT}} = 4.130 \text{ \AA}$ and $c_{\text{SRO}} = 3.948 \text{ \AA}$. The TEM image [Fig. 1(a)] features only a few a -domains in the PZT layer, which are domains with a polarization vector pointing normal to the c -axis of the layer [15]. Accordingly, out-of-plane polarized domains are called c -domains. The small amount of a -domains is confirmed by the very weak scattering observed around 3.12 \AA^{-1} in the static and transient rocking curves in Figs. 2(a)–2(c). We neglect these ferroelastic domains and the switching between the 90° polarizations states in the further discussion. Due to stress relaxation in the mismatched epitaxial PZT film, misfit dislocations (MD) at the SRO interface

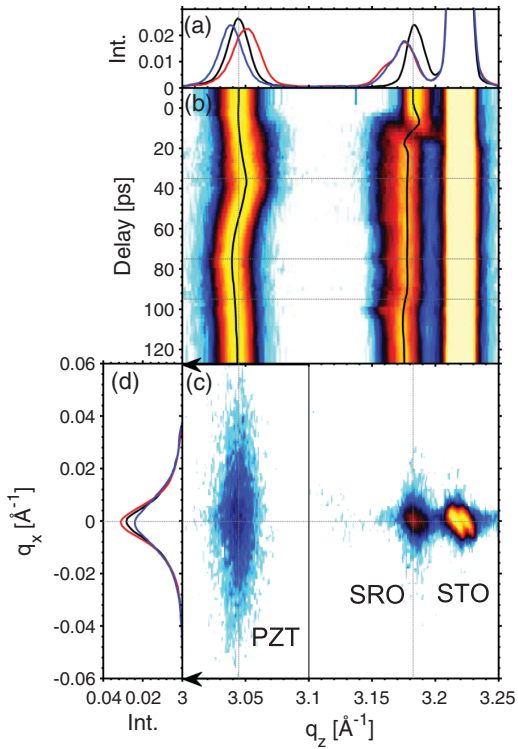


FIG. 2 (color). Transient x-ray diffraction measurements and static reciprocal space map of the PZT-SRO sample. (a) θ - 2θ scans of the structure around the (0 0 2) Bragg reflections of PZT, SRO, and STO before excitation (black) and at delays of maximum peak shift s_z of PZT, at $t = 35 \text{ ps}$ (red) and $t = 75 \text{ ps}$ (blue). (b) Transient θ - 2θ scans for continuous variation of $-10 < t < 125 \text{ ps}$. The horizontal dashed lines indicate the delays of the selected plots shown in panels (a) and (d). The solid black lines indicate the center of the Bragg peaks. (c) The reciprocal space map of the PZT-SRO double layer sample before excitation features a rather broad PZT peak in q_x direction. All peaks widths suffer from an additional broadening due to the convergence and energy bandwidth of the incident x-rays. (d) Intensity of the PZT peak integrated over the q_z dimension before excitation (black) and at delays of change of peak width w_x of PZT, at $t = 35 \text{ ps}$ (red) and $t = 95 \text{ ps}$ (blue).

and threading dislocations (TD) expanding through the entire layer are visible in Fig. 1(a) [15]. As a result, lateral regions below 100 nm size are observable in PZT, whereas the SRO layer is free of such inhomogeneities. Nevertheless, the AFM topography in Fig. 1(b) reveals that the mean roughness of the PZT surface is below 2 \AA .

In order to characterize the response of the PZT film to ultrashort stress pulses, we excited the SRO electrode with near-infrared (800 nm) femtosecond light pulses with a pulse duration of $\tau_{\text{opt}} = 40 \text{ fs}$ and monitored the induced lattice dynamics by UXR experiments at a laser-driven plasma x-ray source (PXS) [16,17] in a pump-probe scheme. The generated hard x-ray pulses [$E = 8.05 \text{ keV}$ ($\text{Cu } K_\alpha$), $\tau_{\text{x-ray}} = 150 \text{ fs}$] were collected by a Montel multilayer mirror and focused onto the sample with a convergence of 0.3° . The diffracted photons were accumulated with a CMOS hybrid-pixel area detector in classical θ - 2θ geometry. This allowed for detecting symmetrically and asymmetrically diffracted x-ray photons at the same time, avoiding time-consuming mesh scans in order to measure reciprocal space maps (RSM) around specific Bragg reflections [18–21]. Consequently, we acquired information both on in-plane and out-of-plane structure dynamics utilizing this time-resolved version of RSM. The temporal overlap of the optical pump and x-ray probe pulses was determined in an independent cross correlation experiment [22] and was set to the delay 0 ps.

First, we discuss the conventional x-ray diffraction from lattice planes parallel to the surface. Figure 2(a) shows the θ - 2θ scans for three different time delays between optical pump and x-ray probe pulses. The black line represents the unexcited lattice and we can confirm the lattice constants of the three constituting materials from the respective Bragg angles. The photoinduced dynamics are evident from the changes of the three material specific Bragg reflections, which are shown in Fig. 2(b). By fitting each Bragg reflection for each material with a Gaussian, we can extract the peak width $w_z(t)$ (FWHM) and peak center $c_z(t)$ for each delay t in the q_z dimension. For the later analysis, it is convenient to introduce the peak shift $s_z(t) = c_z(t) - c_z(0)$. The absorption of the pump pulse takes place exclusively in the SRO electrode layer, leading to a quasi-instantaneous temperature rise. The heat expansion of SRO by 0.35% is limited by the speed of sound in the material and proceeds within 24 ps, evidenced by the shift to smaller Bragg angles [23]. On the same time scale, the substrate shows a tiny shoulder at the high-angle side according to the compression of STO adjacent to the expanding metal layer. Similarly, the PZT film is first compressed by the strain imposed from the expanding SRO; however, it expands after the strain wave is reflected from the sample surface [24]. A detailed evaluation and discussion will be given below.

While this evaluation of UXR signals is straightforward and the example shows the power of the method, we

now discuss how to gain the information on the in-plane dynamics. The RSM before excitation is shown as a contour plot in Fig. 2(c). In general, the size of the reciprocal lattice points in the RSM is inversely proportional to the length scale of coherently scattering regions of the crystal in the according in-plane and out-of-plane directions. The additional broadening due to the instrument function of the x-ray diffraction setup, which is mainly given by the 0.3° convergence and Cu K_α energy bandwidth of the incident x-rays, can be seen in the peak profile of the structurally perfect STO substrate in the RSM. Figure 2(d) shows the diffraction signal integrated over the q_z range of the PZT peak. Similar to the convention above, we define the width (FWHM) and shift for the q_x dimension as $s_x(t)$ and $w_x(t)$. The large static value of w_x^{PZT} is consistent with the average size of the lateral regions in the PZT layer of about 50 nm observed in the TEM image [Fig. 1(a)]. In crystallography, this broadening of w_x can be described by the model of mosaicity [25], assuming the crystal to consist of small mosaic blocks. These blocks are homogeneous in themselves but the x-rays scattered from different blocks do not sum up coherently. The in-plane size of the blocks defines the lateral correlation length which is inversely proportional to the broadening of the RSM in q_x . Tilting of the blocks can give rise to an additional broadening. These two effects may be distinguished by measuring a RSM around an asymmetrical Bragg reflection [18]. Figure 2(d) shows that w_x increases considerably for snapshots recorded after the reflection of the strain wave at the sample surface.

In order to discuss our experimental results, we apply a 1D model of the sample structure to simulate the lattice dynamics by a linear chain model of masses and springs [26]. These simulations are well established to predict the out-of-plane dynamics but do not consider the in-plane dynamics directly. Therefore, we employ the out-of-plane phonon damping as an adjustable parameter to couple energy to in-plane motion. First, we calculate the temperature rise in the SRO after optical excitation [Fig. 3(a)] from the laser fluence, absorption depth, and heat capacity of this metal. The quasi-instantaneous thermal stress excites coherent acoustic phonons (strain waves) which are launched from the interfaces to the PZT layer and STO substrate. Calculated strain profiles for different delays are depicted in Fig. 3(b). Since heat diffusion from the SRO into the PZT layer can be neglected on this short time scale (≈ 100 ps) [27], the PZT lattice dynamics are exclusively determined by the compression wave traveling from the SRO-PZT interface to the PZT-air interface. Here, the strain wave is reflected and converted into an expansion wave traveling back to the SRO layer and further into the STO substrate. Due to the good acoustic impedance matching of the three materials, we neglect reflections at layer interfaces.

From the simulated spatiotemporal strain map, the resulting transient changes of the x-ray diffraction profile

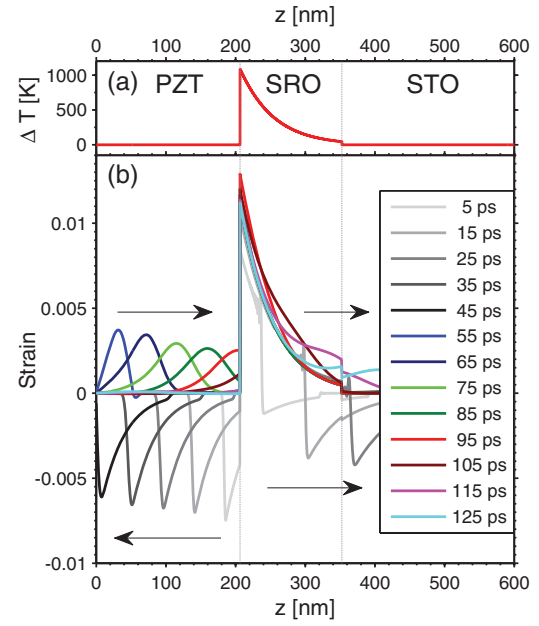


FIG. 3 (color). Simulation results for the temperature gradient and lattice dynamics after optical excitation. (a) The optical pump laser causes a quasi-instantaneous temperature increase only in the metallic SRO layer at delay zero. (b) The excited lattice dynamics are calculated by a 1D linear chain model. The strain profiles show a coherent sound wave with a sharp leading edge traveling from the PZT-SRO interface to the PZT-air interface. It is converted to an expansion wave that undergoes much stronger damping transforming it into a smooth and broad strain profile.

in q_z dimension for the PZT and SRO layers are calculated by dynamical x-ray diffraction theory [28]. Taking the elastic constants of each material, we can use the damping of coherent phonons by impurities and coupling to in-plane motion as adjustable parameters. Figures 4(a), 4(b), 4(d), and 4(e) show the excellent agreement of the simulated x-ray diffraction data with the measured values for s_z and w_z .

The peak shift s_z is a measure of the change of the average c -axis lattice parameter of the PZT and SRO layers, which was qualitatively discussed above. The change of w_z essentially reflects the inhomogeneous strain, which in SRO is given by the short absorption length of the optical pump light leading to a stress exponentially decaying with z . Initially, SRO only expands near the PZT interface. At 12 ps after excitation, the expansion wave has propagated through half the SRO layer, which leads to a maximum w_z^{SRO} [Fig. 4(d)], that in fact reflects a splitting of the SRO Bragg peak [23,26]. Due to the peak splitting, the Gaussian fit indicates a compression of the SRO layer for s_z^{SRO} as long as only a small fraction of SRO is expanded. Similarly to SRO, w_z^{PZT} rises and the peak shifts to larger angles as the compression travels through the PZT

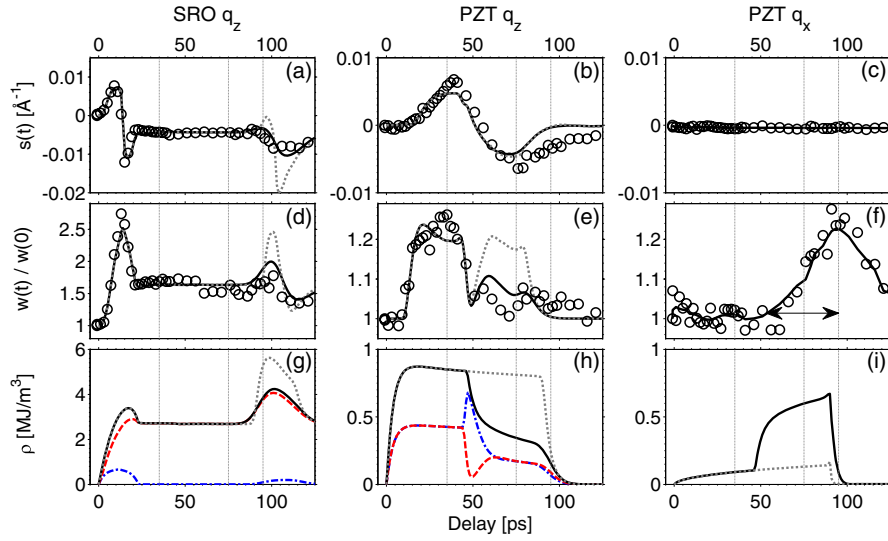


FIG. 4 (color online). (a–f) Comparison of experimental data (circles) with the simulation results (solid black lines). In panels (c) and (f), the solid lines are only guides to the eye. All grey dotted lines are the analogue to the black lines assuming constant damping in PZT. Panels (g) and (h) show the kinetic (dashed-dotted blue), potential (dashed red), and total (solid black) energy density in the according layer. (i) Damped energy density of out-of-plane motion in PZT.

layer [Figs. 4(b) and 4(e)]. Later, s_z^{PZT} becomes negative when the sound wave is reflected at the surface ($t > 50$ ps) and propagates back to the substrate. w_z^{PZT} is much smaller for $t > 50$ ps although the tensile strain during expansion, s_z^{PZT} , has nearly the same magnitude as the preceding compression. This implies that the strain pulse in PZT broadens in space rendering the layer less inhomogeneously strained when the layer expands.

In order to fit these four transient data sets for PZT and SRO [Figs. 4(a), 4(b), 4(d), and 4(e)] simultaneously in our simulations, we have introduced phonon damping in PZT as the only free parameter. The best fit for the four data sets was achieved when the damping factor in PZT is chosen 50 times larger for expansive out-of-plane strain compared to compressive strain of the same magnitude. The according results are plotted as solid black lines in Figs. 4(a), 4(b), 4(d), and 4(e). The grey dotted lines represent the results for a constant damping factor in PZT for expansion and compression. We can exclude pure surface scattering as the reason for the asymmetric damping behavior since this would lead to a much smaller amplitude of s_z^{PZT} in order to achieve the same decrease of w_z^{PZT} for the expansive strain. The increase of the damping in PZT is visualized in Fig. 3(b) where the colored lines ($t > 50$ ps) show a smooth out-of-plane expansion, whereas the greyish lines ($t < 50$ ps) show the inhomogeneous compression before the reflection at the surface changes the sign of the strain wave.

From our lattice dynamics simulations, we can also determine the kinetic (dashed-dotted blue), potential (dashed red), and total (solid black) energy density of the

out-of-plane coherent phonons in each layer [Figs. 4(g) and 4(h)]. We introduced the phonon damping in PZT to couple energy to lateral phonons. This energy is essentially the difference of the total energy of out-of-plane coherent phonons in PZT with and without damping. The result is plotted in Fig. 4(i) where the grey dotted line corresponds again to the case of constant damping. The increase of the lateral energy density in PZT [Fig. 4(i)] goes along with a considerable increase of w_x^{PZT} that reflects a change of the inhomogeneity in-plane, probably because the lateral blocks develop an inhomogeneous in-plane strain that is dynamically coupled to the out-of-plane motion according to the Poisson ratio [Fig. 4(f)]. We do not observe the converse effect during the compression of the PZT layer ($t < 50$ ps). The horizontal arrow in Fig. 4(f) indicates the time scale of the buildup of the lateral strain of approx. 50 ps. We can link this time scale to a lateral length scale of approx. 200 nm via the sound velocity of PZT of 4.6 nm/ps. This time scale agrees well with the in-plane block size observed in the TEM image in Fig. 1(a) and w_x^{PZT} of the static RSM in Fig. 2(c).

The analysis of the measured signal alone already suggests the following interpretation: The expansion of SRO sends a compression wave into PZT. The in-plane mosaicity or nanoinhomogeneity is unchanged during this period. When the strain changes sign upon reflection at the surface, PZT expands and according to Poisson ratio, the mosaic blocks must now laterally contract. The in-plane inhomogeneity is increased as millions of in-plane contraction waves start at all the lateral dislocations. We conclude that only out-of-plane expansion of PZT couples energy

to in-plane dynamics and that this effect is essentially suppressed for out-of-plane compression since this would have to expand the mosaic blocks, which is sterically forbidden by the adjacent blocks. This compares favorably with our simulations of the out-of-plane lattice dynamics, requiring an increased damping for the expansion wave in the PZT, which can be understood as an increase of the coupling between in-plane and out-of plane lattice motions.

In conclusion, we have demonstrated the first measurement of the lattice dynamics in a structurally imperfect thin film by ultrafast reciprocal space mapping (URSM). We do not only extract the changes of the lattice constants, i.e., the expansion and compression of materials perpendicular to the surface. In addition, we quantify the coupled response in plane, which turns out to be significantly enhanced for out-of-plan expansion, as it provides the in-plane contraction necessary for the atoms to start moving. URSM will be an important method for understanding the ultrafast response of oxide crystals with their natural tendency to form nanoscale inhomogeneities.

We thank B. Birajdar (Max-Planck-Institut für Mikrostrukturphysik, Halle, Germany) for performing the TEM imaging. This work was supported by the Deutsche Forschungsgemeinschaft via Grant No. BA 2281/3-1 and by the German Bundesministerium für Bildung und Forschung via Grants No. 03WKP03A and No. 05K10IP1.

*bargheer@uni-potsdam.de

- [1] D. G. Schlom, L.-Q. Chen, X. Pan, A. Schmehl, and M. A. Zurbuchen, *J. Am. Ceram. Soc.* **91**, 2429 (2008).
- [2] H. Han, Y. Kim, M. Alexe, D. Hesse, and W. Lee, *Adv. Mater.* **23**, 4599 (2011).
- [3] N. Bassiri-Gharb, I. Fujii, E. Hong, S. Trolier-McKinstry, D. Taylor, and D. Damjanovic, *J. Electroceram.* **19**, 49 (2007).
- [4] Y. Xu, *Ferroelectric Materials and Their Applications* (North-Holland, Amsterdam, 1991).
- [5] C.-L. Jia, K. W. Urban, M. Alexe, D. Hesse, and I. Vrejoiu, *Science* **331**, 1420 (2011).
- [6] K. S. Lee, J. H. Choi, J. Y. Lee, and S. Baik, *J. Appl. Phys.* **90**, 4095 (2001).
- [7] E. Dagotto, *Science* **309**, 257 (2005).
- [8] E. A. Fitzgerald, *Mater. Sci. Rep.* **7**, 87 (1991).
- [9] A. Rousse, C. Rischel, and J.-C. Gauthier, *Rev. Mod. Phys.* **73**, 17 (2001).
- [10] M. Bargheer, N. Zhavoronkov, M. Woerner, and T. Elsaesser, *Chem. Phys. Chem.* **7**, 783 (2006).
- [11] M. Chergui and A. H. Zewail, *Chem. Phys. Chem.* **10**, 28 (2009).
- [12] D. Daranciang *et al.*, *Phys. Rev. Lett.* **108**, 087601 (2012).
- [13] C. von Korff Schmising, M. Bargheer, M. Kiel, N. Zhavoronkov, M. Woerner, T. Elsaesser, I. Vrejoiu, D. Hesse, and M. Alexe, *Phys. Rev. Lett.* **98**, 257601 (2007).
- [14] H. Ichikawa, S. Nozawa, T. Sato, A. Tomita, K. Ichyanagi, M. Chollet, L. Guerin, N. Dean, A. Cavalleri, S.-i. Adachi, T.-h. Arima, H. Sawa, Y. Ogimoto, M. Nakamura, R. Tamaki, K. Miyano, and S.-y. Koshihara, *Nat. Mater.* **10**, 101 (2011).
- [15] I. Vrejoiu, G. Le Rhun, N. D. Zakharov, D. Hesse, L. Pintilie, and M. Alexe, *Philos. Mag.* **86**, 4477 (2006).
- [16] F. Zamponi, Z. Ansari, C. von Korff Schmising, P. Rothhardt, N. Zhavoronkov, M. Woerner, T. Elsaesser, M. Bargheer, T. Trobitzsch-Ryll, and M. Haschke, *Appl. Phys. A* **96**, 51 (2009).
- [17] D. Schick, A. Bojahr, M. Herzog, C. von Korff Schmising, R. Shayduk, W. Leitenberger, P. Gaal, and M. Bargheer, *Rev. Sci. Instrum.* **83**, 025104 (2012).
- [18] P. F. Fewster, *Crit. Rev. Solid State Mater. Sci.* **22**, 69 (1997).
- [19] V. Holy, U. Pietsch, and T. Baumbach, *High-Resolution X-Ray Scattering from Thin Films and Multilayers*, Springer Tracts in Modern Physics (Springer, Berlin, 1999).
- [20] J. F. Woitok and A. Kharchenko, *Powder Diffr.* **20**, 125 (2005).
- [21] P. F. Fewster, *J. Appl. Crystallogr.* **37**, 565 (2004).
- [22] A. Bojahr, D. Schick, L. Maerten, M. Herzog, I. Vrejoiu, C. von Korff Schmising, C. Milne, S. L. Johnson, and M. Bargheer, *Phys. Rev. B* **85**, 224302 (2012).
- [23] D. Schick, P. Gaal, A. Bojahr, W. Leitenberger, R. Shayduk, A. Hertwig, I. Vrejoiu, M. Herzog, and M. Bargheer (to be published).
- [24] S. H. Lee, A. L. Cavalieri, D. M. Fritz, M. C. Swan, R. S. Hegde, M. Reason, R. S. Goldman, and D. A. Reis, *Phys. Rev. Lett.* **95**, 246104 (2005).
- [25] J. Als-Nielsen and D. McMorrow, *Elements of Modern X-Ray Physics* (John Wiley & Sons, Ltd., New York, 2001).
- [26] M. Herzog, D. Schick, P. Gaal, R. Shayduk, C. von Korff Schmising, and M. Bargheer, *Appl. Phys. A* **106**, 489 (2012).
- [27] R. Shayduk, H. A. Navirian, W. Leitenberger, J. Goldshteyn, I. Vrejoiu, M. Weinelt, P. Gaal, M. Herzog, C. von Korff Schmising, and M. Bargheer, *New J. Phys.* **13**, 093032 (2011).
- [28] M. Herzog, D. Schick, W. Leitenberger, R. Shayduk, R. M. van der Veen, C. Milne, S. L. Johnson, I. Vrejoiu, and M. Bargheer, *New J. Phys.* **14**, 013004 (2012).